Cancer On-Chip: Disease Models for Testing Microbubble-Mediated Drug Delivery

Matthew Bourn

This dissertation is submitted for the degree of Doctor of Philosophy

University of Leeds

July 2022

DECLARATION

The candidate confirms that the work submitted is his own, except where work which has formed part of jointly-authored publications has been included. The contribution of the cadidate and the other authors to this work has been explicitly indicated below. The candidate confirms that the appropriate credit has been given within the thesis where reference has been made to the work of others.

The work in the first results chapter, Chapter 4 of the thesis has appeared in publication as follows:

High-throughput Microfluidics for Evaluating Microbubble-Enhanced Delivery of Cancer Therapeutics in Spheroid Cultures. *Matthew D. Bourn, Damien V.B. Batchelor, Nicola Ingram, James R. McLaughlan, P. Louise Coletta, Stephen D. Evans, Sally A. Peyman*. Journal of Controlled Release, Vol 326, 2020, Pages 13 - 24.* https://doi.org/10.1016/j.jconrel.2020.06.011.

- Matthew D. Bourn developed the system, performed the experiments, collected and analysed the data, and wrote the manuscript.
- Damien V.B. Batchelor performed the ultrasound exposures on each chip and aided with manuscript methods.
- The remaining authors (supervisors) aided conceptually with experimental planning and with manuscript review.

The work in Chapers 5 and 6 is currently under submission to the journal Biomaterials and will appear in publication as follows:

Microfluidic Tumour Vasculature Networks for the Evaluation of Microbubble-Enhanced Delivery of Targeted Liposomes. *Matthew D. Bourn, Safoura Zahed Mohajerani, Georgia Mavria, Nicola Ingram, P. Louise Coletta, Stephen D. Evans, Sally A. Peyman*. (Submitted 14/01/2022)*

- Matthew D. Bourn developed the system, performed all the experiments and analysis, and wrote the manuscript.
- Safoura Zahed Mohajerani identified the optimal batch of endothelial cells for this work using a separate angiogenesis assay. She then transfected the cells with green fluorescent protein to allow for continuous flourescence imaging.

- All remaining authors acted in a supervisory manner and aided conceptially with experimental planning along with reviewing the manuscript prior to submission.

In some parts of the thesis, figures have been reproduced from publications with permission from the copyright holder (license numbers in brackets):

Figure 1: (a) Permission granted by the Royal Society of Chemistry (0003-2654)
(b) Permission granted by the Royal Society (1184352-1)
Figure 2: (a) Permission granted by Springer Nature (5240141398007)
(c) Permission granted by Springer Nature (5203570420892)
Figure 3: (a) Permission granted by the Royal Society of Chemistry (1473-0189)
Figure 4: (a) Permission granted by the American Institute of Physics (1186650-1)
Figure 5: (b) Permission granted by the Royal Society of Chemistry (1473-0197)
Figure 6: (c) Permission granted by Oxford University Press (5240160144788)
Figure 7: (a) Permission granted by Springer (1184364-1)
Figure 11: (a) Permission granted by Oxford Publishing Limited
Figure 14: (a) Permission granted by Oxford University Press (5240160144788)
Figure 26: (a) Permission granted by the Royal Society of Chemistry (1186727-1)
Figure 27: (a) Permission granted by AIP Publishing (5244261406391)

ACKNOWLEDGEMENTS

I would like to start by thanking my supervisors Dr Sally Peyman, Prof Steve Evans, Dr Louise Coletta and Dr Nicola Ingram for all of the mentoring, guidance, and support over the last 4 years. Sal, you gave me confidence in my abilities and convinced me I could actually be a scientist – despite me sending you some very questionable first drafts. Nikki, without your expertise I wouldn't have got half as far as I did, you're a true asset to the group.

A big thanks to Damien Batchelor, a fellow bubble boy and a huge help with some of this work. You answered my endless ultrasound questions and foolishly agreed to help with my 6am experiments, fun times. I'd also like to thank Delanyo Kpeglo and Safoura Mohajerani for their contributions to this project, your cell expertise was invaluable.

I'd like to thank the entire MNP group for their support, advice, and encouragement throughout the last four years. This project would have been twice as difficult without Charcos Fridays, great nights in the Fenton, and various other beer-related activities. I feel very grateful to have spent time in such a friendly, sociable research group.

A special thanks to Joe, Becca, Callam, Rhiannon, and Cian. I'm so lucky to have such a great group of friends. Here's to many more Bath Squad adventures. To my family, thank you for supporting all of my decisions, and for always reminding me how proud you are. Finally, I'd like to thank my wife, Robyn. Without your endless support I know for certain I wouldn't have made it this far. Your warmth and empathy helped me through the many bad science days and encouraged me to stick it out. I'm excited to see what our future together will hold.

ABSTRACT

The effective delivery of drugs to tumours remains a major challenge in the successful treatment of cancer [1]. Whilst many of the new therapeutic treatments developed show promising results when tested *in vitro*, such observations are rarely translated to clinical trials. This results in upwards of 97 % of anti-cancer therapeutics failing to receive approval for clinical use [2]. One of the primary contributors to this issue is the inability of the simplistic 2D cancer cell *in vitro* models to effectively recreate the *in vivo* microenvironment of tumours. In recent years, it has become increasingly evident that the combined use of multicellular 3D cell cultures and microfluidics offers a means of producing organoid systems which closely mimic tumours – overcoming the limitations of 2D models. Indeed, several experiments conducted with pre-existing anti-cancer compounds using such systems have observed responses similar to that of *in vivo* observations, demonstrating their potential utility [3,4].

Whilst many of the anti-cancer therapeutics successfully developed are capable of killing tumour cells, several factors limit their efficacy. Systemic side effects, insufficient drug accumulation and drug-resistant tumour cells all impact the ability of therapeutics to prevent tumour progression [5]. The use of targeted, drug-loaded nanoparticles has previously been proposed as a means of delivering drugs exclusively to the tumour site, allowing for the localised accumulation of high drug concentrations whilst also minimising systemic side effects [6,7]. Compounds such as Doxil, which consist of Doxorubicin (DOX) encapsulated in liposomes, have been successful in reducing systemic side effects and improving the overall clinical outcome after treatment [8,9]. However, there still remains significant room for further improvements and it is evident that further methods of drug delivery must be developed.

Microbubbles (MBs) offer a potential means of improving drug delivery to tumours through a mechanism known as sonoporation. Due to their size and compressibility, gas-filled MBs oscillate when exposed to ultrasound (US) which matches their resonant frequency. Under high acoustic pressures, MBs undergo inertial cavitation where they expand and contract rapidly, producing locally high pressures and temperatures. If this process occurs sufficiently close to a cell membrane, high shear stresses are exerted on the membrane which leads to the production of pores - this process is known as

sonoporation. The opening of pores has been shown to allow for the increased passage of therapeutics into cells, presenting a method of enhancing drug delivery to tumours [10–13]. Whilst several studies have investigated the use of MBs, many of these studies have been conducted on basic 2D cell models known to be inadequate in reproducing *in vivo* responses to treatments.

This project sought to utilise the recent advances in the organ-on-chip field to further the pre-clinical assessment of MB-mediated drug delivery. Experiments conducted throughout this project present the first instance of MB-mediated therapeutic delivery being tested on novel organ-on-chip systems. Two microfluidic organ-on-chip systems were developed in this project. The first system consists of a series of microfluidic traps which capture solid 3D tumours known as spheroids. Both free and liposomal DOX was co-delivered with MBs under constant flow conditions. Dead cell imaging and analysis of spheroid viability revealed that MBs allowed for increased accumulation of DOX and a greater reduction in spheroid viability when co-delivered with either drug formulation. As MBs would be administered intravenously, the first barrier that must be overcome in the tumour-associated vasculature. The second system developed therefore consisted of a fully perfusable vasculature network which, through tumour media conditioning, mimicked tumour-associated vasculature. This system was used to evaluate the use of MBs in enhancing the accumulation of liposomes (LSs) in tumour tissues. LSs were targeted to a membrane integrin protein found to be upregulated in tumour vasculature. Results found that the use of targeting and MBs greatly improved LS accumulation in tumour vasculature compared to healthy vasculature. This provided evidence that the two-fold localised delivery mechanism of targeting and MBs is a promising method by which localised drug delivery to tumours can be enhanced.

CONTENTS

1 Introduction 30

1.1 OVERVIEW 30

1.2 3D CELL CULTURE TECHNIQUES 31

1.3 MICROFLUIDICS FOR 3D CELL CULTURES 34

1.3.1 Spheroid Microfluidic Models 35

1.3.2 Solid Tumour Microfluidic Models 40

1.3.3 Vascularised Microfluidic Models 42

1.4 MICROBUBBLES: ULTRASOUND CONTRAST AGENTS WITH DRUG DELIVERY POTENTIAL 45

1.4.1 Microbubbles as Contrast Agents 46

1.4.2 Microbubble-Mediated Sonoporation 47

1.5 PROJECT AND THESIS OVERVIEW 49

2 Background Theory 52

2.1 COLORECTAL TUMOUR MICROENVIRONMENT AND STRUCTURE 52

2.1.1 Gene Mutation and Colorectal Cancer Development 52

2.1.2 The Tumour Stroma 54

2.1.3 Tumour Vasculature and Endothelial Components 59

2.1.4 Conclusion 62

2.2 MICROFLUIDIC THEORY 62

2.2.1 Navier-Stokes and Poiseuille Flow 63

2.2.2 Flow Using Hydrostatic Pressure 65

2.2.3 Hydrogel Confinement using Micropillars 68

2.3 MICROBUBBLES 73

2.3.1 Microbubble Composition 74

2.3.2 Microbubble Production 75

2.3.3 Microbubble Response to Ultrasound 77

3 Experimental Methods 80

3.1 MICROFLUIDIC DEVICE FABRICATION 80

3.1.1 Silicon Master Production 80

3.1.2 Soft Lithography *84*
3.1.3 Media Reservoir Design and Fabrication *86*
3.2 CELL CULTURE AND MICROFLUIDIC SYSTEM SETUP 87
3.2.1 HCT116 and HFFF2 Culture *87*
3.2.2 HUVEC, HDF and NHLF Culture *88*
3.2.3 Spheroid Production and Characterisation *89*
3.2.4 Off–Chip Spheroid Exposure to Doxorubicin *89*
3.2.5 Spheroid On-Chip Setup *90*
3.2.6 Off-Chip Angiogenesis Assays *91*
3.2.7 Vasculature On-Chip Setup *92*
3.3 MICROBUBBLE AND LIPOSOME PRODUCTION AND CONJUGATION 94
3.3.1 Lipid Preparation *94*
3.3.2 Tip Sonication *94*
3.3.3 Microbubble Production *95*
3.3.4 Targeted PBS-Liposome Production *98*
3.3.5 Production $\alpha_v\beta_3$ -Targeted Liposome Microbubble Conjugates *100*
3.3.6 DOX-LS Production *101*
3.3.7 Drug-Loaded Microbubble (DLMB) Production *104*
3.4 SPHEROID ON-CHIP EXPERIMENTAL PROTOCOL 105
3.4.1 US Coupling On-Chip *105*
3.4.2 Spheroid On-Chip Exposure to Therapeutics *107*
3.4.3 Spheroid Imaging and Analysis *108*
3.5 VASCULATURE ON-CHIP EXPERIMENTAL PROTOCOL 110
3.5.1 Observation of Vessel Permeability *110*
3.5.2 On-chip Integrin-$\alpha_v\beta_3$ Immunostaining *111*
3.5.3 Liposome Perfusion and Imaging *111*
3.5.4 Microbubble – Liposome Conjugate Perfusion *112*
3.5.5 Quantification of Liposome Perfusion *112*
4 Results I: High-throughput microfluidics for evaluating microbubble enhanced delivery of cancer therapeutics in spheroid cultures 113
4.1 MICROFLUIDIC SPHEROID SYSTEM DESIGN AND MODELLING 114
4.1.1 Trap Design and Modelling *114*

4.1.2 Hydrostatic Flow Considerations *119*
4.1.3 Spheroid Shear Stress Modelling using CFD *121*
4.1.4 Spheroid Culture On-chip *123*
4.2 SPHEROID THERAPEUTIC EXPOSURES 124
4.2.1 Off-Chip Dose Response *124*
4.2.2 Free DOX Dose Response *127*
4.2.3 Ultrasound and Microbubble Spheroid Exposure *130*
4.2.4 Co-delivery of Free DOX, Microbubbles and Ultrasound *134*
4.2.5 Co-delivery of Liposomal DOX and Drug Loaded Microbubbles *137*
4.2.6 Conclusion *146*
5 Results II: Development of a Vasculature On-Chip System 148
5.1 MICROFLUIDIC DESIGN AND CONCEPT 149
5.1.1 Micropillar Design *149*
5.1.2 Flow and Pressure Considerations *150*
5.1.3 Measurement of Hydrostatic Flow Rates *154*
5.1.4 Measurement of Interstitial Flow Rates *156*
5.2 DEVELOPMENT AND CHARACTERISATION OF THE VASCULATURE ON-CHIP SYSTEM 161
5.2.1 Determining Optimal Cell Type and Passage *161*
5.2.2 Characterising Vasculature Networks *176*
5.3 RECREATING TUMOUR VASCULATURE USING TUMOUR CELL MEDIA (TCM) 183
5.3.1 Observation of On-chip Integrin $\alpha_v\beta_3$ Expression *185*
5.3.2 Inducing Integrin $\alpha_v\beta_3$ upregulation with TCM *186*
5.3.3 Conditioning Vasculature Networks with TCM *196*
5.4 CONCLUSION 201
6 Results III: Microbubble-Mediated Delivery of $\alpha_v\beta_3$-targeted Liposomes to Tumour Vasculature Networks 204
6.1 PERFUSION OF A_VB_3-TARGETED LIPOSOMES THROUGH VASCULATURE NETWORKS 205
6.1.1 Targeted Liposome Perfusion through Healthy Networks *205*
6.1.2 Targeted Liposome Perfusion through Tumour Vasculature Networks *214*

6.2 PERFUSION OF A_VB_3-LIPOSOME-MICROBUBBLE CONJUGATES THROUGH VASCULATURE NETWORKS 216
6.3 CONCLUSION 222
7 Conclusions and Future Work 224
7.1 CONCLUSIONS 224
7.2 FUTURE WORK 227
7.2.1 Production of a Vascularised Microfluidic Tumour Model 227
7.2.2 Vasculature Models using Endothelial Progenitor Cells 229
7.2.3 Further Applications of Microfluidic Tumour Models 229
Appendix A 233
Appendix B 234
References 236

LIST OF FIGURES

FIGURE 1 – IMAGES DEPICTING HANGING DROP SPHEROID PRODUCTION THROUGH THE USE OF AN INVERTED DROPLET ARRAY AND HUMIDIFICATION CHAMBER [16], FORCED FLOATING SPHEROID PRODUCTION USING WELLS WITH A LOW ADHESION COATING, AND SPINNER FLASK SPHEROID PRODUCTION [21,22]. ALL FIGURES HAVE BEEN REPRODUCED WITH PERMISSION FROM THE COPYRIGHT HOLDER OF EACH PUBLICATION.....32

FIGURE 2 - DIAGRAMS DEPICTING MICROFLUIDIC SYSTEMS DESIGNED TO PRODUCE SPHEROIDS USING HANGING DROP [42], GRAVITY TRAP [40], AND MICROWELL ARRAY [41] TECHNIQUES. ALL FIGURES HAVE BEEN REPRODUCED WITH PERMISSIONS FROM THE COPYRIGHT HOLDER, RSC [40], AND SPRINGER NATURE [40,41].....36

FIGURE 3 – SINGLE CELL TRAPPING ARRAYS DEVELOPED BY DI CARLO ET AL [45]. A) DIAGRAM SHOWING MULTIPLEXED TRAPPING ARRAYS AND SINGLE CHANNEL INPUT, SCALE BAR 500μM. B) DIAGRAM SHOWING TRAPPING CONCEPT WITH A GAP BELOW THE TRAP ALLOWING FOR MEDIA FLOW AROUND THE CELL. C) A HIGH-RESOLUTION IMAGE TAKEN OF CELLS OCCUPYING MULTIPLE TRAPS ACROSS THE ARRAY. FIGURE HAS BEEN TAKEN FROM DI CARLO ET AL WITH PERMISSION FROM THE COPYRIGHT HOLDER [45]. 38

FIGURE 4 – SCHEMATIC OF THE MICROFLUIDIC MICROSPHERE-TRAP ARRAY DESIGNED BY X. XU ET AL [49]. (A) A TOP-DOWN VIEW OF THE ENTIRE SYSTEM SHOWING THE MICROSPHERE INLET, TRAPPING ARRAYS AND OUTLET. INSET *A* SHOWS A ZOOMED-IN VIEW OF THE TRAP ARRAYS AND INSET *B* A SINGLE TRAP. (B) A DIAGRAM DEPICTING THE TRAPPING MECHANISM. PATH P_1 IS DESIGNED TO HAVE A LOWER HYDRAULIC RESISTANCE THEN PATH P_2 ALLOWING A SPHERE TO BECOME TRAPPED. ONCE THE TRAP IS POPULATED, THE RESISTANCE OF PATH P_1 INCREASES AND THE NEXT BEAD FOLLOWS PATH P_2. FIGURE HAS BEEN TAKEN FROM X. XU ET AL WITH PERMISSION FROM THE COPYRIGHT HOLDER [49]. 39

FIGURE 5 – A) SINGLE CHANNEL-CHAMBER CHIP USED BY AYUSO ET AL. FOR THE INVESTIGATION OF CANCER METABOLISM, GENE EXPRESSION AND NATURAL KILLER CELL CYTOTOXICITY (REPRODUCED FROM AYUSO ET AL UNDER CC LICENCE [34]) [50,51,53].

B) A MULTI-CHAMBER TUMOUR ON-CHIP SYSTEM USED BY LUI ET AL. TO DETERMINE THE EFFECTS OF CAFS ON TUMOUR CELL INVASION (REPRODUCED WITH PERMISSION FROM THE RSC) [54]. C) THE MICROFLUIDIC SYSTEM USED BY CARVALHO ET AL. WITH ENDOTHELIAL CELLS (YELLOW) LINING THE MEDIA CHANNEL ADJACENT TO A SOLID TUMOUR (RED) CHAMBER (REPRODUCED FROM CARVALHO ET AL UNDER CC LICENCE) [55]. 41

FIGURE 6 - A) THE MULTI-TISSUE CHAMBER DEVICE USED IN HUGHES' AND LEE'S LABS. ENDOTHELIAL CELLS (RED) CAN BE OBSERVED SELF-ASSEMBLING ACROSS THE 6 DAYS PERIOD, AT WHICH POINT DEXTRAN FLOWS EXCLUSIVELY WITHIN THE NETWORK (REPRODUCED FROM SOBRINO ET AL UNDER CC LICENCE [49]) [65–68]. B) THE MULTI-CHAMBER SYSTEM USED BY KIM ET AL. TO INVESTIGATE THE ROLE OF PERICYTES IN VESSEL FORMATION. FIBROBLASTS CULTURED IN A SEPARATE CHAMBER WERE OBSERVED TO AFFECT VASCULATURE DEVELOPED THROUGH PARACRINE SIGNALLING (REPRODUCED FROM KIM ET AL UNDER CC LICENCE [70]). C) OBSERVED INTERACTION BETWEEN AN ENDOTHELIAL-FIBROBLAST SPHEROID AND SURROUNDING ENDOTHELIAL CELLS. FIBROBLASTS WERE FOUND TO BE NECESSARY TO INDUCE BRANCHING TOWARDS THE SPHEROID (REPRODUCED WITH PERMISSIONS FROM THE COPYRIGHT HOLDER [71]). 44

FIGURE 7 – ULTRASOUND IMAGES OF (A) DEGASSED WATER (DW) AND MBS IN A MICROFLUIDIC CHANNEL. (B) AN *IN VIVO* TUMOUR BEFORE AND AFTER INJECTION OF MICROBUBBLES. IMAGES FROM A REVIEW ARTICLE BY LEE ET AL. WITH PERMISSIONS FROM THE COPYRIGHT HOLDER [73] 46

FIGURE 8 - PROGRESSION OF THE NORMAL EPITHELIUM TO COLON CARCINOMA SHOWING GENETIC MUTATIONS AND GROWTH FACTORS INFLUENCING TUMOUR PROGRESSION. 53

FIGURE 9 – PRIMARY INFLUENCES OF CANCER-ASSOCIATED FIBROBLASTS IN THE TUMOUR STROMA. FIBROBLASTS SECRETE ECM COMPONENTS, GROWTH FACTORS AND PROMOTE ANGIOGENESIS RESULTING IN INCREASED TUMOUR GROWTH, METASTATIC ABILITY, AND RESISTANCE TO ANTI-CANCER THERAPEUTICS 56

FIGURE 10 - PRIMARY INFLUENCES OF TUMOUR-ASSOCIATED M2 MACROPHAGES IN THE TUMOUR STROMA. MACROPHAGES CONTRIBUTE TO INFLAMMATION AND

IMMUNOSUPPRESSION IN COLORECTAL TUMOURS, DRIVING TUMOUR GROWTH, METASTASIS, AND ANGIOGENESIS. 58

FIGURE 11 – DIAGRAM OF ARBITRARILY SHAPED CHANNEL WITH CROSS-SECTION $\mathcal{C}$ USED WHEN CONSIDERING THE POISEUILLE FLOW SOLUTION FOR FLOW DOWN A MICROFLUIDIC CHANNEL. THIS FIGURE IS ADAPTED FROM LECTURE NOTES BY H. BRUUS [125]. 64

FIGURE 12 – DEPICTION OF FLUID IMBALANCES INDUCING HYDROSTATIC FLOW BETWEEN RESERVOIRS. LOWER DIAGRAMS SHOW THE RECEDING, θR AND ADVANCING, θA CONTACT ANGLES IN INLET AND OUTLET RESERVOIRS, RESPECTIVELY. 66

FIGURE 13 – 20 MM LONG STRAIGHT CHANNEL (LEFT) ALONGSIDE A 150 MM LONG SERPENTINE CHANNEL (RIGHT) EACH WITH A PHYSICAL DESIGN LENGTH OF 20 MM. THE INCREASED CHANNEL LEGNTH RESULTS IN A 7.5-FOLD INCREASE IN HYDRAULIC RESISTANCE IN THE SERPENTINE CHANNEL (CALCULATED WITH A CHANNEL WIDTH OF 0.4 MM AND HEIGHT OF 0.35 MM USED THROUGHOUT THE SPHEROID ON-CHIP SYSTEM). 67

FIGURE 14 - (A) DIAGRAM SHOWING THE USE OF MICROFLUIDIC MICROPILLAR ARRAYS TO CONFINE CELLS, HYDROGELS AND SPHEROIDS (REPRODUCE FROM NASHIMOTO ET AL WITH PERMISSIONS FROM THE COPYRIGHT HOLDER) [55]. (B) DIAGRAMS OF 3-CHANNEL ORGANOPLATE® MICROFLUIDIC DEVICE WHICH IMPLEMENTS THE USE OF PHASEGUIDES™ TO CONFINE ECM/HYDROGELS TO THE CENTRE CHANNEL [72]. (C) IMAGES SHOWING THE USE OF HYDROPHOBIC COATINGS TO CONFINE LIQUIDS (PURPLE) IN MICROFLUIDIC CHANNELS WITHOUT THE USE OF MECHNICAL FEAUTURES. VARIOUS DESIGNS ARE SHOWN TO ILLUSTRATE THE FLEXIBILITY OF THIS TECHNIQUE (REPRODUCED FROM LOSSBERG-ZAHL ET AL UNDER CC LICENCE) [128]. 70

FIGURE 15 – (A) DIAGRAM SHOWING MICROPILLAR CONFINEMENT OF THE HYDROGEL WITH ANNOTATED PARAMETERS DESCRIBED THROUGHOUT EQUATIONS (2-13) - (2-17). (B) A GRAPH OF MODELLED PRESSURE DIFFERENCE ACROSS THE AIR-LIQUID INTERFACE BETWEEN THE MICROPILLARS, ΔP_{GAP} FOR VARYING PILLAR GAP SEPARATIONS AND CONTACT ANGLES, $\theta A *$. (C) A GRAPH OF MODELLED PRESSURE DIFFERENCE ACROSS THE AIR-LIQUID INTERFACE ACROSS THE CENTRE CHAMBER, ΔP_{WIDTH} FOR VARYING CENTRE CHANNEL WIDTHS, W AND CONTACT ANGLES, $\theta A *$. (D) GRAPH MODELLED IN

MATLAB SHOWING HOW THE OVERALL DIFFERENCE IN PRESSURE, ΔP BETWEEN THE TWO PARAMETERS ΔP_{GAP} AND ΔP_{WIDTH} VARIES WITH PILLAR GAP SEPARATION AND CONTACT ANGLE. THE HIGHER THIS VALUE, THE GREATER THE ABILITY OF THE SYSTEM TO CONFINE THE HYDROGEL. 71

FIGURE 16 – (LEFT) A PHOTOGRAPH TAKEN OF MBS SHORTLY AFTER PRODUCTION VIA MECHANICAL AGITATION. (MIDDLE) A MICROSCOPE IMAGE (40 X OBJ) TAKEN OF 10 X DILUTED MBS. (RIGHT) A DIAGRAM DEPICTING THE TYPICAL STRUCTURE OF A MB, WITH A GAS-FILLED CORE AND LIPID MONOLAYER. THE USE OF POLYETHYLENE GLYCOL (PEG) LIPIDS RESULT IN THE FORMATION OF A BRUSH-LIKE STRUCTURE ON THE SURFACE ON THE MB. THE SURFACE CHEMISTRY OF MB CAN BE TAILORED TO ALLOW FOR LIPOSOME OR ANITBODY CONJUGATION. 73

FIGURE 17 - T-JUNCTION (LEFT) AND FLOW FOCUSING (RIGHT) DEVICES SHOWING MICROFLUIDIC MB PRODUCTION. THE LIQUID PHASE (LP), FILLED WITH THE COATING MATERIAL, IMPINGES ONTO A GAS PHASE (GP) CAUSING A PINCH-OFF EFFECT. 76

FIGURE 18 – A) MICROSPRAY BUBBLE FORMATION USING FLOW-FOCUSING DEVICE WITH A 3D EXPANSION. B) HISTOGRAM SHOWING SIZE DISTRIBUTION OF MB POPULATION DETERMINED OPTICALLY. INSERT SHOWS TYPICAL OPTICAL IMAGE OF MBS (FIGURE REPRODUCED FROM PEYMAN ET AL WITH PERMISSIONS UNDER CC LICENCE) [141]. 77

FIGURE 19 – RESONANT FREQUENCY OF MICROBUBBLES AS A FUNCTION OF DIAMETER, DETERMINED EXPERIMENTALLY USING ACOUSTIC PRESSURES BETWEEN 10 – 60 KPA. FIGURES TAKEN FROM IEEE ULTRASONICS SYMPOSIUM 2010 PROCEEDINGS FROM GONG ET AL [145]. 79

FIGURE 20 - DIAGRAM OF PHOTOLITHOGRAPHY PROCESS USED TO PATTERN MICROFLUIDIC DESIGNS ONTO SILICON WAFERS. 81

FIGURE 21 – (A) A CAD SCHEMATIC OF THE MICROFLUIDIC SPHEROID TRAP DESIGN SHOWING THE ENTIRE DEVICE ALONGISDE A CLOSE-UP OF THE SPHEROID TRAP CHAMBER. (B) A CAD SCHEMATIC OF THE MICROFLUIDIC VASCULATURE DESIGN SHOWING THE ENITRE DEVICE ALONGISDE A CLOSE-UP OF THE CELL CHAMBER AND SURROUNDING MEDIA SIDE CHANNELS. 82

FIGURE 22 – IMAGES TAKEN OF THE MICROPILLAR DESIGNS EXPOSED TO A RANGE OF (A) LASER POWERS AND (B) DEFOCUS VALUES FOR THE DOSAGE TEST. IMAGES IN FIGURE 22A SHOW THE RESULT OF INCREASING LASER POWERS FROM 100 MJ/CM^2 TO 700 MJ/CM^2. IMAGES IN 22B SHOW THE EFFECTS OF DIFFERENT DEFOCUS VALUES ALONGSIDE A DEPICTION OF THE LASER FOCAL POINT WHEN EACH SETTING IS USED. 83

FIGURE 23 - DIAGRAM OF SOFT LITHOGRAPHY PROCESS USED TO FABRICATE PDMS MICROFLUIDIC DEVICES FROM SILICON MASTER WAFERS. 85

FIGURE 24 – (A) PHOTOGRAPHS TAKEN OF A POLYCARBONATE RESERVOIR USED FOR HYDROSTATIC FLOW. THE SPOUT AT THE BOTTOM SLOTS INTO A 2 MM HOLE PUNCHED IN THE PDMS MICROFLUIDIC INLET/OUTLET. THE CENTRE IMAGE SHOWS A DELRIN RING (WHITE) FITTED WITH A PTFE MEMBRANE, FORMING A STERILE LID FOR THE RESERVOIR. THE RESERVOIR FITTED WITH THE LID CAN BE SEEN IN THE FINAL IMAGE. (B) A PICTURE SHOWING MEDIA-FILLED RESERVOIRS INTERFACED WITH A SPHEROID TRAP MICROFLUIDIC DEVICE..... 87

FIGURE 25 – HCT116 – HFFF2 CO-CULTURE SPHEROIDS TRAPPED WITHIN THE MICROFLUIDIC TRAP ARRAY AFTER THE SPHEROID LOADING PROCESS. 90

FIGURE 26 – SCHEMATIC OF THE MULTIPLEXED FLOW-FOCUSING DEVICE USED FOR MB FORMATION. LABELS SHOW GAS AND LIPID SOLUTION INLETS WHICH BRANCH INTO 4 SEPARATE FLOW-FOCUSING NOZZELS LABELLED 1 – 4. MBS ARE COLLECTED IN A VIAL ATTACHED TO THE OUTLET (FIGURE TAKEN WITH FROM PEYMAN ET AL WITH PERMISSIONS FROM THE COPYRIGHT HOLDER) [140]..... 96

FIGURE 27 – (A) AN IMAGE OF THE HORIZON MICROFLUIDIC PLATFORM. (B) SCHEMATIC OF THE VIAL HOLDER . THE P-PUMP CHAMBER INCREASES IN PRESSURE WHICH FORCES THE LIPID SOLUTION UP THE METAL NEEDED AND INTO THE DEVICE. (C) AN IMAGE SHOWING THE MICROFLUIDIC CHIP WITH THE MANIFOLD CLAMPED ON TOP TO CREATE A GAS TIGHT SEAL. (D) A SCHEMATIC OF THE MANIFOLD ASSEMLBY COMPLETE WITH TUBING INLETS AND FERRULES (THIS FIGURE WAS TAKEN FROM ABOU-SALEH ET AL WITH PERMISIONS FROM THE COPYRIGHT HOLDER) [148] 97

FIGURE 28 – SCHEMATIC OF TARGETED LIPOSOMES ATTACHED TO THE SURFACE OF A MICROBUBBLE. BIOTIN – NEUTRAVIDIN BINDING WAS USED TO ATTACH THE A_VB_3 ANTIBODIES TO THE LIPOSOME SURFACE AS WELL AS LIPOSOMES TO THE MICROBUBBLE SURFACE. (THIS FIGURE WAS TAKEN FROM N. INGRAM ET AL AND MODIFIED UNDER CC LICENCE) [149]. 100

FIGURE 29 – A) UV-VIS ABSORPTION SPECTRA RECORDED FOR FREE (LEFT) AND LYSED, LIPOSOMAL (RIGHT) DOX-HCL, RECORDED ACROSS A 400 – 600 NM WAVELENGTH RANGE. B) GRAPH SHOWING THE STANDARD 'CURVE' (BLUE) PLOTTED FROM FREE DOX 502 NM ABSORPTION VALUES (GREEN CROSSES). DROP LINES SHOW 502 NM ABSORPTION VALUES FOR DIFFERENT CONCENTRATIONS OF LIPOSOMAL DOX-HCL. 103

FIGURE 30 – BRIGHT FIELD (LEFT) AND FLUORESCENCE (RIGHT) IMAGES SHOWING CO-LOCALISATION OF LS ATTO 488 GREEN, FLUORESCENT LIPID EMISSION FROM THE MB LIPID SHELL. 104

FIGURE 31 - (A) DIAGRAM OF THE SETUP USED TO EXPOSE MBS IN THE SPHEROID TRAP CHAMBER TO US. THE 1MM THICK CHIP MINIMISED US ATTENUATION AND THE GEL STANDOFF PAD ENSURED MBS WERE EXPOSED TO FAR-FIELD, UNIFORM US WAVES. (B) OPTICAL IMAGES TAKEN OF MBS WITHIN THE SPHEROID CHAMBER PRE- AND POST-US. MBS CAN BE OBSERVED IN THE PRE-US IMAGE AS A BACKGROUND OF SMALL PARTICLES. A CLEAR REDUCTION IN MB POPULATION CAN BE OBSERVED POST-US. (C) A GRAPH SHOWING QUANTIFIED MB POPULATIONS IN THE FRONT, CENTRE, AND BACK OF THE SPHEROID CHAMBER PRE- AND POST-US EXPOSURE. RESULTS REVEALED THAT, ON AVERAGE, 99.96 % MBS WERE BURST. 106

FIGURE 32 – SPHEROID TRAP DESIGN SHOWING TRAP RADIUS, u LENGTH, q WIDTH, w SEPARATION, g AND CENTRE CHANNEL LENGTH, l. FLUID RESISTANCE/PRESSURE DROP PATHS CONSIDERED FOR HYDRAULIC RESISTANCE CALCULATIONS ARE SHOWN AND BROKEN DOWN INTO THEIR INDIVIDUAL COMPONENTS. 114

FIGURE 33 – AUTOCAD TRAP ARRAY DESIGNS WITH HYDRAULIC RESISTANCE RATIOS OF (A) 1.3, (B) 2.1 AND (C) 3.1 ALONGSIDE ANSYS FLUENT FLOW SIMULATIONS THROUGH EACH SYSTEM. THE TABLE SHOWS DIMENSIONS OF TRAP DIAMETER, U, TRAP

SEPARATION, *G*, CENTRE CHANNEL LENGTH/WIDTH *L,W* AND TRAP LENGTH,*Q* FOR EACH DESIGN. 117

FIGURE 34 – SPHEROID TRAPPING EFFICIENCY OBSERVED FOR SPHEROID DIAMETERS RANGING BETWEEN 220 AND 350 μM. DATA WAS COLLATED FROM ALL SPHEROID ON-CHIP EXPERIMENTS PERFORMED USING FLOW RATES BETWEEN 0.2 – 0.4 μL/S..... 118

FIGURE 35 – (A) MICROFLUIDIC SPHEROID TRAP SYSTEM DESIGN SHOWING THE CENTRAL TRAP ARRAY CHAMBER WITH INLET AND OUTLET SERPENTINES. (B) GRAPHS SHOWING PREDICTED FLOW RATE, HEIGHT DIFFERENCE AND HYDROSTATIC PRESSURE CHANGES WITH TIME. 119

FIGURE 36 – SCREENSHOT OF MOSAICSUITE IMAGE J PARTICLE TRACKING SOFTWARE DETERMINING PARTICLE TRAJECTORIES. GRAPH SHOWING THEORETICAL AND MEASURED FLOW RATES, DETERMINED USING PARTICLE VELOCITIES. 120

FIGURE 37 – (A) VISUAL OF FLUID STREAMLINES PASSING THROUGH THE TRAP ARRAY WITH 7 SPHEROIDS PRESENT IN THE TRAPS. (B) FIGURE OF WALL SHEAR STRESS ACROSS THE SPHEROID SURFACES. THE GRAPH SHOWS A PLOT OF ALL VALUES FOR EACH SPHEROID, WITH EACH POINT CORRESPONDING TO MESH FACET ON THE SPHEROID SURFACE. . 122

FIGURE 38 – BRIGHTFIELD AND DEAD CELL FLUORESCENT IMAGES OF SPHEROIDS TAKEN AFTER (A) 8 HOURS AND (B) 48 HOURS OF ON-CHIP CULTURE. ALL SCALE BARS ARE 200μM. 124

FIGURE 39 – (A) BRIGHT FIELD AND DOX FLUORESCENCE (GREEN) OVERLAYING IMAGES OF BOTH MONOCULTURE (HCT116) AND COCULTURE (HCT116 – HFFF2) SPHEROIDS AFTER 8 HOURS EXPOSURE TO DOX CONCENTRATIONS BETWEEN 1 - 10μM. (B) MONOCULTURE AND COCULTURE SPHEROID VIABILITY FROM EXPOSURE TO DOX BETWEEN 0.01 μM AND 10 μM – DETERMINED USING CELL TITER-GLO 3D ATP VIABILITY ASSAY. 125

FIGURE 40 – BRIGHT FIELD, DOXORUBICIN (GREEN) AND DEAD CELL (RED) FLUORESCENCE EMISSION FROM SPHEROIDS 48 H POST EXPOSURE TO 0 (CONTROL), 1, 5, AND 7.5 μM DOX. FOR INCREASING CONCENTRATIONS OF DOX, THE STRUCTURAL INTEGRITY OF THE SPHEROID DECREASES AND AN INCREASE IN DEAD CELLS CAN BE OBSERVED (RED). 128

FIGURE 41 – SPHEROID VIABILITY WITH INCREASING CONCENTRATIONS OF DOX, MEASURED 48 HOURS POST EXPOSURE WITH CELL TITER-GLO 3D CELL VIABILITY ASSAY (N = 185). AS WITH THE PREVIOUS OFF-CHIP EXPERIMENT (FIGURE 42), A TYPICAL DOSE RESPONSE TREND WAS AGAIN OBSERVED, WITH A STEEP DROP IN VIABILITY OCCURING AT CONCENTRATIONS GREATER THAN 2 μM..... 129

FIGURE 43 – BRIGHT FIELD, ATTO 488 LIPID (GREEN) AND DEAD CELL (RED) FLUORESCENT EMISSIONS FROM (A) CONTROL, (B) MB ONLY AND, (C) MB + US SPHEROIDS 8 HOURS POST-EXPOSURE. LIPID DEPOSITION WAS OBSERVED IN BOTH MB ONLY AND MB + US CONDITIONS HOWEVER DEAD CELL EMISSION WAS ONLY OBSERVED WHEN US WAS USED, GIVING EVIDENCE THAT IRREVERSIBLE SONOPOATION WAS OCCURING..... 131

FIGURE 44 - BRIGHT FIELD, MB LIPIS (GREEN ATTO 488) AND DEAD CELL (RED) IMAGING OF MB + US SPHEROIDS 48 HOURS AFTER INSONATION SHOWING MB LIPID IS RETAINED BY THE SPHEROIDS AFTER MB + US EXPOSURES..... 132

FIGURE 45- BOXPLOT OF SPHEROID VIABILITIES 48 HOURS POST EXPOSURE TO CONTROL (N = 60), US ONLY (N = 24), MB ONLY (N = 12) AND MB + US (N = 26). EACH POINT REPRESENTS A SINGLE CHIP CONTAINING ON AVERAGE 5 ± 2 SPHEROIDS. ANNOTATED VALUES SHOW MEAN ± S.E AND HASHED REGIONS SHOW THE 95 % CONFIDENCE INTERVALS AROUND THE MEAN..... 133

FIGURE 46 - BRIGHT FIELD, DOX (GREEN) AND DEAD CELL (RED) FLUORESCENT EMISSION FROM SPHEROIDS 48 HOURS POST EXPOSURE TO (A) 3 μM DOX ONLY, (B)) 3 μM DOX WITH US AND, (C)) 3 μM DOX WITH MB + US. A TREND IN INCREASING DOX ACCUMULATION AND DEAD CELL EMISSION CAN BE OBSERVED FROM FIGURE PANES A – C..... 135

FIGURE 47 – SPHEROID VIABILITY 48 HOURS POST EXPOSURE TO 3 μM DOX ONLY (N = 39), WITH US (N = 26) AND WITH MB + US (N = 31). EACH POINT REPRESENTS A SINGLE CHIP CONTAINING ON AVERAGE 5 ± 2 SPHEROIDS. ANNOTATED VALUES SHOW MEAN ± S.E AND HASHED REGIONS SHOW THE 95 % CONFIDENCE INTERVALS AROUND THE MEAN. 136

FIGURE 48 - A SERIES OF DIAGRAMS DEPICTING THE THREE DOX-LS THERAPEUTIC EXPOSURES: (A) DOX-LS ALONE. (B) DOX-LS + MB CO-DELIVERY WITHOUT

conjugation. (C) Drug-loaded MBs (DLMBs) consisting of DOX-LS conjugated to the MB surface using biotin-neutravidin binding (DOX-LS and MB images are not to scale or ratio).....138

Figure 49 - Bright field, DOX (green) and dead cell (red) fluorescent emission from spheroids 48 hours post exposure to (A) DOX-LS and (B) DOX-LS + MB + US. Imaging revealed similar rates of DOX accumulation in the outer layers of spheroids, suggesting DOX-LS were not able to penetrate far into the tumours.....139

Figure 50 - Spheroid viability 48 hours post exposure to control (N = 66), 3 μM DOX (N = 39), DOX-LS (N = 38) and DOX-LS + MB + US (N = 66). Each point represents a single chip containing on average 5 ± 2 spheroids. Annotated values show mean ± S.E and hashed regions show the 95 % confidence intervals around the mean.....140

Figure 51 - Bright field, DOX (gree) and dead cell (red) fluorescent emission from spheroids 48 hours post exposure to DLMB + US (A) x1, (B) x3, and (C) x5. Imaging did not appear to show any significant differences in spheroid integrity, DOX accumulation, or number of dead cells between the three exposure conditions. DOX was again observed to accumulate primarily in the outer layers of the spheroids, suggesting minimal drug penetration had occurred.....142

Figure 52 - Spheroid viability 48 hours post exposure to DOX-LS (N = 38), DOX-LS + MB + US (N = 66), DLMB + US x1 (N = 73), DLMB x3 (N = 70), and DLMB x5 (N = 71). Each point represents a single chip containing on average 7 ± 2 spheroids. Annotated values show mean ± S.E and hashed regions show the 95 % confidence intervals around the mean.....143

Figure 53 – A) AutoCAD design of micropillar array separating the 3 channels. B) Bright field image of a microfluidic device prior to hydrogel filling. C) Microfluidic device showing successful confinement of cell-hydrogel suspension in the centre channel. 150

FIGURE 54 – AUTOCAD DESIGN OF THE COMPLETE VASCULATURE ON-CHIP MICROFLUIDIC DEVICE DESIGN. A CLOSER VIEW OF THE CENTRE CHAMBER AND MICROPILLAR ARRAY CAN BE SEEN IN FIGURE 53. 151

FIGURE 55 – GRAPHS SHOWING THE PREDICTED CHANGES IN (A) LINEAR AND VOLUMETRIC FLOW RATE AND (B) PRESSURE AND HEIGHT DIFFERENCE ALONG A SIDE CHANNEL ACROSS A 24-HOUR PERIOD. 152

FIGURE 56 – A) SURFACE PRESSURE MODELLING DOWN SIDE CHANNELS WITH DIFFERENCE CHOICES OF INLET. B) GRAPH SHOWING THE PRESSURE EQUILIBRATION DOWN A SIDE CHANNEL WITH LOW AND HIGH PRESSURES CREATED AT MICROPILLARS. C) HIGH (RED) AND LOW (BLUE) MICROPILLAR PRESSURES ACROSS 24 HOURS. DIFFERENCE (GREEN) SHOWS CHANGE IN INTERSTITIAL PRESSURE BETWEEN MEDIA CHANGES. 153

FIGURE 57 – MEASURED AND THEORETICAL (P_{CAP} = 0 AND 23 PA) LINEAR FLOW VELOCITIES FOR A RANGE OF RESERVOIR LIQUID HEIGHT DIFFERENCES. THE BLUE LINE SHOWS THE FIT OF MEASURED FLOW VELOCITIES USED TO DETERMINE HYDRAULIC RESISTANCE. R_{HYD} AND CAPILLARY PRESSURE, P_{CAP}. 155

FIGURE 58- GRAPHS SHOWING INTERSTITIAL FLOW VELOCITY (LEFT) AND PERMEABILITY, K_S (RIGHT) WITH FIBRIN GELS MADE WITH DIFFERING FIBRINOGEN CONCENTRATIONS. INSET SHOWS AN EXAMPLE IMAGE OF FLUORESCEIN DIFFUSING THROUGH THE FIBRIN GEL. 157

FIGURE 59 - MERGED IMAGE OF DEXTRAN DIFFUSION INTO AN EMPTY FIBRIN GEL ALONGSIDE A GRAPH SHOWING THE CALCULATED PERMEABILITY COEFFICIENTS FOR EACH CHANNEL POSITION. DEXTRAN ENTERS THE SIDE CHANNEL AT POSITION 1 AND EXITS AT POSITION 9. PERMEABILITY WAS FOUND TO VARY DUE TO THE PRESSURE DIFFERENCE ACROSS THE MICROPILLAR ARRAY. 158

FIGURE 60 – A) MICROFLUIDIC DEVICE WITH REDUCED NUMBER OF MICROPILLARS TO ALLOW FOR HOMOGENEOUS DIFFUSION ACROSS THE CENTRE CHAMBER. B) GRAPH SHOWING CALCULATED PERMEABILITY VALUES AT EACH CHANNEL POSITION, ALONGSIDE AN IMAGE OF DEXTRAN DIFFUSION INTO THE FIBRIN GEL. 160

FIGURE 61 – DIAGRAM OF THE THREE CELLULAR CONFIGURATIONS TESTED IN THIS OFF-CHIP ANGIOGENESIS ASSAY. CONFIGURATION LABELS CORRESPOND TO IMAGES SHOWN THROUGHOUT FIGURES 62 AND 63. 162

FIGURE 62 – FLUORESCENT IMAGES OF GFP-HUVECS CO-CULTURED WITH HFFF2 CELLS. HUVECS WERE SEEDED DIRECTLY ONTO A CONFLUENT LAYER OF HFFF2 CELLS (A), SUSPENDED IN FIBRIN THEN SEEDED ONTO HFFF2 CELLS (B), OR SUSPENDED IN FIBRIN ALONGSIDE HFFF2 CELLS THEN SEEDED (C). IMAGES TAKEN 24, 72 AND 168 HOURS AFTER SEEDING SHOW THE LACK OF HUVEC ACTIVITY WHEN SEEDED WITH HFFF2 CELLS. 163

FIGURE 63- FLUORESCENT IMAGES OF GFP-HUVECS CO-CULTURED WITH HDF CELLS. HUVECS WERE SEEDED DIRECTLY ONTO A CONFLUENT LAYER OF HDF CELLS (A), SUSPENDED IN FIBRIN THEN SEEDED ONTO HDF CELLS (B), OR SUSPENDED IN FIBRIN ALONGSIDE HDF CELLS THEN SEEDED (C). IMAGES TAKEN 24, 72 AND 168 HOURS AFTER SEEDING SHOW HUVECS INTERACTING WITH HDF CELLS AND THE MATRIX PROTEINS THEY HAVE SECRETED. 164

FIGURE 64 – CONFOCAL MICROSCOPY IMAGES TAKEN OF HUVEC (P5) – HDF (P5) ON-CHIP COCULTURES AT 24, 72, 120 AND 168 HOURS AFTER SEEDING INTO THE MICROFLUIDIC DEVICE IN A FIBRIN MATRIX. IMAGES SHOW HUVECS STAINED WITH CELLTRACKER GREEN (BODIPY) APPEARING TO SELF-ASSEMBLE INTO A CONTINUOUS VASCULATURE NETWORK ACROSS A 7-DAY PERIOD. 167

FIGURE 65 – FLUORESCENT IMAGES TAKEN OF RHODAMINE 6G PERFUSION THROUGH VASCULATURE NETWORKS SHOWN IN FIGURE 63. RHODAMINE WAS INITIALLY FLOWED THROUGH THE LOWER CHANNEL WITHOUT SUCCESS. THE UPPER CHANNEL (NOT OBSERVABLE IN THIS IMAGE) WAS THEREFORE TESTED AND RESULTED IN CONFINEMENT OF THE DYE TO REGIONS OF FULLY FORMED VASCULATURE..... 168

FIGURE 66 – CONFOCAL MICROSCOPY IMAGES TAKEN OF HUVEC (P4) – HDF (P4) ON-CHIP COCULTURES AT 24, 72, 120 AND 168 HOURS AFTER SEEDING. IMAGES SHOW HUVECS STAINED WITH CELLTRACKER GREEN (BODIPY) AND HDFS STAINED WITH CELLTRACKER BLUE (CMHC). 169

FIGURE 67 – A) IMAGE ACQUIRED OF TEXAS-RED DEXTRAN PERFUSION THROUGH THE VASCULATURE NETWORK SHOWN IN FIGURE 65. B) OVERLAY OF DEXTRAN, HUVEC AND HDF FLUORESCENCE EMISSION SHOWING PERFUSION EXCLUSIVELY THROUGH THE VASCULATURE LUMENS..... 171

FIGURE 68 - HIGH MAGNIFICATION (100×) IMAGES ACQUIRED OF VASCULATURE STRUCTURES FORMED WITH GFP-TRANSFECTED HUVECS. WHITE ARROWS HIGHLIGHT REGIONS WHERE FILOPODIA CAN BE OBSERVED. 172

FIGURE 69 – CONFOCAL MICROSCOPY IMAGES TAKEN OF GFP-HUVEC (P4) – NHLF (P4) ON-CHIP CO-CULTURES AFTER 24, 48, 120 AND 168 HOURS OF GROWTH. RED BOXES HIGHLIGHT VESSEL ANASTOMOSIS AT THE MICROPILLAR REGIONS..... 174

FIGURE 70 – A SERIES OF IMAGES SHOWING LIPOSOMES (RED) PERFUSING THROUGH VASCULATURE NETWORKS (GREEN). IMAGES ON THE LEFT SHOW LIPOSOMES ENTERING THE NETWORK FROM THE SIDE CHANNEL AT THE PILLAR GAPS. SOME LEAKAGE INTO THE SURROUNDING MATRIX IS OBSERVED HOWEVER THIS ONLY AFFECT VESSELS CLOSE TO THE ENTRANCE. THE VAST MAJORITY OF THE NETWORK WAS NOT AFFECTED BY THIS LEAKAGE, AS SHOWN BY THE IMAGES ON THE LEFT..... 175

FIGURE 71 – A) ANGIOTOOL GUI SHOWING PARAMETERS ABLE TO BE SET BEFORE ANALYSIS. B) ANGIOTOOL IMAGE ANALYSIS WORKFLOW. IMAGES HAVE BEEN TAKEN WITH PERMISSION FROM THE ORIGINAL ANGIOTOOL PUBLICATION BY E. ZUDAIRE ET AL [180]..... 177

FIGURE 72 – A) INITIAL FLUORESCENCE IMAGE OF VASCULATURE NETWORK FORMED WITH GFP-HUVECS (LEFT) ALONGSIDE A CONTRAST ENHANCED IMAGE USED TO ENSURE ACCURATE ANGIOTOOL ANALYSIS (MIDDLE). FINAL IMAGE SHOWS ANGIOTOOL IDENTIFICATION OF NETWORK AREA (YELLOW BOUNDARY), VESSEL LENGTH (RED LINES) AND NETWORK NODES (BLUE DOTS). B) BOXPLOTS OF TOTAL VESSEL LENGTH, JUNCTION DENSITY AND TOTAL VESSEL AREA DETERMINED USING ANGIOTOOL. EACH POINT REPRESENTS A SINGLE NETWORK. THE FINAL GRAPH SHOWS A HISTOGRAM PLOT OF MEASURED VESSEL DIAMETERS FIT WITH A LORENTZIAN CURVE TO DETERMINE THE MODAL VESSEL DIAMETER. 178

FIGURE 73 – TIME LAPSE IMAGES, TAKEN IN 5 MINUTE INTERVALS, OF TEXAS RED DEXTRAN LEAKING OUT THROUGH THE VESSEL WALLS. THESE IMAGES WERE USED TO DETERMINE THE PERMEABILITY COEFFICIENT OF THE VASCUALTURE NETWORK. ... 180

FIGURE 74 – IMAGES OF FRAMES TAKEN FROM VIDEOS CAPTURED OF GREEN, FLUORESCENT 2 μM BEADS TRAVELLING THROUGH VASCULATURE NETWORKS. SEVERAL BEADS WERE OBSERVED TO BECOME TRAPPED WITHIN THE AFTER STICKING TO THE VESSEL WALLS. 10, 1 MINUTE VIDEOS WERE CAPTURED AT 5.9 FPS THEN IMAGEJ USED TO MANUALLY TRACK TRAJECTORIES..... 182

FIGURE 75 – FLUORESCENT CONFOCAL MICROSCOPY IMAGES TAKEN OF MICROFLUIDIC VASCULATURE CULTURES FIXED AND IMMUNOSTAINED AGAINST INTEGRIN A_VB_3. INTEGRIN EMISSION (RED) CAN BE OBSERVED TO BE CO-LOCALISED WITH GFP-HUVECS (BLUE ARROWS) ALONG WITH THE CRESCENT-SHAPED NHLF CELLS SUPPORTING THE VASCULATURE (WHITE ARROWS). 185

FIGURE 76 – A) FLUORESCENT IMAGES OF GFP-HUVEC MONOLAYERS IMMUNOSTAINED FOR A_VB_3 INTEGRIN EXPRESSION (RED). HUVECS WERE GROWN IN A RANGE OF [EGM:TCM] MEDIA RATIOS, AS LABELLED. B) GRAPH OF A_VB_3 INTEGRIN IMMUNOFLUORESCENT EMISSION QUANTIFIED USING FLOW CYTOMETRY. C) FLOW CYTOMETRY DISTRIBUTIONS SHOWING RED AND GREEN FLUORESCENCE EMISSION FOR CELLS GROWN IN EACH MEDIA RATIO. THE TOP RIGHT QUADRANT SHOWS DOUBLE POSITIVE (RED AND GREEN) CELLS AND CAN BE SEEN TO SHIFT RIGHT WITH INCREASING TCM CONCENTRATIONS, SHOWING INCREASED INTEGRIN EXPRESSION..... 187

FIGURE 77 - CONFOCAL MICROSCOPY IMAGES ACQUIRED OF GFP-HUVECS GROWING ON NHLF MONOLAYERS. CO-CULTURES WERE GROWN IN A RANGE OF [EGM:TCM] RATIOS AND THEIR MORPHOLOGY IMAGED 48 AND 96 HOURS AFTER HUVEC SEEDING. 188

FIGURE 78 – FLOW CYTOMETRY DATA SHOWING (A) A SERIES OF GRAPHS SHOWING HISTOGRAM PLOTS AND PEAK FITS OF A_VB_3 INTEGRIN IMMUNOFLUORESCENT EMISSION INTENSITIES FROM GFP-HUVECS. (B) A SERIES OF GRAPHS SHOWING HISTOGRAM PLOTS AND PEAK FITS OF A_VB_3 INTEGRIN IMMUNOFLUORESCENT EMISSION INTENSITIES FROM NHLFS. THE LOWEST TCM CONCENTRATIONS ([1:0]) ARE SHOWN ON THE LEFT AND HIGHEST TCM CONCENTRATIONS ([1:2]) ON THE RIGHT. (C) A GRAPH OF PEAK

IMMUNOFLUROESCENT INTENSITIES FOR GFP-HUVECS. AN INCREASE OF 78 % WAS OBSERVED FROM THE NO-TCM [1:0] VALUE (15,300 ± 200) TO THE HIGHEST [1:2] TCM VALUE (27,100 ± 800). (D) A GRAPH OF PEAK IMMUNOFLUROESCENT INTENSITIES FOR NHLFS. AN INCREASE OF 26 % WAS OBSERVED FROM THE NO-TCM [1:0] VALUE (1800 ± 100) TO THE HIGHEST [1:2] TCM VALUE (2300 ± 100). (E) A GRAPH SHOWING THE PERCENTAGE OF HUVECS AND NHLFS POSITIVE FOR A_VB_3 INTEGRIN EXPRESSION FOR THE SAME RANGE OF [EGM:TCM] RATIOS. THE VAST MAJORITY (95 % +) OF HUVECS WERE POSITIVE REGARDLESS OF TCM CONCENTRATION WHEREAS NHLFS SHOW AN INCREASE IN CELLS POSITIVE FOR A_VB_3 INTEGRIN EXPRESSION FROM 65 % UP TO 85 %. 190

FIGURE 79 - CONFOCAL MICROSCOPY IMAGES ACQUIRED OF GFP-HUVECS EMBEDDING FIBRIN AND GROWING ON NHLF MONOLAYERS. CO-CULTURES WERE GROWN IN A RANGE OF [EGM:TCM] RATIOS AND THEIR MORPHOLOGY IMAGED 48 AND 96 HOURS AFTER HUVEC SEEDING. 192

FIGURE 80 - FLOW CYTOMETRY DATA FOR FIBRIN-CONTAINING CUTLURES SHOWING (A) A SERIES OF GRAPHS SHOWING HISTOGRAM PLOTS AND PEAK FITS OF A_VB_3 INTEGRIN IMMUNOFLUORESCENT EMISSION INTENSITIES FROM GFP-HUVECS. (B) A SERIES OF GRAPHS SHOWING HISTOGRAM PLOTS AND PEAK FITS OF A_VB_3 INTEGRIN IMMUNOFLUORESCENT EMISSION INTENSITIES FROM NHLFS. THE LOWEST TCM CONCENTRATIONS ([1:0]) ARE SHOWN ON THE LEFT AND HIGHEST TCM CONCENTRATIONS ([1:2]) ON THE RIGHT. (C) A GRAPH OF PEAK IMMUNOFLUROESCENT INTENSITIES FOR GFP-HUVECS. AN INCREASE OF 430 % WAS OBSERVED FROM THE NO-TCM [1:0] VALUE (22,000 ± 500) TO THE HIGHEST [1:2] TCM VALUE (81,000 ± 2000). (D) A GRAPH OF PEAK IMMUNOFLURUESCENT INTENSITIES FOR NHLFS. AN INCREASE OF 75 % WAS OBSERVED FROM THE NO-TCM [1:0] VALUE (19,000 ± 300) TO THE HIGHEST [1:2] TCM VALUE (35,000 ± 6000). (E) A GRAPH SHOWING THE PERCENTAGE OF HUVECS AND NHLFS POSITIVE FOR A_VB_3 INTEGRIN EXPRESSION FOR THE SAME RANGE OF [EGM:TCM] RATIOS. THE VAST MAJORITY (90 % +) OF HUVECS WERE POSITIVE REGARDLESS OF TCM CONCENTRATION WHEREAS NHLFS SHOW AN INCREASE IN CELLS POSITIVE FOR A_VB_3 INTEGRIN EXPRESSION FROM 65 % UP TO 85 %. 194

FIGURE 81 – FLUORESCENT IMAGES ACQUIRED (USING 10× OBJECTIVE) OF GFP-HUVECS SELF-ASSEMBLING INTO FULLY PERFUSABLE VASCULATURE NETWORKS 48. 120 AND 168 HOURS AFTER SEEDING. (A) SHOWS HEALTHY CULTURES GROWN USING EGM-2 MEDIA AND (B) SHOWS CULTURES CONDITIONED WITH EGM:TCM [2:1] MEDIA FOR THE FINAL 5 DAYS OF CULTURE. WHITE ARROWS HIGHLIGHT BRANCHING STRUCTURES AND RED ARROWS HIGHLIGHT TORTUOUS, BULBOUS VESSEL MORPHOLOGIES. (C) AND (D) SHOW HIGHER MAGNIFICATION IMAGES OF HEALTHY AND TCM NETWORKS, RESPECTIVELY. 197

FIGURE 82 – BRIGHTFIELD (TOP) AND GFP-HUVEC FLUORESCENT (BOTTOM) IMAGES OF - (A) A NETWORK FORMED USING EGM-2 MEDIA COMPLETE WITH VEGF AND FGF FOR THE ENTIRE 168 HOUR CULTURE. MAINTAINING VEGF AND FGF RESULTED IN THE OVERGROWTH OF DILATED, BULBOUS VESSELS SIMILAR TO MORPHOLOGIES OBSERVED IN TCM CONTAINING CULTURES. (B) A NETWORK FORMED USING EGM:TCM MEDIA IN A [1:1] RATIO. (C) A NETWORK FORMED USING EGM:TCM MEDIA IN A [1:2] RATIO. TCM MEDIA WAS ADDED 48 HOURS AFTER SEEDING. AFTER 168 HOURS OF GROWTH, NETWORKS GROWN IN BOTH [1:1] AND [1:2] TCM MEDIA WERE OBSERVED TO COLLAPSE AND CONTRACT AWAY FROM THE SIDES OF THE CULTURE CHAMBER..... 198

FIGURE 83 - BOXPLOTS OF TOTAL VESSEL LENGTH (A), JUNCTION DENSITY (B), AND TOTAL VESSEL AREA (C) FOR HEALTHY AND TCM NETWORKS, DETERMINED USING ANGIOTOOL IMAGE ANALYSIS. EACH DATA POINT CORRESPONDS TO A SINGLE NETWORK. COMPARISON OF HEALTHY AND TCM NETWORKS FOUND NO STATISTICAL DIFFERENCE BETWEEN TOTAL VESSEL LENGTH OR JUNCTION DENSITY. TOTAL VESSEL AREA WAS CONSISTENTLY LARGER FOR TCM NETWORKS, RESULTING A 14 % INCREASE ON AVERAGE. (D) HISTOGRAM PLOT OF VESSEL DIAMETERS MEASURED USING IMAGEJ. LORENTZIAN FITS USED TO FIND MODAL DIAMETER PEAK, CORRESPONDING TO 24.5 ± 1.1 μM FOR HEALTHY NETWORKS AND 37.5 ± 2.3 μM FOR TCM CONDITIONED NETWORKS. 200

FIGURE 84 – A) MERGED TILE SCAN IMAGE OF GFP-HUVECS AFTER 6 DAYS OF ON-CHIP GROWTH. A CONTINUOUS NETWORK WAS FORMED, COMPLETE WITH ANASTOMOSED VESSELS AT THE MICROPILLAR GAPS. B) MERGED TILE SCAN IMAGE OF RED FLUORESCENT (ATTO647N) LIPOSOMES PERFUSION THROUGH THE NETWORK.

Liposomes can be seen to perfuse through almost all vessels within the network and exit through the adjacent side channel. c) Overlay of images shown in a) and b) - showing confinement of liposomes to the vessels.... 206

Figure 85 – Confocal fluorescent microscopy images of liposomes (red) perfusing through vasculature networks (green) taken using 40x objective. Lack of leakage of liposomes from vessels further demonstrates network and endothelial barrier functionality. 207

Figure 86 – a) Time lapse images showing LS accumulation across several points on the vessel surface. Images were taken in 5 minute intervals using a 40x objective. b) Image taken of an entire network towards then end of LS perfusions. White arrows show regions of LS accumulation which typically correspond to smaller vessels..... 209

Figure 87 – Post-perfusion fluorescent images of LS (red) accumulation after perfusion of 2 μg/mL isotype control LS (a), 2 μg/mL targeted LS (b), 4 μg/mL isotype control LS (c), and 4 μg/mL targeted LS . Images are taken in 1.5 μm z-stack slices with a 100x oil immersion objective..... 211

Figure 88 – Graph showing quantified fluorescent intensity of liposome accumulation for non-targeted liposomes (NT-LS) and liposomes conjugated with 2 μg/mL isotype control antibodies (IC-LS 2 μg/mL), 2 μg/mL A_VB_3 antibodies (T-LS 2 μg/mL), 4 μg/mL isotype control antibodies (IC-LS 4 μg/mL) and, 4 μg/mL A_VB_3 antibodies (T-LS 4 μg/mL). Images such as those in Figure 86 were used to quantify accumulation with each z-stack corresponding to a single box plot point..... 212

Figure 89 - (a) Post-perfusion images of 4ug/mL targeted LS (red) accumulation within TCM-conditioned vasculature networks (green). Images were taken with a 100x oil immersion objective. (b) Graph of quantified fluorescent intensity values for targeted LS accumulation within healthy and TCM vasculature networks. 215

Figure 90 – Confocal fluorescent images of red flourescent LS conjugated to MB perfusing through vasculature (green). The adhesion of LS to the MB

SURFACE CAN BE OBSERVED BY THE INCREASED FLUORESCENT PARTICLE SIZE COMPARED TO LS ONLY PERFUSIONS SHOWN IN FIGURE FIGURE 84. 218

FIGURE 91 - POST-PERFUSION FLUORESCENT IMAGES OF LS (RED) ACCUMULATION AFTER PERFUSION OF 4 μG/ML T-LS-MB THROUGH TCM NETWORKS WITHOUT AN US TRIGGER (A), 4 μG/ML T-LS-MB THROUGH HEALTHY NETWORKS WITH AN US TRIGGER (B), AND 4 μG/ML T-LS-MB THROUGH TCM NETWORKS WITH AN US TRIGGER (C). IMAGES ARE TAKEN IN 1.5 μM Z-STACK SLICES WITH A 100X OIL IMMERSION OBJECTIVE. 219

FIGURE 92 – A BOXPLOT GRAPH SHOWING QUANTIFIED LIPOSOME FLUROESCENCE INTENSITIES IN TCM-NETWORKS EXPOSED WITH T-MB-LS (4 μG/ML) WITH AND WITHOUT US, AND HEALTHY NETWORKS PERFUSED WITH T-MB-LS (4 μG/ML) AND US. EACH POINT REPRESENTS THE AVERAGE INTENSITY ACROSS A SINGLE Z-STACK CAPURED. 221

FIGURE 93 – (A) AUTOCAD DESIGN OF THE TWO-CHAMBER SYSTEM USED TO PRODUCE A VASCULARISED TUMOUR MODEL. (B) FLUORESCENT CONFOCAL MICROSCOPY IMAGES TAKEN ACROSS A 2-WEEK PERIOD OF THE TWO-CHAMBER SYSTEM WITH RED FLUROESCENT HCT116 CELLS SEEDED ALONGSIDE GFP-HUVECS – BOTH SETS OF CELLS ARE CO-CUTLURED WITH NHLFS. TUMOUR CELLS CAN BE OBSERVED TO INVADE THE VASCULATURE CHAMBER. 228

FIGURE 94 – (A) ILLUSTRATION OF TUMOUR CELL DENSITIES FOR DRUG SENSITIVE (PURPLE) AND RESISTANT (GREEN) TUMOUR CELLS AS A FUNCTION OF CONSISTENT MTD TREATMENTS. EACH SUCCESSIVE TREAMTENT REDUCES THE NUMBER OF SENSITIVE CELLS UNTIL ONLY RESISTANT CELLS REMAIN. (B) ILLUSTRATION OF THEORISED TUMOUR CELL DENSITIES IF ADAPTIVE TUMOUR THERAPY WAS USED. USING AN ADAPTIVE DOSE PREVENTS MASS SENSITIVE CELL DEATH AND IN TURN PREVENTS OVERGROWTH OF RESISTANT TUMOUR CELLS (FIGURE HAS BEEN REPRODUCED FROM ZHANG ET AL UNDER CC LICENCE) [217]. 230

FIGURE 95 – BRIGHT-FIELD IMAGES OF (A) LS147T MONOCULTURES AND (B) LST147T – NHLF COCULTURES AFTER 96 HOURS OF GROWTH ON-CHIP. COCULTURES CAN BE SEEN TO CONTRACT AWAY FROM THE WALLS TO FORM A DENSE, SOLID MASS WHEN COMPARED TO THE MULTIPLE MICROTUMOURS FORMED IN THE MONOCULTURE

MODEL. IMMUNOFLUORECENT STAINING OF CEA PRODUCTION IN (C) MONOCUTLURE AND (D) COCULTURE MODELS, SHOWING BOTH CULTURE CONDITIONS RESULT IN THE PRODUCTION OF CEA..... 231

LIST OF ABBREVIATIONS AND ACRONYMS

ATP – Adenosine Triphosphate

APC – Adenomatous Polyposis Coli

BME – Basement Membrane Extract

BSA – Bovine Serum Albumin

CAF – Cancer-associated Fibroblast

CFD – Computational Fluid Dynamics

CRC – Colorectal Cancer

COX-2 – Cylco-Oxygenase-2

DMEM – Dulbeccos Modified Eagles Medium

DLMB – Drug-loaded Microbubble

DOX - Doxorubicin

ECM – Extracellular Matrix

EGM-2 – Endothelial Growth Medium-2

EMT – Epithelial to Mesenchymal Transition

FGF – Fibroblast Growth Factor

GFP – Green Fluroescent Protein

HCT116 – Human Colon Tumour-116

HFFF2 – Human Foetal Foreskin Fibroblast

HIF-1α – Hypoxic Inducible Factor-1α

HUVEC – Human Umbilical Vein Endothelial Cell

LS - Liposome

NHLF – Normal Human Lung Fibroblast

MB – Microbubble

MI – Mechanical Index

MMP – Matrix Metalloproteases

PBS – Phosphate Buffered Saline

PDMS – Polydimethylsiloxane

PDGF – Platelet-Dervied Growth Factor

PGE-2 – Prostaglandin-E2

RFP – Red Fluorescent Protein

TAM – Tumour Associated Macrophages

TCM – Tumour Cell Media

TGF-β – Transforming Growth Factor-β

TNF-α – Tumour Necrosis Factor-α

US – Ultrasound

VEGF – Vascular Endothelial Growth Factor

1 INTRODUCTION

1.1 Overview

This PhD project was formed from a collaboration between the Molecular and Nanoscale Physics (MNP) group within the School of Physics and Astronomy and the Leeds Institute of Medical Research at St James' (LIMR) group within the School of Medicine. The purpose of this project was to develop a microfluidic colorectal cancer cell culture system for the testing and evaluation of microbubble (MB)-mediated drug delivery. The proposed project would initially consist of the design and development of microfluidic devices capable of supporting 3D tumour cell cultures. These models would improve on previously used 2D monolayer models, allowing for greater insight into the efficacy of using MBs to deliver drugs to both solid and vascularised tumours. Once the appropriate systems were developed, the effects of MBs were to be evaluated using several drug formulations proposed to improve drug treatments and address the current challenges faced in the effective treatment of cancer. Confocal fluroescence microscopy and dead cell staining were used to assess the state of on-chip cell cultures in a non-destructive manner whilst well-established viability assays could be used to determine the efficacy of therapeutic treatments as an end-point assay. This multi-faceted project encompassed a broad range of techniques spanning multiple scientific disciplines. The following section will describe the development of complex 'tumour-on-chip' microfluidic cell cultures from simplistic 2D monolayer models. The section will then finish with describing the use of MBs as ultrasound contrast agents, and how their response to ultrasound allows for a potential means of enhancing drug delivery.

1.2 3D Cell Culture Techniques

Culturing cells using 2D surfaces, such as culture flasks or well plates, has long been the conventional method by which cells are grown and used for experiments. However, in recent years it has become apparent that results observed when testing new potential therapeutics on 2D cultures, do not necessarily reflect the observed results *in vivo*. This is due to the failings of 2D cultures to effectively recreate the physiological environment of *in vivo* cells, resulting in cultures lacking the appropriate multicellular compositions, cell-cell connections, and surrounding extracellular matrix (ECM). The most notable effects of these failings are the differences in cell viability, metabolism and differentiation observed in 2D monolayers. Increased cell-cell connections in 3D cultures allow cells to remain viable in sub-optimal conditions, whereas 2D monolayers are considerably more sensitive to changes in environmental conditions. The effects of metabolic differences in 2D and 3D cultures have been observed when testing chemotherapeutics on cancer cells. Both increased and decreased sensitivity has been observed to various drugs, highlighting the need for models which produce results that reflect the *in vivo* effects of drug treatments [14–16]. One of the primary factors affecting the metabolism of cells in 3D cultures is the oxygen and nutrient gradient created by the dense structure of cells. Due to limited oxygen availability, 3D cultures often contain a hypoxic core of minimally viable cells. This is then followed by an outer layer of senescent cells which have ceased dividing but still remain viable. Finally, 3D cultures contain an outermost layer of rapidly dividing cells which have sufficient access to nutrients and oxygen [17–19].

Various methods of forming 3D cultures have since been developed, many of which aim to form a 3D spheroid aggregate of cells known simply as a spheroid. Spheroids are most commonly formed using hanging drop, agitation, forced-floating, and ECM scaffold methods - often using one or more different cell types [16,20–22]. Hanging drop utilises the surface tension of inverted droplets to suspend cells such that aggregation into a 3D culture is possible. Droplets of cell-media suspension are aliquoted onto a plate or tray, which is then carefully inverted, causing cells to fall to the bottom of the droplet meniscus and aggregate. This method is very effective at forming small single spheroids; however, it is only achievable with small volumes of media ($\approx 50\ \mu L$) due to the lack of sufficient surface tension in larger droplets. Furthermore, media changes are generally not possible

meaning culture conditions are static [18]. Several modifications have been made to early hanging drop systems to overcome the initial design limitations - such as the incorporation of an humidification chamber to reduce droplet evaporation, and the use of microchannels to increase droplet loading efficiency (figure 1) [4].

The formation of spheroids through agitation uses a spinner flask to continuously stir the cells. This prevents adherence to the flask and encourages cells to aggregate and form cell-cell connections. Cell concentration and spinner speed can be altered to influence the size of spheroids formed however, in general, this technique allows for little control of spheroid size and produces a range of diameters. Forced floating spheroid formation is perhaps the simplest method of creating 3D cultures. It uses well-plates with a treated surface which prevents cells from adhering, instead causing aggregation into 3D cultures at the bottom of the well [16]. Spheroid size is easily controllable and regular media changes can be performed. This technique can often be labour intensive and time-consuming if 96-well plates require manual low-adhesion coatings. Pre-coated plates are commercially available however, they are expensive which again poses issues for large scale production [18]. Overall, scalability and high-throughput production is a challenge which many spheroid formation techniques face when being considered for industrial/pharmaceutical applicatons. Figure 1 shows a summary of the main spheroid production techniques described above.

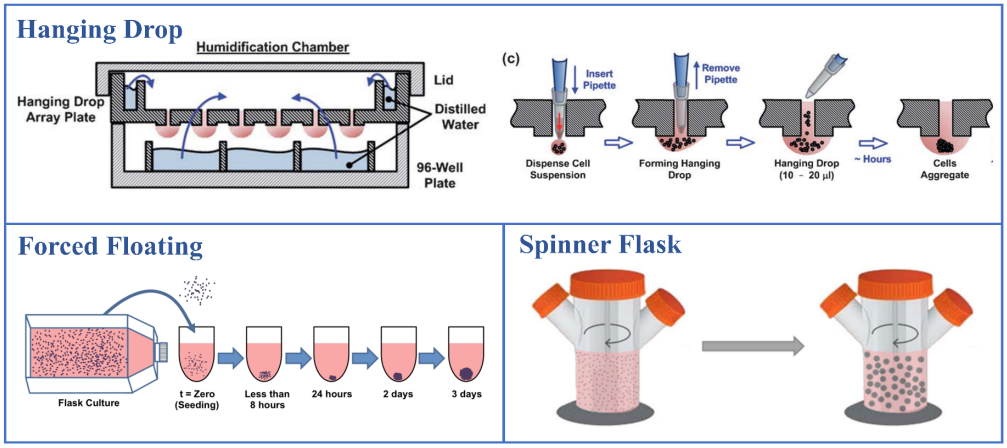

Figure 1 – Images depicting hanging drop spheroid production through the use of an inverted droplet array and humidification chamber [16], forced floating spheroid production using wells with a low adhesion coating, and spinner flask spheroid production [21,22]. All figures have been reproduced with permission from the copyright holder of each publication.

Hydrogel scaffolds, mimicking the ECM, are also often used to support the formation of 3D cultures, furthering their physiological accuracy. The ECM is a complex mixture of proteins and macromolecules which surrounds and supports cells. Proteins such as collagen and elastin provide structural support to tissues whilst fibronectin and laminin facilitate cell adhesion. Proteoglycans in the matrix also allow the ECM to store growth factors and water, releasing each to cells when required [23]. Further detail on the composition and function of the ECM can be found in section 2.1.2.1 (page 54). The incorporation of ECM scaffolds into spheroid production has resulted in spheroids displaying a more compact structure that is more resistant to anticancer drug penetration, which is consistent with *in vivo* observations [24,25].

As ECM is primarily produced by fibroblasts, incorporation of these cells into spheroids is a popular alternative method to directly using ECM scaffolds. Fibroblasts cultured alongside tumour cells differentiate to become cancer-associated fibroblasts (CAFs), also known as myofibroblasts [26,27]. Characterised by the expression of alpha-smooth muscle actin, CAFs secrete a myriad of growth factors, chemokines and ECM proteins that promote tumour growth, metastasis, and drug resistance [27–32]. As a result, CAFs increase the stiffness and densities of tumours, limiting the penetration and effectiveness of many chemotherapeutics. Several studies have investigated the link between the presence of CAFs and the progression of colorectal cancers, finding that an abundance of CAFs is associated with more aggressive tumours and a lower overall rate of disease-free survival [28,33–36]. This emphasises the need for the incorporation of multiple cell types in tumour cultures if a physiologically relevant model is to be achieved.

It is evident that 3D spheroid models are significantly more representative of *in vivo* tissues than 2D monolayers. Nevertheless, these systems are far from a complete model. Static 3D tumour spheroids fail to reproduce the dynamic environment of an *in vivo* tumour, preventing cells from being exposed to the shear stresses, interstitial pressures, and constant flow of nutrients that *in vivo* cells are subject to. Most therapeutic agents are also delivered by direct injection into the cardiovascular system and interact with tissues under flow conditions. Microfluidic technology offers a solution to these limitations, and many systems have been developed to allow for the maintenance of spheroid cultures under constant flow.

1.3 Microfluidics for 3D Cell Cultures

Microfluidics provides a solution to the shortcomings of static 3D cultures by offering a means of growing cell cultures supported by a constant flow of nutrients. The comparable dimensions of microfluidic channels to soft tissues and vessels also allow physiological features such as rates of diffusion, shear stress and interstitial pressures to be reproduced with relative ease. Many microfluidic chip designs also allow for control over chemical gradients, allowing for precise control over the cellular microenvironment. Various methods of fabricating microfluidics have been developed, such as replica moulding, microcontact printing and photolithography [37]. Photolithography, one of the most commonly used techniques, uses the selective exposure of a photoresist to produce patterned microscale structures on a silicon or glass wafer. Microfluidic devices can then be fabricated by soft lithography, which uses a liquid polymer to cast an elastomeric mould of the patterned wafer. Microcontact printing is a process similar to soft lithography however, instead of casting a mold, a PDMS stamp is created with a relief of the designs. This stamp can be immersed in a solution of interest, then the patterns transferred to a substrate. This then allows for seletive patterning of cells and other materials in specific configurations [38].

Polydimethylsiloxane (PDMS) is the most common polymer chosen for microfluidic fabrication, due to its transparency, gas permeability and inert interactions with cells. PDMS has, however, been show to absorb small molecules such as those found within anti-cancer therapeutics - questioning its suitability for drug treatment assays. Furthermore, PDMS' gas permeability prevents straightforward control over oxygen availbility within microfluidic systems, posing issues if hypoxic tumour conditions are looking to be reproduced. Alternate polymers have been developed, such as block copolymer thermoplastics and perfluoropolyethers (PFPE), both of which have shown further potential [39].

1.3.1 Spheroid Microfluidic Models

The previously described spheroid cell culture techniques have been combined with microfluidics to create various systems allowing for the growth and maintenance of spheroid cultures under constant flow. As shown in Figure 2, trapping chambers, microwell arrays and droplet-based systems have all been used to culture and trap spheroids. One example of this is the use of gravity traps to capture pre-grown spheroids in chambers [40]. This method allows for high trapping efficiency, but it is relatively low throughput due to the limited number of traps in each chip. In addition, the spheroids cannot be recovered from the traps for further off-chip assays, due to the flow characteristics through the gravity traps, analysis is therefore limited to imaging-based assays only.

A PDMS platform consisting of an array of polyvinyl alcohol (PVA) coated microwells has also been developed and shown to support the formation of MCF-7 spheroids. This allowed for the rapid and relatively high-throughput formation of spheroids however, the dimensions of the cell loading channels meant that spheroids could not be retrieved [41]. Hanging drop spheroids have also been incorporated into microfluidic networks, allowing for constant perfusion whilst keeping drop meniscuses intact. Communication between cells through this channel network was also demonstrated using drugs activated by specific cellular activity, therefore allowing for investigation of multiple tissue interactions on-chip [42]. Whilst requiring delicate handling throughout, hanging drop systems do allow for the simple retrieval of spheroids in comparison with other types of systems.

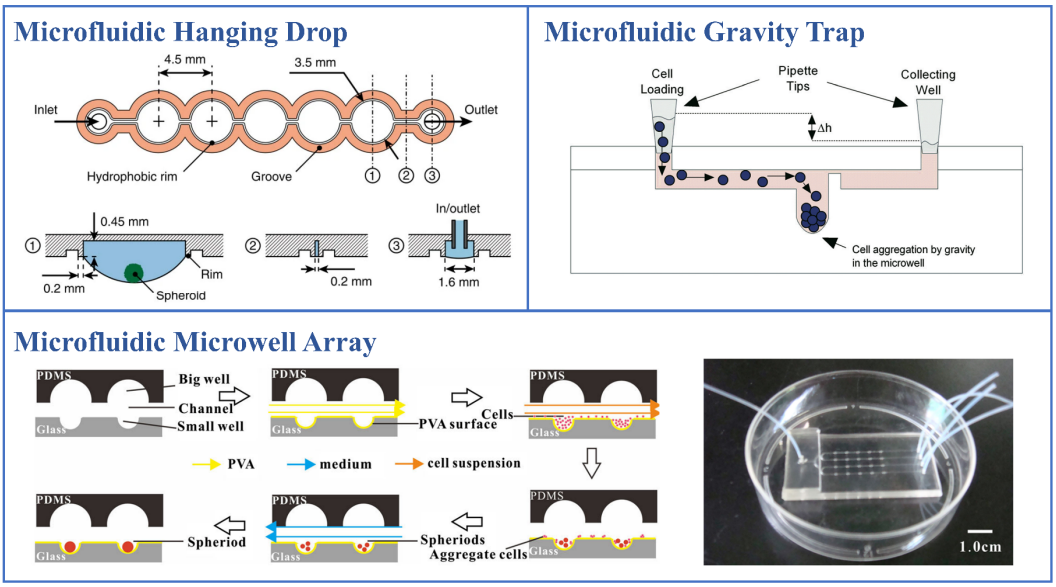

Figure 2 - Diagrams depicting microfluidic systems designed to produce spheroids using hanging drop [42], gravity trap [40], and microwell array [41] techniques. All figures have been reproduced with permissions from the copyright holder, RSC [40], and Springer Nature [40,41].

When designing spheroid on-chip systems, the size of the spheroids, and in turn, the dimensions of the microfluidic device must be large enough to ensure spheroids are comparable to *in vivo* tumours. The distance over which oxygen can diffuse into tissues is typically quoted to be 200 µm [43]. Therefore, spheroid diameters of approximately 400 µm would be required to recreate the hypoxia found at the centre of *in vivo* tumours. The size at which the spheroids are grown then affects the ability to retrieve spheroids from each chip for quantitative off-chip analysis. Whilst qualitative data obtained from imaging alone can provide significant information, quantification of fluorescent images can be problematic due to the scattering effects observed towards the centre of large spheroids. Finally, the ability of each system to test significant numbers of spheroids must be considered if ensemble data is required for the evaluation of therapeutics.

One potential trapping technique, could provide a means of having further control over these aforementioned spheroid on-chip design considerations. Hydrodynamic trapping relies on the use of the hydrodynamic force produced by fluid flow to confine an object in place. This trapping technique has primarily been used to trap single cells but has yet to be fully explored in a spheroid trap format. Pre-existing hydrodynamic spheroid traps

have used serpentine trap channels to sequentially trap multiple spheroids. Whilst this design shows effective trapping, there are limitations on the number of spheroids that can be trapped [44]. Spheroid traps designed using the framework used to develop single cell trap arrays is yet to be fully implemented in microfluidic spheroid systems – presenting an opportunity to develop a spheroid trap array which contains significantly more spheroids. The following sub-section will cover the development of single-cell hydrodynamic traps and the considerations required when designing these systems.

1.3.1.1 Hydrodynamic Trapping Systems

The development of single-cell trapping systems was driven by the requirement for precise control of the biochemical and physical microenvironments of cells. These lab-on-chip systems improve on conventional well-plate-based experiments which only provide ensemble average data on cellular response. The ever-increasing number of new therapeutics developed in the pharmaceutical industry has provided further motivation for progress in this field as improved drug screening methods are required to better understand fundamental cellular processes and molecular interactions.

Dielectrophoresis and gravity traps have been used to trap single cells however, hydrodynamic trapping is the most commonly implemented trapping method of trapping single cells in microfluidic systems. This method relies on the use of topographical trap features to separate and immobilize the cells from the fluid (Figure 3) [45]. The hydrodynamic force then pins the cells into the traps and ensures they remain in place. The challenge in developing effective hydrodynamic trapping arrays is the ability to trap significant numbers of cells evenly across all traps. Designs for these systems have to, therefore, be carefully considered and optimised in order to be fit for purpose. An advantage of this trapping technique is the lack of sophisticated instruments required - aside from the microfluidic fabrication facilities. Alternative single-cell trapping systems such as those using optical trapping or patch clamping require external force generators such as lasers, micropipettes and electrodes to function [46,47].

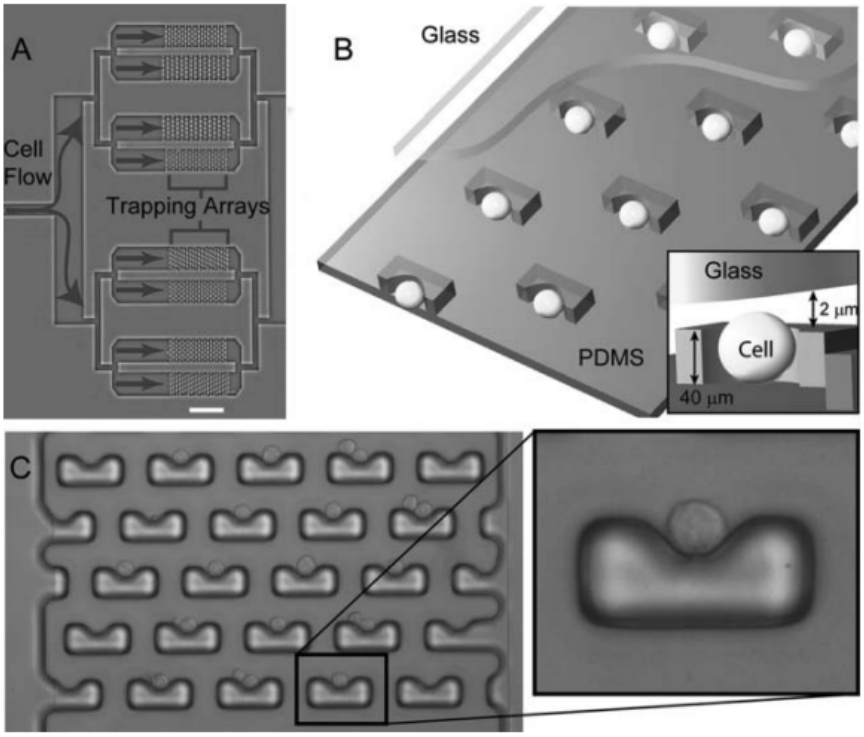

Figure 3 – Single cell trapping arrays developed by Di Carlo et al [45]. A) Diagram showing multiplexed trapping arrays and single channel input, scale bar 500μm. B) Diagram showing trapping concept with a gap below the trap allowing for media flow around the cell. C) A high-resolution image taken of cells occupying multiple traps across the array. Figure has been taken from Di Carlo et al with permission from the copyright holder [45].

One of the first microfluidic trapping systems was developed by Tan and Takeuchi and contained an array of trapping sites that filtered off from the meandering main channel [48]. Hydraulic resistances were calculated such that there was a high probability a single cell would become trapped as it flowed through the meander. A separate, microfluidic trap array was also developed at a similar time by Di Carlo et al [45]. This design consisted of an array of U-shaped traps arranged in a series of rows. A large number of cells would then flow through the array and become captured within each trap. Several trap arrays were multiplexed on one microfluidic chip to increase assay statistics. Figure 3 shows the overall chip design and individual trap features.

This chip design was recently further developed by X. Xu et al and is shown in Figure 4. The trap design was further optimised by considering the ratio of hydraulic resistances through and around each trap [49]. To allow for better control over these resistances, an additional channel was incorporated in the centre of the trap, much like the previous Takeuchi design. Decreasing the hydraulic resistance of the path through the trap (P_1 in

Figure 4b) compared to the path around the trap (P_2 in Figure 4b) increases the probability a microsphere/cell populates the trap. The presence of the microsphere/cell in the trap then increases the resistance through the trap, inducing any future particles to follow path P_2 and populate later traps.

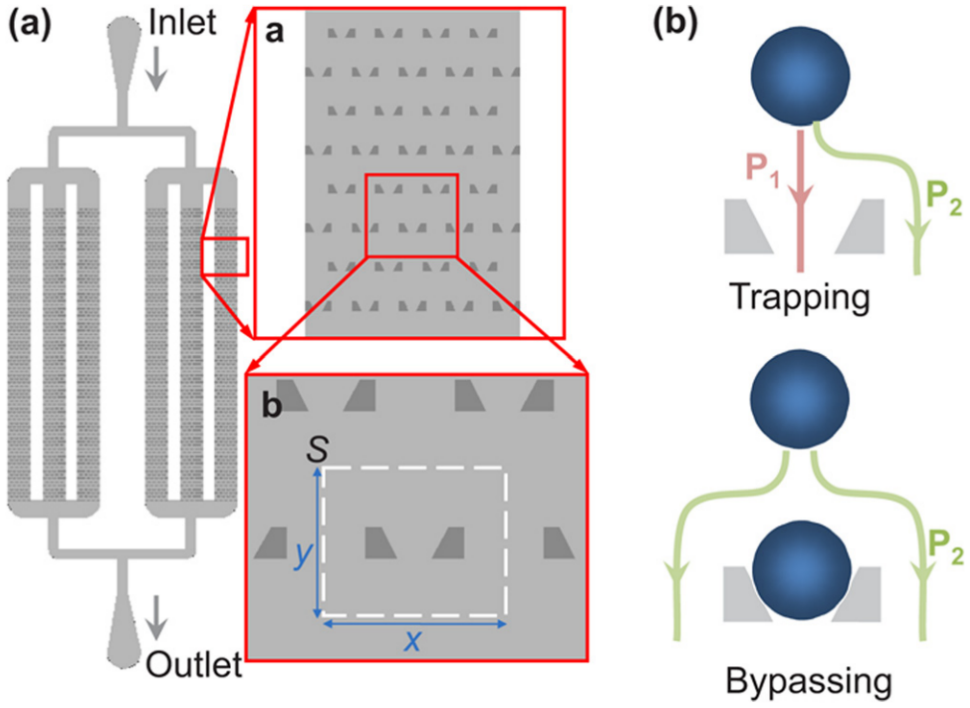

Figure 4 – Schematic of the microfluidic microsphere-trap array designed by X. Xu et al [49]. (a) A top-down view of the entire system showing the microsphere inlet, trapping arrays and outlet. Inset *a* shows a zoomed-in view of the trap arrays and inset *b* a single trap. (b) A diagram depicting the trapping mechanism. Path P_1 is designed to have a lower hydraulic resistance then path P_2 allowing a sphere to become trapped. Once the trap is populated, the resistance of path P_1 increases and the next bead follows path P_2. Figure has been taken from X. Xu et al with permission from the copyright holder [49].

As it will be shown in chapter 4, this fundamental trapping concept can be scaled up to consider spheroids. The underlying theory behind this design will reveal that many of the system dimensions affect the trapping efficiency. Nevertheless, the use of hydrodynamic trapping offers many design freedoms that previously discussed trapping techniques do not. Furthermore, the use of fluid flow to confine spheroids allows for simple spheroid retrieval by reversal of the flow direction – thus overcoming the reliance on qualitative imaging alone.

1.3.2 Solid Tumour Microfluidic Models

Although spheroid trap systems greatly improve on static 3D culture methods, there are still numerous shortcomings in terms of physiological accuracy. Primarily, these cultures fail to recreate the structure of tissues in which cells are supported by a network of vasculature. Incorporation of endothelial components into 3D cultures is essential when investigations concern the efficacy of drug treatments as the endothelial barrier will affect the delivery of the drug to the surrounding tissue. Lack of vasculature further limits the size of the tumours being studied as more advanced tumours will become vascularised to prevent hypoxia-induced necrosis in the tumour core. Microfluidic cultures have since advanced to address these issues, with increasingly complex systems successfully recreating both endothelial barriers and vascular networks.

Microfluidic tumour-on-chip systems have been developed to include the use of pre-patterned channels and chambers which enable the seeding of cancer cells embedded in hydrogel scaffolds. Cell chambers often include many design features, such as micropillar arrays or channel expansions, which allow for the confinement of cell-laden hydrogels to certain regions of the device. Neighbouring media channels then mimic nearby blood vessels, providing nutrients and removing waste products from cultures. Various designs have stemmed from this original concept, some of which are shown in Figure 5. Ayuso et al. used a chip containing a single media channel to recreate a nutrient gradient across a tumour cell chamber (Figure 5a). This recreated the gradient found in many solid tumours *in vivo,* which results in tumour cells adapting their metabolism to maintain rapid cell proliferation. The effects of several metabolic inhibitors were investigated, finding that glycolytic inhibitors only had a significant impact in dense cell cultures where tumour cells were forced to rely on glycolysis for energy [50]. Similar investigations also observed changes in cells gene expression as a result of hypoxia and starvation [51]. Ayuso et al. proceeded to further use this system to further investigate the effects of the immunosuppressive tumour environment on the cytotoxic capacity of natural killer immune cells [52,53]. Figure 5b shows the multi-chamber system developed by Liu et al. used to investigate the effect of CAFs on the invasion of tumour spheroid cells. Results found that tumour cells invaded the adjacent CAF cultures but rarely invaded healthy HFL1 fibroblast cultures, demonstrating the role of CAFs in cancer invasion [54].

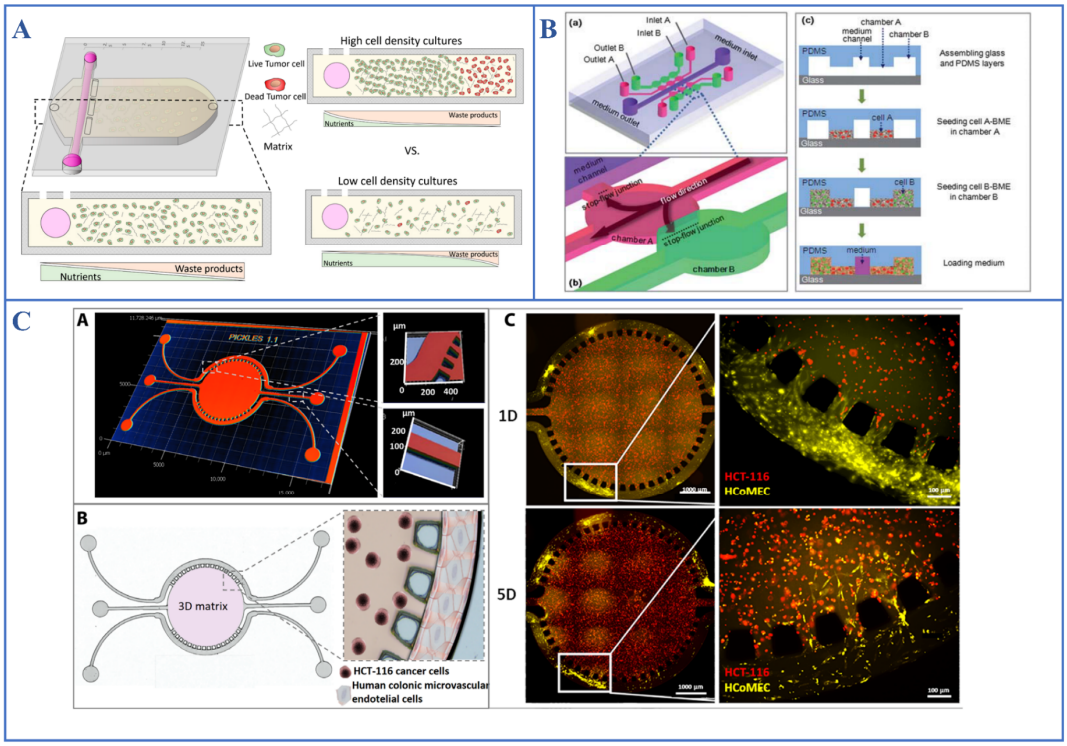

Figure 5 – a) Single channel-chamber chip used by Ayuso et al. for the investigation of cancer metabolism, gene expression and natural killer cell cytotoxicity (reproduced from Ayuso et al under CC licence [34]) [50,51,53]. b) A multi-chamber tumour on-chip system used by Lui et al. to determine the effects of CAFs on tumour cell invasion (reproduced with permission from the RSC) [54]. c) The microfluidic system used by Carvalho et al. with endothelial cells (yellow) lining the media channel adjacent to a solid tumour (red) chamber (reproduced from Carvalho et al under CC licence) [55].

In addition to fibroblasts, endothelial cells have also been incorporated into tumour-on-chip systems to recreate the endothelial barrier present between tumours and vasculature. As shown in Figure 5c, endothelial cells (yellow) can be seeded onto the walls of the media containing channels, where they grow to form a continuous monolayer [55]. Whilst this does not properly recreate the structure of vasculature, it still provides an effective barrier and allows for the interaction between tumours and endothelial cells to be studied. Further insight into tumour-cell interactions was also gained when Zervantonakis et al. investigated the effect of macrophages on tumour cell migration. The presence of macrophages was found to encourage the intravasation of tumour cells due to the presence of tumour necrosis factor-α (TNF-α), which was observed to increase endothelial barrier permeability [56].

The incorporation of additional cell types, such as endothelial and immune cells, into increasingly complex microfluidic systems, has allowed for the study of a range of interactions with tumour cells, elucidating the role of immunosuppression, the extracellular matrix, and hypoxia on tumours ability to resist anticancer treatments. Further knowledge on the mechanisms by which tumour cells extravasate through endothelial barriers and metastasize to other organs has also been gained using multi-chamber tumour on-chip models. Investigations such as these have aided the development of new cancer treatment strategies such as those using nanoparticles and immunotherapeutics [57,58], whilst also improving the high-throughput screening of potential new anti-cancer therapeutics. Although the incorporation of endothelial cells has improved the physiological accuracy of these systems, the native architecture of vasculature networks is not fully recreated in microfluidic channels lined with endothelial cells. The lack of a proper lumenised structure, basement membrane layer, and supporting stromal cells limits the reliability of many conclusions drawn using these rudimentary vasculature models. As a result of these shortcomings, tumour-on-chip microfluidic technology has progressed to developing models which more faithfully recreate vasculature networks.

1.3.3 Vascularised Microfluidic Models

The development of vascularised microfluidic cultures marked an important step forwards in the production of a physiologically complete system. Vasculature plays a crucial role in providing the surrounding tissues with nutrients and oxygen, and blood flow throughout it provides the appropriate biomechanical queues in the form of shear stress and interstitial flow. Furthermore, the development of cancer from a solid tumour with little metastatic potential, to an aggressive, rapidly growing mass requires the development of tumour-associated vasculature. Vascularised tumour systems are therefore essential if *in vivo* tumours are to be fully recreated and their development better understood.

Several simple vasculature structures have been recreated in microfluidic channels using methods such as viscous fingering or needle removal to create lumen-like structures inside hydrogels, or directly coating channels with hydrogels then endothelial cells [59–61]. Recently, however, perfusable vasculature networks have been formed by recreating the

angiogenesis and vasculogenesis which occurs at the site of wounds. If a vessel becomes damaged and begins bleeding, a coagulation process is activated which causes thrombin to polymerise fibrinogen into a fibrin clot – preventing further blood loss [62]. Nearby fibroblasts and other stromal cells migrate into the fibrin matrix and begin secreting growth factors such as vascular endothelial growth factors (VEGF) and stromal cell-derived factor-1 (SDF-1) which recruit endothelial cells from nearby blood vessels as well as circulating endothelial colony-forming cells from the blood. Fibroblasts remodel the fibrin matrix, laying down basement membrane proteins which then allow the endothelial cells to form new blood vessels and repair the damaged tissue [63,64]. It was discovered that this process could be recreated in microfluidic systems by seeding endothelial cells and fibroblasts in a fibrin matrix. Supplying the appropriate growth factors then induces cells to self-assemble into a fully perfusable vasculature network complete with supporting stromal cells.

Several microfluidic devices, such as those shown in Figure 6, have been developed for the formation of perfusable vasculature. One of the most common designs, developed and used by groups headed by C. Hughes and A. Lee and shown in Figure 6a, uses a series of microtissue chambers connected by communication pores [65–67]. Vessels were observed to form through communication pores, allowing for a continuous series of vasculature networks to be connected and supplied by media from adjacent side channels. These networks were found to support the growth of micro tumours which showed comparable rates of growth to tumours *in vivo*. Subsequent testing of anti-cancer therapeutics was found to recreate the *in vivo* responses of tumours to standard-of-care treatments – demonstrating that the system could be an effective tool for evaluating future anti-cancer drugs [68]. Recent work has adapted these microfluidic devices into a 96-well plate format, enabling multiple networks to be easily set up for high-throughput drug screening [69]. Fluorescent dextran molecules have been used to probe the perfusability of networks and determine the permeability of the vessels, confirming that an effective endothelial barrier has developed as vasculature forms. Immunostaining has been performed to confirm the presence of ECM proteins used as collagen I, IV and laminin. Proteins expressed by endothelial cells such as PECAM-1 (CD31) and f-actin have also been imaged to demonstrate *in vivo* behaviour [70,65].

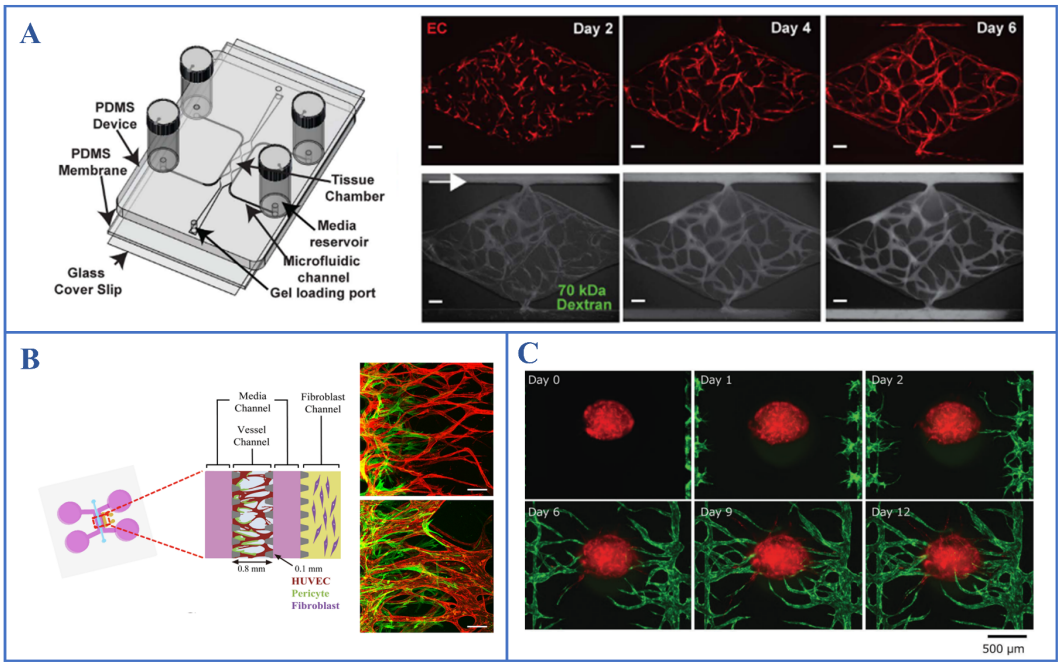

Figure 6 - a) The multi-tissue chamber device used in Hughes' and Lee's labs. Endothelial cells (red) can be observed self-assembling across the 6 days period, at which point dextran flows exclusively within the network (reproduced from Sobrino et al under CC licence [49]) [65–68]. b) The multi-chamber system used by Kim et al. to investigate the role of pericytes in vessel formation. Fibroblasts cultured in a separate chamber were observed to affect vasculature developed through paracrine signalling (reproduced from Kim et al under CC licence [70]). c) Observed interaction between an endothelial-fibroblast spheroid and surrounding endothelial cells. Fibroblasts were found to be necessary to induce branching towards the spheroid (reproduced with permissions from the copyright holder [71]).

Pericytes have also been used in vasculature systems to add further stromal support to vessels. Kim et al. used the system shown in Figure 6b to show that fibroblasts can support vasculature cultures in an indirect, paracrine fashion, and still result in vessel formation when cultured in a separate chamber [70]. Pericytes were found to wrap around vessels and secrete ECM components, fulfilling a similar role to fibroblasts when co-cultured. Vasculature cultures have also been combined with pre-grown spheroids to observe the interaction of solid tumours with nearby vasculature. Nashimoto et al. observed the effects of different spheroids, embedded in a fibrin-collagen hydrogel, on the response of nearby endothelial cells [71]. Endothelial cells did not form any branched structures when spheroids consisted of HUVEC or MCF-7 monocultures. Whereas, HUVEC-NHLF co-

culture spheroids resulted in the formation of branched vessel structures growing towards the spheroid – shown in c. After 7 days, it was found that the vessels perfused the interior of the spheroid and allowed for the administration of therapeutics. This study revealed the requirement for fibroblasts in the formation of vasculature and demonstrated that tumour cells alone were not capable of influencing vessel production.

Although microfluidic vasculature systems have been used to investigate various phenomena, there are still many areas of research that would benefit greatly from the use of more physiologically complex systems. The complexity involved in developing vasculature systems means it can be challenging to set up and use in many labs. Until the recent development of commercialised microfluidic devices capable of supporting vasculature cultures [72], microfluidic device production would often require a photolithography lab and clean room. Maintaining vasculature cultures also requires careful consideration of flow conditions, and often requires the incorporation of reservoirs or syringe pumps contained within incubators to maintain a constant flow. The challenges faced in setting up vasculature systems has resulted in many promising potential anti-cancer treatments continually being tested on inadequate cell systems. As it will be shown, MBs are one of such treatments, in which the majority of investigations have been conducted on 2D cell cultures, basic 3D models, or murine trials.

1.4 Microbubbles: Ultrasound Contrast Agents with Drug Delivery Potential

The introduction of spheroid and solid tumour cultures for drug toxicity assays highlighted one of the main issues with current cancer treatment methods – the lack of drug penetration into solid tumours. The physical barrier of ECM proteins produced by CAFs, along with the inherent drug resistance displayed by quiescent cells, results in many anticancer drugs failing to have a significant effect on tumour progression. As a result, various methods of enhancing drug delivery to tumours have been explored, such as the use of pH-sensitive or antibody-targeted drug carriers, drug-loaded nanoparticles, and ultrasound enhanced delivery. This section will describe the combined use of MBs and US as a method of enhancing therapeutic delivery to cells by creating pores in cell membranes through a process known as sonoporation.

1.4.1 Microbubbles as Contrast Agents

MBs are micron-sized gas particles typically stabilised by a lipid shell. Due to the compressibility of their gas core, MBs are highly responsive to US frequencies within the range of 1 – 15MHz, which cause bubbles to resonate and reflect US waves. When administered to the vasculature, MBs possess different acoustic characteristics to the surrounding tissues, creating a greater mismatch in acoustic impedances than blood alone. This results in an enhancement of US contrast, facilitating the improved imaging of tumour structures. Figure 7 shows US images taken of a microfluidic channel with and without MBs (a) alongside an image of a tumour with and without MBs present (b) [73].

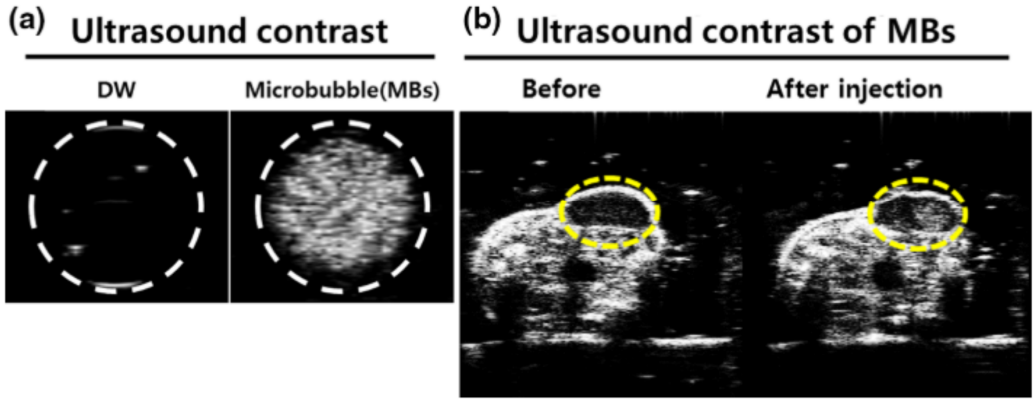

Figure 7 – Ultrasound images of (a) degassed water (DW) and MBs in a microfluidic channel. (b) an *in vivo* tumour before and after injection of microbubbles. Images from a review article by Lee et al. with permissions from the copyright holder [73].

Several commercialised MB contrast agents have been developed for use in US imaging, including SonoVue, Definity, and Optison. Each type differs in mean diameter, shell, and core compositions, making certain bubbles more appropriate for some applications. For instance, SonoVue uses a phospholipid shell encapsulating an SF_6 gas core which results in prolonged bubble stability due to low gas solubility and a stablising shell. Definity bubbles are instead produced with a C_3F_8 gas meaning MBs exhibit increased response to low acoustic US powers. US power, and in turn pressures, used for imaging are relatively low and result in a low mechanical index (M.I) value. M.I is a measure of acoustic pressure and is calculated by dividing the peak negative pressure by the square root of the centre frequency of the US beam (more detail can be found in section 2.3.3,

page 77). In general, the MI for US imaging without contrast agents is kept below 0.3, to avoid any unwanted cavitation effects [74]. Exposing MBs to low acoustic pressures and an MI < 0.05 induces linear oscillation of MBs, in which the incoming US waves are reflected back at the same frequency. US with a MI > 0.05 causes non-linear oscillations of MB resulting in the emission of harmonic frequencies in integer multiples of the original driving frequency. Recording harmonic frequencies allow for an improved signal-to-noise ratio in US contrast imaging [75].

1.4.2 Microbubble-Mediated Sonoporation

The use of higher M.I results in MBs undergoing a process known as cavitation. Stable cavitation, in which bubbles oscillate with small amplitudes, occurs at M.I approximately around 0.4 [76]. The rapid expansion and contraction of the MBs exert forces on nearby cell membranes, creating pores in a process known as sonoporation. Sonoporation has been shown to increase membrane permeability and allow for the increased passage of therapeutics into the cell. Stable cavitation prolongs MB longevity within the system, as many MBs are not destroyed initially. Successive oscillations of MBs result in gas leakage and eventual MB collapse. The use of higher M.I (> 0.5) induces MBs to expand too much greater diameters then collapse and fragment into smaller particles. Significantly higher pressures and temperatures are generated when MBs collapse and results in the generation of shockwaves [77]. This process referred to as inertial cavitation, has been associated with increased cellular uptake as well as irreversible sonoporation – where the pores created in cell membranes fail to reseal and result in cell death [78]. In addition to shockwaves, inertial cavitation also results in the formation of free radicals such as OH^- are formed from decomposing water vapour and other non-condesable gases – causing further damage to cells [79].

MB-mediated sonoporation offers a promising solution to the lack of drug penetration into tumours presenting a method of overcoming the barrier of densly packed cells and ECM. Various investigations into the synergistic effects of co-delivering therapeutics and MBs have been conducted [80–82]. De Cock et al. observed the uptake of model drug molecules FITC-Dextrans into cells using a range of acoustic pressures. Results found that low-pressure stimulation induced an increase in endocytosis, resulting in increased dextran uptake. However, increased uptake at higher pressures was mainly driven by the

formation of membrane pores due to the sonoporation caused when bubbles burst [81]. Further investigation into the effects of acoustic pressure by Wang et al. found that increased pressures or reduced MB-cell membrane distances resulted in the intensified deformation of the cell membrane. This was suggested to allow for enhanced therapeutic delivery and cytoskeletal disruption [80].

Whilst these studies provide insight into the interactions between MBs and cell membranes along with the effects of differing acoustic parameters, the basic 2D models used lack physiological complexity and neglect to incorporate the appropriate cell types, matrix, and cell structures. This limits the ability of these studies to predict the impact of MB-mediated drug delivery on tumours as a whole. Recent studies have begun testing MB therapies on static 3D spheroid cultures, observing the effects of delivery drug-loaded liposomes conjugated to MBs. Roovers et al. have shown that MB-induced sonoporation results in the 'sonoprinting' of DOX-liposomes from MBs onto the spheroid surface. This resulted in increased liposome toxicity compared to DOX-liposomes alone and was hypothesised to allow for lower doses of DOX to be administered in the clinic with the same efficacy [83]. Logan et al. observed similar effects and also incorporated drugs sensitive to US-induced cavitation into the MB complex [84]. As described throughout section 1.2 (page 31), the primary short-coming of static 3D spheroid models is the lack of flow conditions. Static spheroid cultures fail to reproduce the dynamic environment of *in vivo* tumours, and neglect to expose spheroids to the appropriate shear stresses and interstitial pressures. The lack of flow will contribute to inaccurate measurements of drug efficacy, as flow not only drives the interstitial flow of therapeutics into tumours but also allows for the removal of excess drug and cell waste products. The physical and biochemical limitations of current cell models contribute to many novel therapeutics being observed to have promising effects in the lab, but limited effects when tested within the clinic. It is evident that the study of novel cancer treatment strategies, such as those using MB-mediated sonoporation and drug delivery would, benefit greatly from improved microfluidic tumour spheroid models.

A further area in which microfluidic organ-on-chip cultures could be implemented in improving the investigation of MBs is in the production of vascularised systems to investigate the interaction between MBs and the endothelium. The endothelium presents

the first barrier for intravenous therapeutics and must be overcome if effective drug delivery to tumours is to be achieved. Endothelial cell-MB studies have been used to show increased permeability due to sonoporation, indicating that increased passage of therapeutics could occur [85,86]. However, many of these investigations are again carried out on 2D monolayers or pre-patterned 3D configurations. Each of which neglect to recreate the authentic structure of vasculature. *In vivo* studies using murine models overcome this complexity issue but are limited in their ability to effectively observe the interaction between MBs and cells. Results have shown that increased drug efficacy is achieved when co-delivering therapeutics alongside MBs, demonstrating the potential of sonoporation but providing no further insight into its mechanism. It is evident that improved vasculature models are required to better elucidate the mechanism behind MB-mediated drug delivery across the endothelial barrier and into surrounding tissues. A better understanding of this mechanism would allow for the optimisation of MB treatments, maximising their therapeutic effect.

1.5 Project and Thesis Overview

The ever increasing complexity of microfluidic cell culture systems has allowed further insight to be gained into the complex microenvironment of tumours and the mechanisms which drive drug resistance. The incorporation of multiple cell types, completed with ECM components and vasculature has enabled physiologically accurate systems to be developed which closely mimic many *in vivo* responses to therapeutic treatments. Whilst several studies have been conducted on such systems, the majority of potential novel treatment methods are still being tested on relatively simple cell systems which produce results that do not translate to results observed *in vivo*. The use of MB-mediated sonoporation to facilitate drug delivery across the endothelial barrier and enhance drug delivery tumours is one such novel treatment method that would benefit from experimentation on more complex microfluidic systems – herein lies the motivation for this project. This PhD project aimed to investigate the use of MB-mediated drug treatments using 3D tumour-on-chip microfluidic systems to evaluate treatment efficacy. Previous research in this area had only been conducted on simplistic 2D models, presenting an opportunity for novel research to be conducted. The initial aim of the project was to improve on static spheroid models and develop a system capable of allowing MB-

mediated drug delivery to be tested on tumour spheroids under constant flow conditions. Work would then focus on the development of a system incorporating 3D vasculature components that also allowed for MB-related experiments. This would further previous MB research which had only been conducted on inadequate endothelial cell monolayers.

The cancer of particular interest throughout this project is colorectal cancer, also referred to as bowel cancer, which forms in the lining of the large bowel or rectum. Colorectal cancer (CRC) is the fourth most common form of cancer, with an estimated 1:20 people developing the disease - resulting in it being responsible for the third most cancer-related deaths worldwide [87]. As colonoscopies remain the primary detection method for colorectal cancer, only about 40 % of cancers are discovered before they have metastasised to surrounding tissues - at which point 5-year survival rates drop to approximately 72 % [88]. Whilst it is evident that CRC patients would benefit greatly from improved diagnosis tools, the advanced stage at which CRC is often discovered means that effective treatment tools are also crucial to increasing survival rates. The efficacy of many drugs currently used to treat CRC however, is often limited by their systemic side effects. The use of targeted MBs conjugated with drug-loaded liposomes offers a promising solution to this issue, with the localised US release mechanism providing a further means of delivering drugs directly and exclusively to the tumour site.

The following chapter 2.1 will begin by describing the colorectal tumour microenvironment and the roles of the multiple cell types recruited to the tumour site. The theory behind MB composition, production and response to US will then be discussed in chapter 2.2. Finally, chapter 2.3 will contain the equations governing flow and hydrogel confinement within microfluidic systems, allowing the reasoning behind the design features of the microfluidic systems to be understood. The first results chapter I, contains the work carried out in developing and using a microfluidic spheroid trap system for the testing of MB-mediated delivery of Doxorubicin. This is the first instance by which the effects of MB sonoporation have been tested on 3D spheroid cultures under constant flow conditions. Both free and liposomal Doxorubicin was tested with liposomes both conjugated and unconjugated to MBs. The following results chapter II, contains the work done in developing and characterising a vasculature on-chip system. Several different endothelial and fibroblast cell types were tested in a range of configurations to determine

the optimal experimental setup for vasculature formation. Once consistent, perfusable vasculature could be produced, work proceeded to induce vasculature to display a tumour-associated phenotype by conditioning networks with media taken from tumour cell cultures. Integrin $\alpha_v\beta_3$, a cell surface receptor associated with angiogenesis and found to be upregulated in tumour vasculature, was found to be upregulated in endothelial cells as a result of tumour cell media conditioning – indicating a tumour-associated phenotype had been induced. Further observations, such as an increased rate of angiogenesis and lumen size also demonstrated the effects of using tumour cell media. The final results chapter III contains the experiments conducted using the vasculature system to investigate the efficacy of targeting therapeutics to integrin $\alpha_v\beta_3$, finding that liposome accumulation increased with increasing antibody concentrations and further increased within tumour-like vasculature. The use of MBs to further facilitate the accumulation of liposomes was tested and used to demonstrate the potential for $\alpha_v\beta_3$ -targeted MBs to increase the localised delivery of therapeutics to the tumour site.

2 BACKGROUND THEORY

2.1 Colorectal Tumour Microenvironment and Structure

The tumour microenvironment (TME) is a complex, dynamic environment, primarily comprised of cancer, stromal, immune, and endothelial cells, all of which are embedded in the extracellular matrix. Cancer cells directly interact with each of these components, influencing their phenotypes and promoting pro-tumour properties. Accurate recreation of the colorectal microenvironment requires consideration of all of these components with a comprehensive understanding of their impact on tumour progression.

2.1.1 Gene Mutation and Colorectal Cancer Development

The successful development of malignant colorectal cancer (CRC) from a benign colon adenoma requires a cascade of gene mutations. Figure 8 depicts the development of a malignant CRC tumour showing the factors affecting tumour progression at each stage of the tumour's development. Often regarded as the initiation of CRC, mutations in the *adenomatous polyposis coli* (APC) tumour suppressor gene begin the development of small adenomas in colon epithelial tissues. APC mutations interrupt the Wnt signalling process, which regulates the self-renewal of epithelial stem cells in intestinal crypts [89]. It is estimated that 85 % of CRCs contain APC mutations, which are somatic mutations caused by chromosomal instabilities – a characteristic of CRC [90]. The development of these small adenomas into larger adenomas can then be driven by KRAS and BRAF mutations. These mutations activate the MAPK pathway which plays an important role in cell proliferation and survival.

The final transition from a large adenoma to a malignant tumour can be driven by mutations in TP53, SMAD4 or PIK3CA genes. Inactivation of TP53, the gene responsible for p53 protein production, leads to an increase in cellular epithelial to mesenchymal transitions (EMT), resulting in increased cellular invasion and metastasis. SMAD4

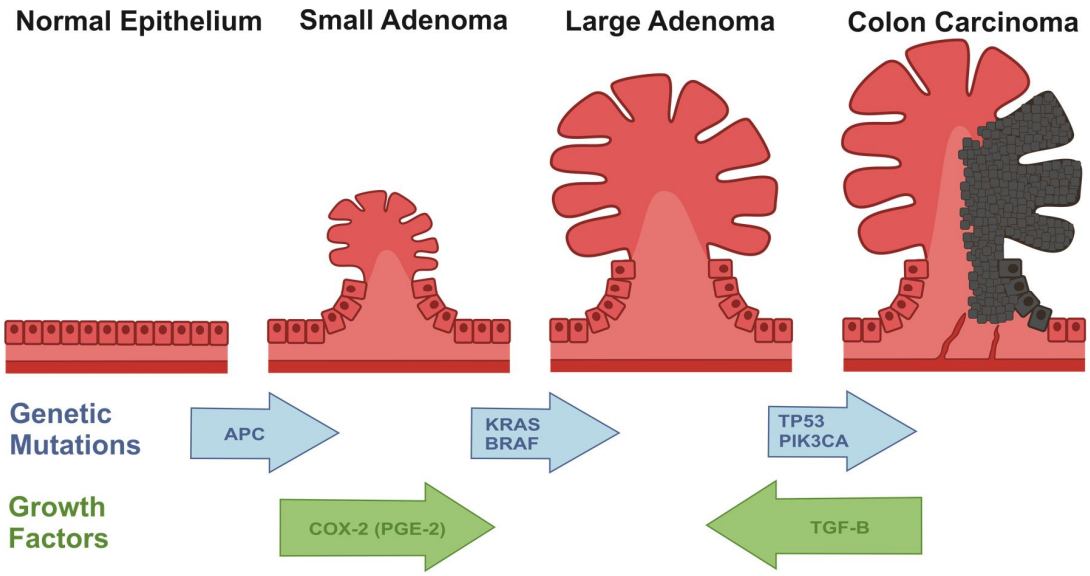

Figure 8 - Progression of the normal epithelium to colon carcinoma showing genetic mutations and growth factors influencing tumour progression.

mutations disrupt TGF-β pathways which also lead to increased EMT. Finally, mutations in PIK3CA oncogenes, which are common in many cancers, cause multiple pro-tumorigenic effects such as increased cell growth, metabolism and survival [91]. Alongside genetic mutations, increased inflammation is a major contributor to early CRC tumour development and is a hallmark characteristic of CRC. Inflammation at the tumour site is caused by increased prostaglandin production, a result of COX-2 enzyme upregulation. This increased inflammation, primarily induced by prostaglandin-E2 (PGE-2), increases blood flow to the tumour site and allows for increased growth and angiogenesis [92,93].

A further effect of PGE-2 is the regulation of immune response to the tumour. PGE-2 controls the function of multiple types of immune cells, which includes the control of cytokine secretion in dendritic cells, prevention of T-cell differentiation and inhibition of B-cell development. The collective effect of this is the overall suppression of anti-tumour immune response and the shift of immune cells to pro-tumorigenic phenotypes [94]. A further, detailed description of the tumour-immune system interplay can be found in section 2.1.2.3 (page 57). Reports indicated that COX-2 pathways are upregulated in approximately 85 % of colorectal adenocarcinomas, demonstrating the significance of this effect on CRC development [95].

2.1.2 The Tumour Stroma

Rapid tumour progression is facilitated by cancer cells innate ability to recruit healthy cells to the tumour site and induce pro-tumorigenic differentiations. Local, chronic inflammation at the colorectal tumour site attracts multiple types of cells such as endothelial cells, fibroblasts, macrophages, monocytes, and dendritic cells, amongst other immune cells. These cells, along with the extracellular matrix, make up the tumour stroma, a complex microenvironment that plays a crucial role in tumour progression. This section will describe the main components of the colorectal tumour stroma and their role in promoting tumour development.

2.1.2.1 The Extracellular Matrix (ECM)

The ECM occupies the intercellular space providing both structural and biochemical support to cells. Fibrous proteins and proteoglycans are the major molecular components of the ECM and collectively facilitate cellular adhesion, proliferation, and migration. The ECM also acts as a store for growth factors, allowing for the store or release of growth factors when prompted by cell-mediated interactions [23]. The composition of the ECM is dictated by the various cells that inhabit it and is unique to each tissue. Structural support is provided by fibrous proteins such as collagen I, fibronectin and elastin. Collagen I, the most abundant protein in the ECM, associates with elastin to form fibres that can undergo repeated deformation when the ECM is stretched. Fibronectin regulates the behaviour and adhesion of cells through integrin binding sites in the protein which become exposed when the protein is subject to force [96].

Hypoxia, the lack of sufficient oxygen, in the centre of tumours has been found to influence ECM restructuring and degradation. In response to hypoxia, tumour cells secrete hypoxia-inducible factors (HIFs) which upregulate the production of proteinases responsible for collagen degradation (MMP-2, -9). This, in turn, allows for increased tumour cell migration and enhanced metastatic ability. In addition to HIF, tumour cells have been observed to change their metabolism in response to hypoxic environments allowing for anaerobic energy production – known as the Warburg effect [97]. This results in the production of lactic acid which, in combination with the carbon dioxide produced, creates an acidic tumour microenvironment. This acidity has been observed to increase tumour progression through the production of pro-metastatic factors [98].

Tumour cells also affect the interstitial pressure throughout the ECM as a result of rapid growth. Mechanical stress forces exerted by rapid tumour growth increase interstitial pressure - encouraging the migration of cells into the surrounding blood and lymphatic vessels. This effect was studied within a microfluidic system with results showing that the increased interstitial pressure activates focal adhesion kinases (FAK) which are associated with increased migratory ability through co-localisation with integrins [99].

2.1.2.2 Cancer-Associated Fibroblasts (CAFs)

Fibroblasts in the surrounding tissue are recruited to the tumour site by PDGF and transforming growth factor-β (TGF-β) produced by cancer cells. Activated by tumour-induced tissue inflammation, fibroblasts differentiate into myofibroblasts, also referred to as cancer-associated fibroblasts (CAFs) and form a major constituent of the tumour stroma.

Primarily characterised by their production of α-smooth actin (α-SMA), myofibroblasts are responsible for a considerable amount of cancer-induced ECM remodelling. This consists of increased collagen and α-SMA deposition which collectively results in a stiffer ECM. Cells respond to this increased stiffness by intracellular contraction, stiffening the cytoskeleton and resulting in an overall increased migratory ability. ECM stiffness also increases interstitial pressure which, as mentioned previously, indirectly increases cell migration through activation of the FAK pathway [100]. In addition to ECM deposition, cancer-associated fibroblasts also degrade the ECM through the production of MMP-2, the enzyme responsible for collagen IV degradation [27]. Degradation and remodelling of collagen fibres perpendicular to the tumour has been observed to correlate with increased cell migration along the length of these collagen tracks [101].

CAFs are also a major source of growth factors and cytokines which facilitate angiogenesis, tumour cell migration and metastasis. Angiogenesis is promoted through a combination of VEGF and FGF, along with SDF-1 which recruits circulating endothelial progenitor cells (EPCs) to the tumour site. Along with stimulating new blood vessel formation, VEGF and SDF-1 have been observed to increase vascular permeability, a major factor influencing transendothelial migration and the overall metastatic ability of the cancer cells [102]. SDF-1 is also known to directly stimulate tumour proliferation, migration, and survival via the CXCR4 receptor. A study of the interaction between

stromal fibroblasts and CRC has also found that CRC cells directly influence fibroblasts causing the upregulation of VEGF and suppression of apoptosis [33]. In addition to this, CAFs influence the TME through the production of carbonic anhydrase IX, an enzyme that acidifies the tumour. This enzyme also activates fibroblast MMPs which further promotes the migratory abilities of the tumour cells [103]. Figure 9 summarises the major pro-tumourigenic influences of cancer-associated fibroblasts in the tumour stroma.

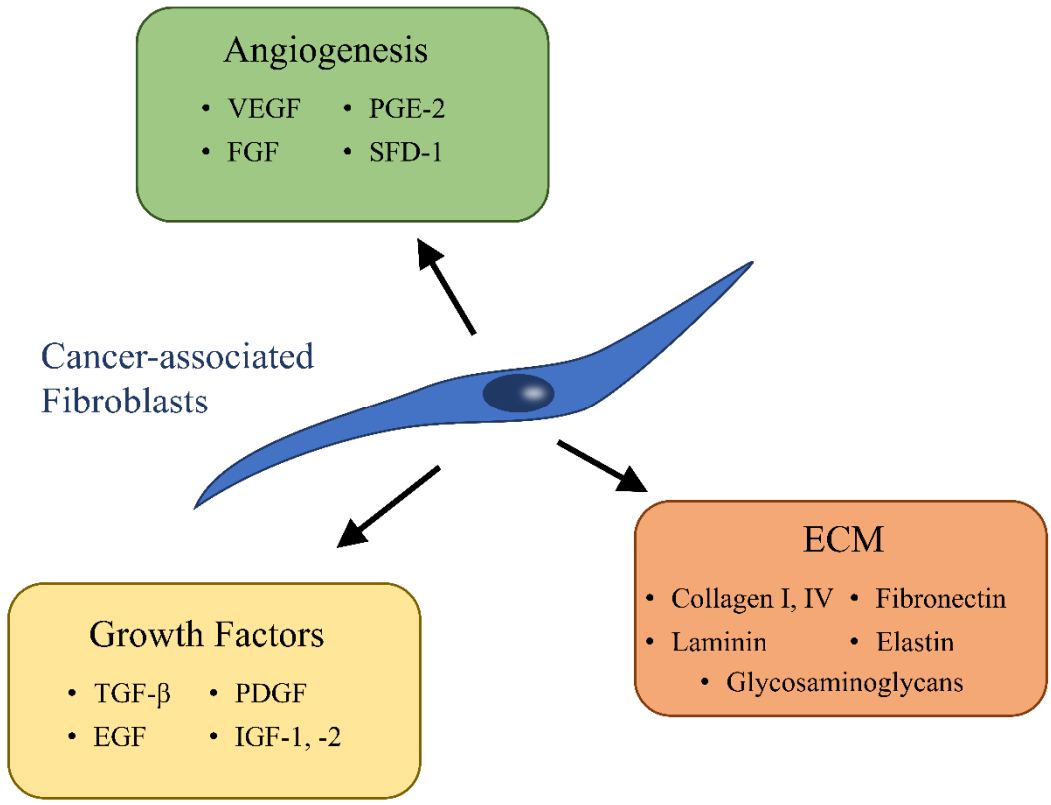

Figure 9 – Primary influences of cancer-associated fibroblasts in the tumour stroma. Fibroblasts secrete ECM components, growth factors and promote angiogenesis resulting in increased tumour growth, metastatic ability, and resistance to anti-cancer therapeutics.

2.1.2.3 Tumour Associated Macrophages (TAMs)

Macrophages are one of the most influential cells recruited to the colorectal tumour microenvironment, playing a crucial role in immunosuppression and the maintenance of chronic inflammation. Inflammatory cytokines produced by fibroblasts and cancer cells recruit monocytes from the blood which undergo an epithelial to mesenchymal transition and become tumour associated. The inflammatory cytokine interleukin-6 (IL-6) produced by tumour and stromal cells induces the differentiation of monocytes into tumour-associated macrophages (TAMs).

Under normal immune response conditions, macrophages may differentiate into either M1 ('fight') macrophages which promote inflammation or M2 ('fix') macrophages which decrease inflammation and encourage tissue repair. Genetic profiling of TAMs extracted from tumours determined that the TAM population is primarily composed of M2 macrophages, which promote angiogenesis through tissue repair mechanisms [104]. A key characteristic of colorectal cancer is chronic inflammation which suggests that the anti-inflammatory effects of M2 macrophages are insufficient in preventing inflammation. This chronic inflammation is crucial to tumour progression with the increase in blood flow allowing for the rapid production of vasculature – another characteristic of CRC. In addition to this, chronic inflammation induces further DNA damage enhancing cancer malignancy.

As mentioned previously, prostaglandin E2 (PGE-2) is upregulated in colorectal tumours due to cyclo-oxygenase (COX)-2 enzyme production induced by inflammatory stimuli and growth factors [105]. Primarily produced by macrophages, PGE-2 mediates immunosuppression by inhibiting white blood cell activation [106]. Analysis of COX-2 expression throughout colorectal tumours has also observed increased expression in cancer-associated fibroblasts and macrophages, suggesting that colorectal cancer cells induce upregulated expression in cells throughout the tumour microenvironment. In addition to immunosuppression, TAMs release various factors which promote angiogenesis and facilitate the migration of cancer cells. Investigation of TNF-α production by macrophages observed impairment of endothelial functionality resulting in a 4.6-fold increase in endothelial permeability. The increased permeability allows for greater transmigration of tumour cells allowing extravasation into surrounding blood

vessels – thus increasing the metastatic potential of the tumour. Figure 10 depicts many of the primary functions of TAM covered throughout this section. Overall, TAMs facilitate the development of colorectal tumours by driving inflammation, immunosuppression, and angiogenesis. This collectively results in increased rates of tumour growth and metastasis.

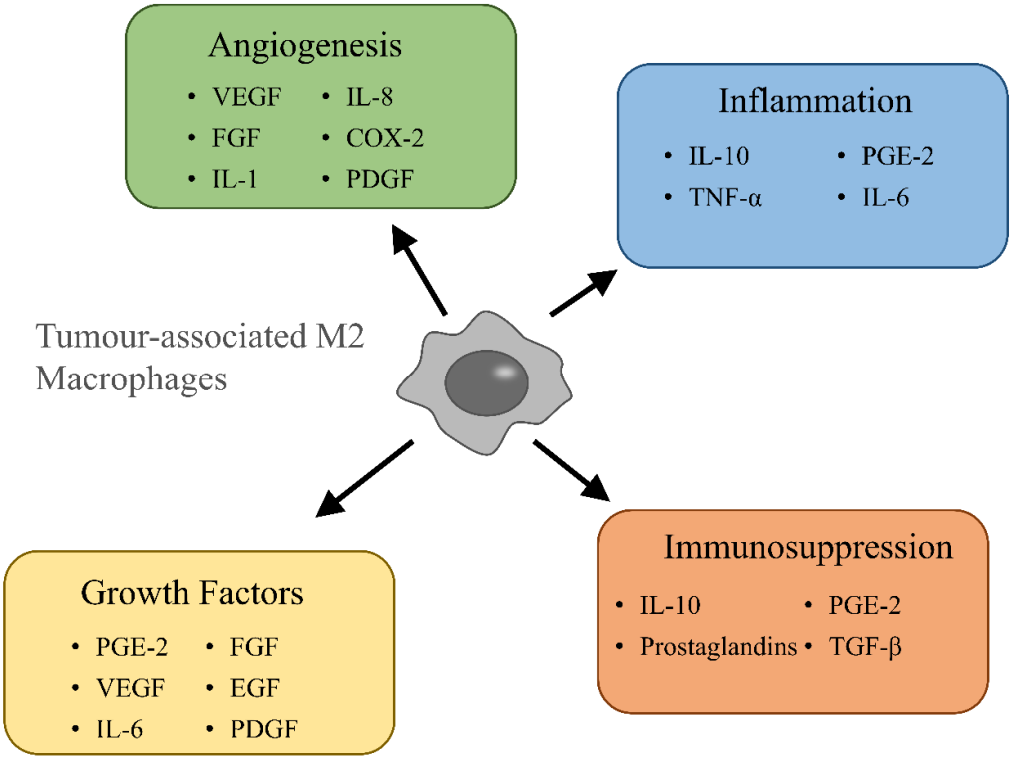

Figure 10 - Primary influences of tumour-associated M2 macrophages in the tumour stroma. Macrophages contribute to inflammation and immunosuppression in colorectal tumours, driving tumour growth, metastasis, and angiogenesis.

Investigation of colorectal tumour – TAM interactions have yet to be completed using microfluidics. Vascularised microfluidic systems have, however, recently been used to investigate the induced extravasation of tumour cells in the presence of monocytes using a system similar to those shown in figure 6. This study observed the differentiation of monocytes into inflammatory and non-inflammatory macrophages, which were subsequently observed to interact with breast cancer (MDA-MB-231) cells supported by the vasculature. Inflammatory macrophages were observed to intravasate significantly more often than non-inflammatory macrophages (87% compared to 12%), supporting

previous *in vivo* observations [107]. Direct contact between tumour cells and macrophages did not appear to affect tumour cells which suggested that monocytes act to impede tumour cells through a paracrine effect. Unexpectedly, macrophages in the extravascular space did not affect the ability of tumour cells to extravasate. Whereas undifferentiated monocytes within the vasculature did impede tumour cell transmigration out of the vasculature. Results overall suggested that intravascular monocytes have more of an anti-metastatic effect than intervascular differentiated macrophages [108].

2.1.3 Tumour Vasculature and Endothelial Components

2.1.3.1 The Angiogenic Switch

The development of tumour vasculature is a crucial step that dictates the progression of a tumour from a solid mass with little metastatic potential, to an aggressive, rapidly growing mass with high metastatic ability. This transition towards vascularisation occurs when the pro-angiogenic factors outweigh the anti-angiogenic factors, inducing what is known as the angiogenic switch [109]. This switch may occur at any point in a tumour's development and is dependent on tumour type and microenvironment. Many tumours do not undergo the angiogenic switch, instead remaining avascular masses which exist in a constant equilibrium between cell growth and apoptosis.

The two main inducers of pro-angiogenic factors in tumours are genetic mutations (discussed in sect. 2.1.1) and physiological stimuli - primarily induced by hypoxia. Solid tumours display hypoxic cores when the size of the tumours exceeds the distance which oxygen can sufficiently diffuse - which is typically around 200 µm. Hypoxia induces the secretion of the aforementioned hypoxia-inducible factor (HIF-a) – a potent driver of angiogenesis. HIF binds to hypoxia-response elements in genes that code for various pro-angiogenic growth factors such as VEGF, PDGF, SDF-1 and FGF resulting in increased production [110]. Many of these growth factors also cause recruitment of fibroblasts and macrophages to the tumour site, which in turn produce more pro-angiogenic growth factors, as previously discussed in section 2.1.2 (page 54) [100].

In addition to this, evidence of a link between hypoxia and the COX-2 pathway has also been observed. Zhao et al investigated the involvement of COX-2/PGE2 signalling in the hypoxia-induced angiogenic response of endothelial cells, finding that exogenous PGE-2 enhanced the effects of hypoxia in human umbilical vein endothelial cells (HUVECs), and increased proliferation and migration [111]. It has also been discovered that reduction of HIF-a results in reduced PGE-2 dependent VEGF production in gastric carcinoma cells [112]. VEGF has been found to correlate with high levels of COX-2 in CRC tumours, suggesting this pathway also promotes angiogenesis [113]. This is shown in later stage CRC tumours which display increased microvascular network density with increased COX-2 levels [114]. The result of which is the correlation of COX-2 increased tumour stage, grade and overall poorer prognosis. Non-steroidal anti-inflammatory drugs (NSAIDs) are known to inhibit the COX-2 enzyme pathway, and treatment with which, have shown to result in decreased angiogenesis in CRC models [115,116]. Overall, these findings indicate HIF involvement in the COX-2 pathway and subsequent angiogenesis however, more research is still required to further elucidate this relationship.

2.1.3.2 Tumour Angiogenesis

The response of endothelial cells to nearby tumour angiogenic factors begins with dilation of the vessel and increased vascular permeability. This is followed by detachment of pericytes and local basement membrane degradation to allow for cell migration into the extravascular space. Endothelial cells multiply and migrate towards the growth factor gradient, using filopodia filaments extending from membrane tips to detect local concentrations. Branching endothelial cells then join with other endothelial cells and begin to form a vascular basal lamina. In healthy tissue angiogenesis, perivascular cells re-associate with the vessel walls and lay down a basement membrane, completing vessel maturation [109,110].

Tumour angiogenesis often does not follow this route as the rapid vessel formation induced by increased angiogenic factors leads to chaotic, disordered network formation. This often results in a dense network of leaky, irregularly shaped vessels that are not properly associated with pericytes. Lack of pericyte involvement results in vessels remaining dependent on host-tissue VEGF production, as opposed to mature vessels which rely on pericyte VEGF production for stability and maintenance [117]. Lack of proper

lymphatic support results in increased interstitial pressure which inhibits blood perfusion and drug penetration into tumours. The lack of blood vessel stability can again be attributed to the angiogenic factor imbalance, with the near-constant angiogenesis earning tumours the description of 'wounds that never heal' [118].

Several anti-angiogenic therapies have been developed in an attempt to block VEGF production and its respective receptor VEGFR2 [119]. Clinical results from anti-VEGF therapies found that it results in endothelial apoptosis, and decreased vessel diameter and density [120]. However, an increase in perfusion and decreased interstitial pressure was also observed, leading to the theory that anti-VEGF therapy results in the normalisation of blood vessels to a more mature state. The use of this treatment alongside conventional chemotherapy drugs found an increase in overall efficacy. However, this treatment could not produce sustained effects in colorectal and breast cancers which were observed to revert to a constant state of angiogenesis once treatment was stopped [121,122].

More recent therapies have aimed to normalise tumour vasculature by delivering oxygen to the tumours. This aims to reduce HIF production, treating the cause of the VEGF production rather than the VEGF itself. Delivery of oxygen-MBs to a microfluidic vessel model was investigated using a system similar to that shown in figure 5a. Results found that pericyte recruitment to the vessel wall was significantly increased. Test of drug penetration into the surrounding matrix then found increased DOX accumulation after pericyte association [123]. Although simplistic in design, this microfluidic system provided evidence that vascular normalisation could be achieved with oxygen. The use of MBs also allowed for observation of vessel normalisation using US contrast imaging. This may provide a solution to a current issue faced in normalisation therapy – determining the final time point of the therapy [124].

2.1.4 Conclusion

A cascade of oncogenic mutations results in the development of malignant colorectal tumours from benign adenomous polyps lining the large intestine. Tumour progression then sees multiple types of cells recruited to the tumour site in response to a variety of growth factors and inflammatory stimuli. Extensive remodelling of the ECM in the tumour microenvironment then results in the formation of a dense, scar-like stromal structure that exhibits strong resistance to therapeutic treatments. An oxygen and nutrient gradient forms as the solid tumour grows and results in hypoxia and necrosis at the tumour core. Hypoxic factors are secreted by multiple cells resulting in the production of various pro-angiogenic factors. Once pro-angiogenic factors outweigh the anti-angiogenic factors, the angiogenic switch occurs and tumour vasculature rapidly forms. The disordered, dense network of vessels do not mature, instead remaining underdeveloped and hyperpermeable. This results in increased interstitial pressure and further limits the penetration of anticancer therapeutics. It is evident that tumours have a very complex, dynamic microenvironment, consisting of multiple cell types and extracellular matrix components. The development of a cancer model incorporating all of these components presents a significant challenge for tumour-on-chip systems. Nevertheless, several key features of tumours have been recreated through the use of 3D tumour-fibroblast co-cultures and the incorporation of endothelial components.

2.2 Microfluidic Theory

Microfluidics refers to the manipulation of fluids on the microscale. Fluid on this length scale behaves differently to large-scale fluid flow due to viscous forces dominating over inertial forces. As a result, flow on the microscale can be well described by a series of equations which then allows for precise manipulation of microscale flow. Microfluidic devices consisting of a network of microchannels, etched or moulded into a solid substrate have been developed which enable fluid to be flowed through. The application of this technology has led to the development of lab-on-a-chip systems which can recreate large-scale, bench-top biological and chemical processes in a controllable microscale system. This section describes the fundamental equations which govern the physics of fluid flow throughout the microfluidic systems used in this project.

2.2.1 Navier-Stokes and Poiseuille Flow

An expression for the volumetric flow rate down a flat, rectangular channel can be derived by applying the Hagen-Poiseuille law to the Navier-Stokes equation. The general Navier Stokes equation for a Newtonian fluid is given by:

$$\rho \cdot (\partial_t \mathbf{v} + (\mathbf{v} \cdot \boldsymbol{\nabla})\mathbf{v}) = \rho \mathbf{g} - \nabla P + \eta \cdot \nabla^2 \mathbf{v} \tag{2-1}$$

Where ρ is the fluid density (kg/m^3), $\mathbf{v}$ is the velocity vector (m/s), $\mathbf{g}$ is gravitational acceleration, P is pressure (Pa) and η is the kinematic viscosity (m^2/s) of the fluid. The terms on the left hand side of equation 2-1 arise from inertial forces due to fluid acceleration, these can be dervied using Newton's second law. The terms on the right hand side arise from external gravitational foces, external pressure forces, and internal viscosity effects, respectively.

The Navier-Stokes equation (2-1) can be simplified if assumption of an incompressible fluid is applied. The mass continuity equation, the first fundamental equation of fluid dynamics, states that:

$$\partial_t \rho + \nabla \cdot (\rho \mathbf{v}) = 0 \tag{2-2}$$

For an incompressible fluid, fluid density ρ is constant with time ($\partial_t \rho = 0$) therefore giving $\nabla \cdot \mathbf{v} = 0$. Applying assumption, along with the assumption that gravitational forces are neglible down a microfluidic channel, allows for the simplification of equation (2-1):

$$\rho \cdot (\partial_t \mathbf{v}) = -\nabla P + \eta \cdot \nabla^2 \mathbf{v} \tag{2-3}$$

The Reynolds number can be used to further characterise the type of flow within a microfluidic channel. Defined as the ratio of inertial forces to viscous forces, the Reynolds number is given by:

$$R_e = \frac{\rho v L}{\mu} \tag{2-4}$$

Where μ is dynamic viscosity (Pa.s) and L is the characteristic length (m) of the channel. For $R_e < 2000$, viscous forces dominate over inertial forces and the fluid flows in smooth, parallel paths known as laminar flow. Above this value turbulent flow occurs, in which the flow exhibits eddy currents, vortices and flow instabilities. In the case where the Reynolds number is vanishingly small ($R_e \ll 1$), a steady-state regime is imposed in which the fluid exhibits what is referred to as Stokes flow. The viscous forces dominate to an extent in which the fluid velocity is steady at all points ($\partial_t v = 0$). This further reduces equation (2-3), reducing the Navier-Stokes equation to:

$$\eta \nabla^2 v = \nabla P \tag{2-5}$$

Considering flow down an arbitrarily shaped channel with a yz plane cross-section $\mathcal{C}$ and boundary $\partial\mathcal{C}$ (depicted in Figure 11) allows an analytical solution of the steady-state Navier Stokes equation to be found. A constant pressure difference, ΔP is maintained across the channel length, L. Vanishing forces in the yz plane along with translational invariance of the channel in the x direction indicates a velocity field independent of x with non-zero x components only.

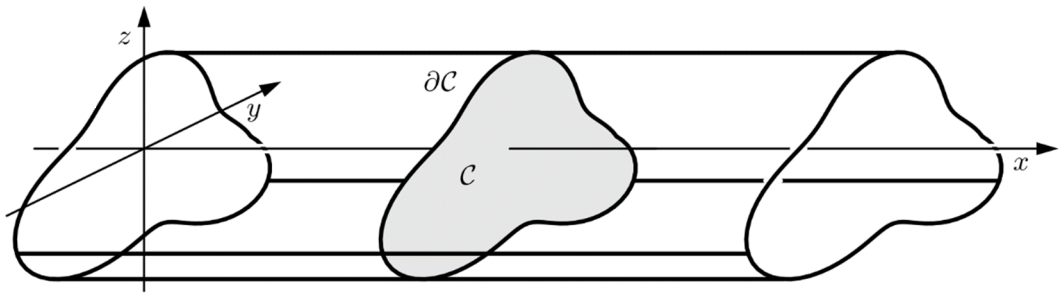

Figure 11 – Diagram of arbitrarily shaped channel with cross-section $\mathcal{C}$ used when considering the Poiseuille flow solution for flow down a microfluidic channel. This figure is adapted from lecture notes by H. Bruus [125].

The second-order partial differential equation the velocity field, $v_x(y,z)$ must therefore satisfy:

$$\left[\partial_y^2 + \partial_z^2\right] v_x(y,z) = -\frac{\Delta P}{\eta L} \qquad \text{for } (y,z)\,\epsilon\,\mathcal{C} \qquad (2\text{-}6)$$

$$v_x(y,z) = 0 \qquad \text{for } (y,z)\,\epsilon\,\partial\mathcal{C} \qquad (2\text{-}7)$$

This is imposing the no-slip boundary condition that the velocity is zero at the channel boundary $\partial\mathcal{C}$. Integration of the velocity field over the yz cross-section $\mathcal{C}$ then gives the volumetric flow rate down the channel. Equation (2-6) is as far as the solution can be worked without consideration of the channel geometry. For a flat, wide ($w > h$) rectangular cross-section channel, a precise analytical solution cannot be derived. Instead, a Fourier series is derived which is subsequently integrated to give:

$$Q = \frac{h^3 w \Delta P}{12\eta L}\left[1 - \frac{0.63h}{w}\right] \qquad (2\text{-}8)$$

Where Q is the volumetric flow rate (m^3/s) and h and w are the height and width (m) of the microfluidic channel, respectively. The full derivation of this solution can be found here [125]. This equation is only precise for steady-state Pouiselle flow down infinitely long channels but can be used as an accurate approximation for the resistance throughout many systems providing the Reynolds number remains small.

2.2.2 Flow Using Hydrostatic Pressure

As opposed to using conventional syringe drivers, flow throughout the devices used in this project was driven by hydrostatic pressure via media reservoirs. The fluid flow down a microfluidic channel due to a hydrostatic pressure imbalance can be defined as the difference in hydrostatic pressure, ΔP(t) (Pa) divided by the hydraulic resistance of the channel, R_{hyd} ($Pa.s/m^3$):

$$Q(t) = \frac{\Delta P(t)}{R_{hyd}} \qquad (2\text{-}9)$$

Where Q(t) is the volumetric flow rate in m^3/s. This relationship is analogous to Ohm's law for electrical circuits.

The pressure difference is dependent on the height difference between reservoir liquid levels, ΔH(t) (m) as well as an additional capillary force term, P_{cap} (Pa):

$$\Delta P(t) = \rho g \Delta H(t) - P_{cap} \quad (2\text{-}10)$$

Where, $$P_{cap} = 2\sigma_{lg}(-cos(\theta_a) + cos(\theta_r))$$

Where ρ is the density of the liquid (kg/m^3), g is gravitational acceleration (m/s^2), σ_{lg} is surface tension (N/m) between the liquid-air interface. θ_a and θ_r are the advancing and receding contact angles of the outlet and inlet reservoir liquids. The capillary force term can be determined experimentally by measuring the contact angles. Alternatively, measurement of the residual height difference between fluids after equilibration would also allow for the calculation of the pressure value. Figure 12 shows a depiction of two reservoirs connected by a simple straight channel of length, L alongside diagrams showing how the advancing and receding contact angles can be observed.

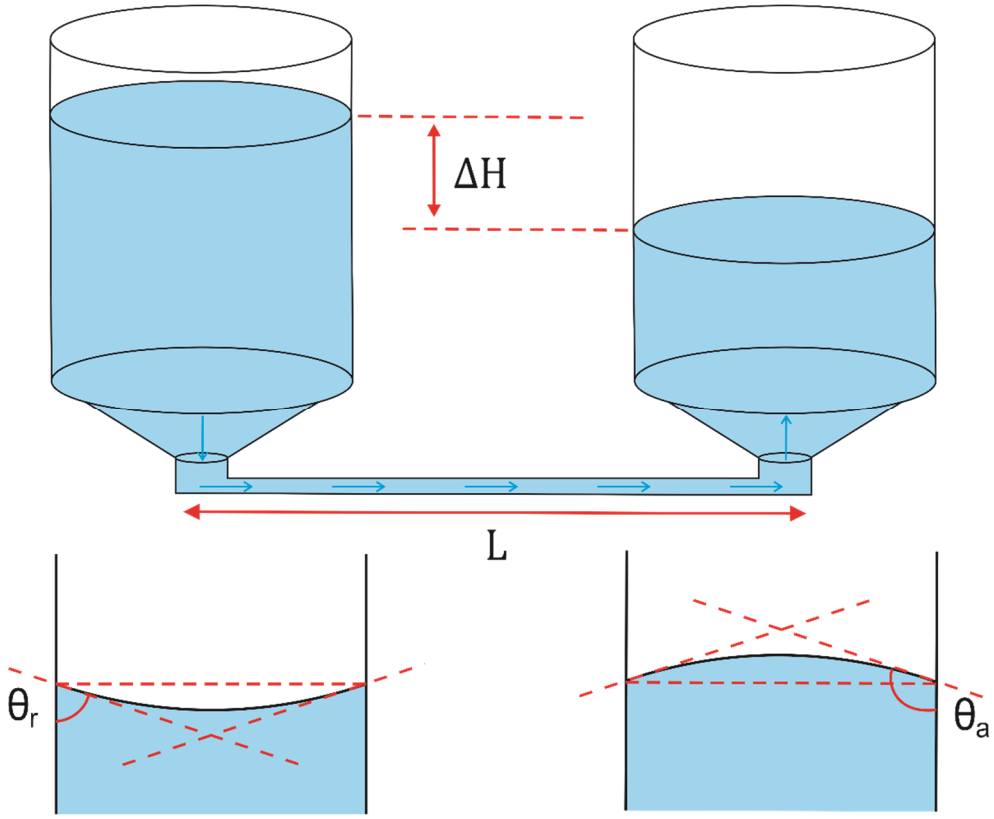

Figure 12 – Depiction of fluid imbalances inducing hydrostatic flow between reservoirs. Lower diagrams show the receding, θ_r and advancing, θ_a contact angles in inlet and outlet reservoirs, respectively.

From equation (2-8) it can be seen that the hydraulic resistance in equation (2-9), R_{hyd} will be given by:

$$R_{hyd} = \frac{12\eta L}{h^3 w}\left(1 - \frac{0.63h}{w}\right)^{-1} \quad (2\text{-}11)$$

The dependence of the hydraulic resistance on channel dimensions allows microfluidics to be designed to give desired flow rates. This is primarily done by altering channel lengths with the use of serpentine channels which consist of tightly bunched zigzagging channels. Here, serpentine channels were used to increase the length and subsequent resistance of the side channels without increasing the overall dimensions of the microfluidic device. Figure 13 shows a typical 20 mm long straight channel alongside a 150 mm long serpentine channel. The physical length of the design remains unchanged however, as R_{hyd} is directly proportional to the channel length, L, the resistance through the serpentine is increased by a factor of 7.5 compared to the straight channel.

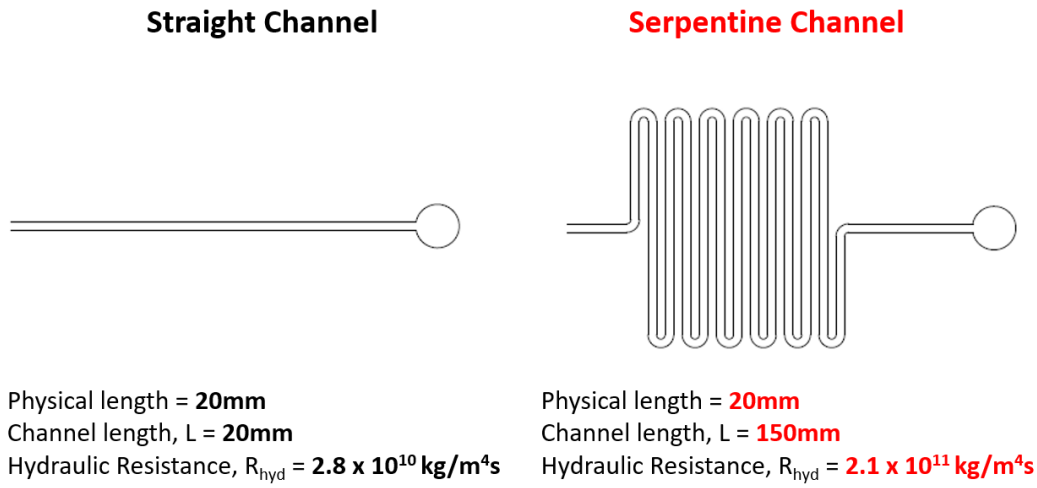

Figure 13 – 20 mm long straight channel (left) alongside a 150 mm long serpentine channel (right) each with a physical design length of 20 mm. The increased channel legnth results in a 7.5-fold increase in hydraulic resistance in the serpentine channel (calculated with a channel width of 0.4 mm and height of 0.35 mm used throughout the spheroid on-chip system).

The time dependence of fluid height difference originates due to the simultaneous emptying and filling of inlet and outlet reservoirs. To find an expression for the rate at which the height difference decays, it is first necessary to find the change in height after a time, t_1 (s):

$$\Delta H(t_1) = \Delta H(t_0) - \frac{2Q(t_0)dt}{\pi r^2} \tag{2-12}$$

Where r is reservoir radius (m) and $dt = t_1 - t_0$. Rearranging equation (2-9) and substituting height terms in the above equation gives:

$$dQ(t) = Q(t_0)\left[1 - \frac{2\rho g dt}{R_{hyd}\pi r^2}\right] \tag{2-13}$$

Note that the capillary pressure term has been omitted as it is independent of time, and only translates the flow rate – time decay curve along the y axis.

Solving equation (2-13) for Q(t) then gives:

$$Q(t) = Q(t_0)\, exp\left(-\frac{t}{\tau}\right) \quad \text{where,} \quad \tau = -\frac{R_{hyd}\pi r^2}{2\rho g} \tag{2-14}$$

This shows that there is an exponential decay of flow rate, with a time constant dependent on hydraulic resistance and reservoir radius, as expected. Equation (2-14) was used to model the decay of volumetric flow rate, channel pressure and linear flow rate with time for both microfluidic systems used in this project.

2.2.3 Hydrogel Confinement using Micropillars

One of the primary advantages of using microfluidic lab-on-a-chip systems is the ability to pattern and confine fluids into desirable configurations. This is of specific interest for organ-on-chip systems which require the precise patterning of cells and fluids to effectively recreate the structures of the *in vivo* tissues being mimicked. Hydrogels are commonly used as a scaffold to support 3D cell cultures Whilst the laminar flow properties of fluids allow for parallel flow profiles and limited mixing by diffusion only,

the use of cell-laden hydrogels requires alternative methods to ensure a successful system setup. Micropillars [71,126,127], phaseguides [72] and hydrophobic patterning [128] have all been used to effectively confine hydrogels in microfluidic devices. Figure 14 depicts the use of each of the techniques in similar microfluidic systems.

Micropillars and phaseguides often rely on the difference in pressure across the hydrogel-air (or liquid) interface to pin the hydrogel in place. More recently, the use of hydrophilic and hydrophobic surface coatings has been implemented and shown to produce successful confinement without the need for physical structures. Specific surfaces within the device can be pre-coated using the laminar flow properties of fluids which enable a wider range of device configurations to be explored compared to pillar-type designs. In the case of this project, micropillars were chosen as the confinement method. The relatively large microfluidic features and equal aspect ratios throughout this system allowed for the production of micropillar features with relative ease.

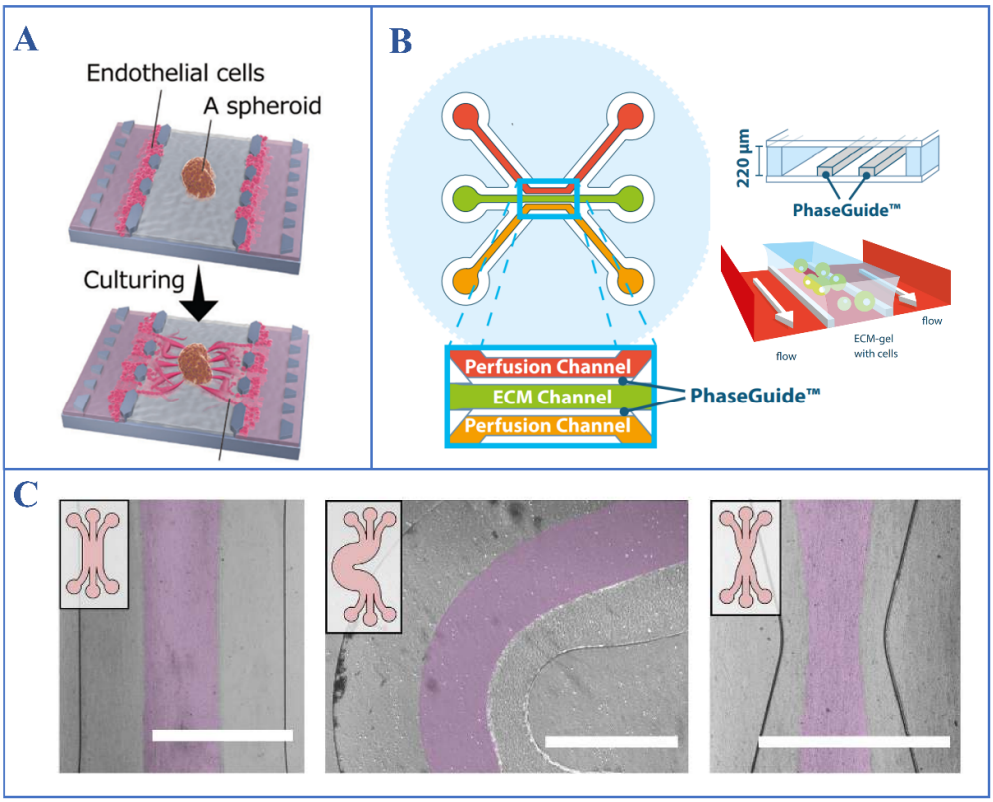

Figure 14 - (a) Diagram showing the use of microfluidic micropillar arrays to confine cells, hydrogels and spheroids (reproduce from Nashimoto et al with permissions from the copyright holder) [55]. (b) Diagrams of 3-channel OrganoPlate® microfluidic device which implements the use of PhaseGuides™ to confine ECM/hydrogels to the centre channel [72]. (c) Images showing the use of hydrophobic coatings to confine liquids (purple) in microfluidic channels without the use of mechnical feautures. Various designs are shown to illustrate the flexibility of this technique (reproduced from Lossberg-Zahl et al under CC licence) [128].

Figure 15a depicts the micropillar design used and highlights some of the parameters considered when designing the system. A crucial requirement for device functionality is the successful confinement of the hydrogel to the centre chamber. Failure to confine the gel results in blockage of the side channels when the gel polymerises, rending the entire chip useless as media can no longer be pumped through the system.

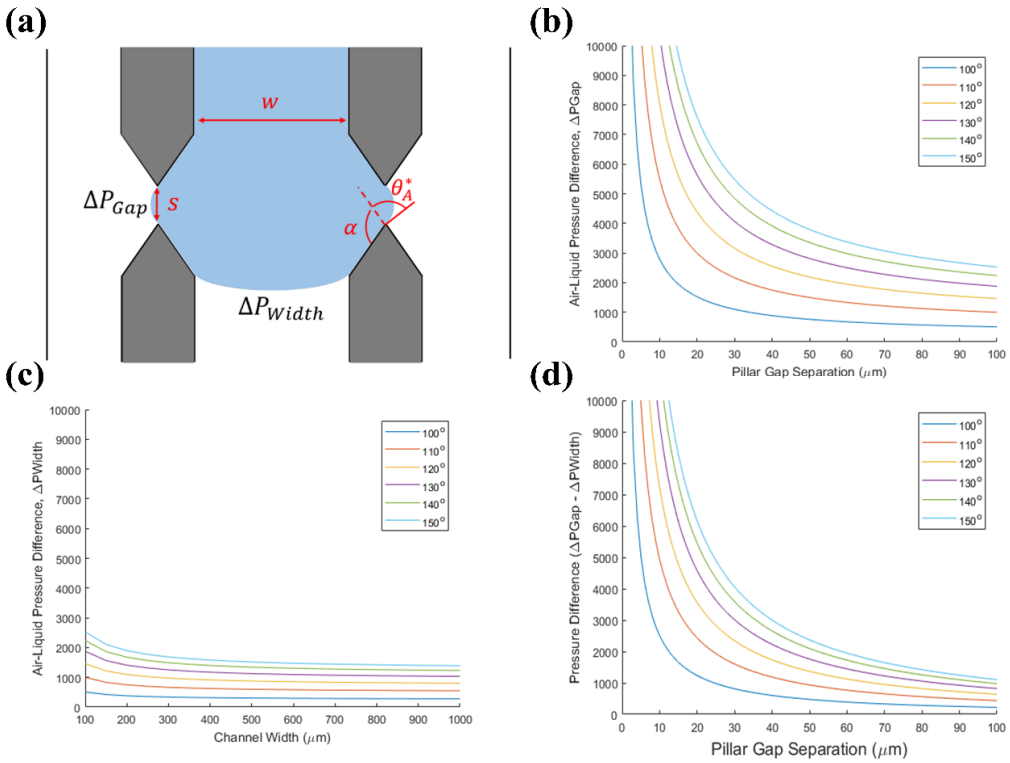

Figure 15 – (a) Diagram showing micropillar confinement of the hydrogel with annotated parameters described throughout equations (2-15) - (2-19). (b) A graph of modelled pressure difference across the air-liquid interface between the micropillars, ΔP_{Gap} for varying pillar gap separations and contact angles, θ_A^*. (c) A graph of modelled pressure difference across the air-liquid interface across the centre chamber, ΔP_{Width} for varying centre channel widths, w and contact angles, θ_A^*. (d) Graph modelled in Matlab showing how the overall difference in pressure, ΔP between the two parameters ΔP_{Gap} and ΔP_{Width} varies with pillar gap separation and contact angle. The higher this value, the greater the ability of the system to confine the hydrogel.

Successful confinement is primarily dependent on the ability of the micropillar array to direct the hydrogel flow down the channel to the outlet when loading. The Young-Laplace equation can be used to describe the confinement of a liquid by micropillars. The general equation describes the pressure difference (Pa) over an interface between two fluids:

$$\Delta P = \gamma\left(\frac{1}{R_1}+\frac{1}{R_2}\right)=\frac{2\gamma}{R} \qquad (2\text{-}15)$$

Where γ is the surface tension of the interface (N/m) and $R_{1,2}$ are the radii of curvature of the liquid meniscuses (m), which can be set equal due to the narrow interfaces formed in

microfluidic systems. Treating the meniscus radius as part of a spheroid allows the radius to be described in terms of the contact angle and interface dimensions:

$$\Delta P = 2\,\gamma\left(\frac{cos\theta_s}{w} + \frac{cos\theta_v}{h}\right) \tag{2-16}$$

Where θ_s and θ_v are the contact angles formed at the side walls and top and bottom walls, respectively. w is the separation between micropillars (m), and h is the channel height (m). The capillary number describes the ratio of viscous forces to surface tension across the interface:

$$C_a = \frac{\mu U_0}{\gamma} \tag{2-17}$$

Where μ is viscosity, U_0 is contact line velocity. Should the fluid be moving slowly enough such that surface tension forces dominate ($C_a < 10^{-3}$), contact angles between walls can be set approximately equal $\theta_s \approx \theta_v \approx \theta_A$. Equation (2-16) shows that an increasing contact angle reduces the pressure difference such that fluid will advance when the advancing contact angle, θ_A exceeds the critical advancing contact angle θ_{Crit}. Micropillars were designed with pointed pillars such that the contact angle, θ_A is instantly reduced by an amount, α when the advancing fluid meets the pillar side wall:

$$\theta_A^* = \theta_A - \alpha \tag{2-18}$$

The difference in pressures between the interface formed between micropillars and the interface across the centre channel width describes the preference of fluid to flow down the channel and not through the micropillars. Using equation (2-16), the difference in pressure differences is given by:

$$\Delta P = \Delta P_{Gap} - \Delta P_{Width} = 2\gamma\left(\frac{cos\theta_A}{s} - \frac{cos\theta_A}{w}\right) \tag{2-19}$$

This shows that an increase in channel width, w or decrease in pillar separation, s results in an increase in confinement, as expected. Figure 15b shows a graph of modelled pressure difference across the air-liquid interface formed across the pillar gap, ΔP_{Gap}, as a function of pillar gap separation, s (μm) and liquid contact angle, θ_A^*. Figure 15c shows the same plot but now for the pressure difference across the air-liquid interface formed across the centre chamber width, ΔP_{Width}. Figure 15d finally shows the overall pressure difference, ΔP between the pillar gap and chamber pressure differences. A higher value

of ΔP results in a greater resistance to the hydrogel bursting into the side channel. Together these graphs show that a decreasing pillar gap separation, *s* results in a higher ΔP value. The same effect occurs with increasing the centre channel width however, as the channel is significantly wider than the pillar separation, the change is less impactful due to the inverse relationship between pressure and channel dimension. The overall pressure difference increases significantly at pillar gap separations < 50 µm imposing an upper limit on a realistic separation. A separation of 30 µm was therefore chosen for micropillars used throughout this project. This allowed for effective confinement whilst also enabling cell interaction across the interface.

2.3 Microbubbles

Microbubbles (MBs) refer to gas particles typically between 0.5 – 10 µm in diameter, which are used as clinical ultrasound contrast agents and, more recently, drug delivery agents. The choice of MB shell and core composition determines their response to US and longevity *in vivo*. MBs must persist within the bloodstream for sufficient time to allow for the target site to be fully perused with MBs. Figure 16 shows MBs shortly after production, along with an image taken of a 10x diluted sample. The diagram depicts the typical structure of a MB, showing the potential surface chemistry modifications, such as liposome or antibody conjugation.

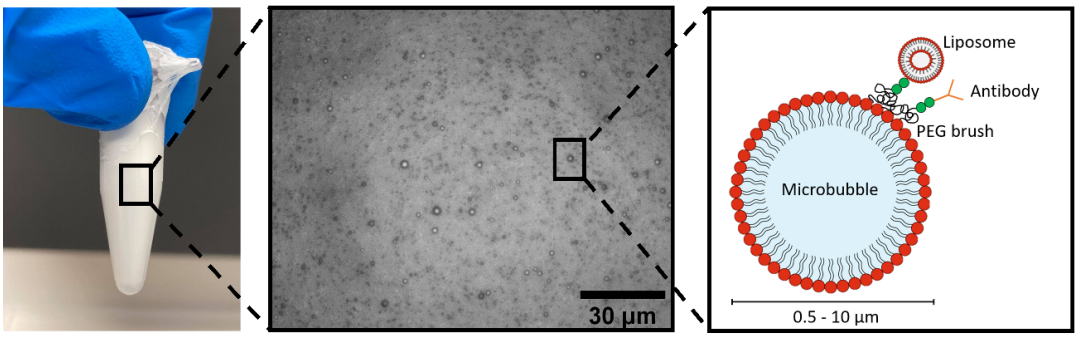

Figure 16 – (Left) A photograph taken of MBs shortly after production via mechanical agitation. (Middle) A microscope image (40 x obj) taken of 10 x diluted MBs. (Right) A diagram depicting the typical structure of a MB, with a gas-filled core and lipid monolayer. The use of polyethylene glycol (PEG) lipids result in the formation of a brush-like structure on the surface on the MB. The surface chemistry of MB can be tailored to allow for liposome or anitbody conjugation.

2.3.1 Microbubble Composition

The first MBs, made by agitating a patient's blood, all encapsulated air [129]. However, the stability of these MBs was less than ideal due to the ability of air to readily diffuse into the blood. MB must be sufficiently stable to allow for complete perfusion of MBs to the site of interest. Low solubility, high molecular weight, hydrophobic gases are now used to reduce gas dissolution and prolong circulation time in the blood to 5 – 10 minutes [130]. Longer circulation times are particularly important for therapeutic, drug-loaded MBs, as more time allows for more MBs to travel through the tumour region [12]. Inert perfluorocarbon gases are typically the most common choice, but sulphur hexafluorides are also used [131].

Coating the outside of MBs with a surfactant shell presents a further barrier to limit gas diffusion. Coatings are usually made from phospholipids, proteins, such as albumin, or biodegradable polymers. Each type of coating dictates the MB response to US, with rigid polymers showing more resistance to oscillations than the fluid-like phospholipid coatings. Furthermore, this fluid-like response results in phospholipid coatings being more resistant to collapse upon US exposure, allowing for longer usage as contrast agents [132]. The biocompatibility and *in vivo* circulation time of phospholipid coated MBs can be greatly improved by using lipids conjugated with polyethene glycol (PEG) [133]. The brush-like structure formed from the long-chain PEG molecules inhibits the immune system's ability to recognise the foreign particle. PEG also reduces MB coalescence through steric hindrance and acts as an anti-fouling layer. For these reasons, phospholipid coated MBs are most commonly used as ultrasound contrast agents and potential drug delivery enhancers.

Phospholipids self-assemble into energetically favourable configurations with their hydrophilic phosphate head groups surrounding the outside of the MB and hydrophobic tail chains directed inwards – as shown in Figure 16. This thermodynamically stable structure reduces surface tension, γ at the liquid-gas interface, which reduces the pressure drop between the inside and outside of the MB. This pressure drop is known as the Laplace pressure defined as:

$$P_{laplace} = P_{in} - P_{out} = -\frac{2\gamma}{R} \tag{2-20}$$

Where R is MB radius (m). The positive Laplace pressure results in MBs having a spherical shape. The rate of diffusion of gas out of an uncoated MB in solution was originally considered by Epstein and Plesset, who derived an expression for the rate of change of the MB radius [134]:

$$\frac{dR}{dt} = -\frac{D(c_s - c_0)}{\rho}\left(\frac{1}{R} + \frac{1}{\sqrt{\pi D t}}\right) \quad (2\text{-}21)$$

Where D is the diffusivity constant (m^2/s), ρ is gas density (g/L), c_0 is the initial dissolved gas concentration (mol/L) and c_s is the concentration at saturation. This relationship shows that increasing the molecular weight of the gas and, in turn, the density, will reduce the rate of radius decrease and increase stability. Thus, demonstrating the advantage of using heavier perfluorocarbons over air. Henry's law also states that the saturation concentration is proportional to the pressure [135]:

$$k_H = \frac{c_s}{P_\infty M_w} \quad (2\text{-}22)$$

Where k_H is a constant, P_∞ is the external pressure (Pa) and M_w molecular weight (g/mol). This shows that the relative decrease in external pressure caused by the reduction in surface tension also reduces the rate of gas diffusion out of the MB.

2.3.2 Microbubble Production

Mechanical agitation was used to create the first MBs and remains the most commonly used production technique. Agitating a solution of gas and coating material using sonication or mechanical shaking emulsifies the gas throughout the solution [136]. The coating material is then adsorbed onto the surface, stabilising the MBs formed. Whilst mechanical shaking is relatively straightforward, there is little control over the size distribution and concentration of MBs produced. The size of MBs formed through high-intensity ultrasound sonication are dependent on frequency, power, and pulse regime however the theoretical relationship between these factors is lacking. Many other techniques have also been developed for MB production, including high shear emulsification, membrane emulsification and ink jet printing - more information can be found on these techniques here [137–139].

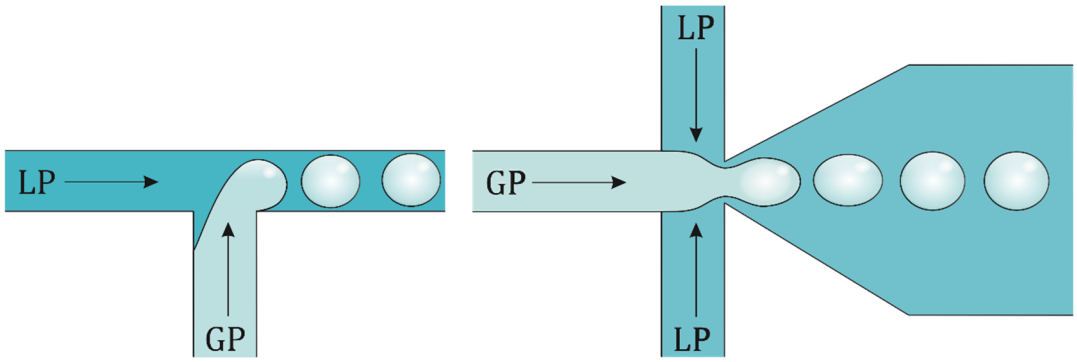

Figure 17 - T-junction (left) and flow focusing (right) devices showing microfluidic MB production. The liquid phase (LP), filled with the coating material, impinges onto a gas phase (GP) causing a pinch-off effect.

More recently, microfluidic devices, designed to produce liquid droplets, have been developed to produce MBs. The main advantage of this technique is the high degree of control over their size distribution and concentration [129]. Capillary T-junctions and flow-focussing channels are the two main types of microfluidic devices used for MB preparation, both of which are shown in Figure 17. In both devices, gas and liquid flow through a nozzle and a pinch-off occurs when the gas-liquid interface becomes sufficiently unstable due to the shear forces overcoming the surface tension of the droplet [136]. MBs produced are naturally very uniform due to the unchanging nozzle size.

The addition of a 3D expansion after the flow focused nozzle results in a greater pressure reduction causing a spray-type production [140]. This has been found to produce consistently high, clinically relevant, MB concentrations ($10^8 – 10^9$ / mL). However, this flow focussed production requires low liquid viscosities and high surfactant concentrations to limit the gas and liquid pressures required. High surfactant concentrations lower surface and interfacial tension by adsorbing onto the interface, thus reducing the gas pressure required for impingement. This results in low MB production rates when compared to those produced using mechanical agitation, meaning multiple flow-focused nozzles are usually multiplexed onto one chip. Current multiplexed designs are capable of producing 1 mL of MB solution with approximately 7 minutes [141].

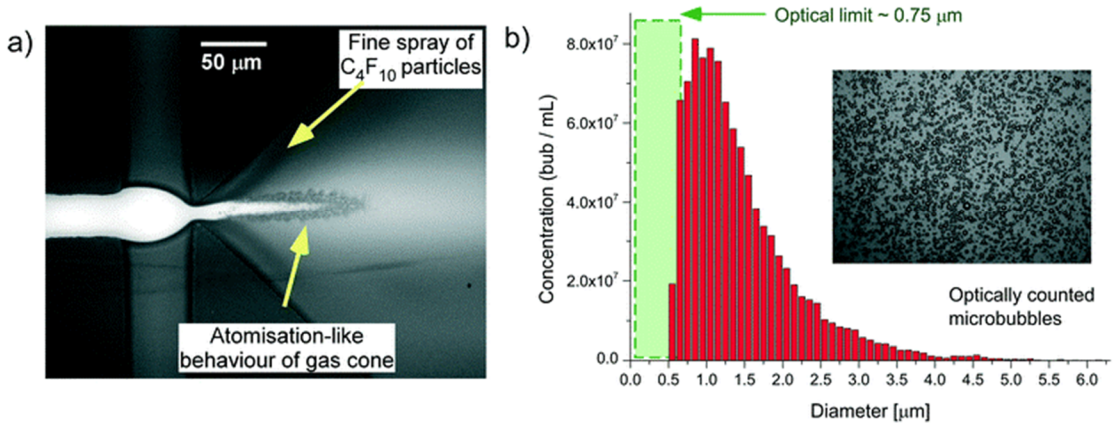

Figure 18 – a) Microspray bubble formation using flow-focusing device with a 3D expansion. b) Histogram showing size distribution of MB population determined optically. Insert shows typical optical image of MBs (figure reproduced from Peyman et al with permissions under CC licence) [141].

Figure 18a shows an image of microspray MB formation using a flow-focussed nozzle with a 3D expansion, alongside a histogram of MB size distribution (Figure 18b). As the size and concentration of MBs are determined optically, MBs below the optical limit of 0.75 µm will not be accounted for. The size distribution and concentration will therefore not take into account the nanoscale MBs (nanobubbles, NBs) produced. Indeed, it has been shown that producing MBs using microspray results in the formation of significant populations of NBs [141]. NBs are of recent interest as their reduced size offers a potential method of improving drug delivery across the endothelial barrier [142].

2.3.3 Microbubble Response to Ultrasound

MBs are highly responsive to US due to the compressibility of their gas core. When exposed to US with sufficient mechanical index (MI), MBs oscillate and generate echoes at harmonic frequencies. Detection of these echoes with an US transducer allows for enhancement of US contrast in clinical imaging [143]. In addition to MB compressibility, the acoustic impedance mismatch between the gas encapsulated within the MBs and the surrounding liquid further contributes to the enhancement of the US contrast. Along with the gas core, the choice of encapsulating shell affects the MB response to US. Phospholipid shells are particularly appealing as they display a high degree of flexibility whilst also ensuring resistance to gas diffusion. As mentioned in section 1.4.1 (page 46),

the MI of an US wave can dictate the magnitude of the MB response. MI is a measure of the US waves ability to cause cavitation-related bioeffects, and is defined as the peak negative pressure, P_- (MPa) divided by the square root of the US frequency (MHz):

$$MI = P_- / \sqrt{f} \tag{2-23}$$

MI is an overall measure of the power of an US beam and therefore gives an indicator of the amount of energy administered by the US pulse [76]. The Rayleigh-Plesset equation can be used to describe the response of a free MB to an US wave. This non-linear differential equation can be linearized to gain insight into the resonance behaviour of MBs. Treating the US wave as a sinusoidal pulse with a small amplitude of oscillation with respect to MB radius reduces the original Rayleigh-Plasset to a classic mass-spring equation:

$$\frac{\partial^2 x}{\partial t^2} + 2z\omega_0 \frac{\partial x}{\partial t} + \omega_0^2 x = \frac{p_A}{\rho R_0} sin\omega t \tag{2-24}$$

Where x is the variation in MB radius (m), z is the damping of the system, p_A is the driving pressure amplitude, ρ is the liquid density, R_0 is the bubble radius at rest (m), ω is the angular US frequency (rad s^{-1}) and, ω_0 the bubble oscillation frequency (Hz). This equation can then be used to estimate the linear resonance frequency:

$$f_0 = \frac{\omega_0}{2\pi\sqrt{1 - z^2}} \tag{2-25}$$

Where the bubble oscillation frequency can be defined as:

$$\omega_0 = \sqrt{\frac{3\kappa P_0}{\rho R_0^2}} \tag{2-26}$$

κ is the polytropic exponent of the encapsulate gas and P_0 is the ambient pressure (Pa). The linear resonance frequency is typically within the low MHz range for MBs up to 10µm, as shown in Figure 19 [144,145]. It is advantageous to have a monodisperse MB population such that the resonant frequency of oscillation is the same for all bubbles. This is difficult to achieve so broadband pulses are typically used for contrast imaging purposes [132]. This is generally not possible for drug delivery applications where longer

bursts are required for stable cavitation effects to become significant. Higher power US pulses which aim to stimulate inertial cavitation are less affected by this issue as MBs are burst after very few pulses.

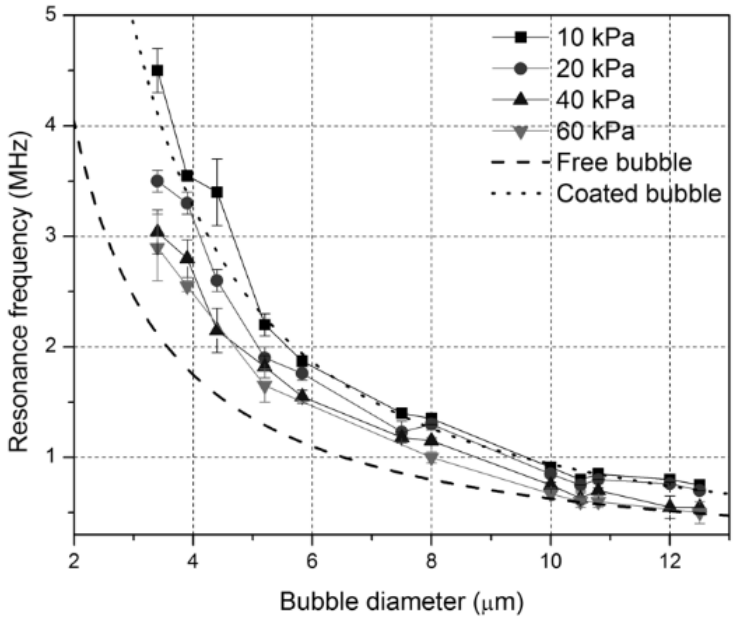

Figure 19 – Resonant frequency of microbubbles as a function of diameter, determined experimentally using acoustic pressures between 10 – 60 kPa. Figures taken from IEEE Ultrasonics symposium 2010 proceedings from Gong et al [145].

3 EXPERIMENTAL METHODS

3.1 Microfluidic Device Fabrication

3.1.1 Silicon Master Production

All silicon master wafers were produced by patterning microfluidic designs onto photoresist-coated wafers using a Direct Write Laser (DWL, Durham Magneto Optics, UK) system. Polydimethylsiloxane (PDMS) devices were then cast from these wafers and bonded to glass slides using oxygen plasma. Microfluidic devices were first designed in AutoCAD (Autodesk) before being exported as .dxf files into CleWin 5 (WieWeb). CleWin was then used to subtract regions of the microfluidic design which did not require exposure. This allowed features within the microfluidic device, such as micropillars, to be selectively exposed correctly. Finally, the design was exported as a Caltech intermediate form (CIF) file and uploaded to the DWL system used to pattern the design. Silicon master wafers were produced using standard photolithography techniques, the process of which is outlined in Figure 20.

First, 3-inch silicon wafers (Pi-KEM) were baked in an oven at 200 ºC for 30 minutes to remove any moisture. Meanwhile, the SU8-2075 photoresist (MicroChem) was removed from the fridge and allowed to warm to room temperature. The wafer was then placed on a spin coater and approximately 3 mL of photoresist poured onto the centre. The speed at which the wafer was span dictates the height of the photoresist. For spheroid trap devices, a spin speed of 1400 rpm for 40 seconds was used to give a height of 180 µm. To ensure that the photoresist was evenly spread across the wafer, the wafer was spun at increasing rates of 200, 400 and 600 rpm, each for 10 seconds at an acceleration of 100 rpm/s, before ramping up to the required speed.

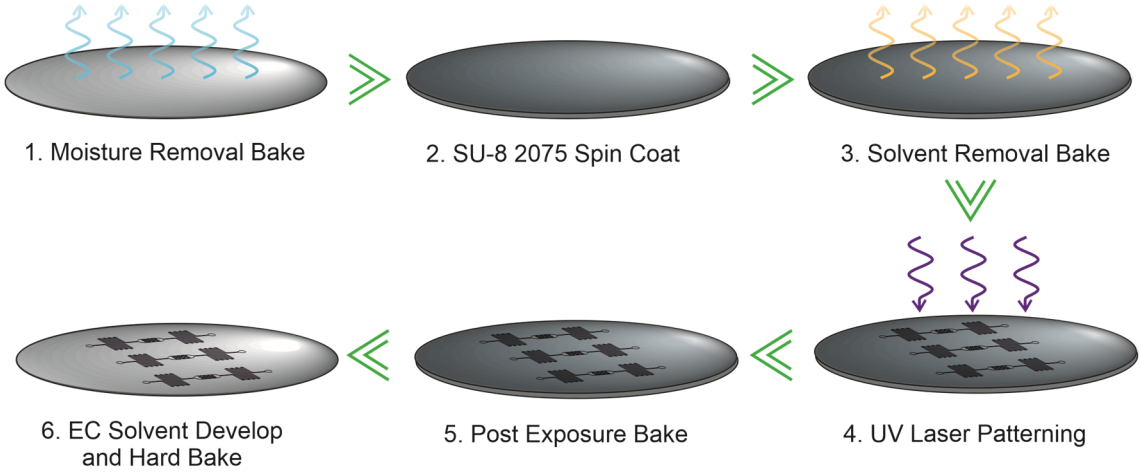

Figure 20 - Diagram of photolithography process used to pattern microfluidic designs onto silicon wafers.

After spinning, wafers were baked at 55 °C for an hour on a hotplate, this removes the solvent from the photoresist and solidifies the layer. The spinning process was then repeated for spheroid trap wafers to produce a total photoresist height of approximately 360 µm. For vasculature on-chip devices, a spin speed of 2000 rpm for 40 seconds was used to give a height of approximately 100 µm. Only a single layer was required for vasculature device wafers.

After the solvent removal bake, the wafer was placed in the DWL which uses a 375 nm UV laser to selectively crosslink the photoresist into the desired pattern. Figure 21 shows CAD schematics of the (a) spheroid trap and (b) vasculature device designs alongside close-ups of the trap chamber and cell chambers. These device designs were uploaded to the DWL for selective laser exposures. Further information on the motivations behind the design features of each device can be found at the beginning of their respective results chapters (4 and 5).

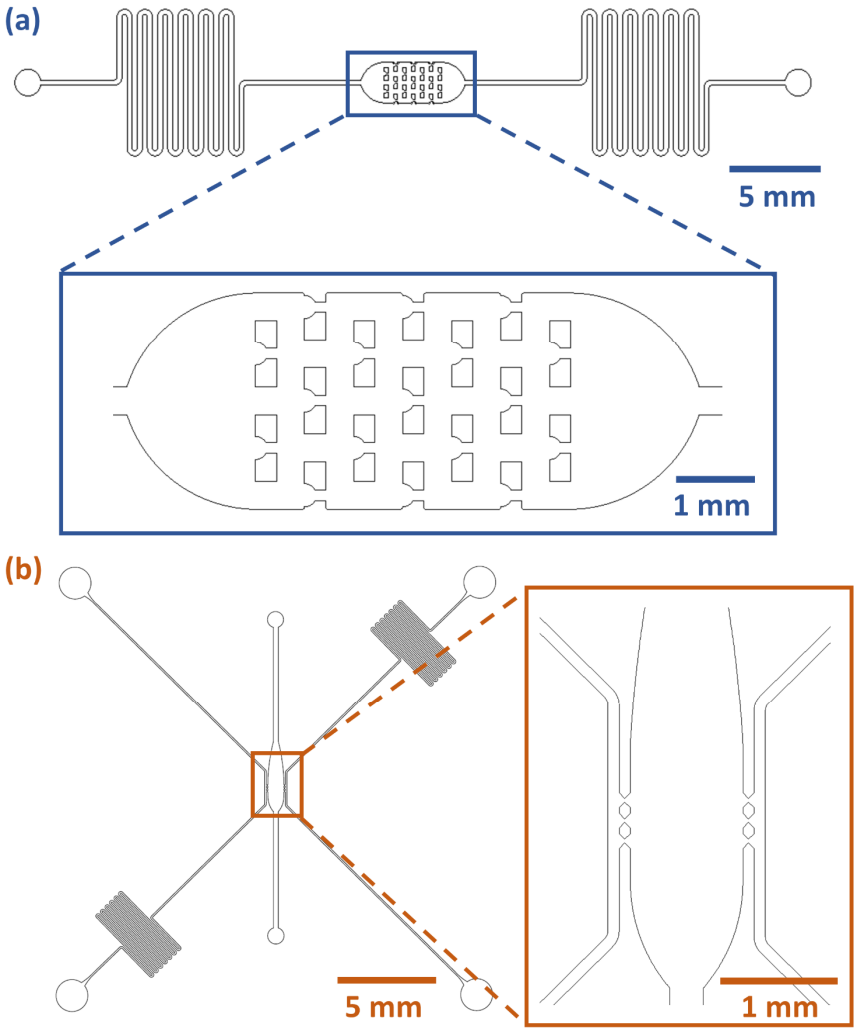

Figure 21 – (a) A CAD schematic of the microfluidic spheroid trap design showing the entire device alongisde a close-up of the spheroid trap chamber. (b) A CAD schematic of the microfluidic vasculature design showing the enitre device alongisde a close-up of the cell chamber and surrounding media side channels.

To determine the optimal laser power and defocus for the SU-8 exposure, a laser dosage test was performed in which an array of small micropillar designs were exposed to laser powers between 100 – 700 mJ/cm^2. For the 100 µm thick vasculature chips, defocus values of 0 µm, + 50 µm, and + 100 µm were chosen to observe how focussing on the top (0 µm), middle (+ 50 µm) and bottom (+100 µm) of the SU-8 photoresist layer affected the profile of the channel walls.

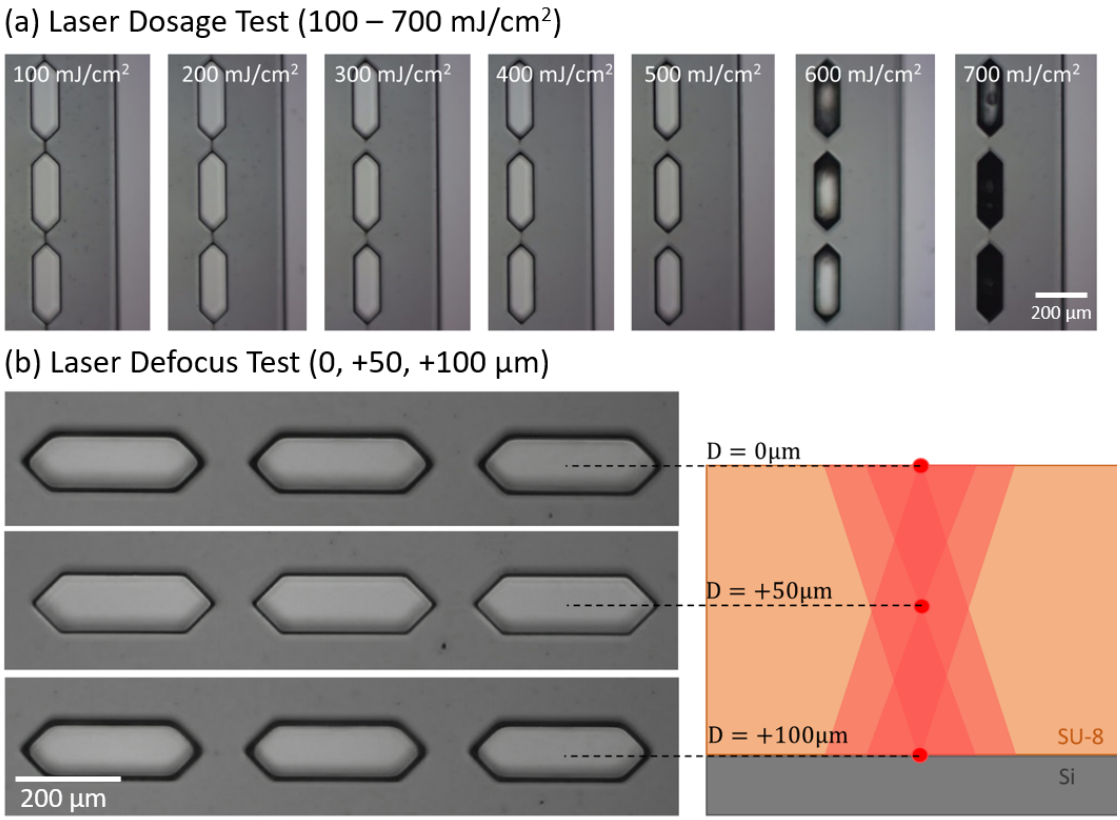

Figure 22 – Images taken of the micropillar designs exposed to a range of (a) laser powers and (b) defocus values for the dosage test. Images in figure 22a show the result of increasing laser powers from 100 mJ/cm^2 to 700 mJ/cm^2. Images in 22b show the effects of different defocus values alongside a depiction of the laser focal point when each setting is used.

Figure 22 shows the results of the laser power and defocus tests. Low powers (100 mJ/cm^2) resulted in incomplete crosslinking and poor adhesion of the photoresist to the wafer. Whereas higher powers such as those 500 mJ/cm^2 and above, resulted in the over-exposure of the photoresist, causing undesired cross-linking of photoresist in the micropillar regions. This prevented proper pillar formation when devices were being cast from the wafers. Focussing the laser directly in the centre of the photoresist layer (+ 50 µm) appeared to produce the sharpest micropillar features compared to the upper and lower settings. Based on these observations, a laser power of 200 mJ/cm^2 and defocus of + 50 µm was used for vasculature on-chip designs. A defocus of + 180 µm was used for 360 µm thick spheroid trap designs.

After DWL exposure, the wafer was then baked at 55 ºC for an hour completing the photoreaction initiated by the UV exposure. After cooling for an hour, the excess photoresist was removed using EC solvent (Microposit), an ethyl lactate-based solvent. The wafer was submerged for approximately 5 minutes with regular rinsing with IPA. Clear IPA after rinsing indicated that all excess photoresist had been removed, which was further checked under the microscope. A spray gun filled with EC solvent was also used to remove photoresist from inside the fine features of the design. Once fully developed, the wafer was hard-baked in an oven at 200ºC for 30 minutes. The temperature was increased and decreased slowly to prevent cracking and delamination of the design. Finally, 3 drops of trimethylchlorosilane (TMSC) was placed in the corner of a petri dish containing the wafer to silanize the wafer surface. TMSC hydrolyses the -OH hydroxyl groups on the silion surface which then allows for the formation of Si-O-Si siloxane linkages. This results in a hydrophobic wafer surface and allows for PDMS to be easily peeled away.

3.1.2 Soft Lithography

3.1.2.1 PDMS Casting

Microfluidic devices were fabricated from PDMS (Sylgard 194 Silicone Elastomer Kit) using standard soft lithography techniques. PDMS was mixed in a 10:1 elastomer base to curing agent weight ratio then centrifuged at 4000rpm for 1 minute to remove large air bubbles. PDMS was poured onto the wafer which was then desiccated for 1 hour to completely degas the PDMS. 30 mL of PDMS was used to produce device thicknesses of 5 mm and 6 mL used for 1 mm thick devices. The PDMS covered wafer was then baked in an oven at 75 ºC for 1 hour to fully cure the PDMS. Once cured, a scalpel was used to cut and free the PDMS stamp from the wafer. Individual devices were separated, and biopsy punches (Miltex) were used to punch inlet/outlets. 1 mm diameter punches were used for cell-hydrogel inlet/outlets whereas 2 mm diameter punches were used for reservoir inlet/outlets. Devices were stored covered with invisible matt tape (Scotch) to prevent dust accumulation in the inlet/outlets.

3.1.2.2 PDMS Slide Coating and Oxygen Plasma Bonding

Prior to bonding, glass slides and coverslips were spin-coated with PDMS to minimise cell interaction with the microfluidic chambers. This ensured homogeneity of PDMS surfaces within the devices and prevented any preferential cell growth across the glass surfaces. Approximately 1 – 2 mL of PDMS was poured onto the centre of each slide or coverslip which was then spun at 1500 rpm for 60 seconds. This produced a layer of PDMS approximately 50 µm thick. Slides were baked on a hotplate at 95 ℃ for 10 minutes then covered with magic tape to protect the surface from dust.

Oxygen plasma (Zepto, Diener Electronics) was used to bond PDMS microfluidics to PDMS coated slides. Surface treatment of PDMS with oxygen plasma removes the surface hydrocarbon groups, leaving behind silanol groups which can then form strong covalent bonds with each other. Devices and slides were placed in the plasma chamber and oxygen was flushed through three times to ensure pure oxygen-filled the chamber only. The chamber was then filled to a pressure between 0.4 – 0.6 mbar and the plasma was initiated. The treatment was stopped after 30 seconds, the chamber was quickly vented, and devices quickly bonded together before the silane bonds recombine. Devices were then baked for an hour to further strengthen the bonding. Figure 23 depicts the soft lithography process from PDMS pouring and degassing to the production of complete microfluidic devices.

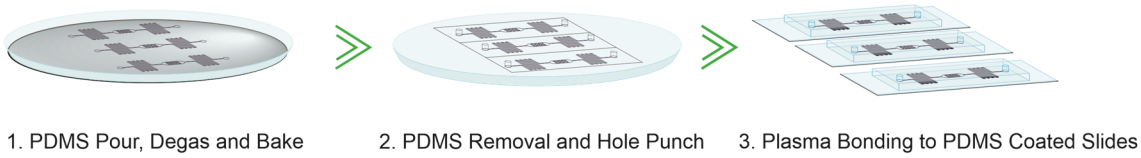

Figure 23 - Diagram of soft lithography process used to fabricate PDMS microfluidic devices from silicon master wafers.

3.1.3 Media Reservoir Design and Fabrication

As an alternative to conventional syringe pumps, small, polycarbonate media reservoirs were interfaced with the device and used to induce flow through microfluidic devices. Reservoirs offer many advantages over syringe pumps, primarily the lack of cumbersome tubing, straightforward pipettable media changes and the ability to independently run multiple chips in parallel. The requirement for long-term organ-on-chip cultures and multiple chips needed for statistical repeats makes these advantages particularly useful, resulting in many on-chip studies implementing the use of reservoirs.

Media reservoirs were fabricated from 16 mm diameter solid polycarbonate rods (Engineering and Design Plastics) cut into 32 mm long pieces. Each piece was hollowed out and fabricated to contain a 2 mm wide spout protruding from the bottom – as shown in Figure 24a. This allowed for simple interfacing with 2 mm hole-punched inlets and outlets on the microfluidic devices. Reservoir lids were fabricated by gluing 0.22 µm PTFE filters (Cole-Parmer) onto the top of Delrin rings (Par-group), which then slotted over the top of the polycarbonate reservoir. 0.22 µm filters prevented bacterial contamination of the media whilst still allowing for gas exchange across the gas permeable membrane. Polycarbonate reservoirs were autoclaved at 120 ºC for 40 minutes and the underside of the reservoir lids was sterilised under UV light for 30 minutes prior to experimental use. Figure 24a shows photographs of a polycarbonate reservoir, reservoir lid with PTFE filter, and reservoir fitted with the lid. Figure 24b shows media-filled reservoirs interfaced with a spheroid trap microfluidic device.

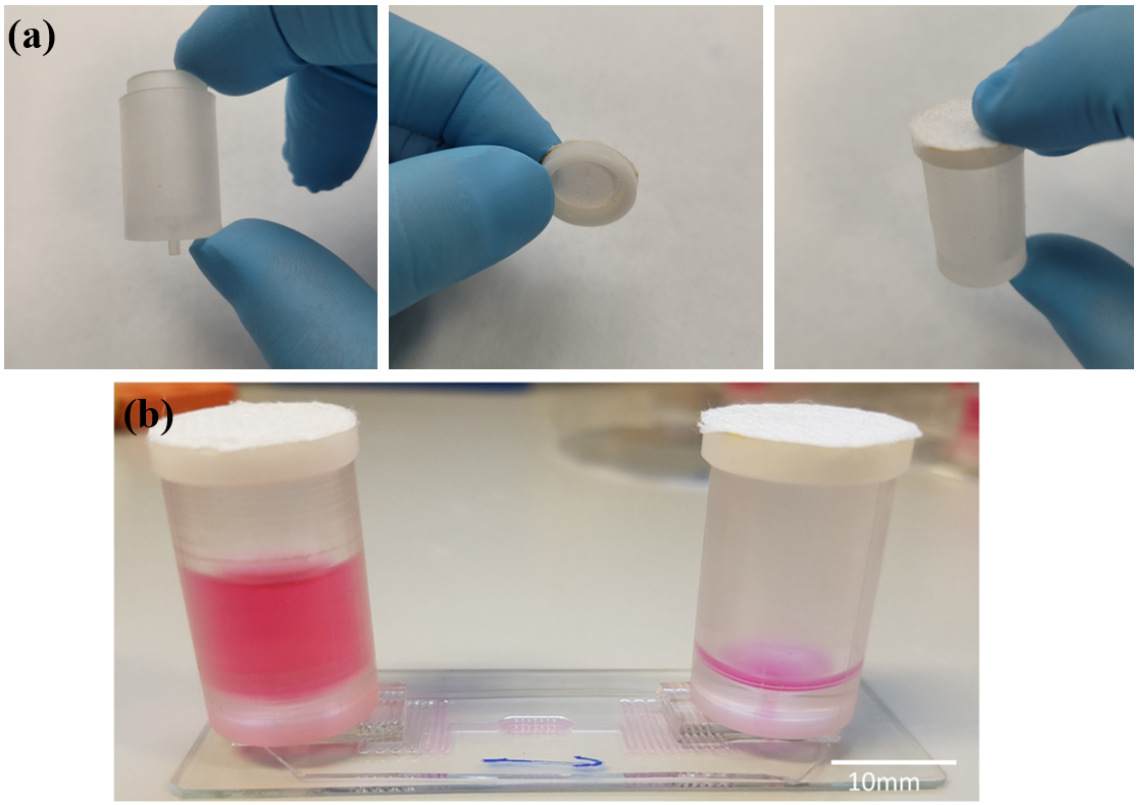

Figure 24 – (a) Photographs taken of a polycarbonate reservoir used for hydrostatic flow. The spout at the bottom slots into a 2 mm hole punched in the PDMS microfluidic inlet/outlet. The centre image shows a Delrin ring (white) fitted with a PTFE membrane, forming a sterile lid for the reservoir. The reservoir fitted with the lid can be seen in the final image. (b) A picture showing media-filled reservoirs interfaced with a spheroid trap microfluidic device.

3.2 Cell Culture and Microfluidic System Setup

All cell work was carried out in a sterile laminar flow hood unless stated otherwise. All reagents and consumables used were sterile to prevent bacterial contamination of the cells.

3.2.1 HCT116 and HFFF2 Culture

HCT116 (ECACC 91091005) and HFFF2 (ECACC 86031405) cells were both originally obtained from ECACC. Cells were STR profiled to ensure authenticity and regularly tested for mycoplasma. Both cell lines are adherent and were grown and maintained in DMEM 10 % FBS (Thermo Fisher, UK), 1 % Glutamax (Gibco, UK) in an incubator at

37 ℃, 5 % CO_2. Frozen cell stocks were rapidly thawed in a water bath at 37 ℃ then transferred to T-75 cell culture flasks. Once the cells had adhered, media was removed, the cells washed with PBS (+Ca, +Mg, Gibco, UK) and fresh media added. This aimed to remove any remaining DMSO that had been used as a cryoprotectant for the frozen cells. Cells were split by first removing media and washing with PBS. TripLE dissociation reagent was then added (1 mL for T – 25, 2 mL for T-75) then the flask was incubated for 5 minutes. Cells that remained attached were removed by gently tapping the side of the culture flask. Passages were carried out twice a week at a ratio between 1:10 – 1:20 for HCT116 and 1:2 – 1:4 for HFFF2 cells, to ensure confluency never exceeded 90 %. Cell passages were kept below 50 for HCT16 and 30 for HFFF2 cells.

3.2.2 HUVEC, HDF and NHLF Culture

HUVECs were obtained by a collaborator from Promocell GE. Optimal batches for vasculature formation were identified using HUVEC tube formation assays, then multiple vials from those optimal batches were purchased. HUVECs were then transfected with a green fluorescent protein and sorted using FACS. Frozen GFP-HUVECs were then acquired from the collaborator at passage 2. HUVECs were cultured in EGM – 2 (Lonza Bioscience, CH) and expanded to passage 3 before being frozen into additional cryovials. HUVECs were defrosted 2 days prior to experimental use, with fresh EGM – 2 being added each day. HUVECs were never used above passage 5 due to the differentiation and lack of vessel formation observed with later passages. HDF cells were purchased from Cell Applications inc, USA (106-104 05N) and grown using the same DMEM formulation used for HCT116 and HFFF2 cells. Cells were expanded up to passage 3 before being frozen into additional cryovials. As with HUVECs, HDFs were defrosted 2 days prior to experimental use with fresh media added every day. HDFs were only used between passages 3 – 6. NHLF cells were purchased from CellSystems (FC-0049) and grown using FibroLife S2 media (LL-0011) also supplied by CellSystems. This media was developed specifically for the culture of fibroblasts and contained all the growth factors required for optimal cell growth. NHLFs were expanded up to passage 3, frozen and defrosted 2 days prior to on-chip setup.

3.2.3 Spheroid Production and Characterisation

As described throughout section 1.4 (page 45), there are various methods of forming 3D spheroid cultures. For this project, it was decided that pre-coated ultra-low adhesion 96 well-plates (Corning, Costar) would be used to form spheroids. The time taken to manually coat 96 well-plates for low adhesion was a previously discussed disadvantage of this technique however, commercially available well-plates overcame this issue. HCT116 and HFFF2 cells were first detached from culture flasks and their concentrations determined using a Neubauer cell counting chamber. Cells were then diluted to a concentration of 7.5×10^2 cells/mL and mixed in a 1:1 ratio. 200 µL of the cell solution was then added to each well of an ultra-low attachment 96 well plate. Well-plates were centrifuged at 300 x g for 5 minutes to aggregate cells in the bottom of each well and decrease spheroid formation time. Spheroids were allowed for form for 5 days at which point spheroids with a diameter suitable for experimentation (300 – 350 µm) were identified using the MATLAB plugin SpheroidSizer [146]. SpheroidSizer determines the outline of each spheroid then calculates the average diameter. The consistently circular spheroid eccentricities ($e \approx 0$) then allowed for the volume of each spheroid to be calculated using the equation for the volume of a sphere.

3.2.4 Off–Chip Spheroid Exposure to Doxorubicin

Spheroids were produced and sized using the same methods outlined in the previous section with the exception of monoculture spheroids, which were formed by seeding a tumour cell suspension only. DOX exposures began by removing 100 µL of the 200 µL of media in each well and adding DOX containing media to give the final desired concentration. Spheroids were exposed to DOX concentrations between 0.01 – 10 µM DOX for 8 hours. 160 µL of media was then removed from each well and 160 µL of PBS was added. This was repeated, and the PBS was replaced with fresh media. Spheroids were then allowed to grow for an additional 48 hours, then subject to the same assay and analysis as described throughout sections 3.4.3.1 and 3.4.3.2 (page 108).

3.2.5 Spheroid On-Chip Setup

Reservoirs complete with lids were fitted into the inlet and outlet of each microfluidic device. Ethanol was then flushed through the system to wet the channel surfaces and ensure that no air bubbles remained lodged within the traps. A 200 µL pipette was used to directly access the inlet of the device, through the bottom of the reservoir. This allowed ethanol to be manually pipetted and air bubbles dislodged. Excess ethanol was removed, and the inlet reservoir filled with PBS, which was allowed to flow for 30 minutes and replace any remaining ethanol. PBS was then removed, and the process was repeated with DMEM. 10 spheroids were then collected from the low adhesion wells and deposited into the inlet reservoir. Spheroids were allowed to flow into the chamber where the hydrodynamic force from fluid flow ensured that spheroids remained trapped.

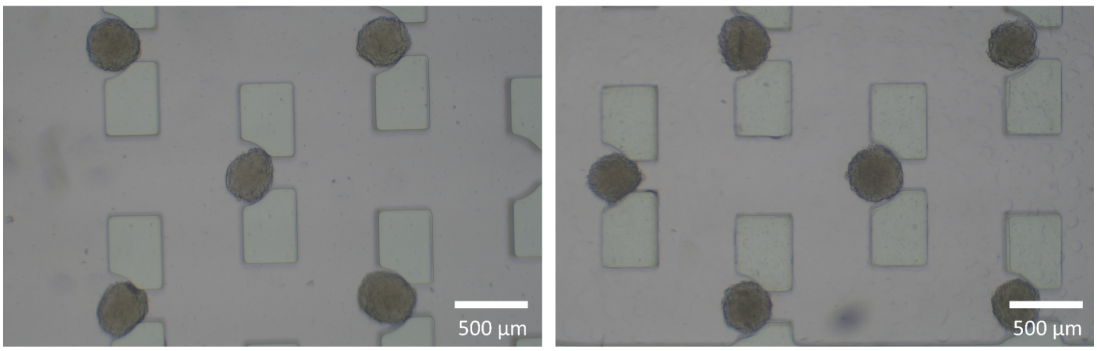

Figure 25 – HCT116 – HFFF2 co-culture spheroids trapped within the microfluidic trap array after the spheroid loading process.

Spheroids were observed to sink to the bottom of the reservoir and flow into the traps before the majority of the fluid. The fluid imbalance between inlet and outlet reservoirs was maintained by removing media in the outlet and cycling it back into the inlet reservoir. This also ensured that any spheroids that failed to flow into a trap could flow through the array again, increasing the likelihood of trapping. This process was repeated 3 times across one hour. It was not uncommon for spheroids to become lodged in the inlet at the bottom of the reservoir spout. In this case, manual pipetting would be used to gently encourage the spheroid to flow down the channel. Figure 25 shows images taken of spheroids captured within the trap array after the spheroid loading process is complete.

3.2.6 Off-Chip Angiogenesis Assays

3.2.6.1 NHLF/HDF and GFP-HUVEC Seeding

Fibroblasts (NHLF or HDF) and GFP-HUVECs were seeded off-chip in a 24-well plate to assess the angiogenic capabilities of HUVECs in different cellular configurations. 4×10^4 NHLFs/HDFs were first seeded in each well and allowed to grow for 3 days into a confluent monolayer. 4×10^4 GFP-HUVECs were then either seeded directly onto the fibroblast monolayer or first suspended in 5 µL fibrin gel then seeded into each well. The incorporation of fibrin recreated on-chip vasculature seeding configurations which consisted of both GFP-HUVECs and fibroblasts being seeded in a fibrin matrix (section 3.2.7.5, page 94). Cell cultures were then grown for an additional 4 days, over which time the interaction of HUVECs with the fibroblasts was imaged regularly. The extent of HUVEC branching and 2D network formation was an indicator of angiogenic ability.

3.2.6.2 Off-chip Immunostaining and Flow Cytometry

Off-chip angiogenesis experiments were also used to assess the effect of tumour cell media (TCM) on integrin $\alpha_v\beta_3$ expression (results section 5.3.2). NHLF and GFP-HUVECs were seeded in the same configuration as described above however, cultures were grown in triplicate wells containing EGM-2:TCM ratios of [1:0], [2:1], [1:1], [1:2]. Immunostaining was used to assess integrin $\alpha_v\beta_3$ expression 4 days after HUVEC seeding. Cells were then detached from wells using TrypLE express (Thermo Fisher). Nattokinase (50 FU/ mL), an enzyme that digests fibrin, was used to break down the fibrin clots in fibrin-containing wells. Cells were centrifuged and washed with PBS, then resuspended at 1×10^6 cells/ mL in a solution of PBS (10 % FBS) and mouse monoclonal IgG1 anti-$\alpha_v\beta_3$ antibody (Abcam, ab190147) diluted 1:2000 with PBS (3 % BSA). Cells were incubated for 30 minutes in the primary antibody solution then centrifuged and washed 3 × with PBS. Cells were then resuspended in a secondary goat anti-mouse Alexa Fluor 647 antibody solution (Abcam, ab150115) diluted 1:2000 with PBS (3 % BSA) and incubated in the dark for a further 30 minutes. Finally, cells were centrifuged and washed 3 × with PBS and resuspended in PBS (10 % FBS) at 1×10^6 cells/ mL .

Flow cytometry was performed by Dr Ruth Hughes and Dr Sally Boxall in the Bioimaging and FACS facility within the faculty of Biological Sciences at the University

of Leeds. A CytoFLEX S (Beckman Coulter) Cytometer was used to simultaneously excite the green fluorescent protein expressed by the HUVECs and AlexaFluor 647 secondary antibody using 488 nm and 638 nm lasers, respectively. Control measurements using unstained GFP-HUVECs (green only), stained non-GFP HUVECs (red only) and unstained NHLFs (double negative) were taken to determine the appropriate gating intensities. A minimum of 10,000 positive events were recorded for each dataset to ensure a robust analysis could be performed. Immunofluorescent intensities for each EGM-2:TCM condition were plotted as histograms and peak fitting functions then used to find the modal peak intensity for each sample. As NHLFs did not emit green fluorescence, it was possible to separate each cell type and calculate the percentage of each cell type positive for integrin $\alpha_v\beta_3$ expression.

3.2.7 Vasculature On-Chip Setup

3.2.7.1 Fibrinogen and Thrombin Preparation

Fibrinogen (100 mg, Sigma) was prepared by dissolving the powder into 10 mL of ultrapure water containing 0.9 % NaCl. The solution was gently mixed at 37 ºC until the fibrinogen had fully dissolved. The 10 mg/mL solution was then separated into 200 µL aliquots and stored in a freezer at -20 ºC for future experimental use. The final working concentration of fibrinogen is estimated to be between 7 – 8 mg/mL after being mixed with thrombin and the small volume of EGM-2 remaining around the cell pellet. Thrombin from human plasma (100U, Sigma) was dissolved in 2mL of 0.1 % (w/v) BSA solution, separated into 20 µL aliquots and stored in the freezer at -20 ºC. Both solutions were stored for 6 months before being replaced with fresh stocks.

3.2.7.2 Cell Seeding On-Chip

HUVEC and HDF/NHLF cells were detached from their culture flasks using the protocol for cell detachment outlined in section 3.2.2 (page 88). Cell concentrations were determined using a Neubauer cell counting chamber. Cells were then mixed in a 2:1 HUVEC: NHLF ratio and centrifuged at 200g for 4 minutes. A loose pellet was desirable as it allowed cells to be easily resuspended in fibrinogen minimising the formation of air bubbles in the gel. The supernatant was removed and the cell pellet was resuspended in fibrinogen (10 mg/mL) to give a total concentration of 1.5×10^7 cells/mL. Combining

cells with fibrinogen starts a slow polymerisation process meaning all cell loading had to be carried out within 15 minutes.

The fibrinogen cell suspension was then split into 10 µL aliquots. Each aliquot was mixed with 0.8 µL of thrombin (50 U/mL) and quickly pipetted into the central chamber of the vasculature device (shown in figure Figure 21a). Once mixed with thrombin, the polymerisation occurs within 20 seconds and the gel becomes unworkable. The polymerisation process was encouraged by heating the chips on a hotplate at 36 ºC for 15 minutes. Reservoirs were then fitted into the side channels and chips placed into the incubator for a further 15 minutes to allow for complete polymerisation.

3.2.7.3 Side Channel Coating

To encourage HUVECs to anastomose with the side channels and form tight junctions at the pillar gap entrances to the centre chamber, each side channel in the devices was coated with a laminin-BME mixture. Basement membrane extract (BME, Cultrex) was diluted 1:10 with PBS to a concentration of approximately 1.5 mg/mL. Laminin (1 mg/mL) and BME (1.5 mg/mL) were then mixed in a 1:1 ratio and pipetted into the side channel. The chip was again placed on a 36 ºC hotplate for 15 minutes to allow the gel mixture to partially polymerise. Media was then pipetted into the side channels to remove the unpolymerized gel and leave a coating along the channel walls.

3.2.7.4 Healthy Vasculature Formation

Endothelial growth media (EGM-2, Lonza) was used to supply cells with the correct growth factors and biochemical queues to form vasculature. EGM-2 media kits arrived as basal medium (EBM-2) and a growth factor kit (SingleQuots Supplements) containing FBS (5 %), hydrocortisone, hFGF-B, VEGF, R3-IGF, ascorbic acid, hEGF, GA-1000 and heparin. EGM-2 complete with all growth factors was added to inlet and outlet reservoirs to give fluid heights of 15 mm and 2 mm, respectively. After 24 hours, fresh media was added, and reservoirs re-levelled such that flow direction and pressures were reversed. Furthermore, EGM-2 complete media was replaced with EGM-2 without hFGF-B or VEGF to induce lumen formation. Reduced growth factor EGM-2 was used throughout the rest of the experiment. Media was replaced and flow was reversed every 24 hours to maintain vessel formation. After 6 days, the vasculature had formed and fully

anastomosed with the micropillar gaps. Fluid was now able to travel across the channel through the vasculature. It was at this point that experimentation could begin.

3.2.7.5 Tumour Vasculature Formation

Tumour cell media (TCM) was used to condition vasculature networks to display tumour vasculature-like properties. HCT116 colorectal cancer cells were first grown to confluency for 5 days without media replacement. Media was then removed and centrifuged at 15,000g to remove debris and dead cells. The TCM supernatant was then removed and mixed with EGM-2 in a ratio of 2:1 (EGM:TCM). For the first 72 hours, vasculature was prepared using the same protocol for the healthy vasculature to allow the cultures to get established. TCM containing media was then added and replaced every 24 hours. The flow direction was also reversed daily as before.

3.3 Microbubble and Liposome Production and Conjugation

3.3.1 Lipid Preparation

Stock lipid solutions were prepared by dissolving lipids to a known concentration, typically between 20 – 25 mg/mL , in a 1:1 mixture of chloroform and methanol. Prior to experiments, lipids were dried under nitrogen for 2 hours to remove the solvent. Lipids were then placed in a desiccator overnight to ensure no solvent remained. The dried film of lipids was then resuspended in the appropriate buffer for the experiment. MBs throughout this project were prepared from a mixture of DPPC and DSPE-PEG2000 in a 95:5 molar ratio and a total lipid concentration of 2 mg/mL. Experiments that required MB conjugation to liposomes would instead use DSPE-PEG2000-Biotin to allow for Neutravidin-Biotin linkages to be formed.

3.3.2 Tip Sonication

Sterile PBS solution containing 1 % glycerol to aid bubble stability [147] was added to the dried lipid film which was then heated at 60 ^{o}C and stirred using a magnetic stir bar. 60 ^{o}C exceeds the phase transition temperature of the lipids which allows for resuspension. After approximately 15 minutes, a cloudy suspension has formed indicating lipids had been resuspended. Prior to lipid sonication, the tip was sonicated in methanol for 10

minutes to ensure no contaminants remained within the system. The lipid solution was then tip sonicated (20 kHz, 150 W, Sonifier 250, Branson, USA) at 4 ^{o}C for 40 minutes producing a solution of liposomes approximately 100 nm in diameter. Sonication resulted in titanium particles from the tip being deposited into the solution. Titanium was removed by centrifuging the solution at 15,000 rpm for 1 minute which caused the precipitation of the titanium pellet. The lipid supernatant was removed, ready for MB production.

3.3.3 Microbubble Production

MBs were produced using both microfluidic and mechanical agitation methods depending on the concentration and formulation required. Microfluidic production techniques produced more monodisperse MB populations compared to mechanical agitation however MBs are typically of a lower concentration. Low concentrations were less of an issue for the larger-scale, spheroid on-chip systems. Whereas, higher MB concentrations were more advantageous when aiming to observe MB-endothelium interactions in the smaller-scale microfluidic vasculature system.

3.3.3.1 Microfluidic Microbubble Production

The microfluidic chips used for MB production were fabricated by Epigem using PMMA. The chips contained a single liquid and gas inlet along with 4 multiplexed flow-focusing nozzles (labelled 1 – 4 on Figure 26) which allowed for the rapid production of MBs. The width of the liquid inlet was 50 µm, the gas inlet was 30 µm and the channel height was 25 µm. Immediately after the nozzle, there was an additional 25 µm expansion to facilitate the microspray formation of MBs.

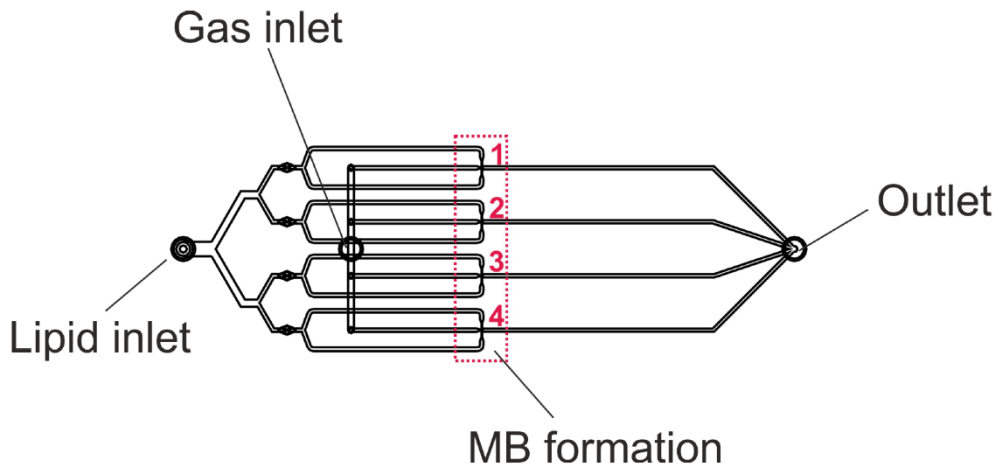

Figure 26 – Schematic of the multiplexed flow-focusing device used for MB formation. Labels show gas and lipid solution inlets which branch into 4 separate flow-focusing nozzels labelled 1 – 4. MBs are collected in a vial attached to the outlet (figure taken with from Peyman et al with permissions from the copyright holder) [140].

The microfluidic chips were interfaced with Horizon V3, a system developed within the MNP group for the microfluidic production of MBs. This system allows for precise control over gas pressures and liquid flow rates through the use of pressure pumps (p-pumps). Figure 27a shows an image of the system alongside a schematic of the p-pump chamber used to supply the liquid flow (Figure 27b). The microfluidic chips are mounted into a custom-built holder, then a polycarbonate manifold containing the inlet tubing is brought into contact with the top of the chip. Two lever-clamp arms are brought into contact with the top of the manifold to form a gas-tight seal. An optical microscope contained within the system allowed for observation of each flow-focusing nozzle, allowing for any blockages to be easily identified. A detailed description of the Horizon V3 design and function can be found here [148].

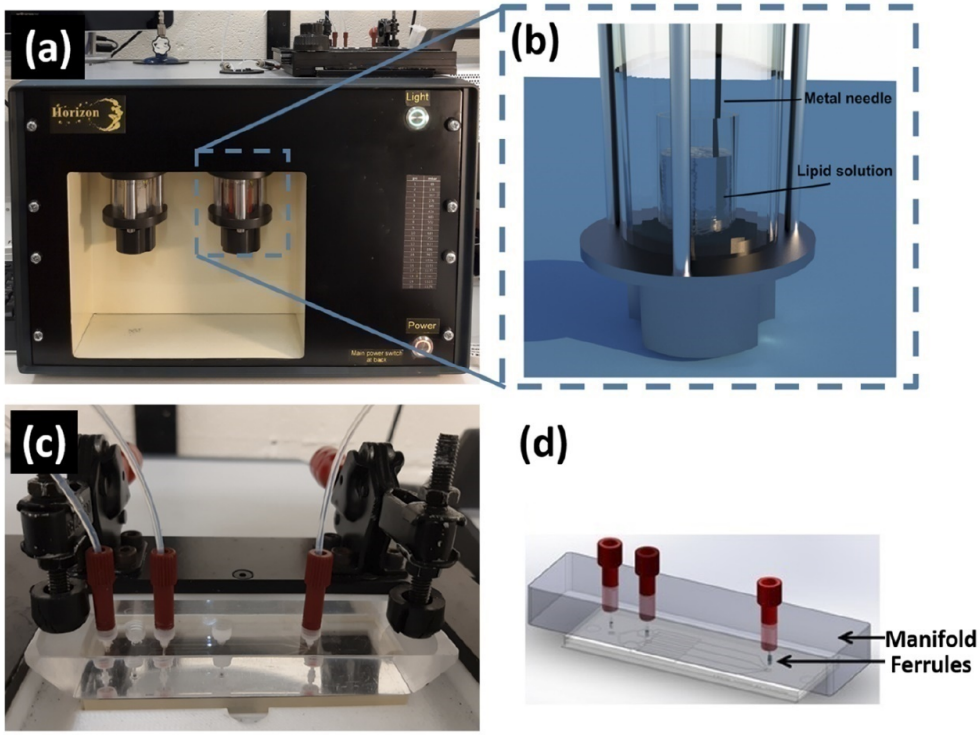

Figure 27 – (a) An image of the Horizon microfluidic platform. (b) Schematic of the vial holder . The p-pump chamber increases in pressure which forces the lipid solution up the metal needed and into the device. (c) An image showing the microfluidic chip with the manifold clamped on top to create a gas tight seal. (d) A schematic of the manifold assemlby complete with tubing inlets and ferrules (This figure was taken from Abou-Saleh et al with permisions from the copyright holder) [148]

MB production was initiated by setting the gas pressure to 15 psi (~ 1 bar) then the liquid flow rate to 100 µL/min. Starting the gas first ensured that no liquid flowed up into the gas lines. Microspray MB began once the liquid entered the nozzle. Gas pressures and liquid flow rates were often altered slightly to ensure that microspray was occurring as shown in Figure 18a. The outlet tubing was inserted into a glass vial to collect the MB solution in preparation for sizing and characterisation.

3.3.3.2 Mechanical Agitation Microbubble Production

MBs were also produced by mechanical agitation through the use of a shaker. C_4F_{10} gas was first bubbled through the lipid solution for 2 minutes at a pressure of 200 mbar. The lid was immediately replaced after gas bubbling and sealed with parafilm to prevent any leakage. The vial was then placed in a shaker (VialMix, Bristol Meyers Squibb) for 45 seconds. The rapid shaking of the gas-saturated lipid solution results in the self-assembly of C_4F_{10} MBs.

3.3.3.3 MB Characterisation

MB size and concentration distribution were measured optically using bright-field microscopy and analysed using a custom MATLAB (2017b, MathWorks, USA) script. 10 µm thick polypropylene spacers were cut from a sheet and used to create a small chamber between a glass slide and coverslip. MB solutions were diluted either 1:10 or 1:100 in PBS then pipetted into the chamber. The glass slide was then inverted to allow MBs to rise and stick to the glass. MBs were given 5 minutes to rise then a Nikon 90i microscope with a 40 × objective was used to image MBs. 15 images were typically captured and analysed using a custom MATLAB script written specifically for MB size and concentration analysis. MBs were typically produced at a concentration between 3 – 7×10^9 MB/mL with an average diameter between 1 and 2 µm.

3.3.4 Targeted PBS-Liposome Production

Blank PBS-LSs were formed for use in vasculature experiments which aimed to observe the effects of targeting LSs to integrin $\alpha_v\beta_3$. No anti-cancer drugs were loaded or encapsulated into these LSs as the primary purpose was to evaluate the effect of targeting on their accumulation within networks. Fluorescent lipids were incorporated into the liposomes to allow for their accumulation to be imaged and quantified.

3.3.4.1 Extrusion

Lipids were first prepared from a mixture of DSPC, Cholesterol and DSPE-PEG2000-Biotin and DOPE-Atto647N in a 55:40:4.8:0.2 molar ratio and a total lipid concentration of 12 mg/mL, consistent with previously used protocols used within our group [149]. Lipids were resuspended in PBS whilst being stirred and heated at 65 ºC – this ensured that the lipids passed their liquid phase transition temperature. After 30 minutes the film was fully resuspended. The extruder was set up using the manufacturer's instructions, with two filter supports on either side of a 400 nm polycarbonate membrane. The 400 nm membrane was soaked in buffer before being placed in between the supports and the extruder tightened together. The extruder block was also heated to 65 ºC. The membrane was first wetted by extruding through 5 times with buffer. The lipid solution was then filled into one syringe and extruded 13 times.

3.3.4.2 Characterisation

LS concentration was characterised using a NanoSight NS300 (Malvern Panalytical). The LS solution was diluted 1:10,000 to the approximate optimal working range of the instrument (10^6 – 10^9 particles/mL). The solution was then flowed through a flow cell using a syringe driver. A 488 nm laser incident on the flow cell then allowed for characterisation of size distribution and concentration, using light scattering and Brownian motion. Measurements were obtained under constant flow for 60 seconds and repeated 5 times across the sample volume. The average concentration was then calculated and used to determine the stock concentration, which was typically in the range of $2 – 4 \times 10^{12}$ lip/mL.

3.3.4.3 $\alpha_v\beta_3$ Antibody Conjugation

Biotin-avidin binding was used to conjugate $\alpha_v\beta_3$ antibodies to the surface of liposomes. Biotinylated antibodies were purchased from Biolegend (304412, 0.5 µg/mL) and were mixed with LSs (10^{11} /mL) to give a final antibody concentration of 2 or 4 µg/mL. Neutravidin (0.25 mg/mL) was then added in excess to the mixture giving a final concentration of 10 µg/mL. Antibodies were allowed to bind to LSs for 20 minutes with regular pipette mixing used. The same protocol was used for biotinylated isotype control antibodies (Biolegend 4000103, 0.5 µg/mL). Isotype control antibodies are antibodies which lack any binding specificity but match the class and type of the primary antibody being used.

3.3.5 Production $\alpha_v\beta_3$ -Targeted Liposome Microbubble Conjugates

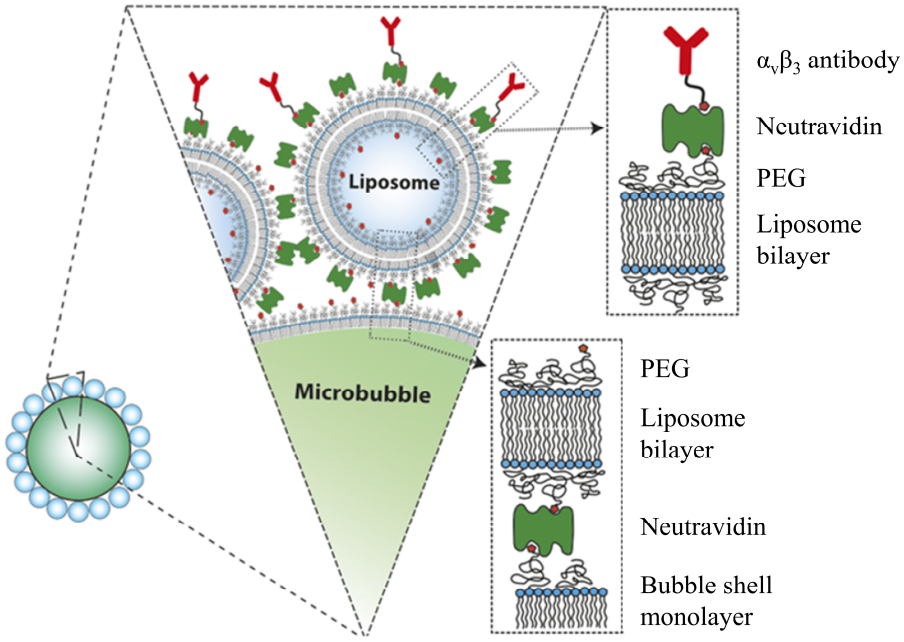

Figure 28 – Schematic of targeted liposomes attached to the surface of a microbubble. Biotin – neutravidin binding was used to attach the $\alpha_v\beta_3$ antibodies to the liposome surface as well as liposomes to the microbubble surface. (This figure was taken from N. Ingram et al and modified under CC licence) [149].

$\alpha_v\beta_3$-targeted liposomes were conjugated to the surface of MBs again using biotin-neutravidin binding. This binding complex consists of biotinylated lipids connected by a neutravidin molecule. Each neutravidin molecule has 4 binding sites for biotin, allowing for multiple linkages to both MB and LS lipids. As mentioned previously, biotinylated DPSE-PEG2000 (5 % molar mass) was used in the lipid preparation step for both MBs and LSs that were to be conjugated. MBs were added to targeted liposomes after the 20-minute antibody conjugation was complete and incubated for a further 20 minutes prior to their use on-chip. Figure 28 shows a schematic of the final $\alpha_v\beta_3$- targeted MB setup, containing a MB coated with liposomes which are in turn coated with antibodies [149]. Ratios of MB : LS : Neutravidin used were typically $10^9 : 10^{11} : 1.5 \times 10^{-8}$ mol.

3.3.6 DOX-LS Production

All DOX-LSs used throughout experiments were formed via extrusion using an Avanti extruder. All steps were performed in a laminar flow hood where possible, in order to minimise the possibility of bacterial infections in cell-based experiments. Tweezers and other tools were also sterilised in ethanol prior to use and sterile containers were used.

3.3.6.1 Extrusion and Dialysis

Lipids were first prepared from a mixture of DSPC, Cholesterol and DSPE-PEG2000 in a 55:40:5 molar ratio and a total lipid concentration of 16 mg/mL. Experiments using LSs conjugated to MBs used DSPE-PEG2000-Biotin to allow for binding. Lipids were resuspended in sterile 300mM ammonium sulphate buffer, pH adjusted to 7.4 using 0.1 M sodium hydroxide. The lipid solution was heated to 65 ºC and vortexed until the lipid film had been fully resuspended. As in the PBS-LS protocol, the extruder was set up using the manufacturer's instructions, using filter supports, a 400 nm membrane, and ensuring the block was also heated to 65 ºC. The lipid solution was then filled into one syringe and extruded 11 times. The LS solution was then transferred from the syringe into a dialysis cassette (Slide-A-Lyzer, Thermo Scientific) and dialysed overnight in ultra-pure water to remove the excess buffer not encapsulated in the LSs.

3.3.6.2 DOX Loading and Column Cleaning

The ammonium sulphate salt encapsulated inside the LSs allowed for active encapsulation of DOX through the pH gradient set up across the membrane. DOX hydrochloride (4mg/mL, Fluorochem, UK) was mixed in a 1:1 ratio with the LS solution in a sterile glass vial and heated at 60 ºC for 5 hours. The solution was agitated regularly to ensure homogenous loading. Excess DOX was then removed using a NAP-5 column (GE Healthcare). The column was opened and allowed to equilibrate with 10 mL of PBS buffer. 0.5 mL of the DOX-LS solution was then added, followed by an additional 1 mL of elution buffer. The advancing from of LSs could be observed in the column. The collection began when the solution began to turn characteristically hazy, indicating LSs were present.

3.3.6.3 Characterisation

LS concentration was first characterised using a Nanosight, using the same protocol as PBS-LS, outlined in section 3.3.4.2 (page 99). In order to determine the amount of DOX encapsulated within the LSs, known concentrations of LSs were lysed and the characteristic absorption peak at 502 nm was measured using a UV – Vis Spectrophotometer (Cary 5000, Agilent). This was then compared to the standard curve, shown in Figure 29b, which was created using the absorbance of known concentrations of free DOX-HCl. The stock LS solution was diluted to a range of known concentrations between $0.5 – 5 \times 10^{10}$ lip/mL. 0.2 % Triton - X100 (Sigma) was then added, and the solution was sonicated for 15 minutes to ensure complete lysis and DOX release. DOX absorption curves for control and liposomal samples were measured between 400 – 600 nm in steps of 0.5 nm. 3 repeat measurements were taken for each sample then averaged. Plotting the free DOX-HCl absorption against concentration gave a straight line, the gradient of which allowed for calculation of the concentration of DOX-HCl per known number of LSs. Figure 29a shows typical absorption spectra for free (left) and lysed, liposomal (right) DOX-HCl at a range of concentrations.

Figure 29b shows the standard curve (blue) plotted from free DOX absorbance values at 502nm. Annotated drop lines (red) show absorbance values for lysed liposome concentrations. The gradient of the standard curve shown in blue in Figure 29b was found to be $(9.77 \pm 0.09) \times 10^{-3}$ μM^{-1}. This value was used to calculate the DOX concentration within LS and equate DOX doses in free and liposomal experiments, allowing for comparisons between delivery methods. Each batch of LSs was characterised shortly after production and stored at 4 ºC for 4 weeks before a fresh batch was required.

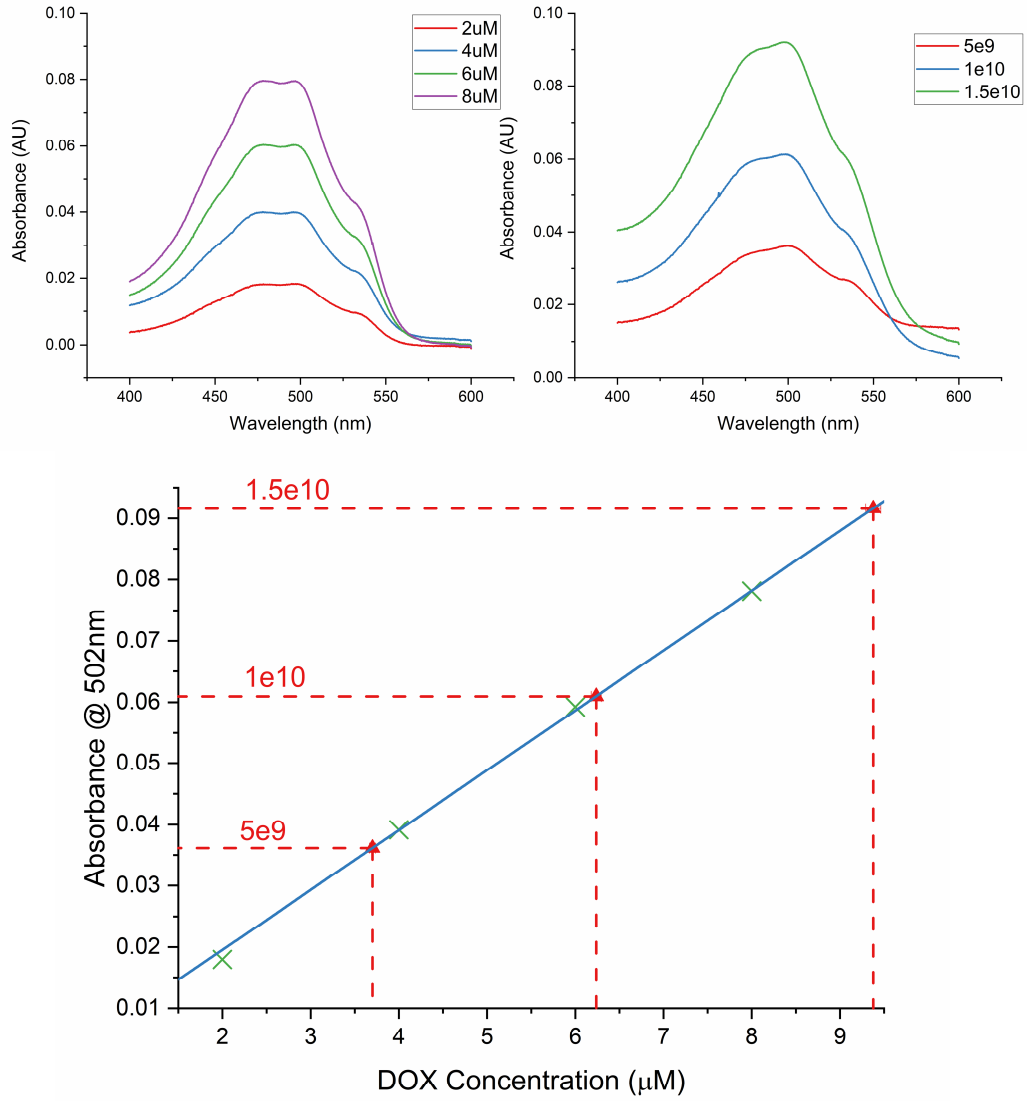

Figure 29 – a) UV-Vis absorption spectra recorded for free (left) and lysed, liposomal (right) DOX-HCl, recorded across a 400 – 600 nm wavelength range. b) Graph showing the standard 'curve' (blue) plotted from free DOX 502 nm absorption values (green crosses). Drop lines show 502 nm absorption values for different concentrations of liposomal DOX-HCl.

3.3.7 Drug-Loaded Microbubble (DLMB) Production

Biotin – Neutravidin binding was used to conjugate MBs and LSs together for DLMB experiments. Conjugation was carried out using a one-pot mixing method where neutravidin was added to LSs, incubated for 30 minutes, then MBs added and incubated for an additional 30 minutes. Ratios of MB : LS : Neutravidin used were typically 10^{8} : 10^{10} : 1.5×10^{-9} mol. Successful binding of MBs and LSs was then observed by incorporating green, fluorescent Atto 488 nm lipids (0.2 %) into LSs and observing the fluorescent ring of LSs around the outside of the MBs. Figure 30 shows images taken observing the co-localisation of LS to the outside of MBs.

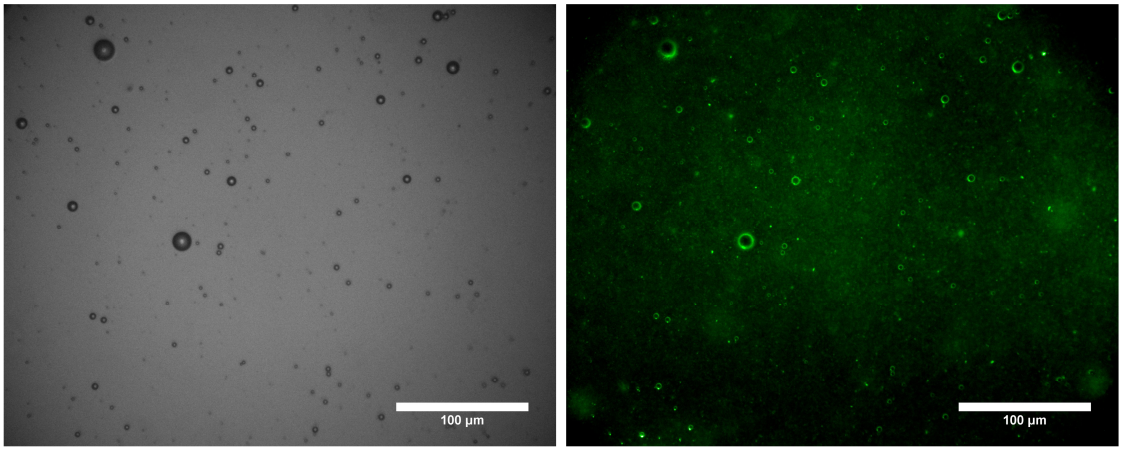

Figure 30 – Bright field (left) and fluorescence (right) images showing co-localisation of LS Atto 488 green, fluorescent lipid emission from the MB lipid shell.

At these ratios, there was approximately a 10 × excess of neutravidin with respect to the number of biotin molecules. Previous tests observed no apparent binding with 1:1 biotin: neutravidin ratios and existing studies throughout literature reported using an excess of neutravidin. A 10 × excess was therefore tested and shown to be successful.

3.4 Spheroid On-chip Experimental Protocol

3.4.1 US Coupling On-Chip

It was necessary to ensure that US was effectively coupled on-chip so that MBs could be burst when loaded into the chamber. Devices were insonated using a 2.24 MHz centre frequency unfocussed transducer (V323-SM, Olympus). Pulses were controlled by a function generator (TG5011, Agilent Technologies) and consisted of a duty cycle of 1 %, pulse repetition frequency of 1kHz for a total duration of 2 s. The free field transducer output was calibrated using a 0.2 mm needle hydrophone (Precision Acoustics) to provide a peak negative pressure of 0.81 ± 0.04 MPa when driven by a +53 dB RF power amplifier (A150, Electronics & Innovation). The transducer was coupled to the top of the microfluidic devices via a gel pad (Aquaflex, Parker Laboratories) and coupling gel. The use of a gel standoff pad meant the spheroid chamber was further than the Rayleigh distance away from the transducer, ensuring that the spheroid chamber was exposed to the far-field, uniform US beam. Figure 31a shows a diagram of the US transducer – microfluidic setup used to expose MBs within the spheroid chamber to US.

MBs were loaded on-chip at a concentration of 1×10^8 MB/mL and exposed to US. Observation of the chamber before and after insonation found no apparent MB destruction had occurred. PDMS is known to attenuate US therefore it was concluded that the 5mm of PDMS had attenuated the US beam such that there wasn't sufficient intensity to destroy MBs. The attenuation of US through a material is given by the relationship:

$$I = I_0 e^{-\alpha x} \tag{3-1}$$

Where I is intensity, α is the attenuation coefficient (cm^{-1}) and x is the thickness of the material the wave is travelling through (in cm). The US attenuation coefficient for 2 MHz US through PDMS was found to be 5.72 ± 0.48 cm^{-1}. This results in approximately 95 % of the US intensity being attenuated when travelling through the 5mm high device.

Microfluidic devices were therefore fabricated to be 1 mm thick, reducing attenuation to 56 %. MBs were again loaded on-chip and insonated and Figure 31b shows images taken of the centre trap chamber before and after US exposure. A significant reduction in the MB population could be observed. The MB counting code was used to determine MB concentrations at the front, centre and back of the spheroid chamber before and after

insonation – shown in Figure 31c. It was found that, on average, 99.96 % of MBs were destroyed by the US pulse. As microfluidic devices were only 1 mm thick, additional pieces of PDMS were bonded over the inlet,outlet regions so that reservoirs and pipette times could securely interface with the chip. The same bonding process was repeated as before, with extra care being taken to properly align the pre-punched inlets and outlets.

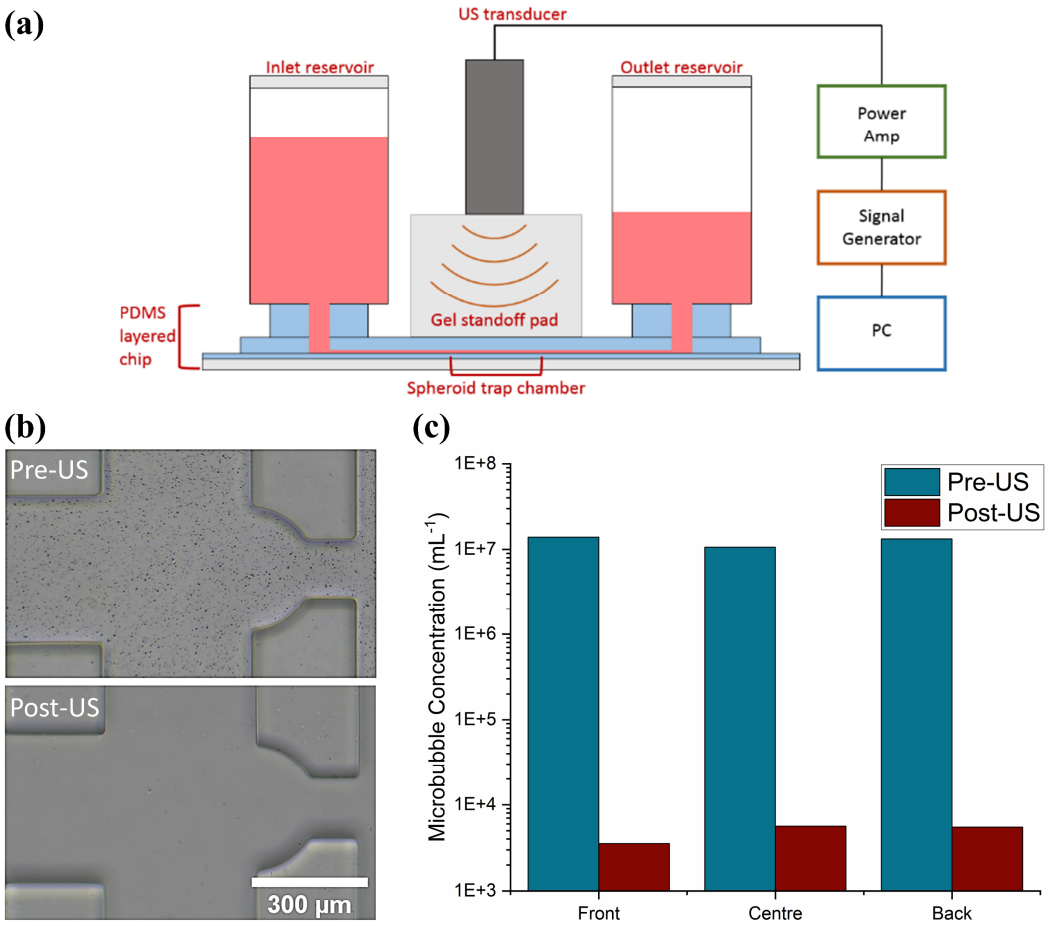

Figure 31 - (a) Diagram of the setup used to expose MBs in the spheroid trap chamber to US. The 1mm thick chip minimised US attenuation and the gel standoff pad ensured MBs were exposed to far-field, uniform US waves. (b) Optical images taken of MBs within the spheroid chamber pre- and post-US. MBs can be observed in the Pre-US image as a background of small particles. A clear reduction in MB population can be observed post-US. (c) A graph showing quantified MB populations in the front, centre, and back of the spheroid chamber pre- and post-US exposure. Results revealed that, on average, 99.96 % MBs were burst.

3.4.2 Spheroid On-Chip Exposure to Therapeutics

Once the spheroid trapping was complete, excess media in the inlet and outlet reservoirs was removed and the therapeutic exposure initiated. Media flow was maintained throughout exposures by periodically cycling media from the outlet reservoir back into the inlet reservoir every 2.5 hours. Flow is only able to be maintained for this period of time due to the reduction in hydrostatic pressure caused by the simultaneous emptying and filling of inlet and outlet reservoirs, respectively.

3.4.2.1 Free DOX, MB + US Exposures

For free DOX exposures without MBs, 2 mL of DOX-DMEM solution was added into the inlet reservoir and allowed to flow through the chip. For MB and DOX co-delivery, 15 µL of MBs at 2×10^8 MB/mL was mixed with 15 µL DOX at twice the concentration being tested, giving 30 µL solution at 10^8 MB/mL and the appropriate DOX concentration. This was then pipetted directly into the channel through the reservoir spout, preventing MBs from rising to the top of the reservoir by their intrinsic buoyancy. This was followed by the 2 mL DOX dose being added to the inlet reservoir. The devices were then insonated when MBs were observed to fill the trap array. Control MB + US exposures without drug followed this same protocol with media not containing DOX. Control exposures of MB only or US only followed the same protocols but without insonation or addition of MBs, respectively.

3.4.2.2 DOX-LS and DLMB Exposures

LS for exposures without MB + US, stock LS samples were diluted such that a dose of DOX equivalent to 2 mL at 3 µM was contained with a 30 µL solution. Unconjugated LS, MB + US exposures used the same number of LS in the 30 µL solution, now with MBs included at a concentration of 10^8 MB/mL. DLMB were produced by conjugating the same amount LSs and MBs as used in unconjugated LS, MB + US experiments. Therefore, allowing for direct observation of the effects of conjugation on treatment efficacy. Devices were insonated when MB solutions had filled the spheroid trap chamber. For DLMB experiments with multiple US exposures, insonation was repeated every 60 seconds, to allow the MB solution to completely refill the trap chamber. 2 mL of fresh media was then added to the reservoirs to initiate flow.

3.4.3 Spheroid Imaging and Analysis

All therapeutic exposures were carried out for 8 hours to allow for sufficient DOX accumulation, then compound containing media replaced with fresh media. Spheroids were allowed to grow on-chip for 48 hours with media again being replaced after 24 hours. This allowed sufficient time for the chemotherapeutics to affect cell division and spheroid growth. Untreated control spheroids were also allowed to grow on-chip for 48 hours and used as a comparison.

3.4.3.1 Confocal Microscopy Imaging

Prior to imaging, dead cells were stained with NucRed Dead (Thermo Fisher Scientific) cell dye for 30 minutes, using 2 drops / mL of media as instructed. Fresh media was added to remove any unbound dye and reduce the background signal. A Leica DMi8/SP8 confocal microscope system was used for fluorescent imaging of spheroids. DOX and NucRed Dead dye were excited sequentially using 488 nm optically pumped semiconductor laser (OPSL) and 638 nm diode laser, respectively. Fluorescence emission for DOX was measured from 410 – 493 nm and dead cell emission was observed between 651 – 799 nm. A 10× objective was used to image spheroids in 5 µm z-stack slices.

3.4.3.2 Viability Assessment

CellTiter-Glo 3D cell viability assay (Promega) was used as an endpoint assay to determine spheroid viability. Spheroids were retrieved from the chip 48 hours after exposure by withdrawing on a pipette inserted into the inlet reservoir spout. The lack of adhesions between cells and PDMS meant that spheroids could be easily dislodged by gentle backflow. Dead cell debris which had broken away from the surface of the spheroid and collected in the outlet was also collected and included in the ATP assay to ensure all cell material was analysed. Spheroids from each chip were deposited in 100 µL volumes into each well of an opaque walled well-plate. 100 µL of assay reagent was mixed into each well and incubated at room temperature for 30 minutes. Luminescence was then recorded on a plate reader (SpectraMax M2E, Molecular Devices) as per assay instructions.

3.4.3.3 Statistical Analysis

To account for variation in initial spheroid diameter, and by extension volume, final luminescence values were normalised with respect to a 300 µm diameter spheroid. Normalisation factors, n_v were determined for each chip using the average volume of the 10 spheroids loaded. The diameter of spheroids used for on-chip experiments typically ranged from 280 µm to 350 µm, giving normalisation factors between 0.8 - 1.6. Viability results from large and small spheroids were found to be intermixed for each dataset, suggesting that there was no significant difference in spheroid response to therapeutic treatment across this diameter range.

Due to the method by which spheroids were retrieved off-chip, individual spheroid viabilities were not able to be acquired. This was due to multiple spheroids and/or fragments of spheroids occupying single assay wells. Average individual spheroid luminescence values, L_{sph} were therefore calculated by dividing the total sum luminescence, L by the total number of spheroids trapped, N_{sph}:

$$L_{sph} = \frac{\sum_{Wells} L}{N_{sph}} \, n_v \tag{3-2}$$

When calculating the total average spheroid luminescence, L_{avg} across all chips subject to the same therapeutic exposure, a weighted average was used to account for the number of spheroids on each chip. In this case, each L_{sph} was multiplied by the number of spheroids from the chip, all these values were then added and divided by the total number of spheroids across all chips:

$$L_{avg} = \frac{\sum_{chips}(L_{sph} \times N_{sph})}{\sum_{chips} L_{sph}} \tag{3-3}$$

The weighted averaged luminescence values for each exposure condition were then divided by the control values and multiplied by 100 to give overall viability percentages. Standard errors attached to these percentages were calculated using individual L_{sph} values from each chip.

Along with standard error, 95 % confidence intervals around the mean were calculated for each dataset. This is the range over which you can be 95 % certain contains the true mean of the dataset. The 95 % confidence interval range was calculated using the following equation:

$$95\ \%\ C.I = \bar{x}\ \pm\ Z_{\propto/2}\frac{SD}{\sqrt{N}} \tag{3-4}$$

Where $\bar{x}$ is the mean, $Z_{\propto/2}$ is the critical value equal to 1.96 for 95 % confidence intervals with $\propto$ equal to 0.05. SD is the standard deviation and N is the total number of spheroids.

Finally, a Mann-Whitney (MW) non-parametric U test was performed to determine p-values and award statistical significance stars. A classic t-test could not be performed in this case as the data was not normally distributed around the mean, meaning a non-parametric test was required. The MW test orders all of the data points in the two datasets from lowest to highest and assigns a rank to each point. U values are determined by the number of times a point from one dataset is higher than a point from the other dataset, this is repeated for all points and U, P and Z values were calculated from the results.

3.5 Vasculature On-chip Experimental Protocol

The successful production of both healthy and tumour cell media (TCM)-conditioned vasculature networks (outlined in section 3.2.7, page 92), along with the production of integrin $\alpha_v\beta_3$-targeted LS-MB allowed for vasculature on-chip work to progress with perfusion experiments.

3.5.1 Observation of Vessel Permeability

Texas red dextran (70 kDa, Invitrogen) was used to probe the permeability of the endothelial barrier. Dextran stock was prepared by dissolving 25 mg in 5 mL of Milli-Q water for a final concentration of 5 mg/mL. This solution was then diluted to 1:50 in PBS for a working concentration of 100 µg/mL. Interstitial flow across the chamber was maximised by filling the inlet reservoir with 2.2 mL of Dextran and removing all but 200 µL of media from all other reservoirs. Shortly after flow was initiated, dextran could be observed to begin flow down the side channel. The mark-and-find feature on the Leica DMi8/SP8 confocal microscope was then used to automatically image several locations

across the network in 5-minute intervals. Imaging was performed for an hour to observe dextran leakage out of vessels and into the surrounding matrix. ImageJ was then used to quantify the mean grayscale intensity of each image and the permeability calculated using equation (5-3).

3.5.2 On-chip Integrin-$\alpha_v\beta_3$ Immunostaining

Immunostaining of microfluidic vasculature cultures was performed by first perfusing the networks with PBS for 60 minutes. Cultures were then fixed with 4 % paraformaldehyde for 90 minutes which was followed by a further 60 minute PBS wash. Cultures were permeabilised by flowing 0.3 % Triton-X100 for 30 minutes then a blocking solution of PBS (3 % BSA, 0.3 M Glycine, 0.1 % Triton-X100) was perfused for 60 minutes. Primary antibody (Abcam, ab190147) was diluted 1:1000 in PBS (3 % BSA) and perfused through the network overnight at 4 ^{o}C. A 60 minute PBS wash was then performed then the secondary antibody (Abcam, ab150115) diluted 1:1000 in PBS (3 % BSA) was perfused for 3 hours. A final 90 minute PBS wash was performed then the cultures were imaged using a Leica DMi8/SP8 confocal microscope.

3.5.3 Liposome Perfusion and Imaging

The inlet reservoir for perfusion was first filled with 2.2 mL of media and the corresponding outlet filled with 0.5 mL. The inlet and outlet reservoirs in the adjacent media channel were filled with 0.3 mL and 0.1 mL, respectively. This configuration maximised the interstitial pressure across the vasculature chamber, maximising the intramural flow through the network. Once the flow was initiated, 30 μL of liposomes (10^{11} /mL) were deposited into the bottom of the inlet reservoir and allowed to perfuse through the network for 1 hour. Perfusion through the network was imaged using a Leica DMi8/SP8 confocal microscope, with the GFP and atto647N being excited with 488 nm and 638 nm diode lasers, respectively. The ‘mark and find’ feature was used to periodically image the network at multiple locations to observe liposome and dextran perfusion across the network. 1 hour after perfusion began, liposome-containing media in the inlet reservoir was replaced with fresh media, which was allowed to perfuse through the network for an additional hour. This rinsed all of the free liposome solution from the network, ensuring that all of the remaining liposomes were those which had accumulated

within the vasculature. Post-perfusion images were then taken using a 100x objective, which captured confocal z-stacks using a 1.5 µm slice thickness.

3.5.4 Microbubble – Liposome Conjugate Perfusion

Targeted liposomes were produced and conjugated to microbubbles using the protocols described throughout sections 3.3.4 and 0 (page 94). Reservoirs were filled to the same levels as in the liposome only perfusions then 30 µL of targeted liposome-microbubble conjugates (T-LS-MB) were added to the inlet reservoir. T-LS-MB were allowed to perfuse into the network and after approximately 10 minutes were found to fully populate the vasculature. Microbubbles in this system were burst using the same setup and US parameters used in the previous spheroid-on-chip system. As described in section 3.4.1 (page 105), a gel standoff pad was placed over the microfluidic chamber and the 2.25 MHz US transducer was placed on top of the pad. A 2 second US pulse using a 1 % duty cycle, 1 kHz pulse repetition frequency was applied, using a +53 dB RF power amplifier to deliver a peak negative pressure of 0.81 ± 0.04 MPa. PDMS microfluidic chips were again produced to be approximately 1mm thick to minimise US attenuation and ensure MB were burst. The perfusion was then allowed to continue for an hour total before the same washing and imaging steps were completed as with liposome only perfusions.

3.5.5 Quantification of Liposome Perfusion

Post-perfusion z-stack images of liposome fluorescence were used to quantify the amount of accumulation within the vasculature networks. ImageJ particle analysis tool was used to identify liposomes and quantify their fluorescent intensity. Contrast enhancement was first performed on captured images to reduce any background fluorescence and ensure that liposomes were correctly identified. Z-stacks were duplicated, and the duplicates were binarized using the threshold tool. Measurements were set to the original stack, using the binarized stack as a mask for the original stack. The ‘analyse particles’ tool was then used to quantify liposomes fluorescence. The values from each stack of images were averaged and plotted as a single data point on a boxplot graph. Between 5 – 8 z-stacks were taken for each microfluidic chip used, depending on time constraints.

4 RESULTS I: HIGH-THROUGHPUT MICROFLUIDICS FOR EVALUATING MICROBUBBLE ENHANCED DELIVERY OF CANCER THERAPEUTICS IN SPHEROID CULTURES

This chapter contains results obtained from the testing of MB-mediated drug delivery on tumour spheroids, investigated using a microfluidic spheroid trap system. The trap system was designed and developed so that pre-grown HCT116 - HFFF2 colorectal cancer spheroids could be loaded on-chip, exposed to therapeutics under physiological flow conditions, and retrieved for quantitative analysis. The commonly used chemotherapy drug Doxorubicin (DOX) was chosen as the drug to be co-delivered with MBs. Confocal microscopy imaging was used to observe spheroid degradation, cell death, and drug accumulation – by using the inherent fluorescence of DOX. Cell Titer-Glo 3D ATP viability assay was then used to quantify spheroid viabilities. Both free and liposomal DOX was co-delivered with MBs to observe the effects of differing drug formulations. This work presented the first study into the effects of MB-mediated drug delivery in tumour spheroid cultures under constant flow conditions.

4.1 Microfluidic Spheroid System Design and Modelling

4.1.1 Trap Design and Modelling

As discussed throughout section 1.3.1.1 (page 37), spheroid trap designs were based on the single-cell hydrodynamic traps originally developed by Di Carlo and further considered by X. Xu et al [45,49]. These traps were scaled-up to allow for the trapping of spheroids approximately 300 – 350 µm in diameter. The CAD schematic for the entire spheroid trap chip and spheroid chamber can be seen in Figure 21a. Figure 32 shows the trap design, consisting of a U-shaped trap with a channel through the centre. These traps rely on the hydrodynamic force produced by fluid flow to ensure that the spheroids remain in place. This mechanism of trapping has the benefit of allowing for simple spheroid retrieval through the reversal of flow and hydrodynamic force. This is providing that there is minimal adhesion between the trap and cell/spheroid.

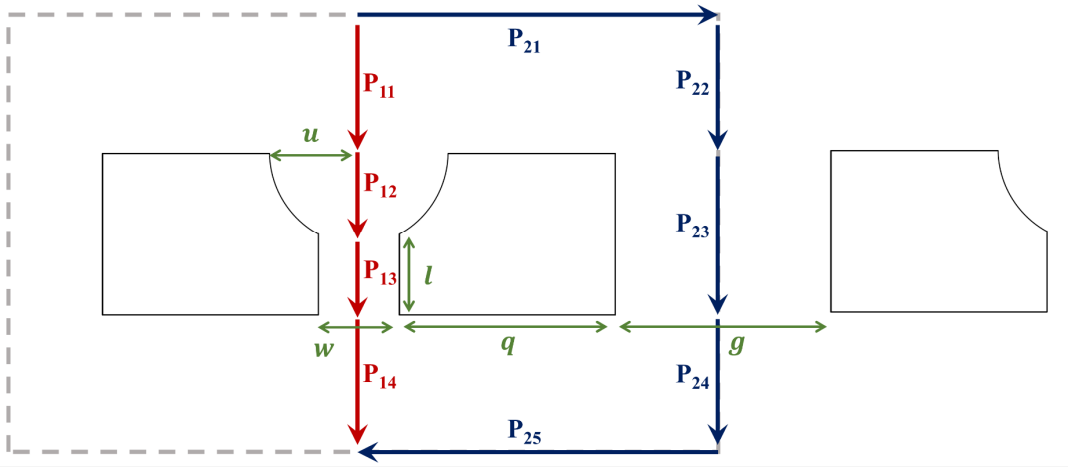

Figure 32 – Spheroid trap design showing trap radius, u length, q width, w separation, g and centre channel length, l. Fluid resistance/pressure drop paths considered for hydraulic resistance calculations are shown and broken down into their individual components.

The overall design of the trap is based on consideration of the hydraulic resistances through, R_1 and around, R_2 each trap. This can be calculated by considering the pressure drops along the paths P_1 (ΔP_1) and P_2 (ΔP_2), respectively. Pressure drops can be calculated by breaking down each path into a series of sub-paths:

$$\Delta P_1 = \Delta P_{11} + \Delta P_{12} + \Delta P_{13} + \Delta P_{14}, \quad \Delta P_2 = \Delta P_{21} + \Delta P_{22} + \Delta P_{23} + \Delta P_{24} + \Delta P_{25} \qquad (4\text{-}1)$$

The general expression for the pressure drop down a rectangular microfluidic channel can be derived using Darcy-Weisbach and Hagen-Poiseuille flow equations and is given by:

$$\Delta P = \frac{f(\beta)\mu Q C^2 L}{32A^3} \tag{4-2}$$

Where μ is fluid viscosity (Pa.s), L is the channel length (m), Q is the volumetric flow rate (m^3/s), and A and C are the channel's cross-sectional area and perimeter (m). $f(\beta)$ is a known polynomial of the aspect ratio β, given by:

$$f(\beta) = 96(1 - 1.3553\beta + 1.9467\beta^2 - 1.7012\beta^3 + 0.9564\beta^4 - 0.2537\beta^5) \tag{4-3}$$

Where β is the height-to-width ratio (h / w) of the channel. This is providing that $0 \leq \beta \geq 1$. The width of the channel for the terms ΔP_{11}, ΔP_{14}, ΔP_{22}, ΔP_{24} is the width of the entire channel, making these terms negligible. Cancelling and equating terms reduces the equations in (4-1) to:

$$\Delta P_1 = \Delta P_{12} + \Delta P_{13}, \qquad \Delta P_2 = 2\Delta P_{21} + \Delta P_{23} \tag{4-4}$$

The circular shape of the trap makes the calculation of ΔP_{12} difficult due to the constantly varying channel width. An approximate solution was therefore calculated, using the average width, $\overline{w}$ of the channel:

$$\Delta P_{12} = \frac{Q_1 \mu}{8} \frac{f\left(\frac{\overline{w}}{h}, \frac{h}{\overline{w}}\right)(\overline{w} + h)^2}{(\overline{w}h)^3}.u \qquad \text{where,} \qquad \overline{w} = \frac{\frac{\pi u^2}{2} + w}{u} \tag{4-5}$$

Where u is the trap radius (m) and h is channel height (m). Calculation of ΔP_{23} showed that trap separation, g (green label in Figure 32) determined the pressure drop around the trap:

$$\Delta P_{23} = \frac{Q_2 \mu}{8} \frac{f\left(\frac{g}{h}, \frac{h}{g}\right)(g + h)^2}{(gh)^3}.(u + l) \tag{4-6}$$

X. Xu et al. applied several constraints to the system to ensure maximum trapping efficiency. This included an area constraint to ensure traps were large enough to adhere to the glass surface, and a minimum distance between traps to prevent blockages occurring when multiple beads were flowing through simultaneously. These factors were not an issue when this framework was scaled up to trap spheroids. Blockages were not expected to be a problem as significantly fewer spheroids would be flowed through the chip. Spheroid trap arrays would also consist of fewer, larger traps than the microsphere arrays, meaning trap area was not a concern. Larger traps, however, limited the number that could be contained within the array. To maximise the number of traps, the distance between traps, g was kept to a minimum and only just wider than the spheroids ($g \leq 2u + 80$). The consequence of limiting trap separation, g was that the hydraulic resistance ratio could now only primarily be altered by varying the centre channel width, w. This imposed a separate set of constraints to ensure that the trap channel did not allow for spheroids to deform through from the constant hydrodynamic pressure ($w \leq 2u - x$), where x is a yet to be determined value. Traps were designed to allow for spheroids between 300 – 330 µm in diameter to be captured, with u = 160 µm. Microfluidic fabrication using photolithography produced a chamber height, h of 360 µm. This allowed for sufficient space around spheroids for fluid flow to occur when trapped. Both trap length, q and the distance between traps, g were fixed at a minimum value of 400 µm. The entire array was designed to contain 17 separate traps arranged into 7 rows of 2 or 3 traps. These were all contained within a trap chamber measuring 3000 µm wide by 8000 µm long. A schematic of the microfluidic spheroid trap system can be seen in Figure 21a.

Traps with three separate ratios of hydraulic resistances R_1/R_2 = 1.3, 2.1 and 3.1 were designed using centre channel lengths/widths of 250 µm, 150 µm and 115 µm, respectively. This channel was designed to be square so $l = w$. Figure 33 shows the spheroid traps designed for each resistance ratio, alongside Ansys fluent flow simulations performed on each array. Further details of Ansys simulation parameters can be found in section 4.1.3. As expected, modelling results showed increased fluid flow through the traps with lower resistance ratios. Spheroid trapping was then tested in each design by flowing 10 spheroids on-chip at a flow rate of 0.6 µL/s and observing their passage through the array.

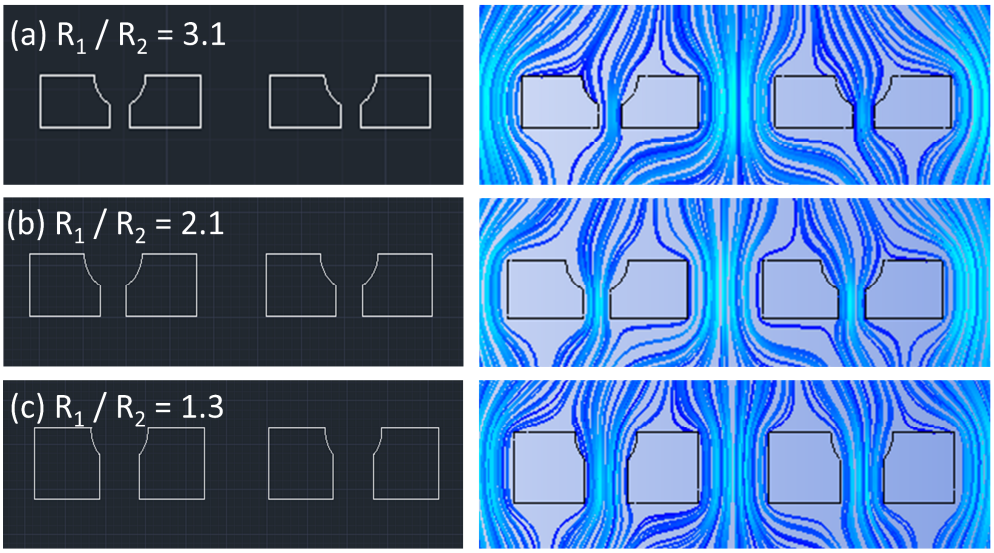

R_1 / R_2	Radius, *u* (µm)	Trap Separation, *g* (µm)	*l*, *w* (µm)	Trap length, *q* (µm)
1.3	160	400	250	400
2.1	160	400	150	400
3.1	160	400	115	400

Figure 33 – AutoCAD trap designs with hydraulic resistance ratios of (a) 1.3, (b) 2.1 and (c) 3.1 alongside Ansys Fluent flow simulations through each trap design. The table shows dimensions of trap diameter, *u*, trap separation, *g*, centre channel length/width *l*,*w* and trap length,*q* for each design.

R = 1.3 traps were initially allowed for a high number of spheroids to be trapped, however, after a short period of time (~ 10 minutes), the 320 µm spheroids began deforming through the 250 µm centre channel due to the constant hydrodynamic pressure. This then resulted in spheroids eventually flowing out of the trap array, concluding that this ratio was not suitable for the trapping of 320 µm spheroids. From this, it was clear that $x > 70\ \mu m$. R = 2.1 traps resulted in approximately 40 % of spheroids being trapped within the array however, no spheroid deformation was observed, and spheroids were able to remain within the traps indefinitely. Testing of R = 3.1 traps resulted in approximately 10 % of spheroids being trapped, fewer when compared to R = 2.1, and expected due to the reduced flow through traps. The decision was therefore made to proceed with the use of R = 2.1 trap designs for this study.

The initial 40 % trapping efficiency could be increased by cycling the spheroid-containing reservoir media through the chip once more, which resulted in, on average, 6 out of 10 spheroids being trapped on-chip. It was also discovered throughout this testing process that spheroid trapping improved as the reservoir media levels decreased revealing that lower flow rates allowed for increased trapping efficiency. Flow rates between 0.2 – 0.4 µL/s were chosen for spheroid loading, which balanced the rate at which spheroids flowed through the device with trapping efficiency. High flow rates increased inertia of the spheroids causing spheroids to overshoot the traps in many cases where they would have become otherwise trapped. For this same reason, smaller spheroids (< 280 µm in diameter) were less likely to become trapped. This imposed the lower limit on spheroid diameter of approximately 280 µm, with the chamber height imposing an upper limit of 350 µm. Figure 34 shows a graph of observed trapping efficiencies for a range of spheroid diameters, collected from all spheroid on-chip experiments performed.

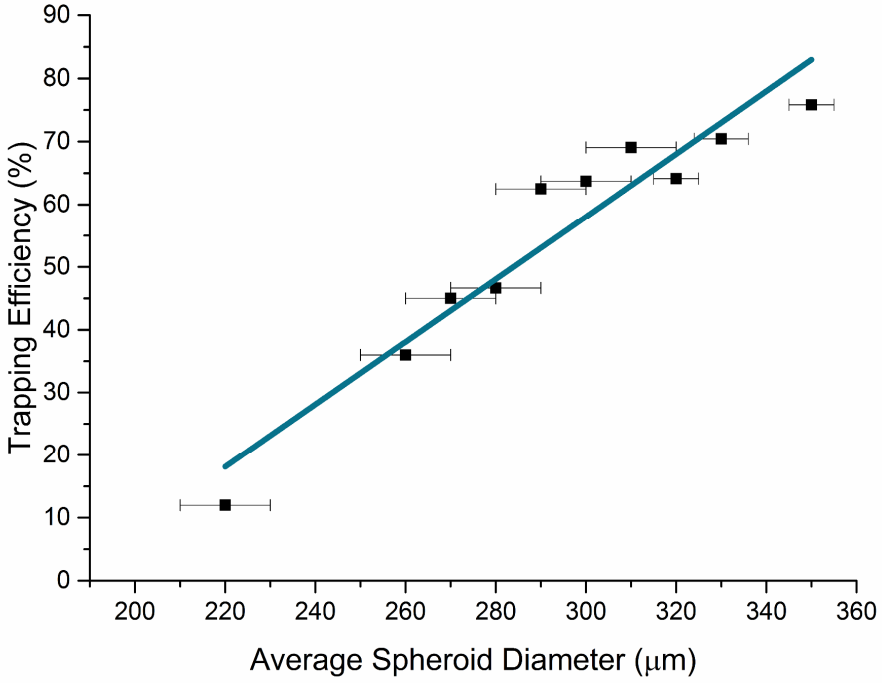

Figure 34 – Spheroid trapping efficiency observed for spheroid diameters ranging between 220 and 350 µm. Data was collated from all spheroid on-chip experiments performed using flow rates between 0.2 – 0.4 µL/s.

4.1.2 Hydrostatic Flow Considerations

In order to achieve physiological rates of flow through the spheroid chamber, careful consideration of the channel dimensions was required. As previously described in section 2.2.2 (page 65), the flow rate induced by a hydrostatic pressure imbalance is directly dependent on the channel dimensions. For this system, spheroid size requirements meant that channel length was the only parameter that could be altered enough to achieve the 0.1 – 1 mm/s flow rates typically found within capillaries [150]. To produce these flow rates, two serpentine channels were incorporated before and after the spheroid trap chamber, each 13 mm in length. Figure 35a shows the complete microfluidic trap system design.

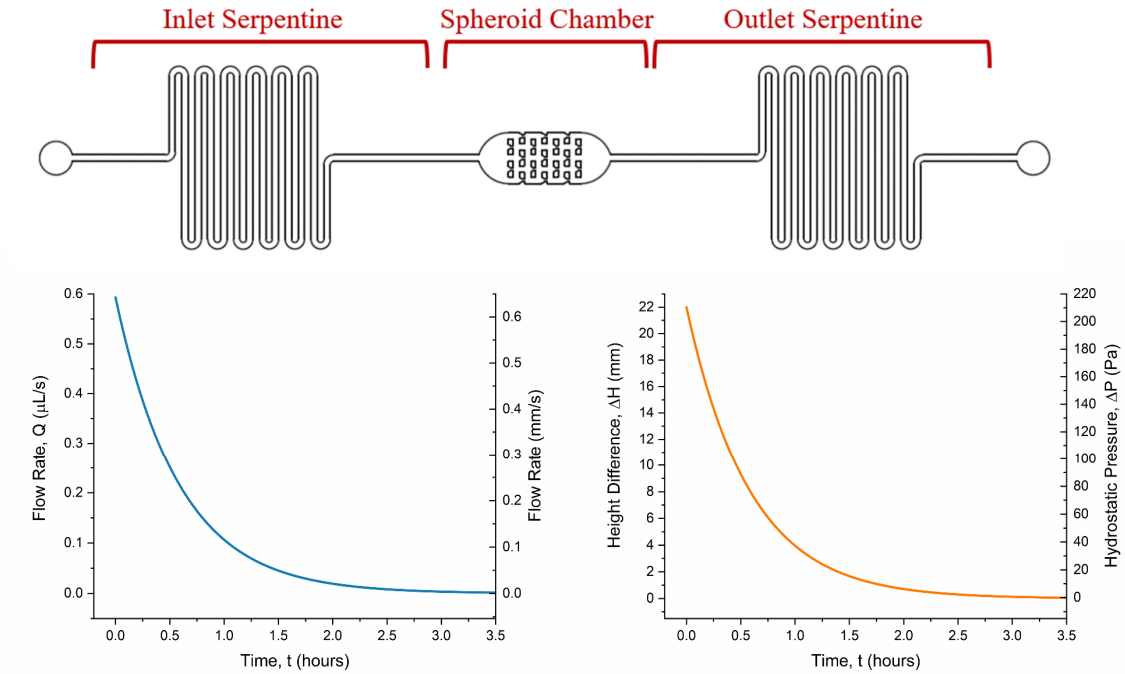

Figure 35 – (a) Microfluidic spheroid trap system design showing the central trap array chamber with inlet and outlet serpentines. (b) Graphs showing predicted flow rate, height difference and hydrostatic pressure changes with time.

Figure 35b shows graphs of flow rate, height difference and hydrostatic pressure modelled as a function of time. The linear flow rate through the trapping chamber was also calculated using the dimensions of the chamber. The exponential decay of flow rate can easily be observed across the 3.5-hour time period. Reservoirs were re-levelled every 2.5 hours to maintain flow during therapeutic exposures.

To determine whether actual flow rates matched theoretical flow rates, 2 µm fluorescent beads were tracked flowing through the centre chamber at a range of height differences. MosaicSuite Image J particle tracking plugin was used to measure bead trajectories which were then converted to linear flow velocities using code written in Matlab. Figure 36 shows the graph of measured and theoretical flow rates alongside an image of tracked particle trajectories. Linear velocities were found to vary between 0.2 – 0.85 mm/s across height differences of 5 – 20 mm. This corresponded to volumetric flow rates of 0.19 – 0.78 µL/s. The actual hydraulic resistance of the system was determined using the gradient of the graph and found to be $(2.5 \pm 0.1) \times 10^{11}$ Pa.s/m^3. This was 1.1×10^{11} Pa.s/m^3 lower than the theoretical resistance of 3.6×10^{11} Pa.s/m^3.

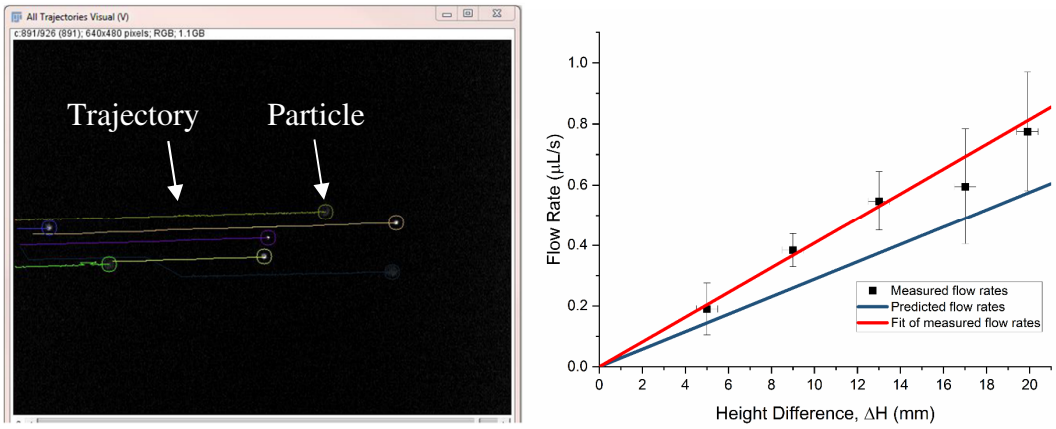

Figure 36 – Screenshot of MosaicSuite Image J particle tracking software determining particle trajectories. Graph showing theoretical and measured flow rates, determined using particle velocities.

This disagreement could, in part, be attributed to an assumption made in the Poiseuille flow model when calculating the hydraulic resistance of the channel. This assumes a very flat, wide channel ($h / w \rightarrow 0$) which was not the case for the serpentine channels in this device ($h / w \rightarrow 1$). Nevertheless, flow rates achieved using hydrostatic pressure successfully emulated flow velocities found within capillaries.

4.1.3 Spheroid Shear Stress Modelling using CFD

In addition to physiologically accurate flow rates, it was also necessary to ensure that spheroids were being exposed to similar shear stresses cells would experience *in vivo*. This was achieved using computational fluid dynamics (CFD) to model the flow of fluid through a trap array containing several trapped spheroids. CFD refers to the use of computational hardware to model the flow of fluids by applying the fundamental mathematical equations of fluid dynamics covered in section 2.2.1. In this instance, the CFD software Ansys Fluent was used to model the flow of fluid throughout the microfluidic spheroid trap system, to visualize the behaviour of the flow and determine the resultant shear stress experienced by the trapped spheroids.

A 3D geometric model of the microfluidic trap system was created using AutoCAD to extrude the 2D trap design to a height of 360 µm – the height at which microfluidic devices were fabricated to be. Traps were designed with 7 spheroids occupying the first three rows of traps. This was representative of experimental conditions, which saw 6 ± 2 spheroids being trapped primarily within the first three rows of each chip. Spheroids were 320 µm in diameter to represent the on-chip conditions immediately after spheroid loading, therefore showing the shear stresses spheroids experienced whilst being exposed to therapeutics. This design was then imported into Ansys fluent and defined as a hollow structure with an inlet, outlet, and channel walls. The spheroids were defined as solid spheres as shown in Figure 37a.

Next, the boundary and initial conditions for the simulation were defined. The inlet velocity was set to 0.85 mm/s (0.78 µL/s) - the velocity which was measured by tracking fluorescent beads as they flowed throughout the trap array (section 4.1.2). The outlet boundary was then defined using a pressure condition which was set to equal zero. A no-slip boundary condition was then imposed for the channel walls which uses the assumption that the fluid at the solid boundary will have zero velocity relative to the boundary. The final step prior to intiating the simulation was to divide the surface of the model into a framework of cells known as a mesh. This allows for computation of values such as shear stress at individual points across the model. Several types of mesh such as structured, unstructured and hybrid meshes can be used to create either uniform, regular

shapes (structured) or irregular shapes (unstructured). Structured allows for easily identified and accessed points whereas unstructured reduces computation time due to the lack of limitation on shape. In this case, a hybrid mesh was used which combines the two approaches. A hybrid mesh allowed for structured geometric meshing across the regular channel/chamber and trap walls whilst also allowing for irregular meshing of the more complex spheres located within the traps.

Finally, the Ansys Fluent solver settings were set to use parallel processing using the two cores available on the computer being used to run the simulations. The Ansys Fluent solver uses a finite volume method solver which discretises the conservation form of the partial differential equations which govern fluidics. This solver method is one of the most commonly implemented due to its realtively straightforward mathematics along with the ability to accommodate any type of mesh.

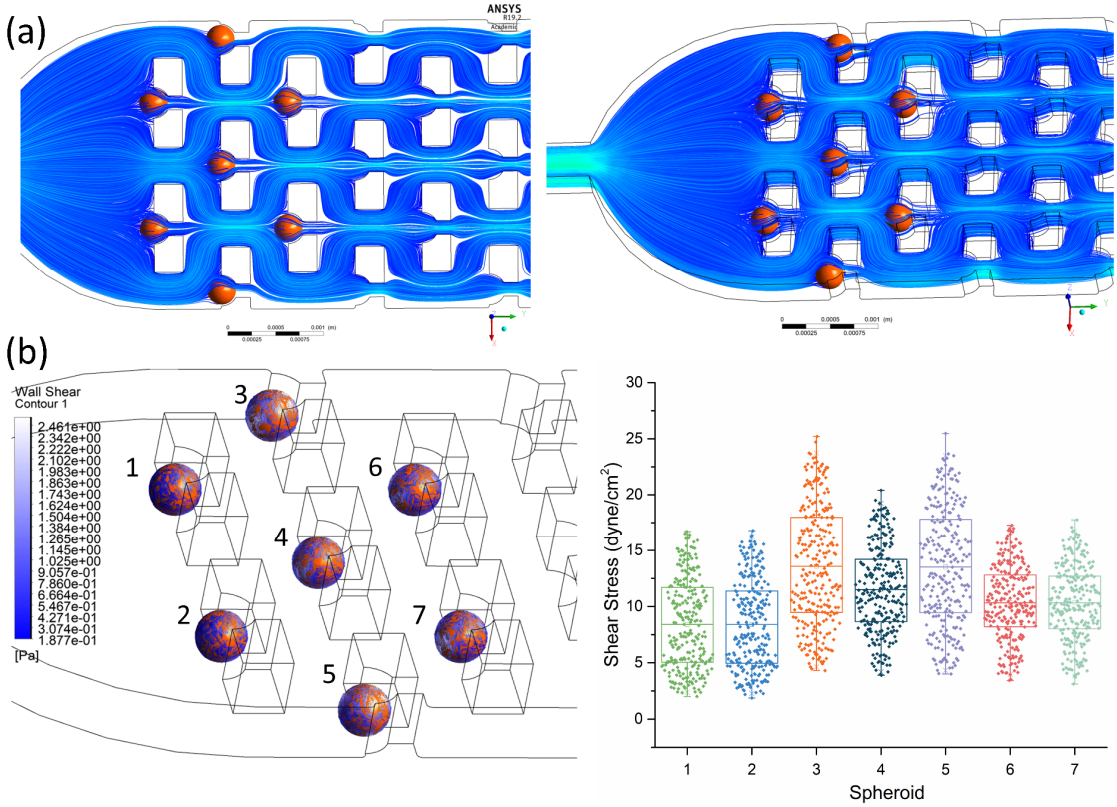

Figure 37 – (a) Visual of fluid streamlines passing through the trap array with 7 spheroids present in the traps. (b) Figure of wall shear stress across the spheroid surfaces. The graph shows a plot of all values for each spheroid, with each point corresponding to mesh facet on the spheroid surface.

Figure 37a shows the flow streamlines produced from a flow rate of 0.8 µL/s. Flow can be seen to be occurring through and around the spheroids (orange) in the traps. The resulting shear stress induced on the spheroid surface can be observed in Figure 37b. Regions of high shear stress are shown in white and low shear stress in blue. The graph shows box plots of the shear stresses across each spheroid, where each data point represents a mesh face on the surface of the spheroid. Values were typically found to vary between 2 – 25 dynes/cm^2 with an average value of 11 ± 2 dynes/cm^2. Due to the trap geometry, spheroids occupying the first row of traps experience slightly lower average shear stresses (8.5 dynes/cm^2) than spheroids across the rest of the traps. Furthermore, spheroids in traps set against the device walls (traps 3 and 5) experience higher shear stresses (13 dynes/cm^2) due to the presence of the wall. Nevertheless, all predicted shear stresses fall well within the range of physiological values (1 - 70 dynes/cm^2) [150].

4.1.4 Spheroid Culture On-chip

Prior to on-chip therapeutic experimentation, it was necessary to observe the growth of spheroids on-chip to ensure the device allowed for the capture and maintenance of spheroid cultures. 10 spheroids were loaded on-chip and 6 successfully trapped within the array. Spheroids were grown underflow for 48 hours with media replaced after 24 hours. Bright-field and dead cell imaging (using NucRed Dead staining) was performed after 8 hours and 48 hours on-chip.

Spheroids were observed to grow into and around the traps across the 48-hour period. Monolayers extending out of the spheroid periphery showed that spheroids had anchored to the bottom of the chip surface. This was confirmed when gentle backflow through the system did not result in spheroids being freed from the traps. However, manually increasing the flow rate by withdrawing on a pipette attached to the inlet, resulted in spheroids dislodging from traps. This showed that intact spheroids could indeed be retrieved off-chip for post-exposure analysis. The dead cell fluorescent stain showed no observable dead cells after 8 hours and very few cells after 48 hours. This further confirmed that this system was suitable for spheroid culture maintenance and therapeutic testing.

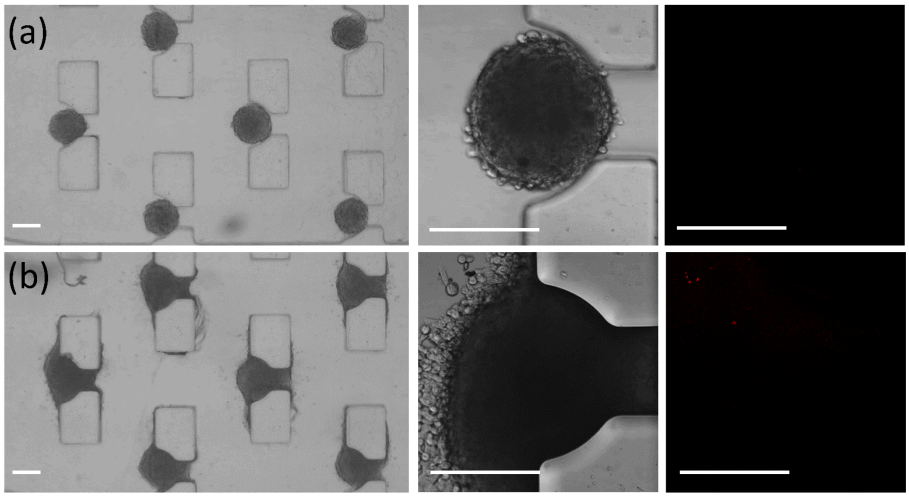

Figure 38 – Brightfield and dead cell fluorescent images of spheroids taken after (a) 8 hours and (b) 48 hours of on-chip culture. All scale bars are 200µm.

4.2 Spheroid Therapeutic Exposures

Once the spheroid trap system was optimised and spheroid cultures successfully maintained for 48 hours, the next step was to treat the on-chip cultures with an anti-cancer therapeutic. The anthracycline drug Doxorubicin (DOX) was chosen to test MB-enhanced drug efficacy. DOX is widely used to treat various types of cancer however, its efficacy is limited by its toxic side effects, primarily cardiomyopathy [5,151]. DOX is therefore an ideal candidate for MB therapy, which seeks to improve drug delivery to the tumour site specifically. It is expected that this localised delivery mechanism may reduce the systemic side effects of drugs or allow for increased efficacy to a point at which lower drug doses may be used.

4.2.1 Off-Chip Dose Response

Prior to spheroid on-chip therapeutic exposures, spheroids were subject to DOX treatments off-chip. This initial investigation off-chip was used to observe the dose-response of both monoculture and coculture spheroids and observe the effect of incorporating fibroblasts into spheroids. As described previously, fibroblasts cultured alongside tumour cells become cancer-associated and secrete increased amounts of ECM proteins. This leads to a denser tumour environment that is more difficult for drugs to penetrate, resulting in decreased drug efficacy.

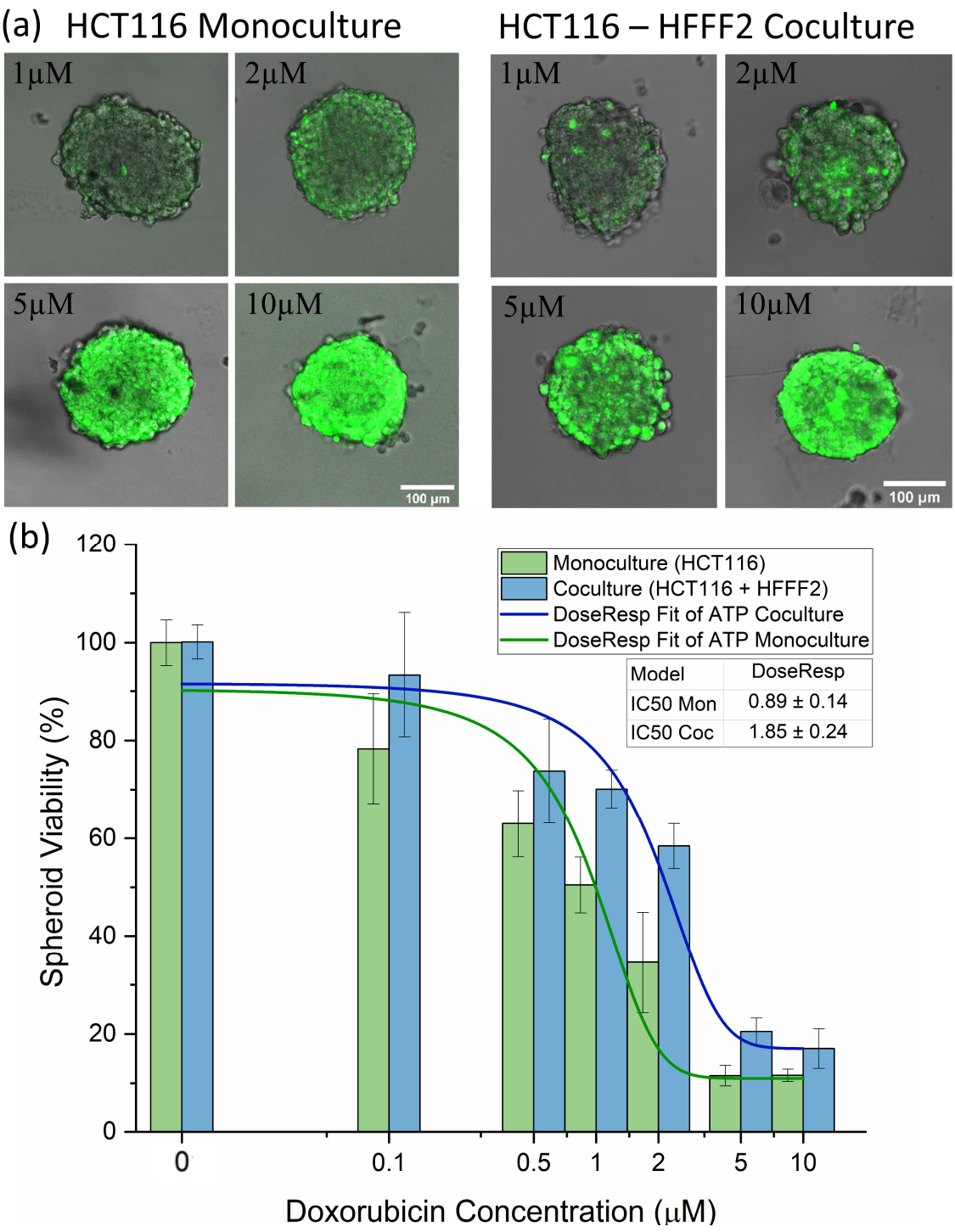

Figure 39 – (a) Bright field and DOX fluorescence (green) overlaying images of both monoculture (HCT116) and coculture (HCT116 – HFFF2) spheroids after 8 hours exposure to DOX concentrations between 1 - 10µM. (b) Monoculture and coculture spheroid viability from exposure to DOX between 0.01 µM and 10 µM – determined using Cell Titer-Glo 3D ATP viability assay.

Spheroids were exposed to DOX and analysed using protocols described throughout section 3.2.4 (page 89). Due to its intrinsic fluorescence, DOX accumulation in spheroids was observed using the confocal fluorescence microscopy settings described in section 3.4.3.1 (page 108). Imaging was performed shortly after DOX removal, 8 hours after the exposure had begun. Figure 39a shows overlaid bright field and DOX fluorescence images taken of both monoculture and co-culture spheroids. The intensity of DOX fluorescence increased with increasing drug concentrations, as expected. By eye, there was no observable difference in the magnitude of DOX accumulation between monoculture (green bars) and coculture (blue bars) spheroids, however, this may be due to the relatively early time point at which the spheroids were imaged.

Spheroid ATP viability assay results, shown in Figure 39b, revealed a typical dose-response curve trend. Luminescence values for each set of spheroids were normalised with respect to control spheroids, which were taken to be 100 % viable. Both monoculture and coculture spheroids initially show no inhibition from exposure to 0.01 μM DOX. Increasing the concentration to 0.1 μM however, found that monoculture spheroid viability was significantly affected, with an average value of (78 ± 11 %). Coculture spheroids were found to have an average viability of (93 ± 12 %), higher than that of monoculture but not statistically significant. Treatment with 10 μM observed minimal viabilities of (11 ± 1 %) and (17 ± 4 %) for monoculture and coculture spheroids, respectively. As expected, coculture spheroids were consistently more resistance to therapeutic treatments, with higher coculture viabilities being observed at every treatment concentration. A dose-response curve was fitted to each dataset and the 50 % inhibitory concentration (IC_{50}) value was determined to be 0.9 ± 0.1 μM and 1.9 ± 0.2 μM for monoculture and coculture spheroids, respectively. The significant differences in IC_{50} values confirm the presence of drug resistance in co-culture spheroids. This indicates that fibroblasts have been successfully incorporated into the tumour cultures, and their phenotypes have been influenced to display pro-tumorigenic properties. This agrees with previous observations throughout literature which have reported increased drug resistance in co-culture spheroids containing fibroblasts [152–154]. Future experiments would therefore only involve the use of HCT116 - HFFF2 co-culture spheroids, as these cultures more accurately recreate aspects of *in vivo* tumours than HCT116 monoculture spheroids.

4.2.2 Free DOX Dose Response

To demonstrate the suitability of the microfluidic device for the investigation of microbubble (MB) enhanced drug delivery, a proof-of-principle exposure of trapped spheroids to free DOX was performed. This also served as an initial experiment to determine a suitable DOX concentration for future MB co-delivery experiments. Spheroids were loaded on-chip and exposed to DOX as described throughout sections 3.2.5 and 3.4.2 (page 107). The same 0 – 10 μM range of DOX concentrations were used as in the previous off-chip exposures, allowing for comparison of IC_{50} values. 185 spheroids were successfully loaded into 38 chips across a series of separate experiments. Spheroids were exposed to DOX for 8 hours then allowed to grow on-chip in fresh media for a further 48 hours, at which point fluorescent imaging and viability assays were performed.

Figure 40 shows the bright field, DOX and dead cell fluorescent images taken 48 hours after exposure of DOX. Relatively low levels of DOX were observed throughout the spheroids exposed to 1 μM DOX and few dead cells were found around spheroid periphery. This DOX concentration did not appear to affect spheroid structural integrity, shown by the consistently dense outer layers of the spheroid. Bright-field images of spheroid exposed to 5 μM DOX however, revealed that degradation of the outer layers of the spheroid and a clear reduction in spheroid structural integrity. Dead cell fluorescence confirmed mass cell death had occurred within these layers. High levels of DOX emission were observed in the spheroid core, which still appeared intact and alive. Exposure to 7.5 μM DOX caused further degradation of the spheroid outer layers. The mass cell death resulted in the loss of spheroid integrity, which resulted in these layers being washed away underflow as the spheroid was unable to maintain its structure. The spheroid core remaining in the trap also showed significant dead cell emission, suggesting the spheroid was minimally viable.

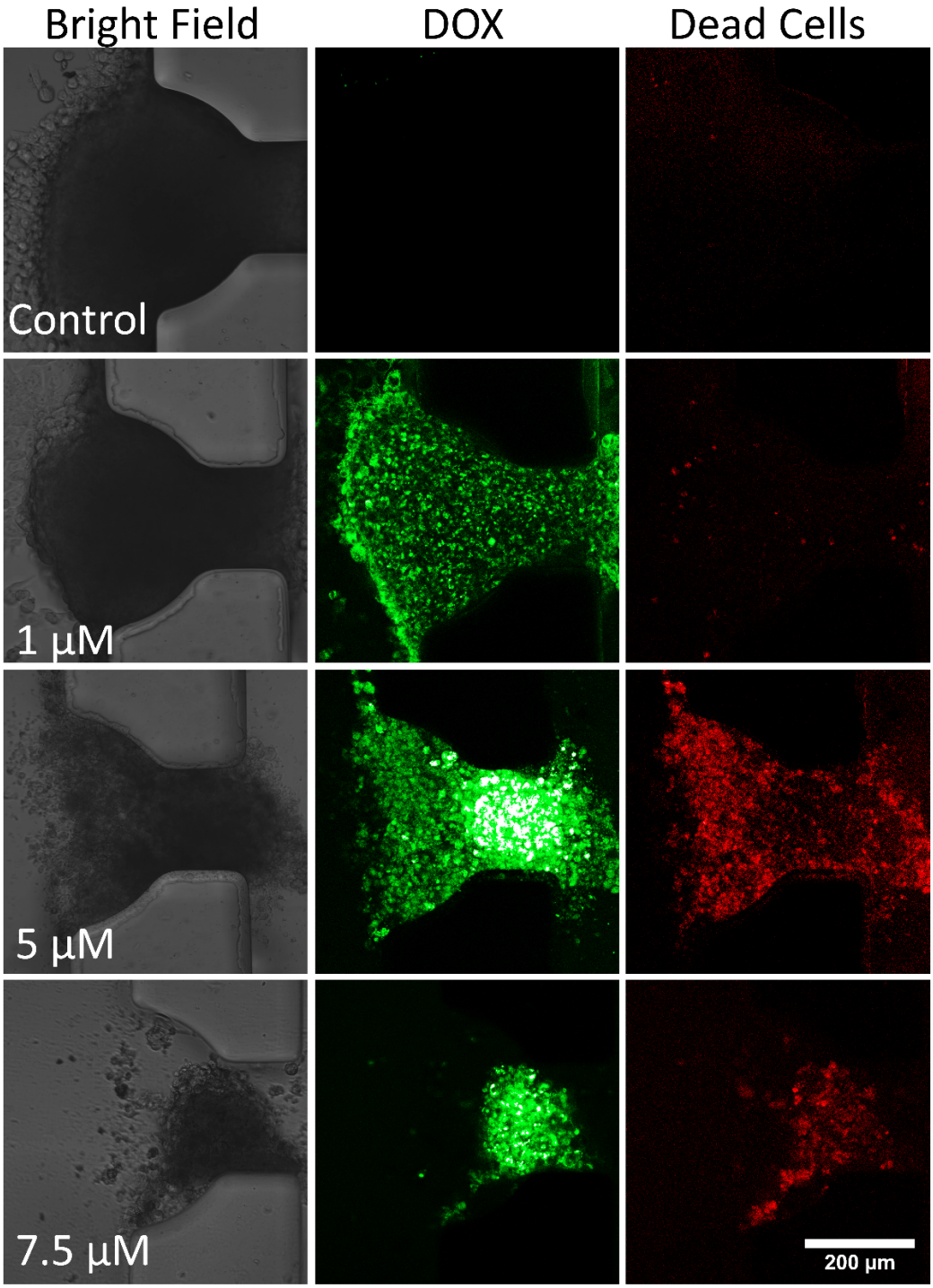

Figure 40 – Bright field, doxorubicin (green) and dead cell (red) fluorescence emission from spheroids 48 h post exposure to 0 (control), 1, 5, and 7.5 µm DOX. For increasing concentrations of DOX, the structural integrity of the spheroid decreases and an increase in dead cells can be observed (red).

After imaging was performed, spheroids were retrieved off-chip for viability assessment by attaching a pipette to the inlet reservoir and withdrawing the liquid. The lack of adhesion between the spheroids and PDMS allowed spheroids to be easily dislodged from the traps using backflow. To ensure ATP measurements were accurate, all material from the chip was collected, including the cell debris observed around many of the minimally viable spheroids. Each chip was checked to ensure it was clear of cells before the ATP assay was performed.

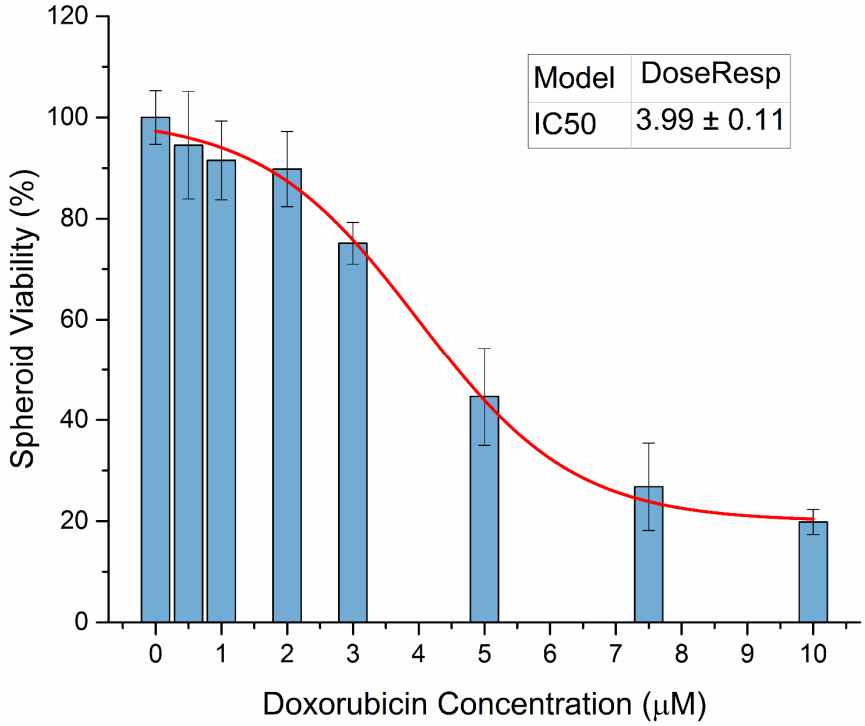

Figure 41 – Spheroid viability with increasing concentrations of DOX, measured 48 hours post exposure with Cell Titer-Glo 3D cell viability assay (n = 185). As with the previous off-chip experiment (figure 42), a typical dose response trend was again observed, with a steep drop in viability occuring at concentrations greater than 2 µM

Figure 41 shows a graph of decreasing spheroid viability with increasing DOX concentration. Results showed that 1 µM DOX had minimal effect on spheroids viability (91 ± 8 %), which agreed with imaging observations. 5 µM DOX was found to have a greater effect (45 ± 9 %), whilst 7.5 µM DOX reduced viability substantially more (27 ± 9 %). Finally, the highest 10 µM DOX dose resulted in a minimally viable spheroid (20 ± 2 %). Results for spheroid viability showed a typical dose-response trend, with low

doses having minimal effect up until a threshold concentration which causes significant reductions in viability. The steep decline in viability then plateaus when higher doses of drug fail to have an additional effect. In this case, the remaining viable cells were likely to be quiescent cells which show resistance to many therapeutics due to their low metabolic activity. A dose-response curve fitted revealed an IC_{50} value of 4 ± 0.1 µM. This value is significantly higher than the 1.9 ± 0.2 µM IC_{50} value for coculture spheroids in off-chip experiments. Several intrinsic differences exist between the two types of experiments which may contribute to these differences, such as the manual washing steps required for off-chip experiments and the relatively lower volumes of media available in each well. Another potential factor affecting spheroid viability is the influence of shear stress and flow on-chip. Perfusion of media through the chip provides nutrients and removes waste products, leading to differences in the rates of spheroid growth on and off-chip. From the on-chip IC_{50} value, it was decided that a concentration of 3 µM would be used for future MB-codelivery experiments. This dosage resulted in a moderate reduction in spheroids viability (75 ± 4 %) when administered as free drug alone, allowing for further reductions in viability to be observed when enhanced with MBs.

Overall, this initial set of on-chip experiments showed that high numbers of spheroids could be consistently trapped on-chip (average occupancy of 6 ± 2 spheroids). The stand-alone design of the system, with independent reservoirs for each chip, allowed for multiple chips to be run in parallel with varying exposure conditions. Agreements between imaging observations and ATP assay results also gave confidence in this systems ability to produce reliable, consistent results.

4.2.3 Ultrasound and Microbubble Spheroid Exposure

To determine the effects of co-delivering DOX with MBs, it was first necessary to observe the effect of the US trigger (+ US alone), MBs (without US) and MB + US exposures on spheroid viability. Furthermore, the incorporation of Atto 488 fluorescent lipids into the MBs, allowed for observation of the interaction between MBs and spheroids. Observation of lipid deposition and associated cell death would be an indicator that MB-induced sonoporation was occurring. An increase in lipid transfer from MBs after destruction would also suggest that this effect would facilitate the uptake of DOX.

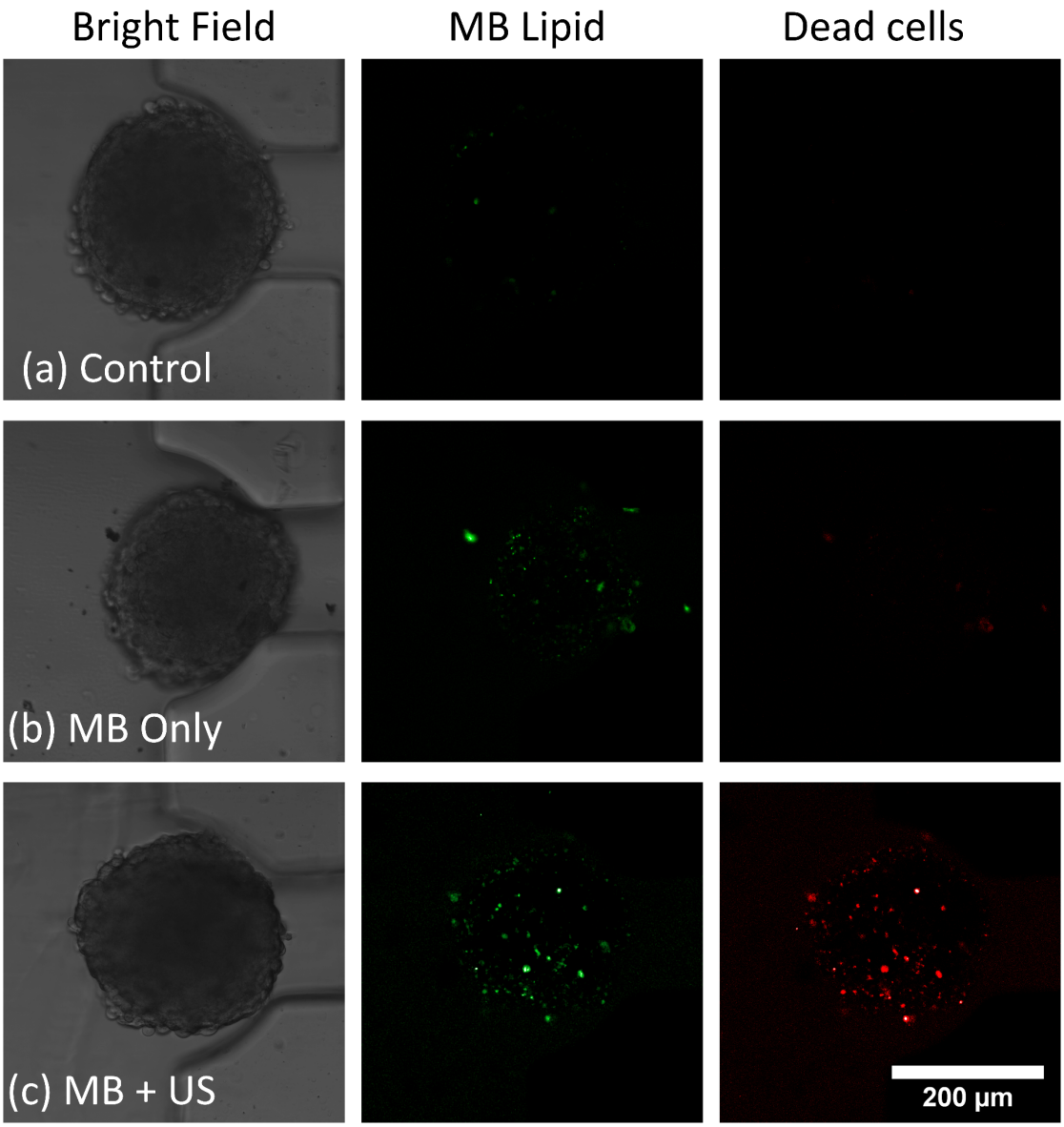

Figure 43 – Bright field, Atto 488 lipid (green) and dead cell (red) fluorescent emissions from (a) control, (b) MB only and, (c) MB + US spheroids 8 hours post-exposure. Lipid deposition was observed in both MB only and MB + US conditions however dead cell emission was only observed when US was used, giving evidence that irreversible sonopoation was occuring.

Spheroids were loaded on-chip and exposed to US only, MB only and MB + US, using methods outlined throughout section 3.4.2 (page 107). As opposed to the previous section, imaging was performed 8 hours after insonation - so that any initial cell death caused by the US burst could be observed. Figure 43 shows images taken of control (a), MB only (b) and MB + US (c) spheroids trapped on-chip. As expected, no fluorescent

lipid or dead cell emission was observed in control spheroids. Spheroids exposed to MB only showed small amounts of fluorescent lipid (green) scattered across the surface however, no dead cell emission (red) was observed to be correlated locally with lipid deposition. This suggests that lipids are passively transferred from MBs to spheroids as they flow across the surface. MBs may also become trapped between cells on the spheroid surface resulting in the gas slowly dissolving into the solution, leaving fluorescent lipid adhered to the surface. Spheroids exposed to MB + US showed increased amounts of lipid fluorescence compared with MB only spheroids. Furthermore, dead cell emission in these spheroids showed direct overlap with lipid locations. This correlation suggested that MB destruction with US resulted in irreversible sonoporation, in which cell death occurs as a result of pore formation in cell membranes. Figure 44 shows images taken of spheroids an additional 48 hours after being exposed to MB + US. Imaging revealed that fluorescent lipid (green) could still be observed across the spheroid surface. Showing that fluorescent lipids are retained by the spheroid cells which again supported the theory that MBs would facilitate the uptake of DOX.

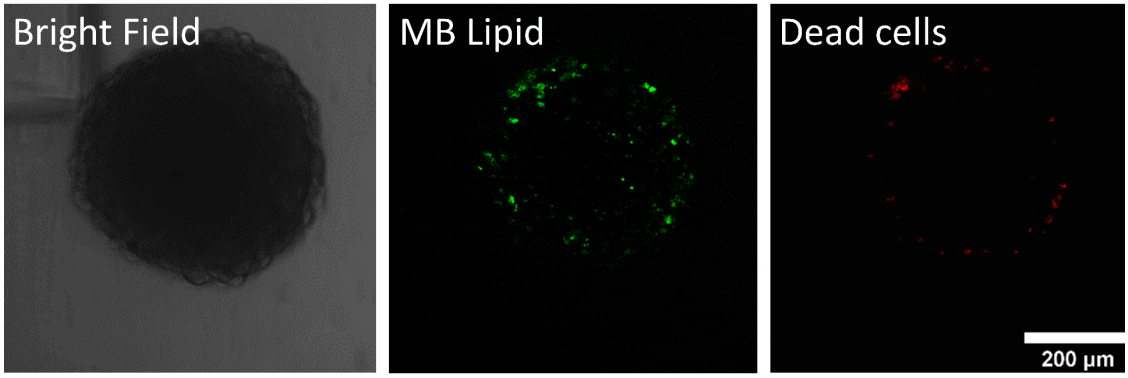

Figure 44 - Bright field, MB lipis (Green Atto 488) and dead cell (red) imaging of MB + US spheroids 48 hours after insonation showing MB lipid is retained by the spheroids after MB + US exposures.

Cell death emission after 48 hours was still visible in some regions where lipids remained, however, emission was greatly reduced compared to images taken 8 hours after exposure. The dead cells observed here are likely remnants of cells killed by the initial MB-induced sonoporation. This indicates that MB + US exposure does not cause any persisting adverse effects on the spheroids.

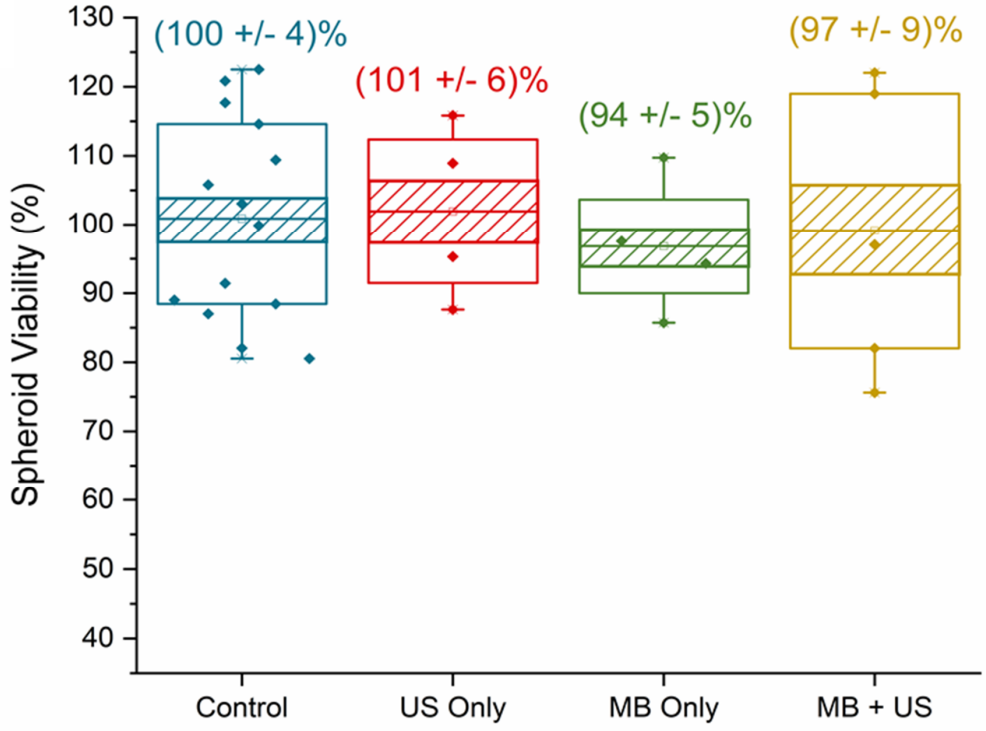

Figure 45- Boxplot of spheroid viabilities 48 hours post exposure to Control (n = 60), US only (n = 24), MB only (n = 12) and MB + US (n = 26). Each point represents a single chip containing on average 5 ± 2 spheroids. Annotated values show mean ± S.E and hashed regions show the 95 % confidence intervals around the mean.

Figure 45 shows ATP spheroid viability measurements for control, US only, MB only and, MB + US control experiments. Here, percentage viability is calculated by taking the average ATP luminescence values of control spheroids as 100 % viable. This results in some larger than average spheroids displaying viabilities above 100 %. Assessment of spheroid viability revealed that all exposure conditions did not have any significant effect on spheroid viability. Both US only (101 ± 6 %) and MB only (94 ± 5 %) values all fell within the range of values observed in control experiments. All but one MB + US chip viability value also fell within this range however, the overall average viability value (97 ± 9 %) agreed with control values. This slight variation in viability from MB + US exposures can be attributed to the initial cell death caused by sonoporation. Calculation of the 95 % confidence interval for each condition gave values of ± 3 %, ± 4 %, ± 3 % and ± 7 % for control, US only, MB only and MB + US exposures, respectively. All of these values overlap with the average control viability value (with error), meaning there

is a 95 % probability that all viability values are contained with the range of control values. This lack of statistical significance between results was confirmed further by performing a Mann-Whitney p-test, which found no statistical significance between results. Overall, this series of control experiments demonstrated that MB, US, or a combination of the two did not have any substantial effect on spheroid viability. It can be confidently concluded that any potential enhanced drug efficacy can be attributed to MBs facilitating drug delivery to the tumour spheroids. Furthermore, observations throughout this set of experiments showed strong evidence that MB-induced sonoporation was occurring and resulted in cell death in many cases. Experimentation was then able to move onto the co-delivery of free DOX with MBs, and the effects of MB-induced sonoporation on drug delivery to spheroids investigated.

4.2.4 Co-delivery of Free DOX, Microbubbles and Ultrasound

The effectiveness of US triggered MBs as drug delivery enhancers was investigated by co-delivering 3 µM DOX with MBs to spheroids. This series of experiments was performed using the same experimental setup and timeframe as previous experiments, which is described in detail throughout section 3.4 (page 105). Along with the complete therapeutic combination of DOX + MB + US, a DOX + US (without MB) control exposure was included. The purpose of this was to ensure that any increased drug efficacy observed could conclusively be attributed to the effect of MB-induced sonoporation. Several synergistic effects of delivering therapeutics alongside US have been previously observed, and the mechanisms behind the increased drug efficacy have been described throughout section 1.4.2 (page 47).

Figure 46 shows the bright field, DOX and dead cell emission images taken 48 hours post-exposure to each condition. 3 µM DOX alone shows results comparable to the low dose DOX exposures shown in Figure 40, with low levels of DOX observed to have accumulated across the spheroid and very few dead cells observed around the spheroid periphery. In contrast to this, significantly increased levels of drug accumulation and cell death were observed with DOX + MB + US. This was accompanied by a decrease in spheroid integrity and density, observations which were also made with higher DOX doses in Figure 40. Interestingly, some synergistic effects of delivering DOX with US were also observed. Increased drug accumulation and cell death were induced with the

addition of US however, this did not appear to be to the same extent as the full exposure condition. The same can be said for spheroid integrity, with bright field imaging showing some degradation of the outer layers, corresponding to dead cell regions. Spheroids were once again retrieved off-chip after 48 hours for viability analysis.

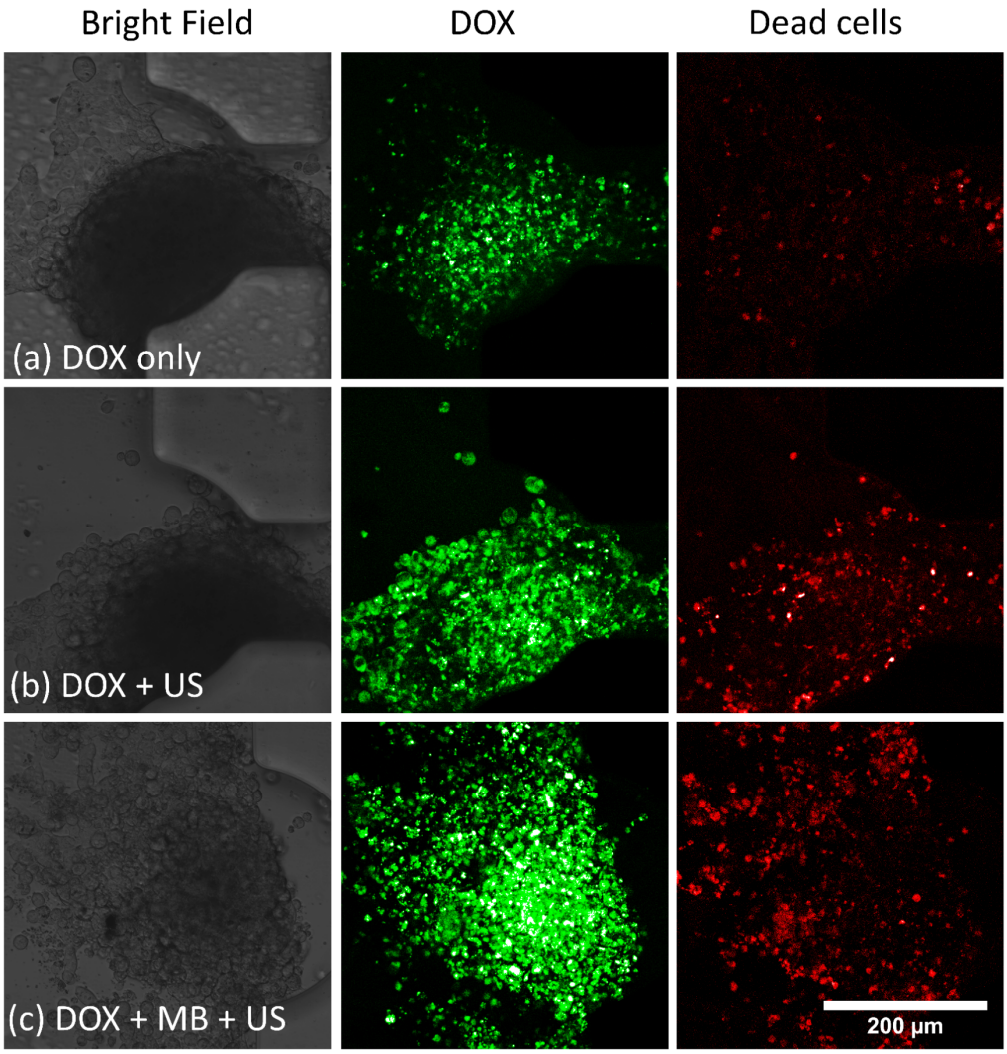

Figure 46 - Bright field, DOX (green) and dead cell (red) fluorescent emission from spheroids 48 hours post exposure to (a) 3 µM DOX only, (b)) 3 µM DOX with US and, (c)) 3 µM DOX with MB + US. A trend in increasing DOX accumulation and dead cell emission can be observed from figure panes a – c.

Figure 47 shows the boxplot of spheroid viability for each exposure condition. Results show that the combination of 3 µM DOX + US reduced spheroid viability to (61 ± 1 %), an approximate 15 % decrease compared to 3 µM DOX alone. DOX + MB + US decreased spheroid viability further yet, showing an average value of (48 ± 2 %).

Calculation of 95 % confidence interval values gave ± 4 %, ± 1 %, ± 2 % for 3 µM DOX, 3 µM DOX + US and 3 µM DOX + MB + US, respectively. Performing a Mann-Whitney p-test (section 3.4.3.3, page 109) revealed that p-values were < 0.0001 (****), further illustrating the statistical significance between the different exposure conditions.

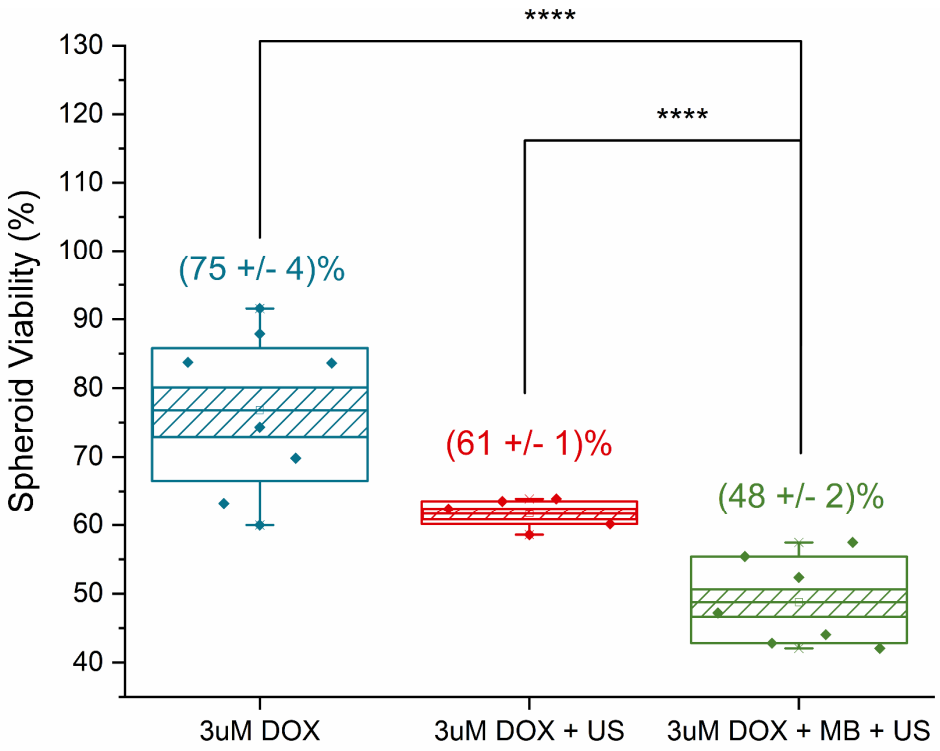

Figure 47 – Spheroid viability 48 hours post exposure to 3 µM DOX only (n = 39), with US (n = 26) and with MB + US (n = 31). Each point represents a single chip containing on average 5 ± 2 spheroids. Annotated values show mean ± S.E and hashed regions show the 95 % confidence intervals around the mean.

Using the dose-response equation used to fit the curve in Figure 41, the free DOX dose required to reduce spheroid viability to 48 % was calculated to be approximately 4.8 µM. This shows that the use of MB + US increases drug efficacy by approximately 60 %. A very similar viability value of 45 ± 9 % was found with 5 µM DOX exposure, which also showed comparable amounts of spheroid degradation, drug accumulation and cell death. Together these imaging observations and viability values support the supposition that the use of MB-enhanced drug delivery can be used to achieve an equivalent therapeutic effect with a lower drug dose – offering a potential means of reducing the systemic DOX side effects associated with high dose treatments.

4.2.5 Co-delivery of Liposomal DOX and Drug Loaded Microbubbles

It was previously shown that the efficacy of free DOX could be significantly improved when co-delivered with MB + US. However, in a clinical setting, the side effects of free DOX often present too many limitations to be a viable option. Encapsulation of DOX inside LSs offers a solution to this issue. The limited leakage of DOX from LS reduces the systemic drug dose and, in turn, the associated systemic side effects. As a result, liposomal DOX has been observed to have an improved toxicity profile and reduced cardiac effects compared to its free counterpart. DOX-LSs also offer an additional opportunity for MB-enhanced drug delivery. DOX-LSs can be conjugated to MBs which, through the use of a local US trigger, can be used to deliver DOX-LSs locally to the tumour site – further reducing systemic drug doses. Early 2D monolayer cell studies into this drug delivery mechanism have shown promising results however, there is currently a need for more testing of MB-mediated DOX-LS delivery on representative *in vitro* models.

The following set of experiments investigated the effects of delivering DOX-LS conjugated to MBs in complexes referred to as drug-loaded microbubbles (DLMBs). Figure 48 depicts the three liposomal configurations spheroids were exposed to throughout this study. DLMB treatment was compared with DOX-LS and a co-delivery of unconjugated DOX-LS and MBs. This also allowed the effect of conjugation on drug delivery to be investigated and both exposures compared to standard LS treatment. In addition to this, the effect of multiple US exposures with DLMBs was investigated. The DLMB solution loaded on-chip can fill the volume of the spheroid chamber multiple times, therefore a single US burst is not sufficient in bursting all DLMBs. It was therefore theorised that multiple US treatments would increase the delivery of liposomes to spheroids due to their direct conjugation to the outside of the MBs. The attachment of LS to the surface of MBs has been shown to affect the acoustic properties of the MBs, primarily increasing the acoustic threshold for MBs oscillations [155]. However, this effect has been shownto be neglible for high acoustic pressures (> 570 KPa) such as those used throughout this study [156].

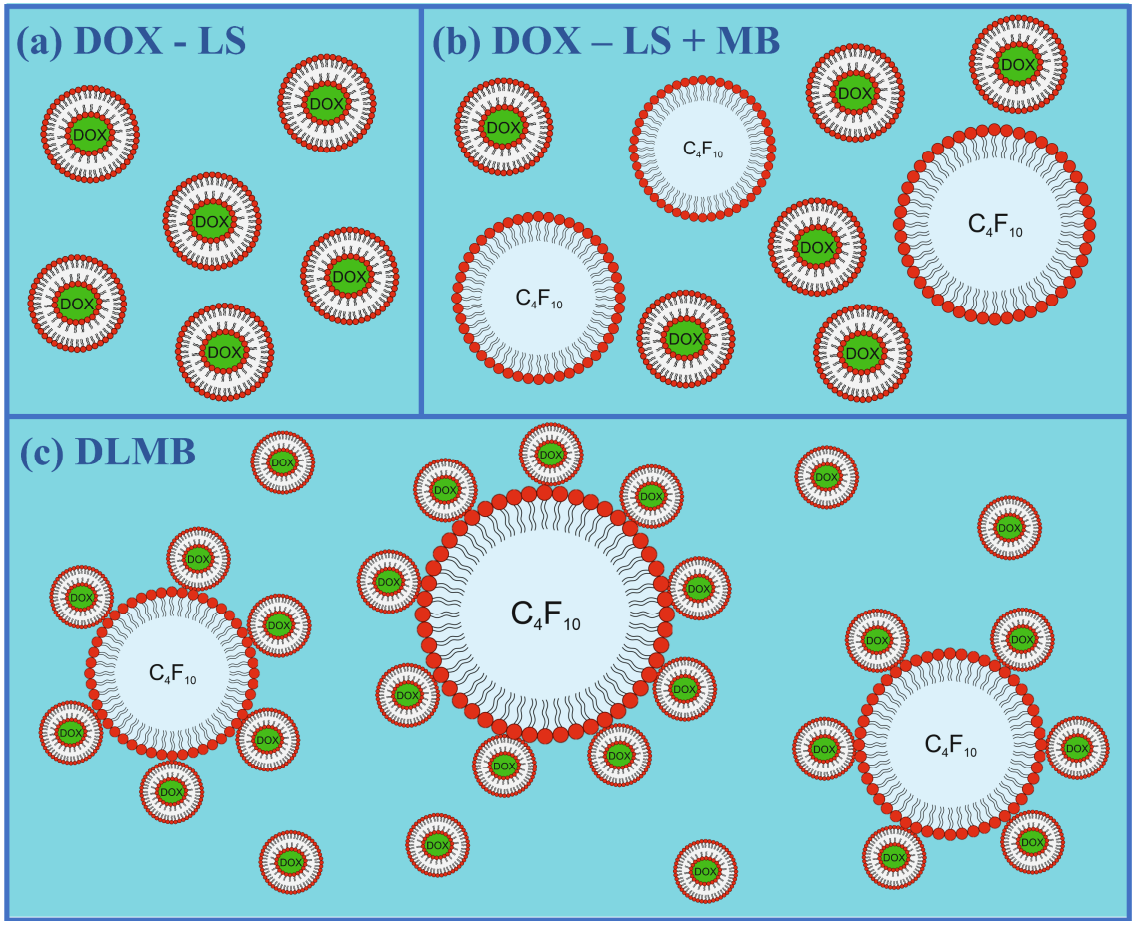

Figure 48 - A series of diagrams depicting the three DOX-LS therapeutic exposures: (a) DOX-LS alone. (b) DOX-LS + MB co-delivery without conjugation. (c) Drug-loaded MBs (DLMBs) consisting of DOX-LS conjugated to the MB surface using biotin-neutravidin binding (DOX-LS and MB images are not to scale or ratio).

4.2.5.1 DOX-Liposome Co-delivery with Microbubbles

DOX-LSs were produced and characterised using methods described in detail throughout section 3.3.6 (page 101). For all experiments using DOX-LS, the total DOX dose was equated to the 3 μM free DOX dose used in the previous set of experiments by characterising the amount of DOX encapsulated in each liposome (section 3.3.6.3, page 102). This allowed for comparison between drug delivery methods. To first observe whether the co-delivery of unconjugated MB and DOX-LS facilitated drug delivery, spheroids were exposed to DOX-LS and DOX-LS + MB + US. For MB exposures, both DOX-LS and MBs were prepared to twice the desired concentration and mixed in a 1:1

ratio. As before, drug exposure occurred for 8 hours then fresh media was added, and spheroids were allowed to grow on-chip for a further 48 hours before imaging and assaying.

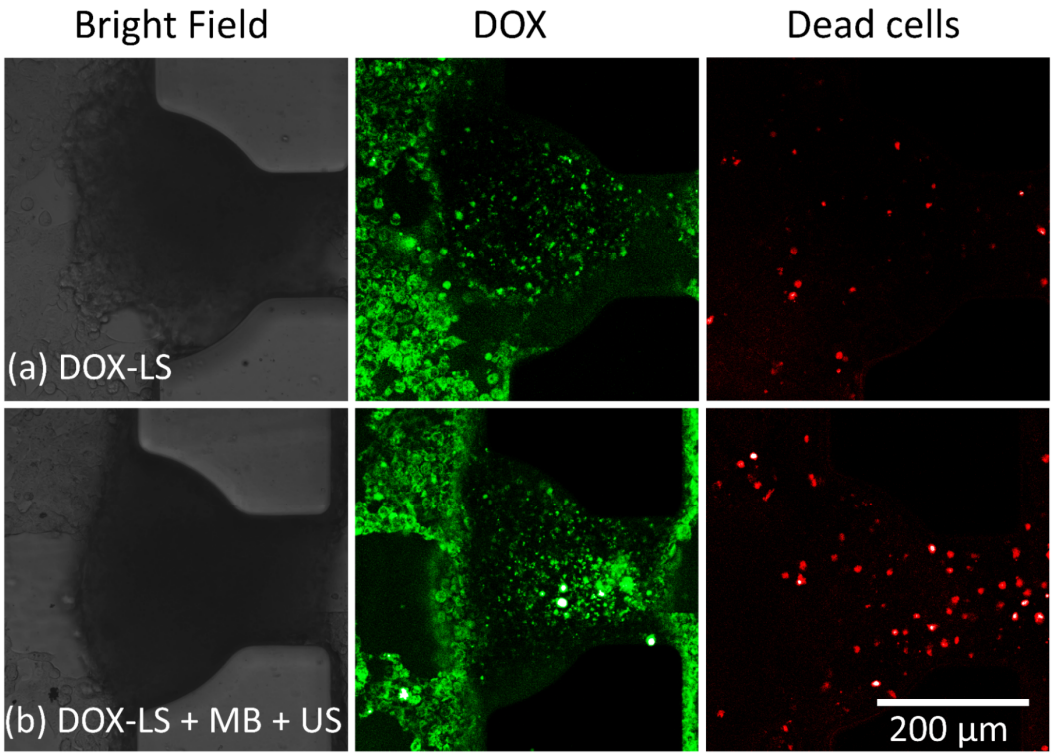

Figure 49 - Bright field, DOX (green) and dead cell (red) fluorescent emission from spheroids 48 hours post exposure to (a) DOX-LS and (b) DOX-LS + MB + US. Imaging revealed similar rates of DOX accumulation in the outer layers of spheroids, suggesting DOX-LS were not able to penetrate far into the tumours.

Figure 49 shows the bright field, DOX and dead cell fluorescence images taken of spheroids 48 hours post-exposure to (a) DOX-LS and (b) DOX-LS + MB + US. Observations found spheroid morphology was consistent, drug accumulation appeared of a similar magnitude and distribution, and dead cell levels were similar on average. In contrast to free DOX exposures where the drug was found to accumulate across the spheroid, DOX from LS was only found in the outer layers of the spheroid. Concentrations in these regions were observed to be significantly higher than in free drug exposures. These observations suggest that DOX-LS are not able to penetrate deep into the tumour structure, and instead release high concentrations of drug to the outer regions. Spheroids were retrieved off-chip and the ATP assay was performed.

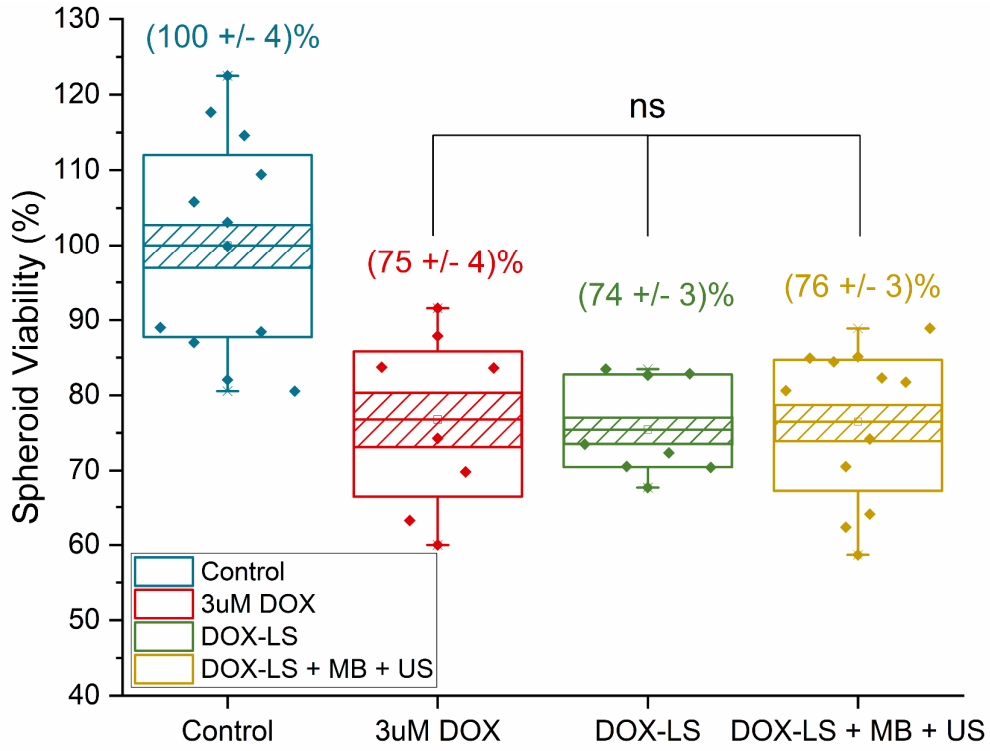

Figure 50 - Spheroid viability 48 hours post exposure to control (n = 66), 3 µM DOX (n = 39), DOX-LS (n = 38) and DOX-LS + MB + US (n = 66). Each point represents a single chip containing on average 5 ± 2 spheroids. Annotated values show mean ± S.E and hashed regions show the 95 % confidence intervals around the mean.

Figure 50 shows DOX-LS and DOX-LS + MB + US spheroid viabilities alongside previously shown control and 3 µM DOX values. Results found near-identical viability values of (74 ± 3 %) and (76 ± 3 %) for DOX-LS and DOX-LS + MB + US exposures, respectively. These values were also identical to free 3 µM DOX viability of (75 ± 4 %). Calculation of 95 % confidence intervals found values of ± 2 % for both DOX-LS exposures. Together imaging and assay results show that the co-delivery of DOX-LS with MB + US does not appear to facilitate increased uptake of LSs into the spheroid. Drug efficacy is unchanged with the addition of MB + US and spheroid viability remains the same. This is somewhat counterintuitive, as the micron-sized pores created in cell membranes from MB cavitation could feasibly allow for the increased passage of nanoscale DOX-LS into cells. Furthermore, sonoporation should theroetically also allow increased uptake of therapeutics into the interellular spaces filled with ECM. This could also faciltiate increased DOX-LS efficacy as DOX could diffuse from the ECM into the

cell cytoplasm. These unexpected results do, however, agree with results observed by Roovers et al. which also found a lack of increased DOX-LS efficacy when co-delivered with MB + US [83]. LSs in their system, however, were delivered under static conditions to spheroids significantly smaller (< 200 µm) than those used in this system.

In addition to this, both treatments with DOX-LS appeared to have the same efficacy as the equivalent free DOX dose. This largely disagrees with previous studies which often show free DOX having a greater effect than DOX-LS. The apparent increase in liposomal DOX efficacy observed in this study could be attributed to increased mass transport of DOX-LS into the outer layers of spheroids. Research from Kang et al. found that the uptake of polystyrene nanospheres into various tumour cells was increased 50 % on average when cells were subject to shear stress of 0.5 dyne/cm^2 [157,158]. Shear stresses in this system were modelled to be over an order of magnitude higher (approximately 11 ± 2 dyne/cm^2). It is unknown how cells will respond to increased shear stress, however; it is likely that similar increased mass transport effects are still occurring. Shear stress has also been found to increase the effectiveness of liposomal DOX compared to static delivery, although this study also demonstrated that free DOX reduced cell viability more than that of DOX-LS under the same conditions [159]. Another potential explanation for the apparent increase in DOX-LS efficacy is the method by which the drug is delivered on-chip. A total dose of DOX-LS equivalent to the 2mL, 3 µM free DOX dose was initially loaded on-chip in a 30 µL volume, followed by 2mL of media. The initial local DOX-LS concentration will therefore be considerably higher and may have allowed for increased instantaneous accumulation.

4.2.5.2 Delivery of Drug-loaded Microbubbles

Experiments then progressed into investigating the efficacy of delivering DLMBs to spheroids. The effect of three increasing US exposure conditions was tested, using 1, 3 and 5 US bursts. 60 seconds was given between US bursts to allow for DLMBs to repopulate the chamber. Section 3.3.7 (page 104) details the production and characterisation of DLMBs, which use biotinylated lipids and streptavidin to conjugate DOX-LS to the outside of MBs. The ratio of MBs: DOX-LS used for DLMBs was kept consistent with the ratios used in previous DOX-LS + MB + US experiments, meaning the only difference for single US exposures was the conjugation of particles.

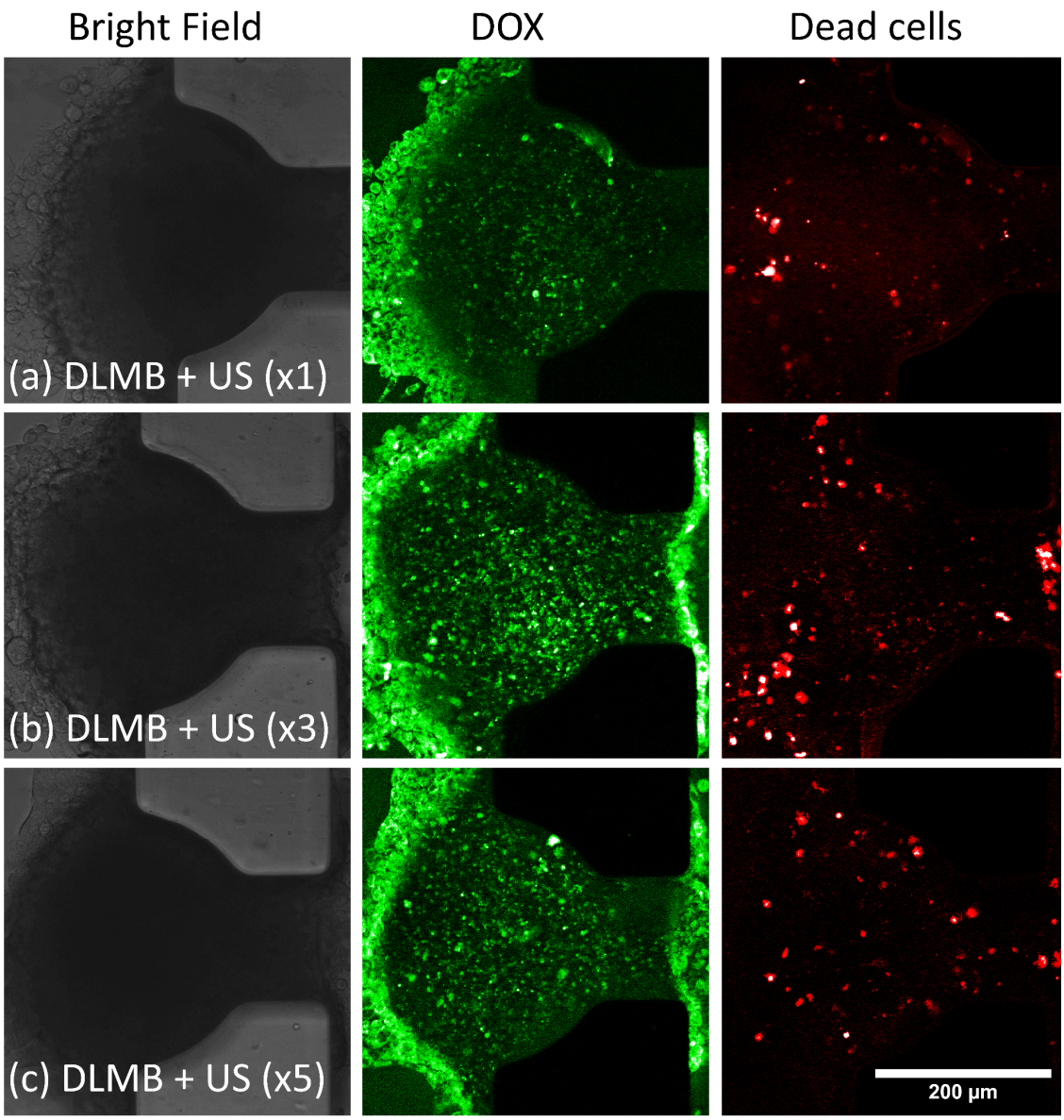

Figure 51 - Bright field, DOX (gree) and dead cell (red) fluorescent emission from spheroids 48 hours post exposure to DLMB + US (a) x1, (b) x3, and (c) x5. Imaging did not appear to show any significant differences in spheroid integrity, DOX accumulation, or number of dead cells between the three exposure conditions. DOX was again observed to accumulate primarily in the outer layers of the spheroids, suggesting minimal drug penetration had occurred.

Figure 51 shows confocal microscopy images taken of spheroids 48 hours post-treatment. Bright-field images showed no observable differences in morphology across the three treatments. DOX imaging showed high levels of drug accumulation in the outer layers of the spheroids. The same distribution of the drug was observed with previous DOX-LS exposures however, more drug appears to have accumulated with the use of DLMBs. Again, no trend in drug accumulation was observed with increasing US exposure. Finally, imaging of dead cell emission revealed significant amounts of dead cells across the spheroid surfaces in all cases. Higher levels of emission were observed in spheroids exposed to US x3 and x5 compared to the single US exposure case however, the overall differences did not appear significant.

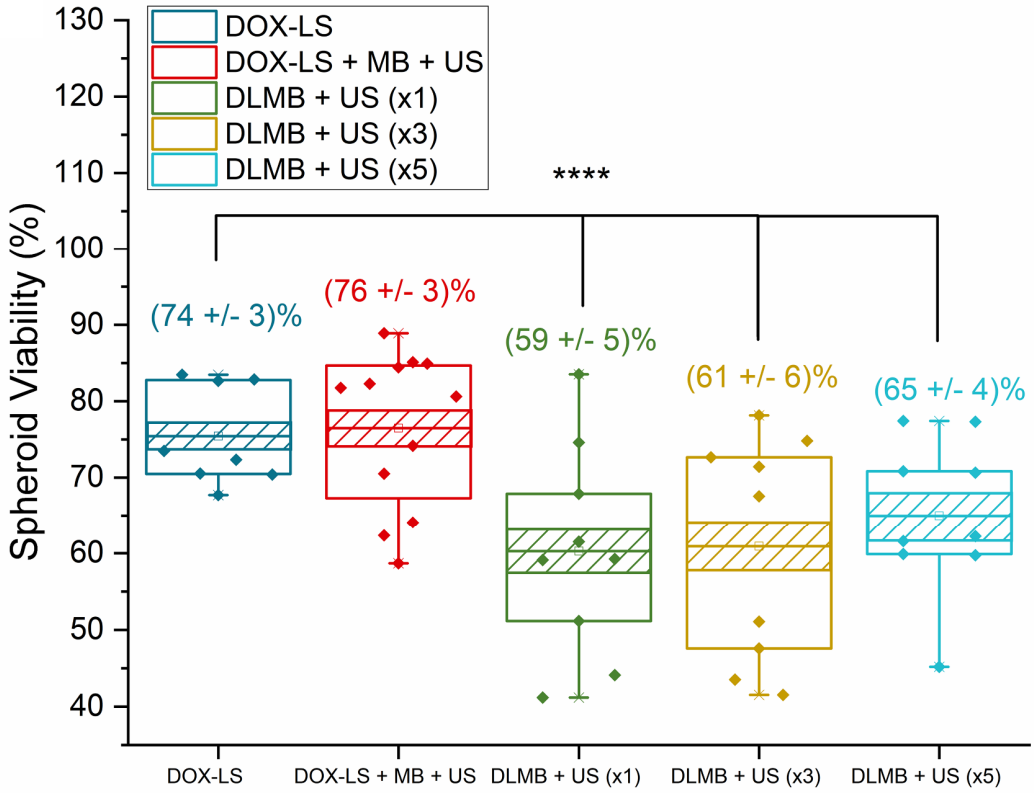

Figure 52 - Spheroid viability 48 hours post exposure to DOX-LS (n = 38), DOX-LS + MB + US (n = 66), DLMB + US x1 (n = 73), DLMB x3 (n = 70), and DLMB x5 (n = 71). Each point represents a single chip containing on average 7 ± 2 spheroids. Annotated values show mean ± S.E and hashed regions show the 95 % confidence intervals around the mean.

Spheroid viability values for all DLMB and DOX-LS exposures are shown in Figure 52. DLMB + US values were found to be (59 ± 5 %), (61 ± 6 %) and (65 ± 4 %) for x1, x3, and x5 US exposures, respectively. Calculation of 95 % confidence intervals found values of ± 3 %, ± 3 % and ± 2 % for respective US exposures. Together these results show no substantial difference from increasing numbers of US exposures. However, a comparison between DOX-LS only and DLMB + US viability values show, on average, DLMBs reduce spheroid viability an additional 15 % compared to DOX-LS. This agrees with imaging observations that saw increased drug accumulation in DLMB + US spheroids. Compared to previous viability results, spheroids exposed to DLMBs were found to have a wide range of values – minimum value of 43 %, maximum of 82 %. This suggests that there is either varying numbers of DOX-LS being delivered to the spheroids or, varying amounts of release occurring from DOX-LS. Allowing a longer period of time between drug exposure and analysis of viability may reduce the spread in data as more complete DOX release from DOX-LS occurs. This is providing that similar numbers of DOX-LS are delivered to each set of spheroids. A longer incubation period after drug exposure would also allow for the effects of MB-enhanced DOX-LS delivery to be better observed, as the delayed-release mechanism from LS does not appear to allow for DOX to take complete effect.

Overall, results found that the number of US exposures did not appear to affect DLMB efficacy. It is suggested that the outer layer of cells on the spheroid surface become saturated with DOX-LS after the first US exposure, rendering any further exposures relatively ineffective as more DOX-LS are delivered to cells already containing cytotoxic numbers of DOX-LS. Perhaps a more effective treatment regime could use repeat exposures with longer time intervals. This could allow time for the initial DOX-LS exposure to take effect and cause outer layer cell death. Subsequent exposures would then target the remaining healthy cells revealed as the outer layer cells die. On the contrary, more DOX-LS may have been delivered with subsequent US pulses, but the effects of increased DOX-LS accumulation were not apparent over this relatively short incubation period. Increased incubation time before analysis could again provide more information about the effects of subsequent US exposures.

Imaging of drug accumulation in all DOX-LS containing experiments found that DOX was primarily localised to the outer layers of spheroid cells. What is most interesting about this observation, is the fact that the cells containing large amounts of DOX were not present in the spheroid at the time of treatment. These outer layer cells imaged 48 hours after treatment were observed to grow within the first 24 hours and were not present in the spheroid at the time of treatment. It is suggested that the initial slow release kinetics of DOX from the LS allows for cells to continue to divide even after the initial DLMB treatment, as the early stage DOX concentrations have not yet reached cytotoxic levels. As more DOX is released from LS, concentrations become significant enough to cause cell death and decrease spheroid viability. Release of DOX from Doxil and similar DOX-LS under physiological conditions has previously been reported to be very slow, showing only 5 % release over 24 hours [160]. Seynhave et al. studied the intracellular release of DOX from Doxil LS, comparing results with free DOX treatments. Measuring the amount of DOX within cells 24 hours after treatment found a significantly lower amount from cells exposed to Doxil, again indicating minimal DOX release across this time [161]. Similar observations were also made by Roovers et al. in a recent MB spheroid paper, in which DOX-LS were found to release little DOX 72 hours after MB destruction [83].

Contrary to these observations, spheroids exposed to DOX-LS throughout this study had growth inhibited substantially. Viability results, along with imaging observations, suggest that significant amounts of DOX was being released from LS throughout the 48-hour period. A potential mechanism for this release could be the presence of ammonia at the tumour spheroid site. Ammonia is produced by tumour cells by glutaminolysis, the metabolic process which tumour cells often favour over the normal glycolytic pathway in order to meet cell energy requirements [162]. A recent study investigated drug release from Doxil with ammonia, finding that drug release is increased up to 80 % across 49 hours in the presence of 50mM ammonium sulphate [163]. This process of release is similar to that of the DOX-LS loading process, where the uncharged DOX diffuses across the liposome membrane and then becomes deprotonated, preventing it from passing back through the bilayer [164]. A further driver of this potential glutaminolysis release mechanism may be the hypoxic conditions created at the centre of tumour spheroids. Glutaminase 1 (GSL1) is the enzyme responsible for the production of glutamate and ammonia from glutamine and has been observed to be stimulated by the production of hypoxic inducible factor 1

(HIF1) in colorectal cancers [165]. HIF1 is a potent inducer of cancer cell proliferation, invasion and metastasis, all of which were found to be dependent on the upregulation of GSL1 and subsequent glutaminolysis. The lack of hypoxic conditions in the relatively small, 100 µm spheroids used throughout Roovers et al. MB study could therefore be a factor in the lack of drug release observed in their study. In comparison, spheroids used throughout this study begin at approximately 320 µm and have been observed to grow up to 500 µm after on-chip culture. Solid tumours this size will display hypoxic effects in in their core, which may have facilitated DOX release from LS. Direct observation of GSL1/HIF1 involvement in DOX-LS release would be required to confirm this connection.

4.2.6 Conclusion

This study presented a new microfluidic system allowing the trapping, culture and MB-therapeutic testing of tumour spheroids under physiological flow conditions. Reservoirs supplied passive, gravity-driven flow with velocities mimicking those found in blood capillaries. The use of reservoirs over conventional syringe pumps eliminated the issues associated with operating syringe pumps and tubing in conjunction with an incubator. Furthermore, separate media sources allowed multiple devices to be run in parallel with different therapeutic exposures. The high-throughput capabilities of this system were demonstrated when up to 100 spheroids were trapped across 12 self-contained devices. A total of 690 spheroids were loaded on-chip and analysed in experiments throughout this study. The trap design allowed for simple spheroid retrieval through the reversal of flow, enabling the quantitative analysis of spheroid viability off-chip using an ATP viability assay. This was combined with fluorescent confocal microscopy imaging which observed spheroid degradation, drug accumulation and cell death. Agreement between imaging observations and viability values provided confidence in this systems ability to produce reliable, consistent results.

Overall, the co-delivery of MB + US with DOX has been shown to increase drug efficacy in both free and liposomal formulations. DLMBs have been shown to offer a promising method of delivering drugs to tumours, offering both increased efficacy and localised delivery in comparison to DOX-LS alone. It is evident that the bursting of DLMBs facilitates the uptake of DOX-LS in the tumour tissues, however, this process does not

appear to result in the instantaneous release of DOX from DOX-LS. This is advantageous in minimising the systemic dose of DOX whilst also ensuring the maximum localised DOX-LS delivery.

Several questions in this study do remain unanswered, primarily the mechanism behind the release of DOX from LSs, as well as the long-term effect of multiple US treatments with DLMBs. The decision was made not to carry out any further investigation of these effects using this system. Instead, the focus moved to the development of a vascularised organoid model. Whilst this study has shown that MB-induced sonoporation is an effective mechanism at facilitating drug delivery, the lack of associated vasculature within the spheroids limits the ability of this study to investigate MB-mediated drug delivery across the endothelial barrier. MBs will be delivered intramurally when administered to patients, meaning that the tumour vasculature endothelium will be the first barrier that will have to be overcome if effective drug delivery is to be achieved. Experimentation, therefore, progressed into the development of a vasculature on-chip system allowing for the effects of MB-mediated sonoporation to be further investigated.

5 RESULTS II: DEVELOPMENT OF A VASCULATURE ON-CHIP SYSTEM

This chapter contains the work carried out in developing and characterising a perfusable microfluidic vasculature system which allowed for further investigation of the effects of microbubble (MB)-mediated sonoporation. The previous solid tumour system demonstrated that the use of MBs improved the efficacy of both free and liposomal Doxorubicin. However, MBs would be administered intravenously if given to a patient, meaning vasculature and the endothelium will be the initial barrier for MB-mediated drug delivery. Networks recreating both healthy and tumour vasculature properties have been developed to allow for the investigation of using targeted antibodies on the surface of MBs and liposomes (LSs). Vasculature displaying tumour-like properties was created by conditioning networks with media taken from tumour cell cultures. This was found to induce continual angiogenesis and increase the expression of integrins on the endothelial cell surface – indicating tumour-like vasculature had been successfully induced. The use of microfluidics to house vasculature cultures allows for the perfusion of therapeutics exclusively throughout the vessel networks, at flow rates and shear stresses similar to those found within *in vivo* vessel networks.

5.1 Microfluidic Design and Concept

The overall vasculature on-chip microfluidic design was based on the concept of a 3-channel microfluidic device containing a central hydrogel chamber and media-containing side channels. This design is one which has existed throughout literature for some time, with examples shown and discussed throughout section 1.3.3 (page 42). The design was taken and modified for this project such that the correct conditions could be created for the formation of vasculature. As described previously throughout section 1.3.3 (page 42), the formation of vasculature on-chip requires specific intramural and interstitial pressures to provide the cells with the appropriate biomechanical queues for vessel formation. This section describes the major design features of the microfluidic device along with the subsequent characterisation of intramural and interstitial flow rates throughout the system.

5.1.1 Micropillar Design

The first point of consideration when designing this system was the ability of the micropillar array to successfully confine the hydrogel to the centre chamber. Optimisation of this feature would ensure that devices could be filled with a high rate of success. In addition to this, pillar gaps and channel features must also be a physiologically appropriate size – specifically the diameter of vessels found within capillary networks typically associated with tumours. For example, pillar gaps of 1 μm would naturally result in perfect confinement but would not allow for sufficient exchange of nutrients or for vessel formation through the gap. The hydrogel confinement model described throughout section 2.2.3 (page 68) was used when considering the size and separation of the micropillar array.

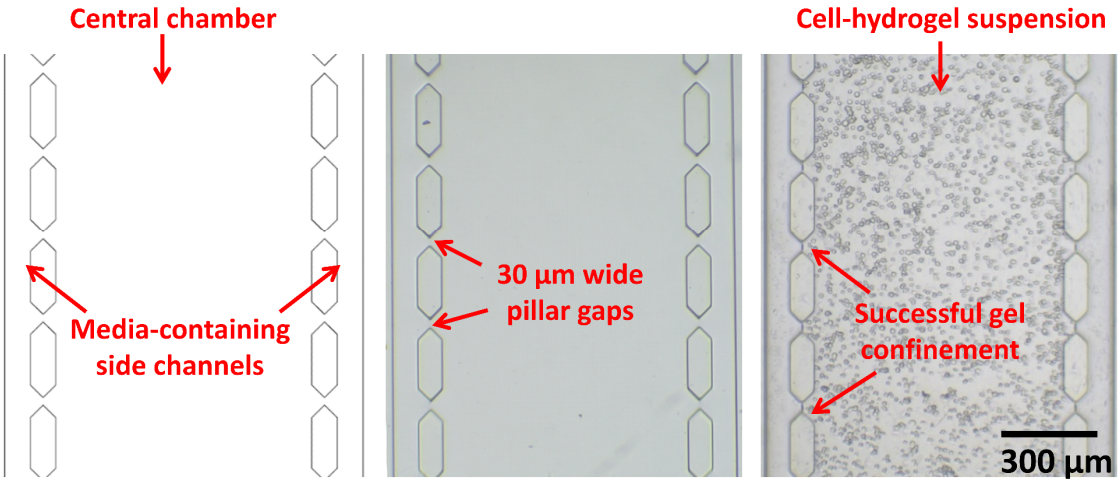

Figure 53 – a) AutoCAD design of micropillar array separating the 3 channels. b) Bright field image of a microfluidic device prior to hydrogel filling. c) Microfluidic device showing successful confinement of cell-hydrogel suspension in the centre channel.

Figure 53a - c shows the final micropillar array design along with images taken of a microfluidic device before and after successful cell-hydrogel confinement. Pillars were designed to have a 45 ° pointed shape, to allow for the reduction of the contact angle when the meniscus reaches the interface. A pillar gap separation of 30µm was used with a centre channel width of 1000 µm as this was calculated to produce a sufficiently high-pressure difference across the interfaces, such that the hydrogel would preferentially flow down the channel (shown in Figure 15). The ability of this array to confine the hydrogel was tested and found to be successful approximately 80% of the time. However, the 20% failure rate was primarily due to issues with premature hydrogel polymerisation resulting in uneven channel filling and pressure instabilities.

5.1.2 Flow and Pressure Considerations

Careful design of the side channel dimensions was necessary to ensure that the appropriate flow and pressure was provided to the centre cell chamber. As with the previous microfluidic spheroid trap chip, hydrostatic flow considerations were calculated using the hydrostatic flow model and equations described throughout section 2.2.2 (page 65). Flow was again provided by the same media reservoirs, however, unlike in the spheroid trap system, there were no constraints on the media channel dimensions. This

allowed for more freedom in the flow parameters as channel widths and lengths could be altered to optimise the hydraulic resistances needed (see section 2.2.2, page 65). Absolute flow rate down each side channel was an important parameter to consider as flow rates had to emulate those found in arteries and veins of a similar size - in order to effectively recreate the high and low-pressure entrance and exit to the vasculature network being formed. Furthermore, it has been shown throughout literature that alternating each side channel between arterial and venule pressures resulted in more effective anastomosis with the pillar gaps at the side channel entrances [166]. It was therefore necessary to design side channels that could create a range of both venule and arterial flow rates.

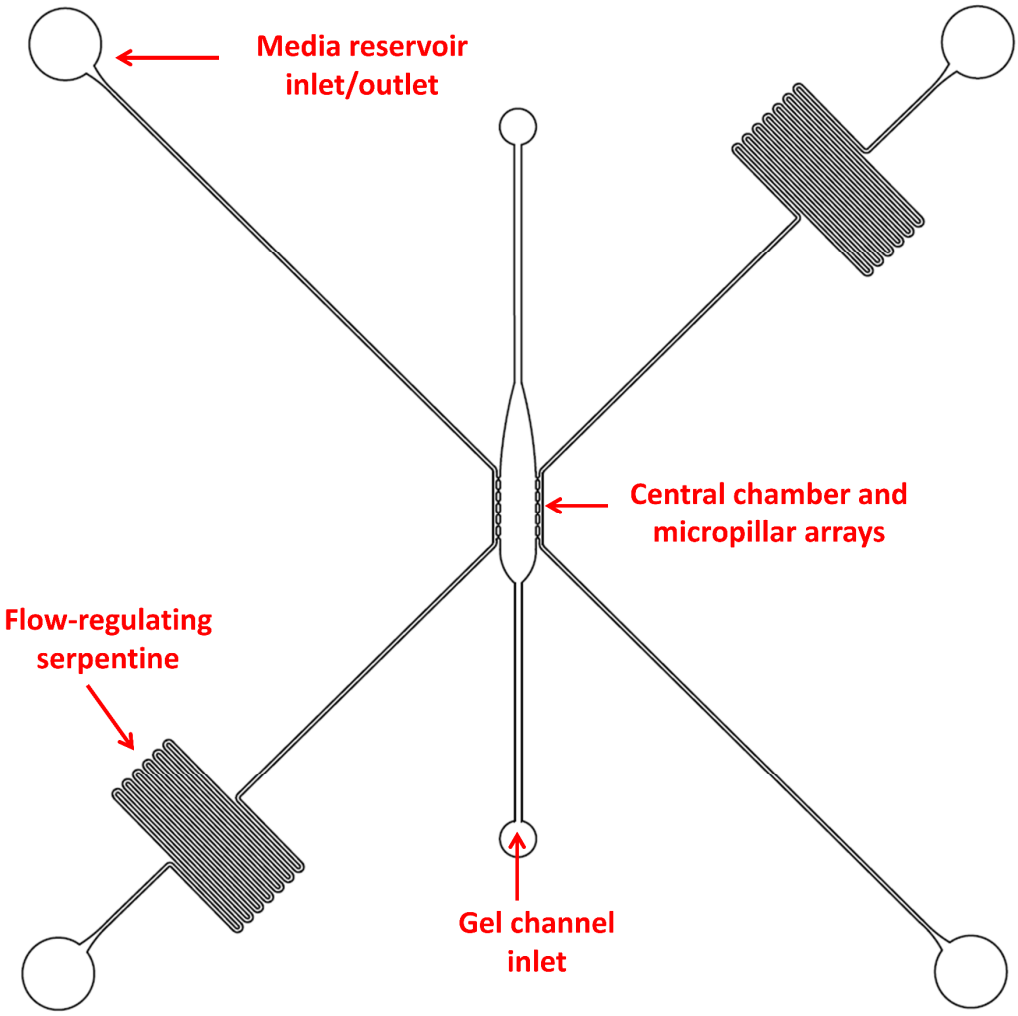

Figure 54 – AutoCAD design of the complete vasculature on-chip microfluidic device design. A closer view of the centre chamber and micropillar array can be seen in Figure 53.

Figure 54 shows the complete microfluidic device design, consisting of the central vasculature chamber and adjacent side channels. Sufficient separation between inlets and the centre chamber was required to allow for space for the reservoirs and US transducer. Serpentines were incorporated to give a total side channel length of 0.1 m. Equation (2-14) was again used to model the change in flow rate and pressure with time. Figure 55 shows graphs of predicted flow rates, pressures and height differences produced from initial inlet and outlet fluid height differences of 12 mm and 2 mm, respectively. Media changes and reservoir re-levels were carried out every day therefore these parameters were modelled across 24 hours.

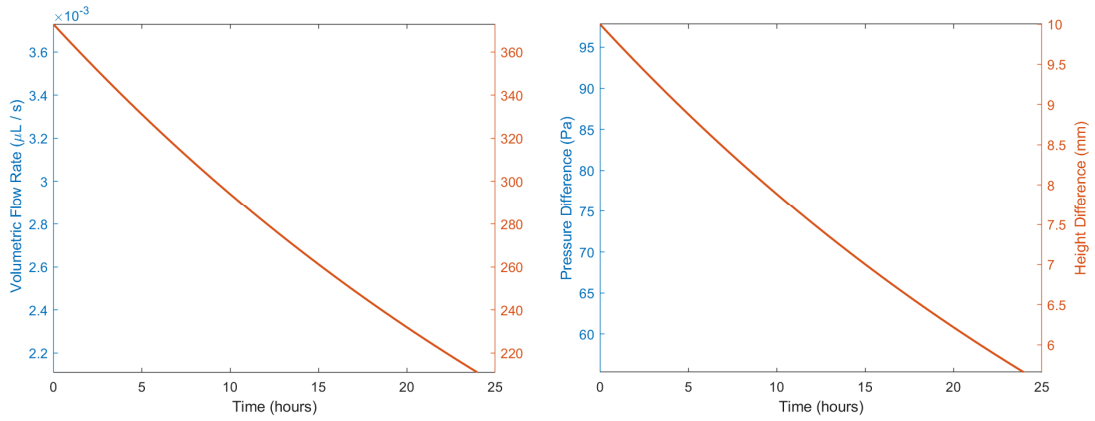

Figure 55 – Graphs showing the predicted changes in (a) Linear and volumetric flow rate and (b) Pressure and height difference along a side channel across a 24-hour period.

The asymmetric positioning of the serpentine channel meant that the channel pressure experienced at the micropillar region was dependent on the direction of flow. Ansys Fluent was used to model the pressure equilibration down the length of the channel from a 117 Pa (12 mmH_2O) pressure inlet and a 19.5 Pa (2 mmH_2O) pressure outlet. If the inlet was selected such that the micropillar region was positioned before the serpentine (i.e the top left inlet in Figure 54), there would only be 17.2 mm of channel before the micropillars. This results in a surface pressure of 101.8 Pa. However, when the inlet and outlets were swapped (inlet now being bottom left), there would be 82.3 mm of channel before the micropillars, resulting in a surface pressure of 35.8 Pa.

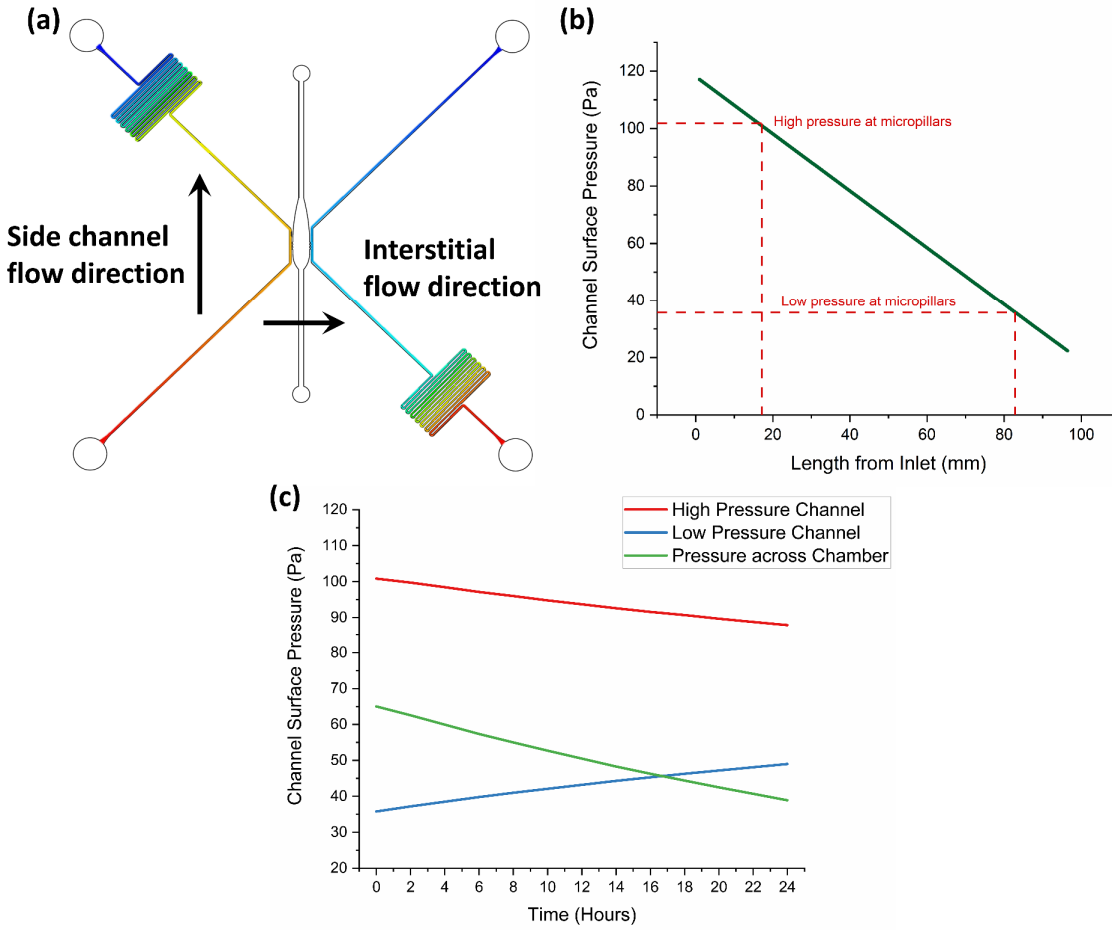

Figure 56 – a) Surface pressure modelling down side channels with difference choices of inlet. b) Graph showing the pressure equilibration down a side channel with low and high pressures created at micropillars. c) High (red) and low (blue) micropillar pressures across 24 hours. Difference (green) shows change in interstitial pressure between media changes.

Figure 56a shows the surface pressure equilibration down the side channels when different inlet choices are made. Red indicates high pressures located close to the media reservoir inlets and blue shows lower pressures which form as the pressure equilibrates along the length of the microfluidic channel. The graph shown in Figure 56b is a plot of surface pressure as a function of channel length. Drop lines show potential micropillar region pressures depending on the choice of inlet. A crucial factor that dictates the successful formation of vasculature on-chip is the interstitial pressure created across the centre chamber. The importance of the correct interstitial pressures on biomechanical queues has been previously described in section 1.3.3 (page 42). The interstitial pressure

created across the channel can be found by calculating the difference between high- and low-pressure side channels. Again, this pressure difference will not be constant due to the time-dependent flow rates. Figure 56c shows the modelled change in side channel and interstitial pressures across a 24-hour period. Interestingly, the micropillar pressure in the low-pressure (blue) channel increases with time. This is due to the outlet reservoir filling with time and increasing the back pressure. The interstitial pressure across the channel was found to decrease from an initial pressure of 60.2 Pa down to 39.8 Pa after 24 hours. This remains with the physiological limits for interstitial pressure, thus showing that this system, with regular 24-hour media refills, could provide the appropriate biomechanical queues for vasculature formation.

5.1.3 Measurement of Hydrostatic Flow Rates

As with the previous spheroid on-chip system, flow rates through this chip were measured by tracking fluorescent beads. The centre chamber was first filled with blank fibrin gel to recreate the on-chip culture setup. 2µm green, fluorescent beads (Molecular Probes, FluroSpheres) were diluted in PBS to a concentration of 5 x 10^4 b/mL and added to the inlet reservoir. Reservoir height differences between 5 mmH_2O and 20 mmH_2O were set up and videos were taken of beads flowing through the channel. Bead trajectories were then measured, and their velocity was determined using the known video frame rate.

Figure 57 shows the plot of measured and theoretical flow velocity against reservoirs height difference. Theoretical flow velocities were initially plotted using a capillary pressure, $P_{cap} = 0$ which sets the line to intercept the origin (see equations (2-9) and (2-10)). However, from the measured flow rates, it was apparent that P_{cap} was non-zero. Fitting a straight line to measured flow rates allowed for the hydraulic resistance, R_{hyd} and P_{cap} to be determined using the gradient and intercept:

$$Q = \frac{\rho g \Delta H - P_{cap}}{R_{hyd}} = \left(\frac{\rho g}{R_{hyd}}\right)\Delta H - \frac{P_{cap}}{R_{hyd}} \tag{5-1}$$

$$R_{hyd} = (2.4 \pm 0.1) \times 10^{13} \qquad P_{cap} = 23 \pm 5 \text{ Pa}$$

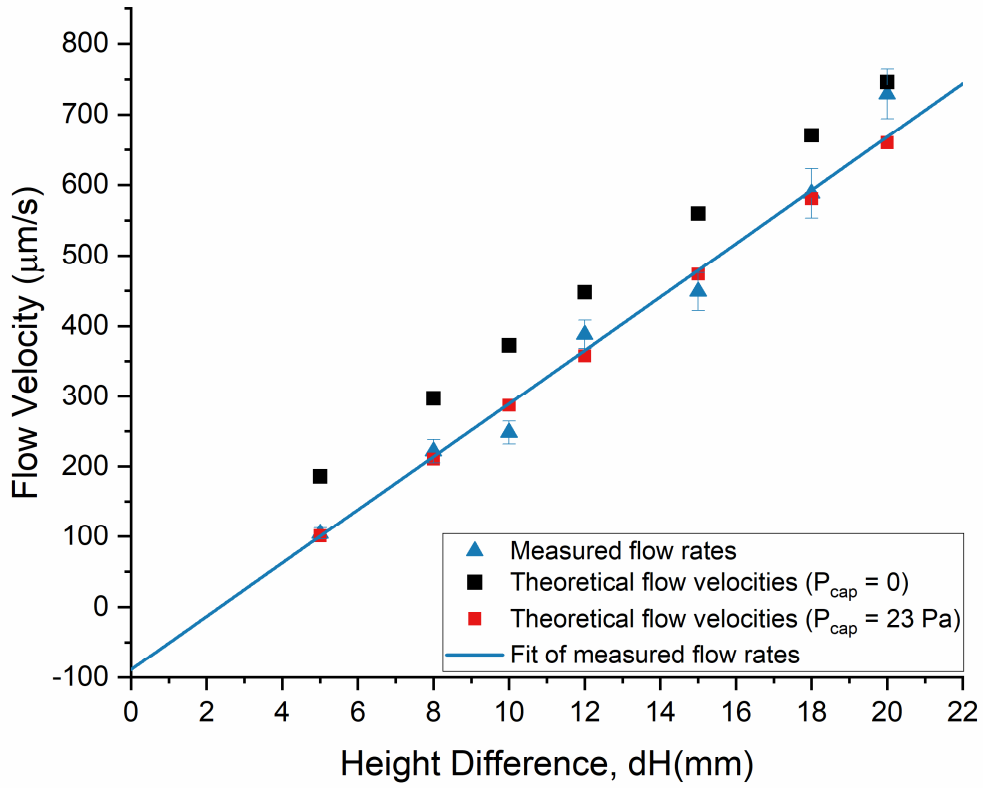

Figure 57 – Measured and theoretical (P_{cap} = 0 and 23 Pa) linear flow velocities for a range of reservoir liquid height differences. The blue line shows the fit of measured flow velocities used to determine hydraulic resistance. R_{hyd} and capillary pressure, P_{cap}.

The measured value of R_{hyd} was approximately 8% lower than the theoretically calculated value of 2.6 x 10^{13}. The theoretical flow velocities were replotted using P_{cap} = 23 – shown in red in Figure 57. Due to this inherent resistance to hydrostatic pressure, the inlet reservoir height used throughout experiments was increased from 12 mm to 15 mm. Overall, there was close agreement between theoretical and measured flow velocities meaning this device was able to provide suitable flow rates and pressures to vasculature cell cultures. Comparison with the previous hydrostatic resistance values determined for the spheroid trap system (section 4.1.2, page 119) reveals that the theoretical values match the experimental values significantly better in the vasculature system. This demonstrates how the accuracy of the microfluidic model increases as the channel dimensions approach ($h / w \rightarrow 0$) – an assumption applied within the flow model.

5.1.4 Measurement of Interstitial Flow Rates

Subjecting cells to the appropriate interstitial flow rates is crucial to ensure cells receive the appropriate biomechanical queues for vasculogenesis. It has been shown in previous studies that endothelial cells react to interstitial flow by elongating and growing in the direction of flow. In addition to this, the interstitial flow must be significant enough to provide sufficient amounts of nutrients and growth factors to cells. The rate of interstitial flow through a fibrin hydrogel will be directly linked to the concentration of fibrinogen used in the clotting process. The concentration of thrombin, the enzyme used to cleave fibrinogen and form fibrin, has also been shown to affect the fibrin clot structure with low concentrations resulting in the slow formation of large fibrin loosely organised fibrils and high concentrations producing a denser network of thinner fibrils [167]. As the concentration of thrombin used throughout previous on-chip studies is relatively consistent, only the effect of fibrinogen was considered in this study.

To determine the rate of interstitial flow and the effect of differing fibrinogen concentrations, blank fibrin gels were loaded into the centre chamber using fibrinogen concentrations of 2.5, 5, 7.5 and 10 mg/mL. Side channels were filled with PBS then inlet and outlet reservoirs filled with 15 mmH_2O and 2 mmH_2O, respectively. As discussed throughout section 5.1.2 (page 150), the asymmetric serpentine positioning resulted in a pressure differential across the channel, creating interstitial flow. PBS in the high-pressure channel, defined as the channel with the serpentine at the outlet, was mixed with fluorescein to a final concentration of 1 µM. This allowed for observation of diffusion across the gel in the centre channel using fluorescence microscopy. The velocity of the fluid movement through the gel was calculated using the known length of the chamber and the time over which diffusion was recorded. Darcy's law was then used to calculate the permeability of the gel using the known velocity and pressure drop across the two adjacent side channels:

$$K_s = \frac{QL\mu}{\Delta PA} \tag{5-2}$$

Where K_s is the permeability (often referred to as the Darcy flux), Q is the volumetric flow rate, μ is the dynamic viscosity of the fluid, ΔP is the pressure drop across the channel and L and A are the length and area of the gel through which the fluid is moving.

Figure 58 shows graphs of interstitial flow velcoity (µm/s) and K_s against the range of fibrinogen concentrations. Interstitial flow velocities were found to remain within the optimal range for angiogenesis, 1 – 10 µm/s, across all fibrinogen concentrations [43]. K_s was observed to decrease with increasing fibrinogen concentrations, as expected. The trend was linear, showing a decrease in permeability of approximately 45 %, from using 2.5 mg/mL to 10 mg/mL. From these observations, it was decided that a fibrinogen concentration of 10 mg/mL would be used to resuspend cells. However, the final working concentration is estimated to be in the range of 7 – 8 mg/mL after the fibrinogen is diluted in the small amount of cell media remaining around the pellet, along with the thrombin used to clot the gel. These dilutions become significant due to the small volumes used whilst mixing the fibrin gel for each individual device. This fibrinogen concentration is estimated to produce interstitial flow velocities of approximately 3 µm/s, found to be within the optimal range of interstitial flow rates required to stimulate vessel formation [168].

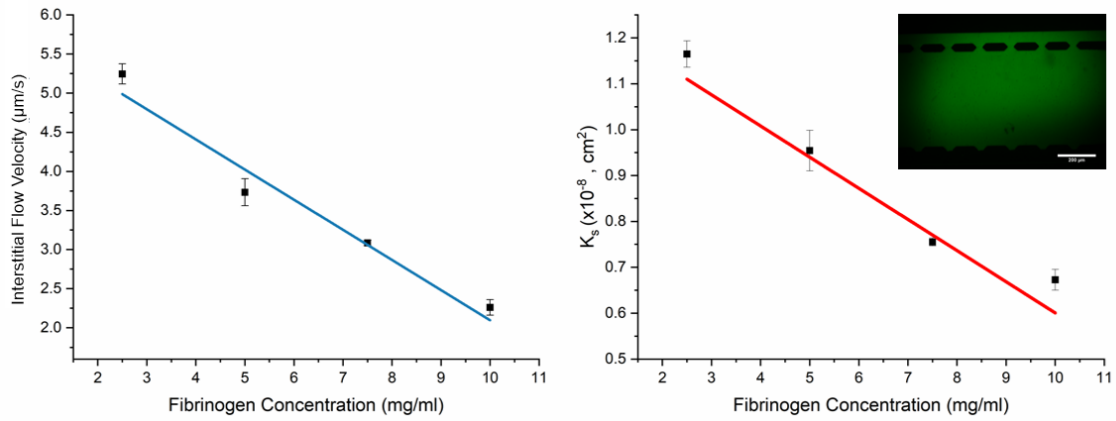

Figure 58- Graphs showing interstitial flow velocity (left) and Permeability, K_s (right) with fibrin gels made with differing fibrinogen concentrations. Inset shows an example image of fluorescein diffusing through the fibrin gel.

Future vasculature perfusion experiments planned to use Texas red dextran as a dye to measure permeability across vessel walls. Prior to this, Texas red dextran was flowed through the side channel and a confocal microscope used to periodically image regions of a blank fibrin gel to attempt to determine gel permeability. Shortly after imaging began, it was apparent that the Dextran did not uniformly diffuse across the gel from the side channel. This was more apparent on the shorter imaging timescales, compared to the

longer videos captured of fluorescein diffusion. To quanitfy the variation in apparent permeability, the gel channel was split into 9 regions which were periodically imaged and the permeability calculated.

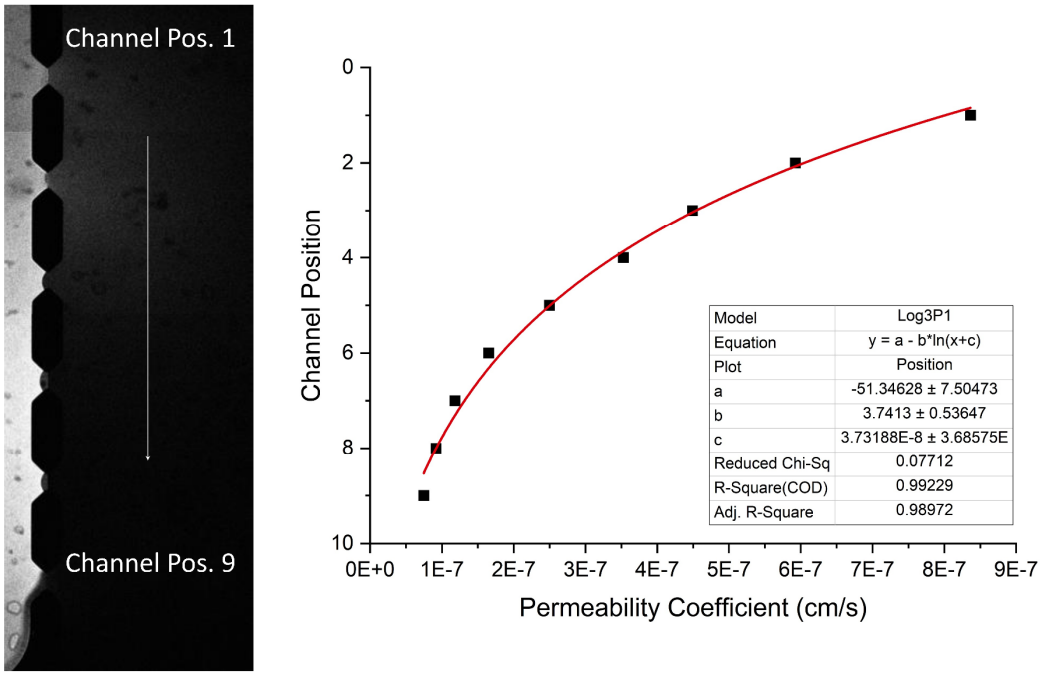

Figure 59 - Merged image of Dextran diffusion into an empty fibrin gel alongside a graph showing the calculated permeability coefficients for each channel position. Dextran enters the side channel at position 1 and exits at position 9. Permeability was found to vary due to the pressure difference across the micropillar array.

Figure 59 shows an image taken of dextran diffusing into an empty fibrin gel, alongside a graph of the calculated permeability coefficients. As many of the terms in the Darcy equation, such as pressure drop and volumetric flow rate, will not be accurately known when fluid is perfusing through vessels, an alternative model for determining permeability was used:

$$P_D = \frac{1}{I_i - I_b}\left(\frac{I_f - I_i}{\Delta t}\right)\frac{d}{4} \qquad (5\text{-}3)$$

Where I_i, I_f, and I_b are the initial, final and background fluorescent intensities. Δt is the duration between images and d is the vessel diameter. This permeability model was originally developed by Yuan et al [169] and further simplified by Lee et al when being

applied to a microfluidic vasculature model [170]. The original model was used to determine albumin permeability in tumour vessels and relied on the haematocrit and the volume to surface area. However, in the simplified model, the terms can be reduced as there is no haemoglobin present and the vessel is assumed to fill a significant portion of the chamber. This allows volume and area terms to be reduced to only require a value for the diameter and fluorescent intensity values with time. A full derivation of the microfluidic model can be found in Lee et al's supplementary information [170].

As Figure 59 shows, permeability across the fibrin gel was calculated to vary over an order of magnitude from position 1 (~10^{-6} cm/s) to position 9 (~10^{-7} cm/s). This is due to the pressure differential across the micropillar array, resulting in positions closer to the inlet showing more Dextran diffusion than positions further removed. Whilst this pressure gradient was expected and is not a concern for nutrient diffusion, the magnitude at which it affects permeability measurements was an issue for future vessel permeability measurements. Vessels close to channel inlets will appear to have a higher permeability, resulting in inaccuracies when measuring the effects of MBs on the endothelial barrier.

A solution to this issue was found by reducing the number of pillars in the array from 5 to 2 and shortening the length of the pillars from 100 µm to 50µm. Figure 60 shows the reduced micropillar design alongside the graph of calculated permeability values from the repeated experiment. Permeability was found to vary significantly less than in the previous design, with an average value calculated to be $(7.4 \pm 0.7) \times 10^{-7}$. This permeability value will change as fibroblasts remodel the matrix as the vasculature develops, however the consistent values will allow for accurate measurements of future vessel permeabilities.

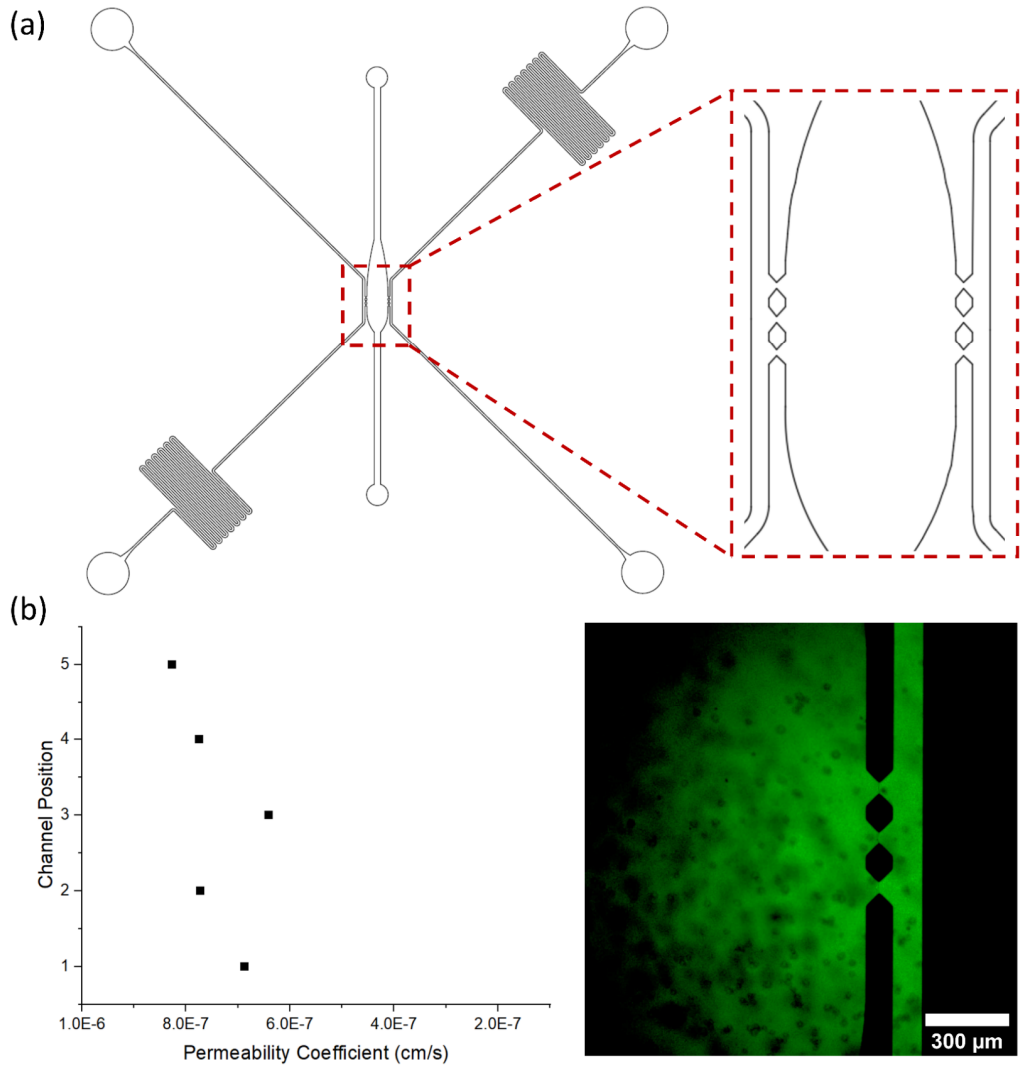

Figure 60 – a) Microfluidic device with reduced number of micropillars to allow for homogeneous diffusion across the centre chamber. b) Graph showing calculated permeability values at each channel position, alongside an image of dextran diffusion into the fibrin gel.

5.2 Development and Characterisation of the Vasculature On-chip System

5.2.1 Determining Optimal Cell Type and Passage

The formation of a perfusable vasculature network requires successfully inducing endothelial cells to undergo angiogenesis. This not only requires careful consideration of the biochemical and biomechanical stimuli but also the use of the appropriate cell types. Not all endothelial cells will have the ability to undergo angiogenesis whilst not all stromal fibroblast cells will secret the appropriate growth factors and ECM components to support a vasculature network. Furthermore, the number of passages cells undergo before being used for these assays will have an impact on their angiogenic ability. Cells will mature with increasing passages and display reduced angiogenic ability with time. This can be, in part, attributed to the reduced cell migration and actin filament elongation observed after cells have undergone multiple passages [171]. This section contains the work carried out in identifying the optimal cell types and passages for vascular network formation.

5.2.1.1 Off-Chip Angiogenesis Assay

Prior to the start of any on-chip experiments, an initial off-chip experiment was completed to observe the difference in the angiogenic ability of different cell lines. A common off-chip assay consists of growing endothelial cells on a confluent layer of fibroblasts seeded days earlier. The layer of fibroblasts secretes ECM proteins as they grow which the endothelial cells then grow on top of when seeded. The endothelial cells interact with the ECM and, if the appropriate ECM proteins and growth factors are present, form a network of branched vessel-like structures. This form of 2D branching assay can therefore assess both the angiogenic ability of endothelial cells and fibroblasts and has been used to observe the effects of gene knockdowns and anti-angiogenic therapies [172–174]. To better inform on-chip experiments, additional cell-ECM configurations were included which were more similar to the on-chip experimental configurations. This included suspending endothelial cells in fibrin before seeding onto the fibroblast layer, as well as seeding both fibroblasts and endothelial cells in a fibrin gel at the same time. Figure 61 depicts the three cellular configurations tested throughout this assay. This final condition is identical

to the setup which was proposed for on-chip experiments. Further details of the experimental setup can be found in section 3.2.6 (page 91).

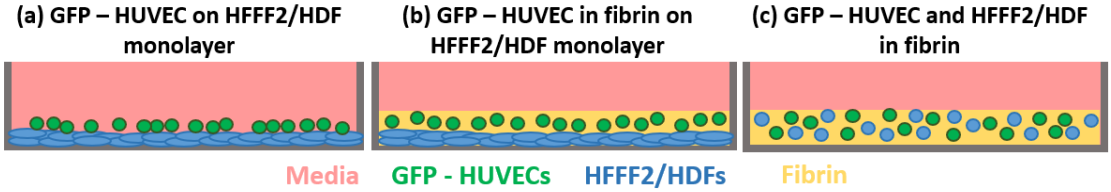

Figure 61 – Diagram of the three cellular configurations tested in this off-chip angiogenesis assay. Configuration labels correspond to images shown throughout figures 62 and 63.

The endothelial cells chosen for this assay were human umbilical vein endothelial cells (HUVECs). These cells are collected from the lining of umbilical cords and can be easily grown in a range of different conditions. Their relative immaturity results in HUVECs having a relatively high angiogenic potential at low passages ($p < 6$), making them a very common choice for 2D and 3D vasculature experiments. As these cells were known to be appropriate for this assay, this experiment instead focused on the choice of appropriate fibroblasts. The two types of fibroblasts being tested in this initial investigation were the human foetal foreskin fibroblast (HFFF2) cells previously used in colorectal cancer spheroids, and human dermal fibroblast (HDF) cells which were recommended by a collaborator who had previously performed these 2D assays. HDFs were reported to have high angiogenic potential if used at low passages ($p < 8$) and have been previously shown to induce endothelial branching in 2D assays such as these [173]. HDFs, in this case, were initially used at p5. Whereas HFFF2 cells had not previously been used in vasculature work, and in this case, were only available at passage 12 and above.

Figure 62 shows images acquired of HFFF2 – HUVEC cultures from each of the three experimental conditions with the labels corresponding to the experimental setups shown in Figure 61. HUVECs used throughout this experiment were transfected with GFP to allow for fluorescent imaging and observation of their behaviour. In each case, it was evident after 48 hours that HFFF2 cells were not producing the appropriate growth factors or ECM to induce any branching of HUVECs. The inclusion of fibrin into the cultures did not appear to have any effect on the HUVECs behaviour, suggesting that the lack of appropriate growth factors and matrix proteins other than fibrin was the main issue.

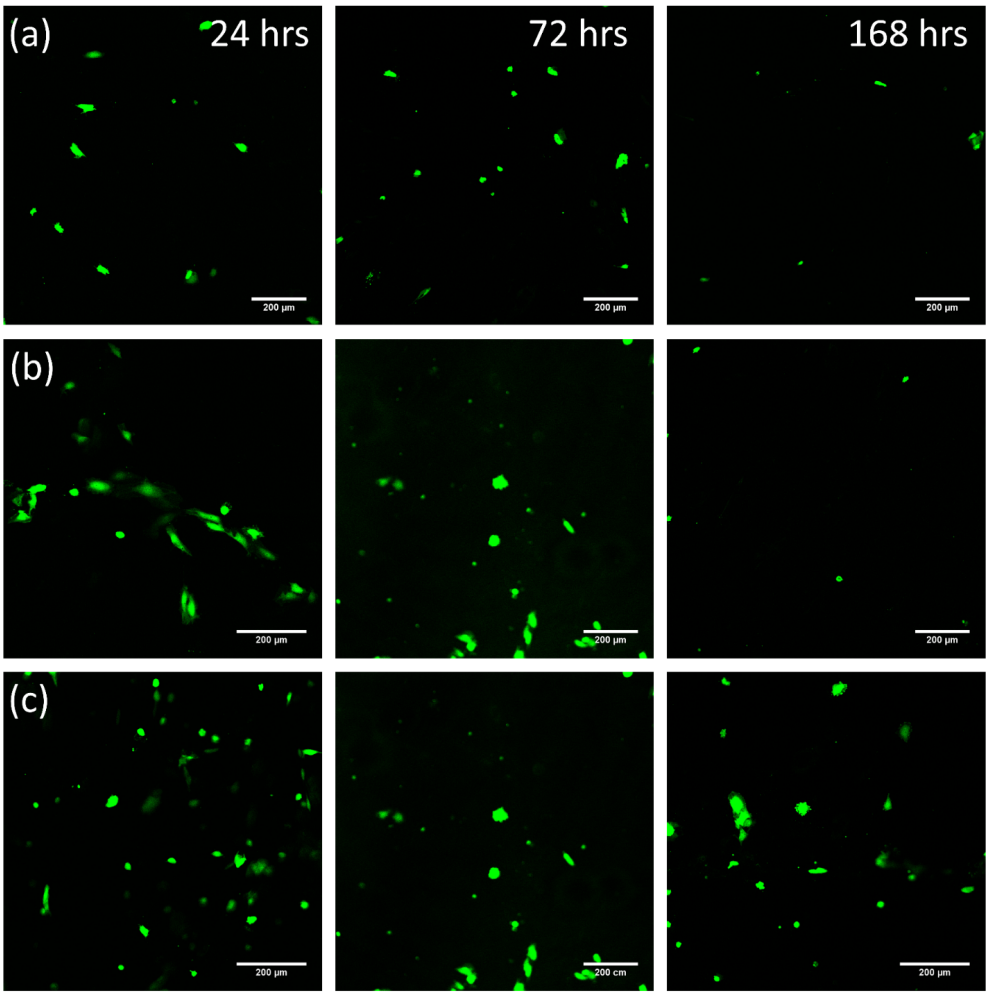

Figure 62 – Fluorescent images of GFP-HUVECs co-cultured with HFFF2 cells. HUVECs were seeded directly onto a confluent layer of HFFF2 cells (a), suspended in fibrin then seeded onto HFFF2 cells (b), or suspended in fibrin alongside HFFF2 cells then seeded (c). Images taken 24, 72 and 168 hours after seeding show the lack of HUVEC activity when seeded with HFFF2 cells.

HUVECs co-cultured with HDFs showed significantly different morphologies compared to those grown with HFFF2s. Figure 63 shows images of HUVECs captured after 24, 72 and 216 hours of culture. HUVECs were observed to form branched networks of 2D vessel structures in each of the three seeding configurations. HUVECs grown directly onto the layer of fibroblasts appeared to create the most continuous networks after 9 days, however, this could be attributed to HUVECs being distributed more densely than in the fibrin containing conditions. The use of 10 µL fibrin gels increased HUVEC separation due to the increased volume in which the cells were distributed. A result of this was the

observation of increased cell elongation as cells were stretching to form connections with nearby cells - this can be observed in HUVECs grown in fibrin on top of the HDF layer in Figure 63b. HUVECs suspended with HDFs in fibrin were observed to initially progress at a slower rate than the other two conditions. This was expected, as fibroblasts in this condition were not able to secrete ECM and growth factors prior to HUVEC seeding.

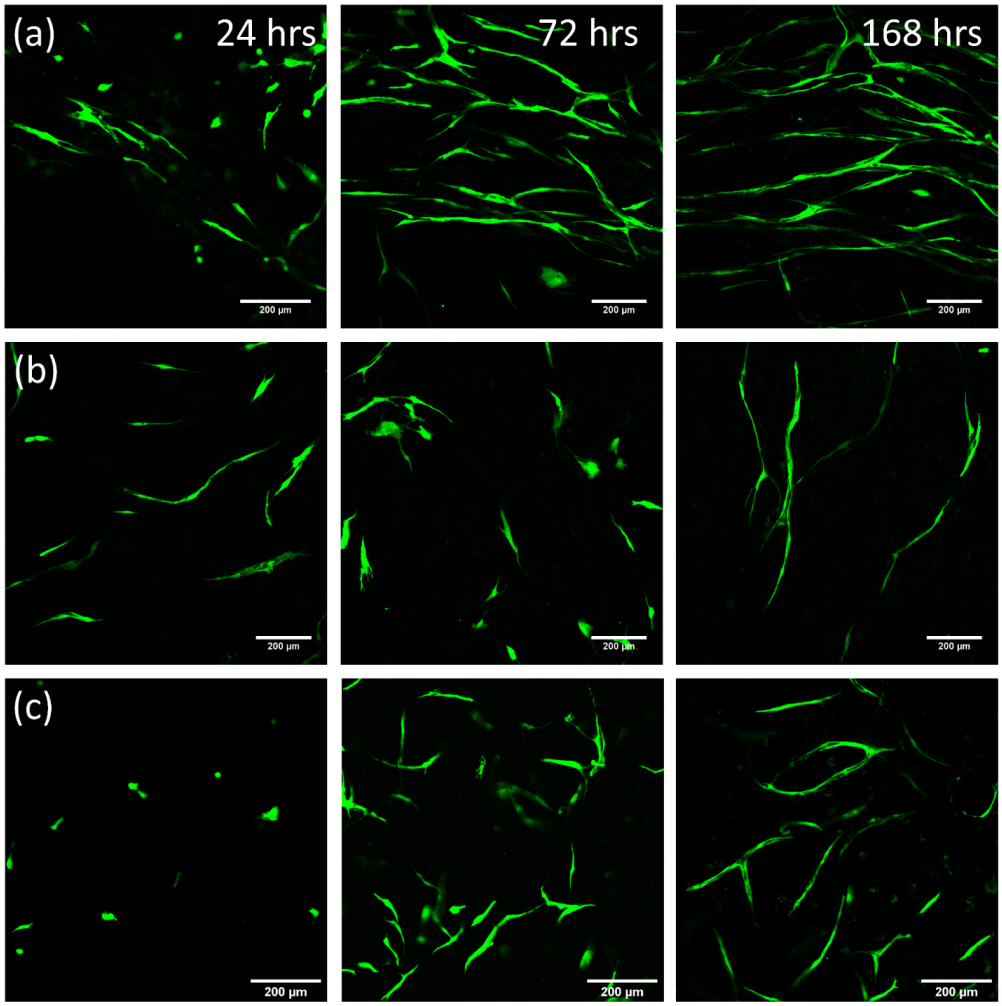

Figure 63- Fluorescent images of GFP-HUVECs co-cultured with HDF cells. HUVECs were seeded directly onto a confluent layer of HDF cells (a), suspended in fibrin then seeded onto HDF cells (b), or suspended in fibrin alongside HDF cells then seeded (c). Images taken 24, 72 and 168 hours after seeding show HUVECs interacting with HDF cells and the matrix proteins they have secreted.

The similarities observed between the two fibrin-containing conditions suggests that fibroblasts influence HUVEC behaviour in a paracrine fashion, and do not require direct contact with endothelial cells to induce sprouting and elongation. This agrees with reports throughout literature that have used microfluidic systems with separate chambers for endothelial cells and fibroblasts and attained similar results [70,175]. Observations throughout this experiment revealed that HFFF2 cells were not suitable supporting cells for angiogenesis-related experiments, and as such, they would not be used in any experiments moving forward. HDF cells, however, showed promising angiogenic ability both with and without the inclusion of fibrin. It was decided that a HUVEC-HDF suspension in fibrin would be used for on-chip microfluidic experiments as the use of a hydrogel allows for spatial confinement of cells within each chamber.

5.2.1.2 Determining Optimal HUVEC and HDF Cell Passages

As mentioned previously, the passage at which cells are used for experiments can greatly impact their ability to form vessels. Primary cells, such as HUVECs and HDFs, are only able to undergo a finite number of passages before their genotypic and phenotypic characteristics begin varying too significantly. This is primarily due to the non-native condition in which these cells are cultured, resulting in the cells not being exposed to the appropriate biological queues they would be otherwise subject to *in vivo*. The effect of using high passage cells is particularly apparent in experiments aiming to induce angiogenesis, as this is a process that involves many immature, stem-cell-like cells when occurring *in vivo.* Cell passages must therefore be carefully considered to ensure that sufficient numbers of cells are generated for experiments without exceeding their optimal passage number.

Publications involving the use of self-assembled vasculature will often quote the passage they use their cells to be typically p3 – p6 for endothelial cells and p4 – p8 for fibroblast/stromal cells [66,70,170,176]. However, one issue with this is that the number of cells seeded after each split, and the confluency at which cells are harvested will often vary between experimental protocols. Meaning passage numbers will not be truly consistent between different investigations. A more accurate metric that better describes the age of cells is the population doubling number (PDL).

PDL is described as the number of times the cells in the population have doubled since their isolation from primary tissues and considers the density at which cells are seeded and collected. It can be calculated using [177]:

$$\mathrm{PDL} = 3.32\left(\log\frac{Total\ number\ of\ viable\ cells\ harvested}{Total\ number\ of\ viable\ cells\ seeded}\right) \quad (5\text{-}4)$$

The factor of 3.32 originates from the -log(0.5) factored out. The maximum number of population doublings primary cells can undergo is often quoted by suppliers, and in many cases is given as 12. This typically corresponds to approximately 10 passages if supplier passage protocols are followed closely. However, for the production of vasculature networks, 10 passages/12 PDL is already known to be too high. This section contains the work carried out in finding the optimal passage/PDL number for vasculature formation.

In conventional cell culture techniques, cells are maintained in continuous culture before being used for experiments, to eliminate any negative effects from cells being cryogenically frozen. This was not possible for this series of experiments, as cell passages had to be minimised whilst the number of available cells maximised. Cell stocks were therefore grown out then refrozen in individual cryovials which were to be defrosted 3 days before on-chip cell seeding. This allowed for cells stocks to be used efficiently but at the cost of reducing overall cell viability in the cultures. This also meant that the cells would undergo at least one additional population doubling and passage after being defrosted.

The passage at which HDFs were seeded was first considered and initially chosen to be p5 – the same passage used for the previous 2D sprouting assay. Cells arrived frozen at p2 meaning cultures could be expanded at least twice up to p4 before being refrozen – giving p5 cells after defrosting and growing for two days. Fibroblasts at p5 were well within the quoted range for on-chip vasculature experiments (p4 – p8) [67,178], and any inaccuracies due to different population doublings would likely remain within this range. Calculation of the PDL for p5 HDFs gave a value of approximately 7, depending on the final numbers harvested. This was again well within the limits recommended by suppliers. The passage at which HUVECs were used was of much greater importance, as this is known to affect the cells angiogenic potential and ability to form long-reaching branches. Passage 2 HUVECs were initially expanded out in the same manner as HDFs, giving p5

cells when seeded on-chip. Throughout early on-chip experiments, non-GFP cells were used, therefore CellTracker Green (BODIPY, Invitrogen) was used to stain cells for 30 minutes prior to detaching and seeding. This allowed for HUVECs to be tracked for up to 7 days due to their lack of division when seeded in fibrin. HUVEC and HDF cells were initially seeded at a concentration of 6×10^6 and 4×10^6 cells/mL, respectively. These values were chosen using values stated in similar on-chip vasculature studies [66,179].

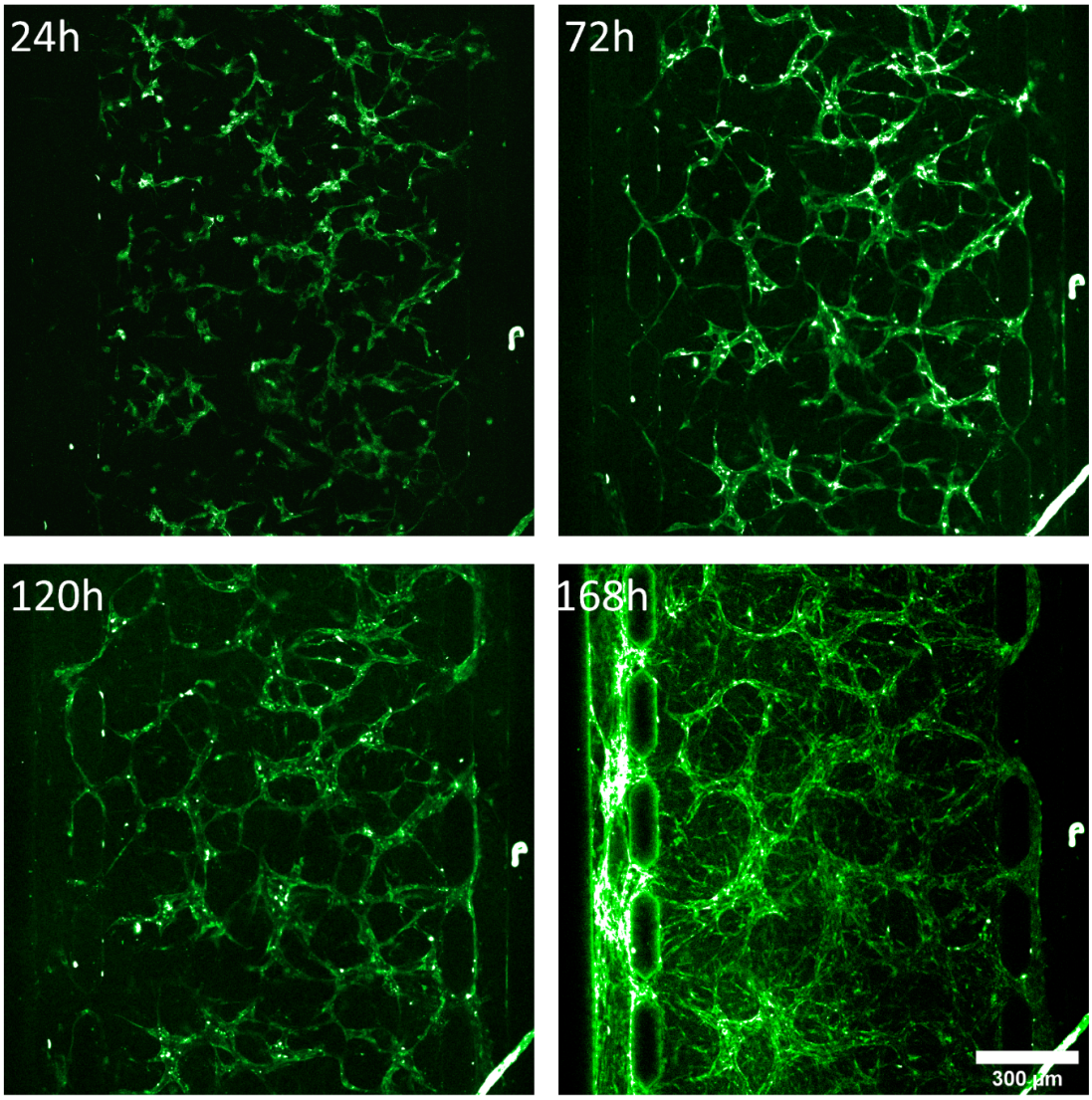

Figure 64 – Confocal microscopy images taken of HUVEC (p5) – HDF (p5) on-chip cocultures at 24, 72, 120 and 168 hours after seeding into the microfluidic device in a fibrin matrix. Images show HUVECs stained with CellTracker green (BODIPY) appearing to self-assemble into a continuous vasculature network across a 7-day period.

Figure 64 shows confocal microscopy images taken of vasculature cultures 24, 72, 120 and 168 hours after cell seeding. HUVECs, shown in green, can be observed to begin interacting with the fibrin matrix as little as 24 hours after seeding. HUVECs elongate to form cell-cell connections as the cultures develop, eventually forming an almost continuous network after 120 hours. HUVECs were then observed to broaden, appearing to form lumen-like structures. Due to the failure to properly alter side channel flow and interstitial pressures, HUVECs were observed to grow preferentially into the left side channel. This progression from single cells to complete networks closely matched observations reported throughout literature however, one main difference was the timescale over which cultures were forming. Previously published vasculature systems typically reported the formation of continuous networks after 5 – 7 days of culture [43,68], however, networks only appeared to become perfusable after a minimum of 7 days (168 hours) culture in this system. Perfusability of the networks after 7 days was tested by flowing Rhodamine 6G, a red fluorescent dye, through one of the side channels.

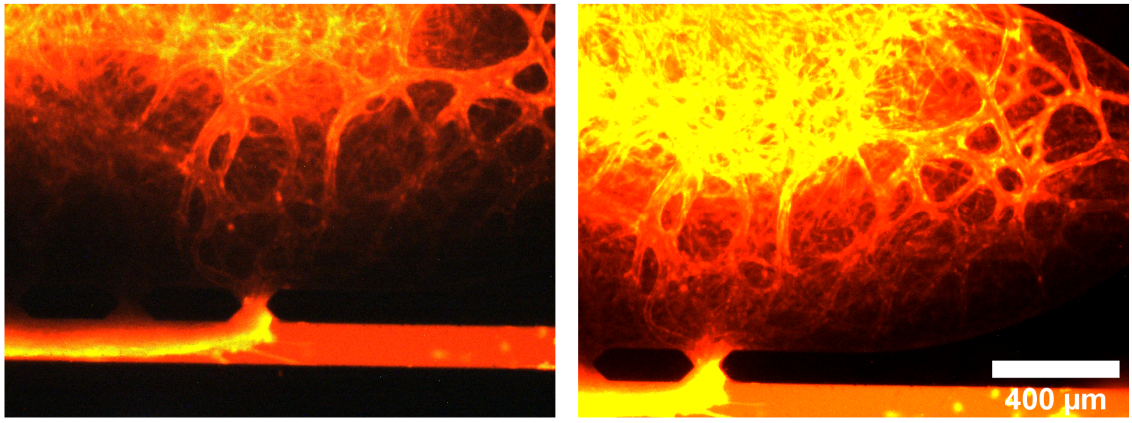

Figure 65 – Fluorescent images taken of Rhodamine 6G perfusion through vasculature networks shown in Figure 64. Rhodamine was initially flowed through the lower channel without success. The upper channel (not observable in this image) was therefore tested and resulted in confinement of the dye to regions of fully formed vasculature.

Figure 65 shows images taken of Rhodamine perfusion through the vasculature network shown in Figure 64. The dye was initially flowed through the lower side channel (observable in Figure 65) and observed to merely diffuse into the culture chamber, indicating no perfusable vessels had formed. Rhodamine was instead added to the upper

channel at which point it was observed to rapidly flow into the chamber. Vessels far removed from the chamber entrance appeared to show successful confinement of the dye, indicating that perfusable vessels had successfully formed. The significant leakage at the chamber entrance, however, indicated that the majority of the network was underdeveloped. The slow timescale for network formation along with the evidence of underdeveloped structures even after 7 days indicated that the HUVECs were not able to undergo sufficient angiogenesis to form a complete network. It was theorised that lower passage cells may be a solution to this issue so HUVECs and HDFs grown only to p4 were tested in a subsequent experiment.

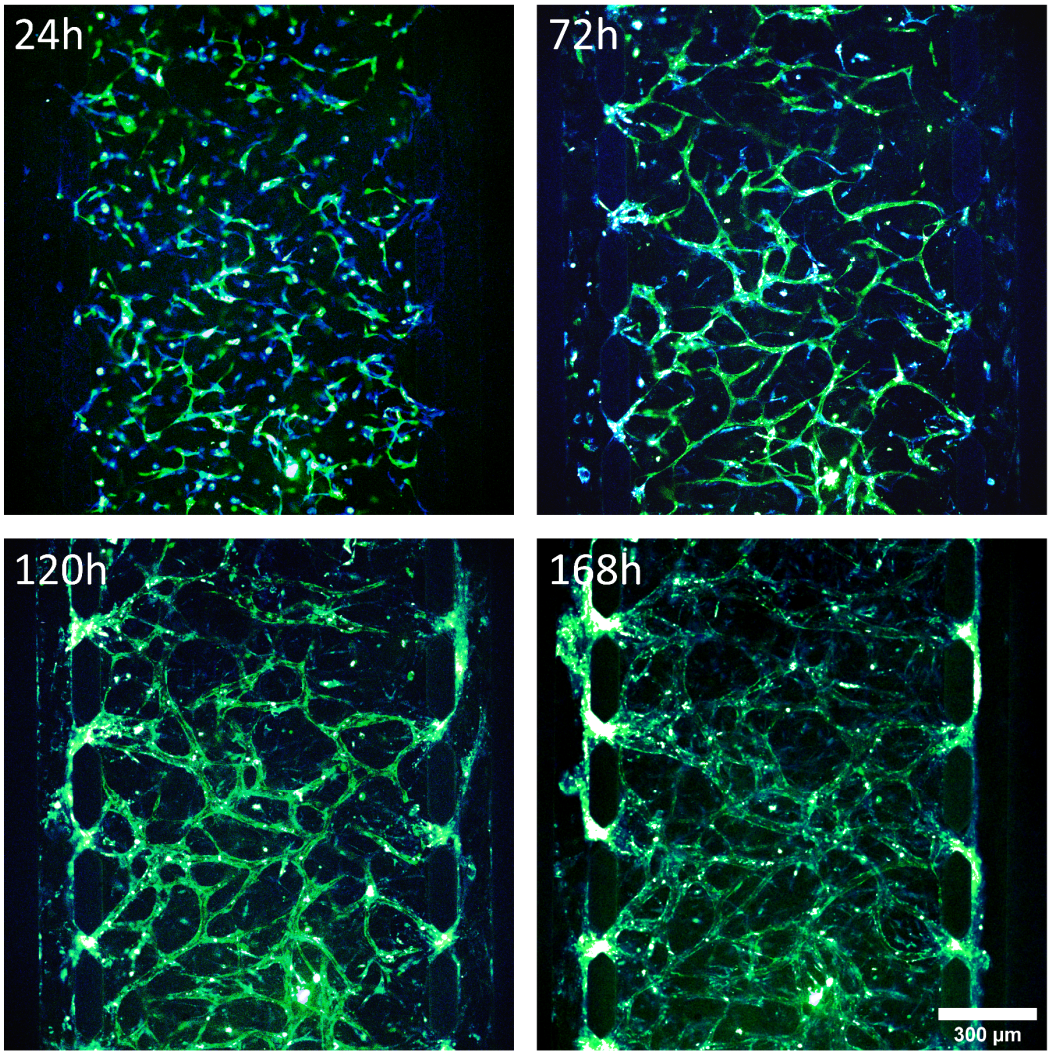

Figure 66 – Confocal microscopy images taken of HUVEC (p4) – HDF (p4) on-chip cocultures at 24, 72, 120 and 168 hours after seeding. Images show HUVECs stained with CellTracker Green (BODIPY) and HDFs stained with CellTracker Blue (CMHC).

Figure 66 shows confocal microscopy images taken of HUVEC – HDF (p4) on-chip cultures after 24, 72, 120 and 168 hours after seeding. CellTracker green was again used to stain HUVECs but now HDFs were also stained with CellTracker Blue (CMHC, Invitrogen). This aimed to observe fibroblast association with the vessels to see how the stromal and endothelial cells self-assembled. As Figure 66 shows, blue HDF fluorescence rapidly diminished with time due to the high rate of growth of fibroblasts in the fibrin gel. As CellTracker is a membrane stain, its fluorescence is halved when the cell divides, meaning rapidly growing cells reduce in fluorescence faster than slow-growing cells. In comparison, HUVEC cells emission only dropped slightly across the 7-day period, confirming that HUVECs were minimally dividing in the fibrin gel. Emission appeared to primarily drop due to the elongation of the HUVECs, which reduced the density of the dye in the cell membrane. These observations match those made in the 2D assay (section 5.2.1.1, page 161), which also observed no endothelial cell division when seeded in any configuration.

Comparison between vasculature networks formed using p4 and p5 cells shows a significant improvement with lower passage cells. Evidence of a complete perfusable network could be observed after 120 hours, compared to a barely continuous network with higher passage cells. After 7 days, p4 HUVECs appeared to have formed a lumenised network with vessel openings forming at the centre chamber pillar gaps. Perfusion was again tested, however now a red fluorescent dextran (70kDa) solution was used to image flow. Dextrans are polysaccharide molecules commonly used to characterise perfusion and permeability of vasculature networks due to their well-defined size. Dextran was flowed down the side channel and was immediately observed to enter the vasculature network and exclusively flow through the vessels.

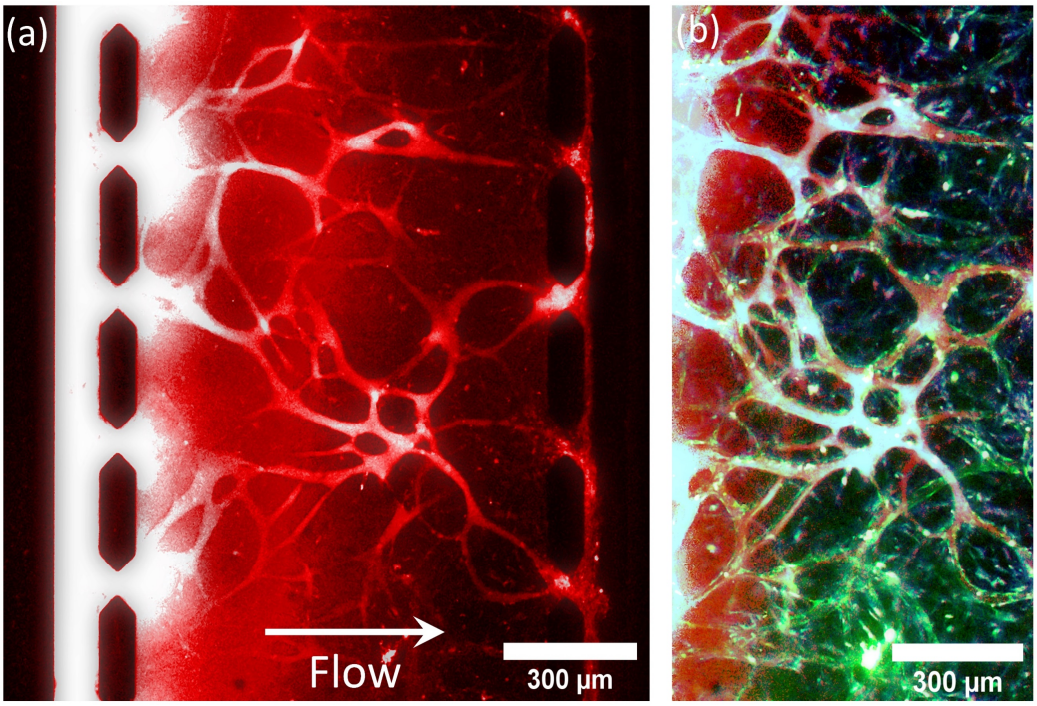

Figure 67 – a) Image acquired of Texas-red dextran perfusion through the vasculature network shown in Figure 66. b) Overlay of dextran, HUVEC and HDF fluorescence emission showing perfusion exclusively through the vasculature lumens.

Figure 67a shows an image taken of dextran flowing through the network approximately 20 minutes after flow was initiated. Figure 67b shows an overlayed image of all three fluorescent channels, showing how dextran was confined to flowing through the vasculature lumens. Leakage of dextran was observed at the chamber entrances, where the vessel openings met with the pillar gaps -this indicated that a perfect seal of vessels with the pillars had not been achieved. This was not unexpected, as cells adhere very poorly to PDMS, meaning little pressure is needed to separate the cells from the chamber walls. Nevertheless, flow throughout the network was considerably more significant, and dextran was observed to exit the network through the adjacent side channel. Despite the successful formation of a perfusable vasculature network observed in Figure 67, the overall success rate of devices setup was low (~10 – 20 %). Few instances of perfusable networks were observed across the many devices seeded, indicating that the system was

in further need of optimisation before experiments could continue. The main issue appeared to be the formation of 'closed' networks, which resulted in dextran flowing exclusively around the vessel network and into the surrounding matrix.

5.2.1.3 Vasculature Cultures using GFP-HUVECs and Normal Human Lung Fibroblasts (NHLFs)

The consistently limited vessel formation observed with HDFs prompted the testing of an alternative fibroblast cell type. Normal human lung fibroblasts (NHLFs) are another commonly used cell type throughout vasculature studies and are the most prevalent fibroblast cell type used to produce perfusable vasculature within microfluidic devices. Cells were acquired, grown to passage 3 and frozen into individual vials in preparation for experiments.

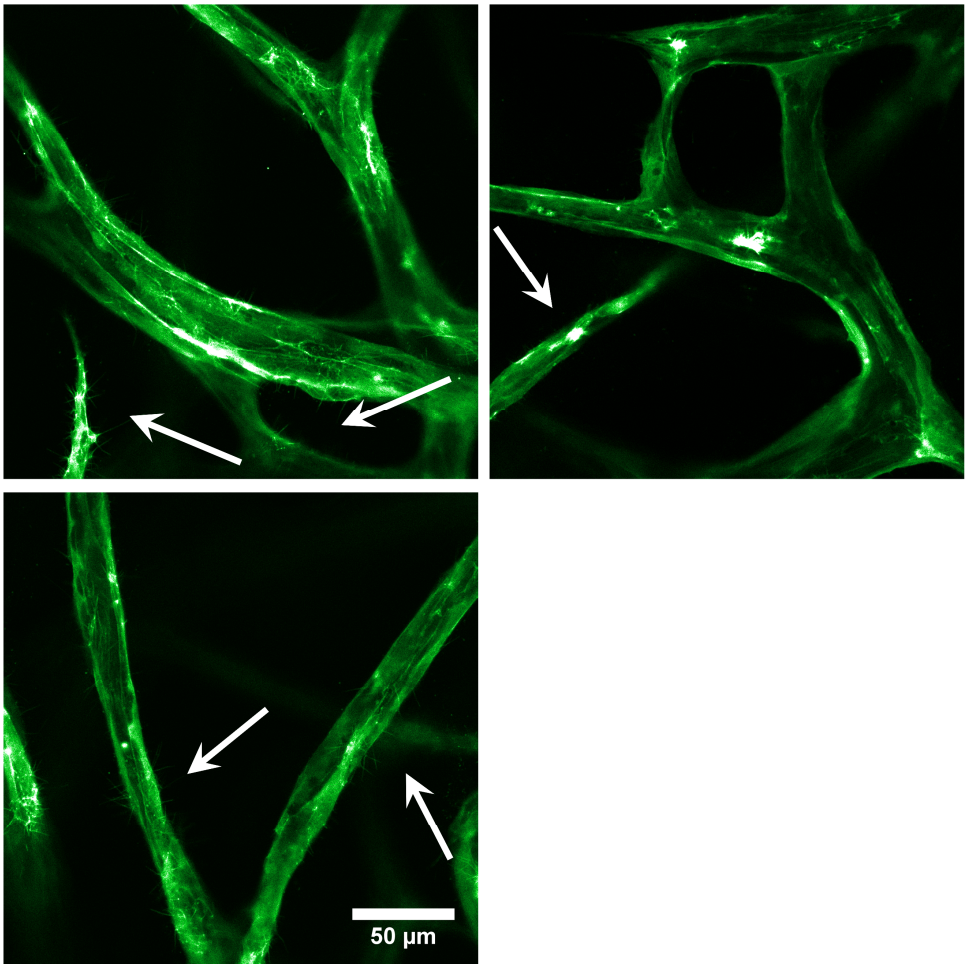

Figure 68 - High magnification (100×) images acquired of vasculature structures formed with GFP-transfected HUVECs. White arrows highlight regions where filopodia can be observed.

Furthermore, the previous issues with effectively imaging HUVECs throughout their culture on-chip was overcome by using HUVECs transfected with GFP. A collaborator acquired several vials of HUVECs (CellSystems) and identified the batch with the highest angiogenic potential using 2D sprouting assays. Several vials of these cells were purchased, then the cells were transfected with GFP. Figure 68 shows high magnification 100 × images acquired of GFP-transfected HUVECs which have formed vessel structures. Close inspection shows that even the sub-micron sized filopodia (white arrows) extending out from sprouting tips can be identified – highlighting the improvement in imaging ability. As an additional alteration to the previous vasculature seeding protocol, the side channels were coated with a mixture of laminin (1mg/mL) and basement membrane extract (BME, Cultrex) to encourage more efficient anastomosis of vessels with the side channels and reduce leakage at the pillar gaps. BME is a soluble form for basement membrane purified from Engelbreth-Holm-Swarm (EHS) tumour. It primarily contains collagen IV, entactin and heparin sulphate proteoglycan – the major constituents of the basement membrane layer which surrounds blood vessels. Both BME and laminin are potent many of the matrix proteins found in the basement membrane layer which surrounds vessels. The presence of these proteins induces endothelial cells to anastomose with the side channels and form a tighter seal when compared to PDMS alone. Finally, it was at this point that the micropillar design changes discussed in section 5.1.4 (page 156) were implemented, to allow for improved permeability measurements. GFP-HUVECs and NHLFs were seeded in this optimised on-chip configuration at a concentration of 1×10^7 cells/mL and 5×10^6 cells/mL, respectively. Cultures were imaged regularly in the same manner as in previous experiments and are shown in Figure 69.

After as little as 48 hours, it was obvious that this experimental setup was significantly more successful than previous experiments with non-GFP HUVECs and HDF cells. HUVECs appeared to form a continuous branching network more readily, potentially a consequence of using lower passage 4 cells. The most significant differences were observed 120 hours after seeding, with HUVECs forming lumenised structures much wider than previously seen. This was suspected to be due to the NHLFs, which may have been secreting increased levels of VEGF to induce vessel expansion. After 168 hours, it appeared that a completely perfusable vasculature network had formed with each pillar gap leading to a vessel lumen.

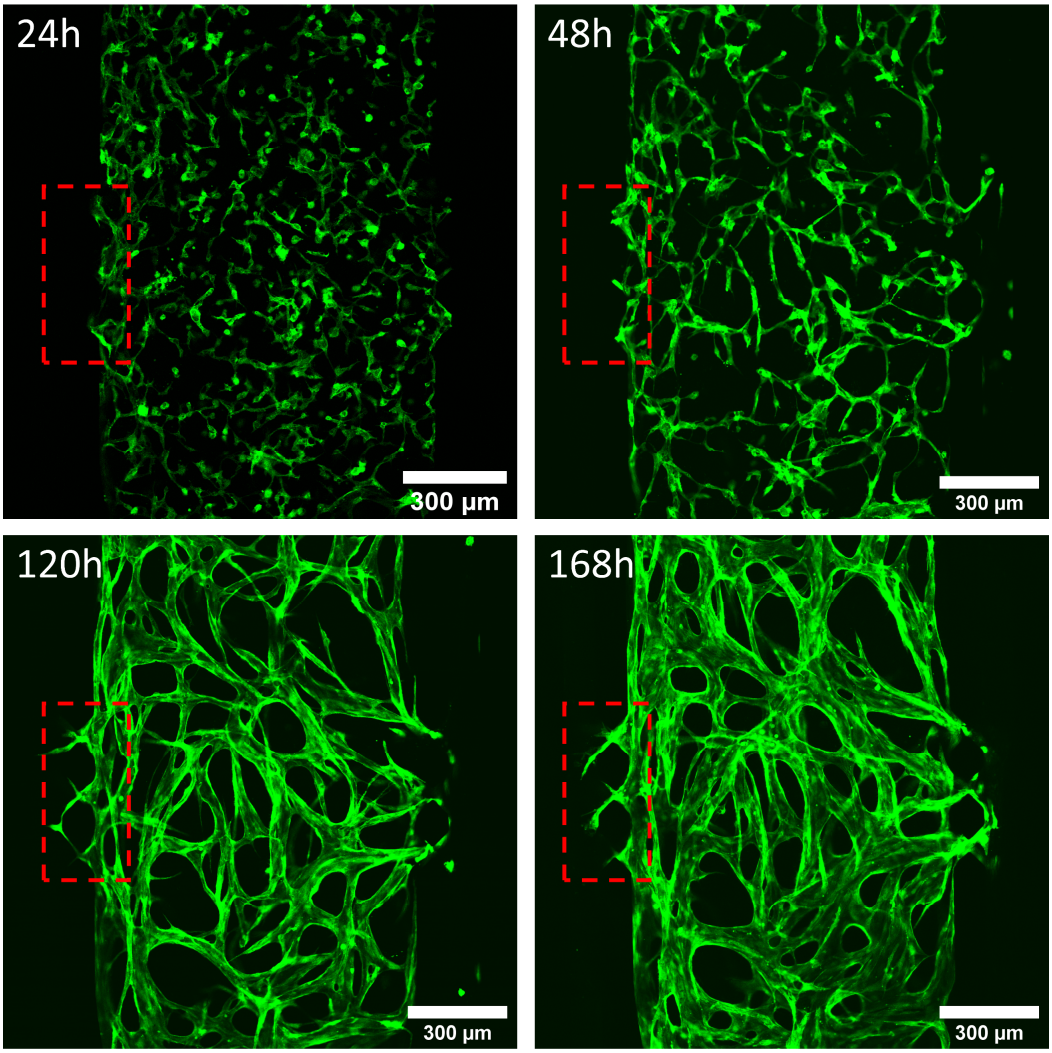

Figure 69 – Confocal microscopy images taken of GFP-HUVEC (p4) – NHLF (p4) on-chip co-cultures after 24, 48, 120 and 168 hours of growth. Red boxes highlight vessel anastomosis at the micropillar regions.

Perfusion this time was tested using liposomes (LSs), as experiments moving forwards would focus on observing the extent of LSs accumulation within the vasculature networks. PBS-LS were produced via extrusion as detailed in section 3.3.4 (page 98), and red fluorescent atto647N lipids were incorporated to allow for imaging of perfusion. 2.2 mL of LSs (10^{11} /mL) were deposited into a high-pressure inlet reservoir and the corresponding outlet was filled with 0.5 mL of media. Intramural flow throughout the network was maximised by reducing inlet and outlet levels in the adjacent channel to 0.3 mL and 0.1 mL. Shortly after flow was initiated, LSs were observed to begin flowing

through the network and into the adjacent side channel. Figure 70 shows images acquired of the vasculature network and LS perfusion. Imaging revealed that the vast majority of the vessels were populated with LSs, with the flow extending outwards from the inlet channel. As with dextran perfusions, some leakage of LSs was observed at the pillar gap region near the channel entrance. The magnitude of this leakage, however, was less significant than previously observed - due to the increased size of the LSs and the increased adherence of cells to the pillars due to side-channel coating. Only vessels close to the chamber entrance were affected by the leakage and reliable measurements for vessel permeability and LS accumulation could still be performed on the majority of vessels across the network.

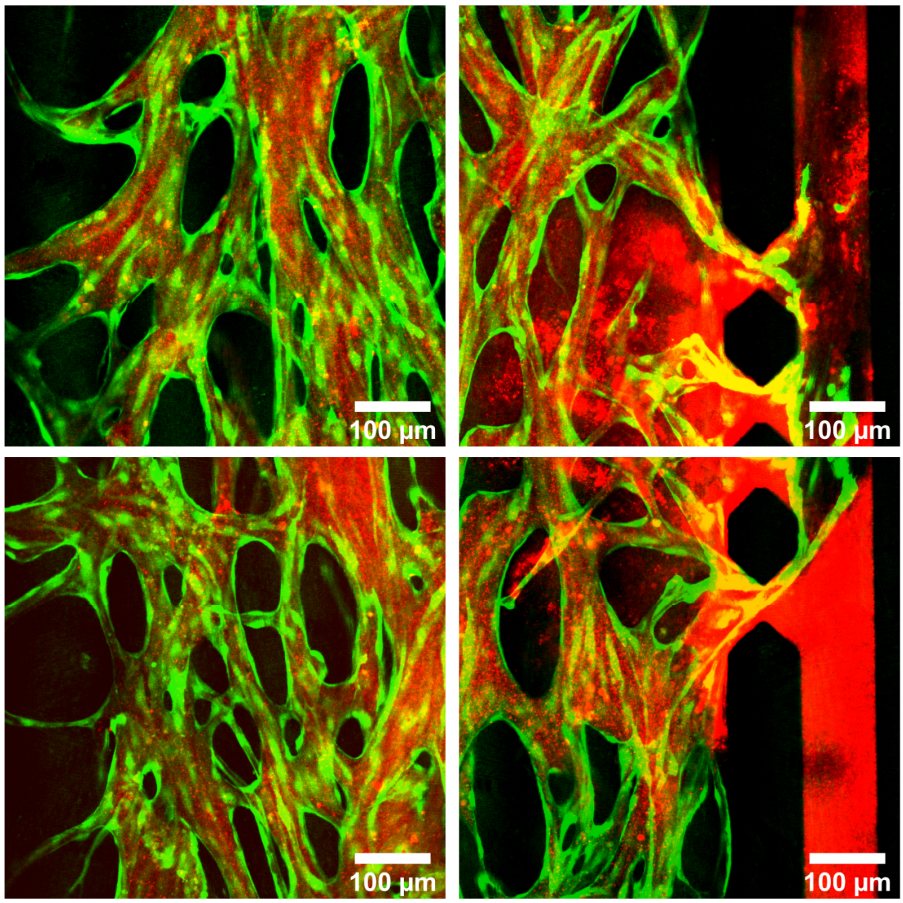

Figure 70 – A series of images showing liposomes (red) perfusing through vasculature networks (green). Images on the left show liposomes entering the network from the side channel at the pillar gaps. Some leakage into the surrounding matrix is observed however this only affect vessels close to the entrance. The vast majority of the network was not affected by this leakage, as shown by the images on the left.

Overall, the use of passage 4 GFP-HUVECs and NHLFs was found to significantly improve the success rate of perfusable network production. Approximately 40 % of all cultures setup were suitable for experimental use, compared to the > 20 % success rate previously observed with HDF cells. With no feasible way of further minimising the leakage at the pillar gaps, it was decided that this experimental setup was suitable for experiments moving forward. Work next focused on characterising the vasculature networks setup to ensure consistent networks could be produced.

5.2.2 Characterising Vasculature Networks

Before perfusion experiments could proceed any further, it was necessary to characterise the vasculature system to ensure that physiologically relevant networks were being produced. Characterisation of vessel/network morphology, vessel permeability and flow rate throughout the network were all performed and compared to *in vivo* values.

5.2.2.1 AngioTool Analysis

AngioTool is a software developed for the quantitative analysis of vasculature networks from microscope images [180]. It allows for the measurement of several parameters, such as network area, vessel length and vascular density, and is a useful tool for quantifying the consistency of network morphologies. Figure 71 shows the AngioTool GUI alongside a depiction of the image analysis workflow. Multiple vessel diameters can be chosen, and in this case, 10 – 150 µm was selected in 5 µm increments – to ensure all vessels are correctly identified. 'Small particles' as large as 200 µm are removed to ensure that no isolated endothelial cells in the side channels are identified as vessels. Finally, the 'Fill Holes' value was set to 1200 µm, to ensure that the intervascular space was correctly removed.

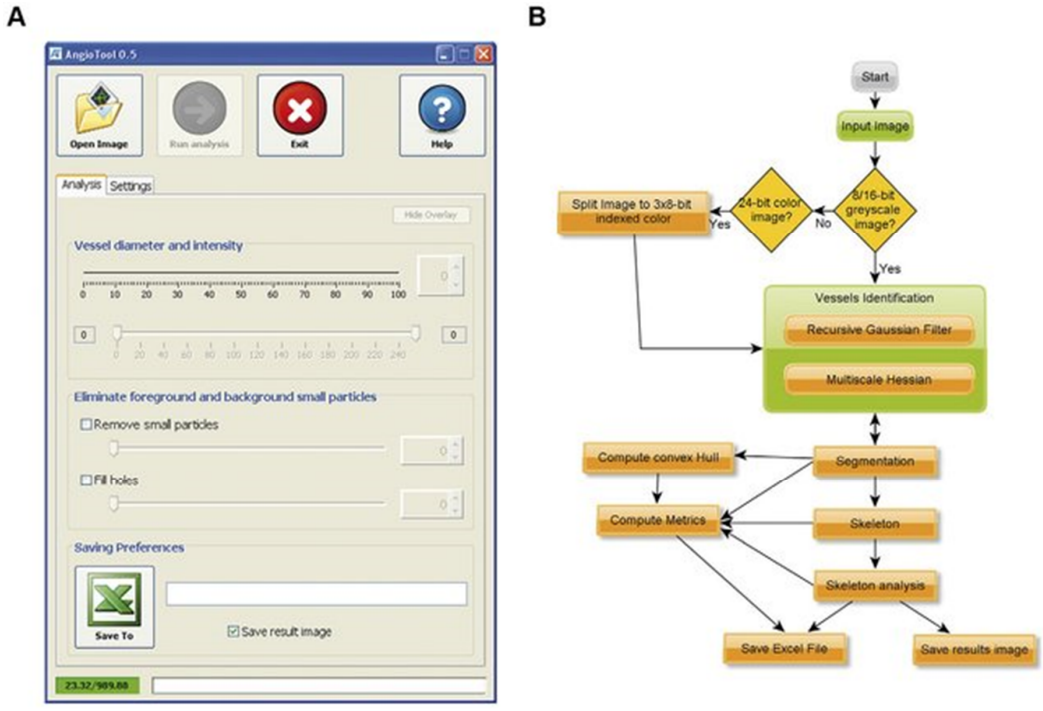

Figure 71 – A) AngioTool GUI showing parameters able to be set before analysis. B) AngioTool image analysis workflow. Images have been taken with permission from the original AngioTool publication by E. Zudaire et al [180].

Prior to analysis, brightness and contrast enhancement was applied to vasculature images captured. This prevented any areas of differing fluorescent intensity on the vessel surface from being misidentified. Figure 72a shows an example of a vasculature network being analysed. The initial fluorescence image captured (left) is enhanced (middle) then analysed with AngioTool (right). Vessels are identified in red, nodes/junctions in blue and the vessel area outlined in yellow.

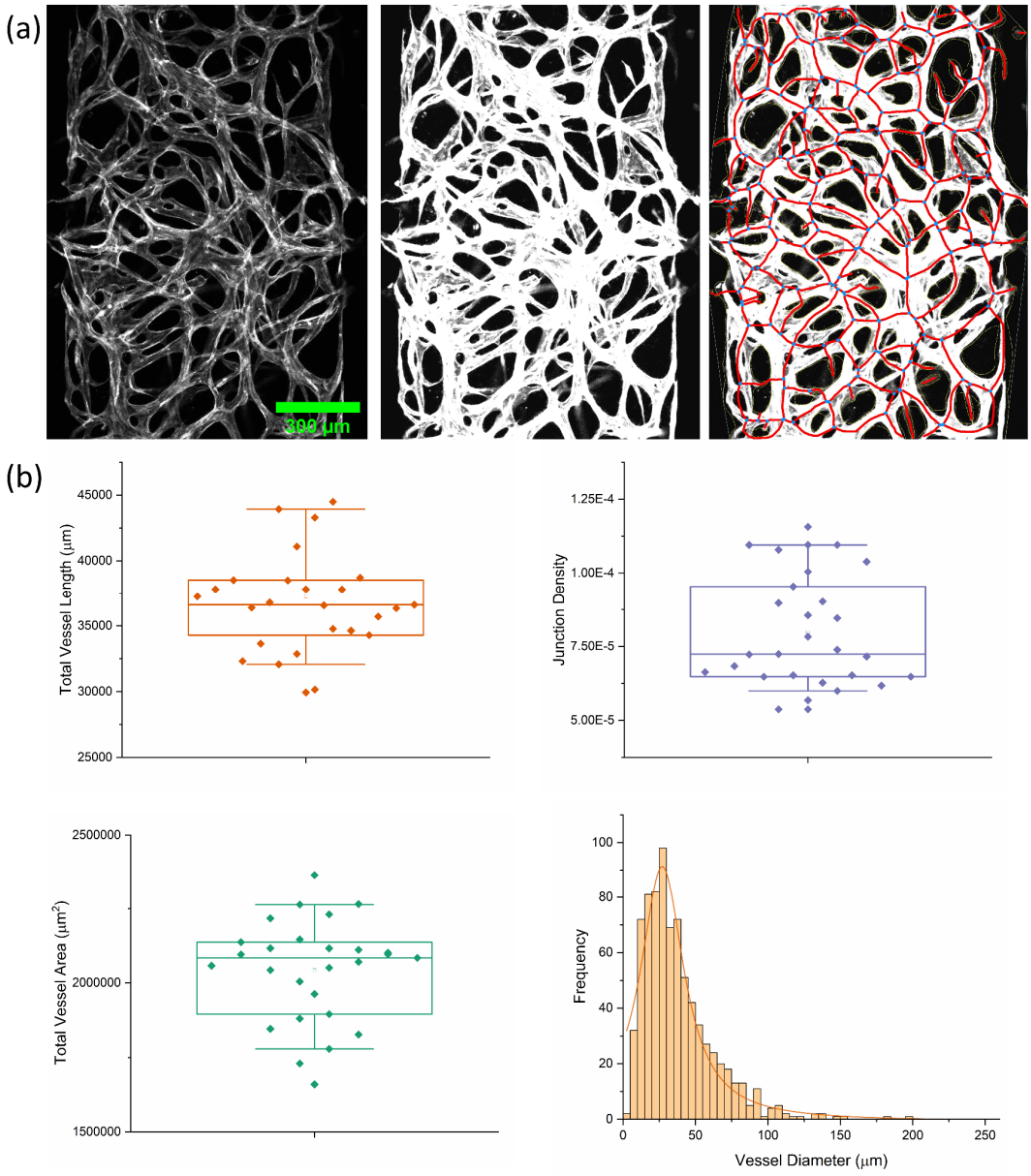

Figure 72 – a) Initial fluorescence image of vasculature network formed with GFP-HUVECs (left) alongside a contrast enhanced image used to ensure accurate AngioTool analysis (middle). Final image shows AngioTool identification of network area (yellow boundary), vessel length (red lines) and network nodes (blue dots). b) Boxplots of total vessel length, junction density and total vessel area determined using AngioTool. Each point represents a single network. The final graph shows a histogram plot of measured vessel diameters fit with a Lorentzian curve to determine the modal vessel diameter.

AngioTool analysis, shown throughout the boxplots in Figure 72b, revealed that on average, networks had a total vessel area of $(2 \pm 0.2) \times 10^6$ µm^2, a total vessel length of $(3.7 \pm 0.5) \times 10^4$ µm^2, and a junction density of $(8.2 \pm 2.8) \times 10^{-5}$ µm^2. Error-values of ~ ± 10 % in vessel area and length showed networks did not vary too drastically between chips. Junction density was found to vary considerably more, with standard deviation values of approximately ± 30%. In addition to these parameters, vessel diameters across each chip were determined using ImageJ to measure the diameters across the skeletonised AngioTool images. An average of 40 vessels were measured for each network and plotted in the histogram also shown in Figure 72b. A Lorentzian fit was used to find the modal average vessel diameter which was 24.5 ± 1.1 µm. 93 % of vessel diameters were found to range between 10 -100 µm, typically matching sizes found in pre-capillary arterioles and post-capillary venules which range up to 100 µm in diameter [181,182]. Whereas only 4.5 % of vessels were found to resemble capillaries with a diameter < 10 µm. This shows that this network more closely resembles a network of pre-capillary vessels rather than a capillary network.

5.2.2.2 Determining Vessel Permeability

As discussed previously, fluorescent Dextrans are commonly used molecules for probing the permeability of vasculature networks. These molecules have a well-defined size and stable fluorescent emission. Determining vasculature permeability is important to demonstrate an effective endothelial barrier has formed and is showing comparable function to vessels *in vivo*. The commonly used permeability model described in equation (5-3) was used to calculate a permeability value using the initial and final fluorescence intensities from around the vessel.

Dextran was flowed into the vasculature network and several regions periodically imaged to observe the gradual leakage of dextran from the vessels. Figure 73 shows an example set of images taken at a single location in 10-minute intervals. The background fluorescence can be observed to increase with each image, whilst the fluorescence inside the vessel remains relatively constant. ImageJ was used to manually identify the regions inside and outside the vessel, then the mean grayscale intensity of each region was quantified. Permeability calculations revealed an average value of $(3.9 \pm 0.6) \times 10^{-7}$ cm/s – showing good agreement with previous values throughout literature, which typically

quote permeability values between (0.5 – 5.6) × 10^{-7} cm/s [65,68,166]. Observation of an effective endothelial barrier by measurement of dextran perfusion exclusively through the vasculature gave confidence in this systems ability to effectively mimic a healthy vasculature network. Work now progressed with the formation of vasculature which displayed properties similar to that of tumour vasculature.

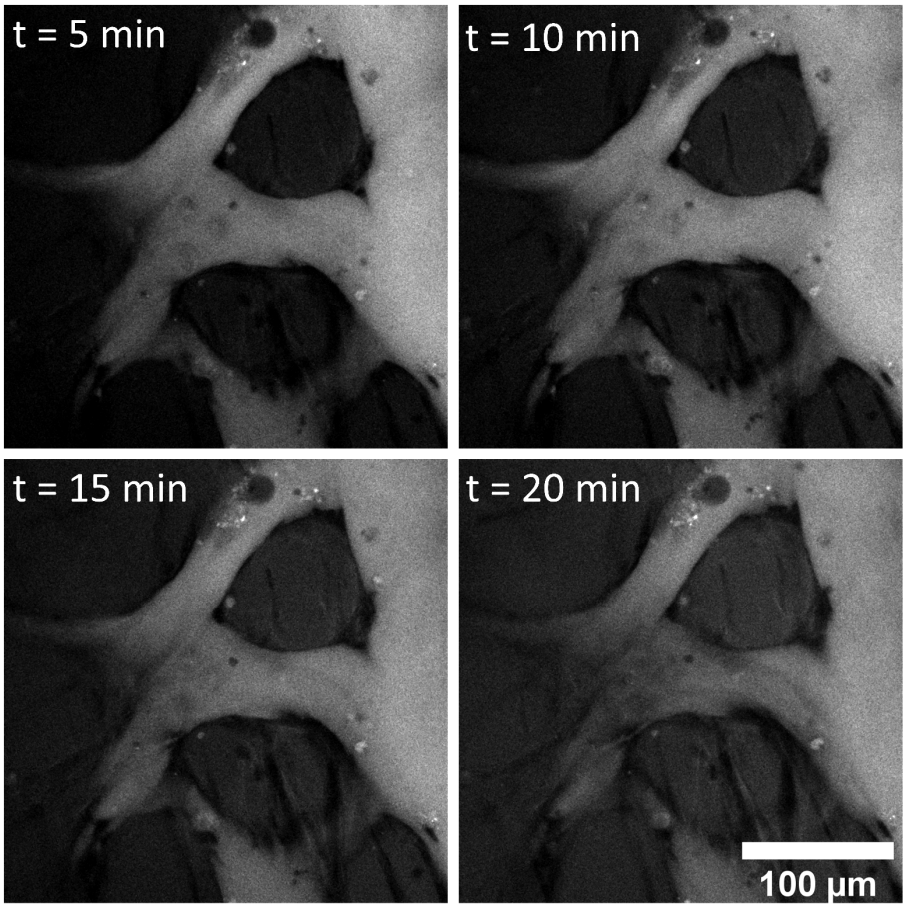

Figure 73 – Time lapse images, taken in 5 minute intervals, of texas red dextran leaking out through the vessel walls. These images were used to determine the permeability coefficient of the vascualture network.

5.2.2.3 Measurement of Flow Rate through Vasculature Networks

Flow throughout the vasculature networks was characterised by again tracking fluorescent beads flowing through the network. Measurement of flow rate was necessary to ensure that flow was occurring at a physiological rate, and in turn, exposing vessels to the appropriate shear stresses. The same 2 µm green, fluorescent fluorospheres were used as with previous experiments. GFP-HUVECs also emitted at the same wavelength however the much brighter beads were very easily distinguished from the vasculature. Intramural flow throughout the network was again maximised by filling reservoirs to the previously described levels (section 5.2.1.3, page 172). Figure 74 shows several frames from videos taken of the beads traversing the network.

Several beads were observed to become trapped within the network, appearing to stick to the surface of the vessels. The majority of beads were able to traverse the network and leave through the channel exit also shown in Figure 74. Beads were observed to show varying speeds as they travelled through vessels of differing diameters due to the differing cross-sectional areas affecting flow rate. Bead trajectories were recorded across 10, 1-minute videos using a frame rate of 5.9 fps. The frame-to-frame velocities were then calculated for each bead by knowing the image scaling and frame time. Overall, it was found that beads travelled on average 91 ± 10 µm/s through the network, with a minimum speed of 16 µm/s and maximum of 230 µm/s being recorded. This value is close to what is found in typical capillary networks, which see velocities between 100 – 1000 µm/s. An approximate value for shear stress was then calculated using the equation for shear stress within a circular cross-section pipe:

$$\tau_w = \frac{4\pi\mu V}{R} \qquad (5\text{-}5)$$

This gave a shear stress value of 0.92 dyne/cm^2 (0.15 – 2.3 dyne/cm^2) which is only marginally lower than the average shear stresses found within capillaries (1 – 100 dyne/cm^2).

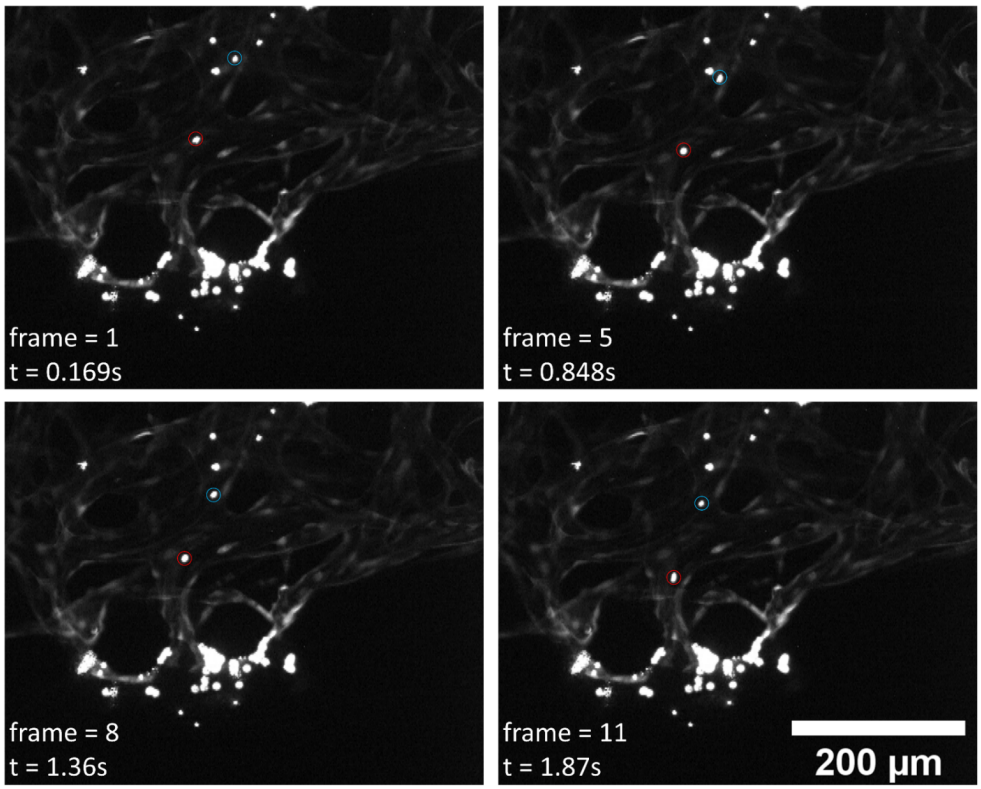

Figure 74 – Images of frames taken from videos captured of green, fluorescent 2 µm beads travelling through vasculature networks. Several beads were observed to become trapped within the after sticking to the vessel walls. 10, 1 minute videos were captured at 5.9 fps then ImageJ used to manually track trajectories.

Low shear stress values are in part due to the difference in viscosity between blood in capillaries, typically found to range between 3.5 – 5.5 mPa.s [183], and media used in this system which is approximately 1 Pa.s. The average shear stress experienced throughout the vasculature is approximately 10 % lower than the physiological range of values typically found throughout vasculature. However, many frame-to-frame velocities measured from bead perfusions recorded velocities that corresponded to significant shear stress values within the physiological threshold. Overall, the sub-optimal shear stress rates will likely result in targeting results showing slightly higher rates of efficacy. This is not of concern as control experiments, such as those without MB or those using isotype antibodies, were included to allow for LS accumulation to be compared across various conditions. Valid conclusions can still, therefore, be drawn regarding the increased accumulation of LSs when targeting and MB are used.

5.3 Recreating Tumour Vasculature using Tumour Cell Media (TCM)

As discussed throughout section 2.1.2 (page 54), the survivability of cancer is often attributed to the ability of tumour cells to recruit healthy cells such as fibroblasts and macrophages to the tumour site and induce them to differentiate to display pro-tumourigenic phenotypes. This recruitment is primarily driven by the pro-inflammatory cytokines and growth factors secreted by tumour cells. As a result, the indirect influence of tumour cells on healthy cell cultures has been of recent investigation. Various studies have conditioned several types of healthy cells with media taken from tumour cell cultures to observe the paracrine effects of tumours. For example, Katanasaka et al used tumour cell media (TCM) taken from HT1080 cells to condition HUVECs. This resulted in increased proliferation and angiogenic tube formation when compared with VEGF stimulated cells. Analysis of protein expression found that most differentially expressed proteins were downregulated (88%) with TCM, compared to an upregulation of 59% when VEGF was used – highlighting the importance of using the correct angiogenic stimuli [184]. Hida et al also investigated the effects of conditioning HUVECs, finding that endothelial cells acquire drug-resistant characteristics when cultured in TCM. It was discovered that these characteristics are reversed when cells are re-cultured in TCM-free media, revealing the reversible effects of TCM conditioning [185]. The presence of high levels of VEGF and other various inflammatory cytokines (CXCL1, 2) have been reported in media taken from patient-derived colorectal tumours and have been proposed as the main drivers of endothelial cell conditioning [186]. Sawa-Wejksza et al have shown that media taken from several colorectal cell lines (HT29, LS180, SW949 and SW620) could be used to induce THP-1 monocytes to differentiate into a non-adherent population of M1 and M2 macrophages, consistent with populations of tumour-associated macrophages found *in vivo* [187]. These observations, along with various other studies [188,189], have demonstrated that the cytokines and soluble factors tumour cells secrete influence tumour-associated cells in a paracrine fashion, and can be used to condition cells to display similar properties to *in vivo* tumour-associated cells. This same premise was applied to the microfluidic vasculature system developed throughout this chapter - with TCM being used to condition healthy vasculature networks to display tumour-vasculature-like properties. The direct incorporation of tumour cells within vasculature

models presents many challenges to ensure that the cultures progress in a similar fashion to tumours growing *in vivo*. Optimisation of seeding densities and timing is required to prevent tumour cells from overwhelming the healthy vascualture. Conversely, if cells are seeded too sparsely, then tumour development and influence of the vasculature will be limited. The method of indirectly inducing vascualture to display tumour-associated properties avoids many of these issues, whilst still allowing evaluation of targeted therapies - such as those using MBs.

One receptor of recent interest in tumour vasculature studies is integrin $\alpha_v\beta_3$, an ECM-binding receptor found primarily on endothelial cells. Integrin $\alpha_v\beta_3$ binds to various matrix proteins found around newly forming blood vessels, such as fibrinogen, vitronectin and fibronectin [190]. As a result, integrin $\alpha_v\beta_3$ has been found to be crucial for angiogenesis and blocking of the signalling pathway has been found to reduce neovascularisation in tumour tissues [191–194]. The constant pro-angiogenic signalling induced by tumour cells results in $\alpha_v\beta_3$ being upregulated in tumour vasculature, presenting it as a potential target for drug-loaded carriers [195,196]. Integrin $\alpha_v\beta_3$ upregulation in mammary fibroblasts conditioned with pro-inflammatory breast cancer factors has been previously reported, indicating that soluble factors secreted by tumour cells can affect integrin expression [197].

This section contains results and observations made when TCM taken from HCT116 cell cultures was used to condition HUVEC cultures and vasculature networks. Experiments began with simple 2D HUVEC models then progressed to more complex co-cultures and finally to observation of the effects of TCM in on-chip vasculature cultures. The effect of TCM on $\alpha_v\beta_3$ expression was of particular interest as this integrin will be investigated as a potential site for targeting MBs and LSs. Furthermore, an increase in $\alpha_v\beta_3$ expression is correlated with increased rates of angiogenesis [192,194,195]. Therefore, any observed increase in $\alpha_v\beta_3$ expression would not only indicate that TCM was inducing tumour-like levels of integrin expression, but also that TCM was driving increased rates of angiogenesis.

5.3.1 Observation of On-chip Integrin $\alpha_v\beta_3$ Expression

To first observe the extent of integrin $\alpha_v\beta_3$ expression in the healthy microfluidic vasculature cultures shown throughout the previous section, cultures were fixed and immunostained with an antibody against integrin $\alpha_v\beta_3$ (methods section 3.5.2, page 111). An Alexa Fluor 647 secondary antibody was used to allow for simultaneous fluorescent imaging of integrin emission and GFP-HUVEC emission. Figure 75 shows fluorescent images captured of integrin expression (red) within microfluidic vasculature networks.

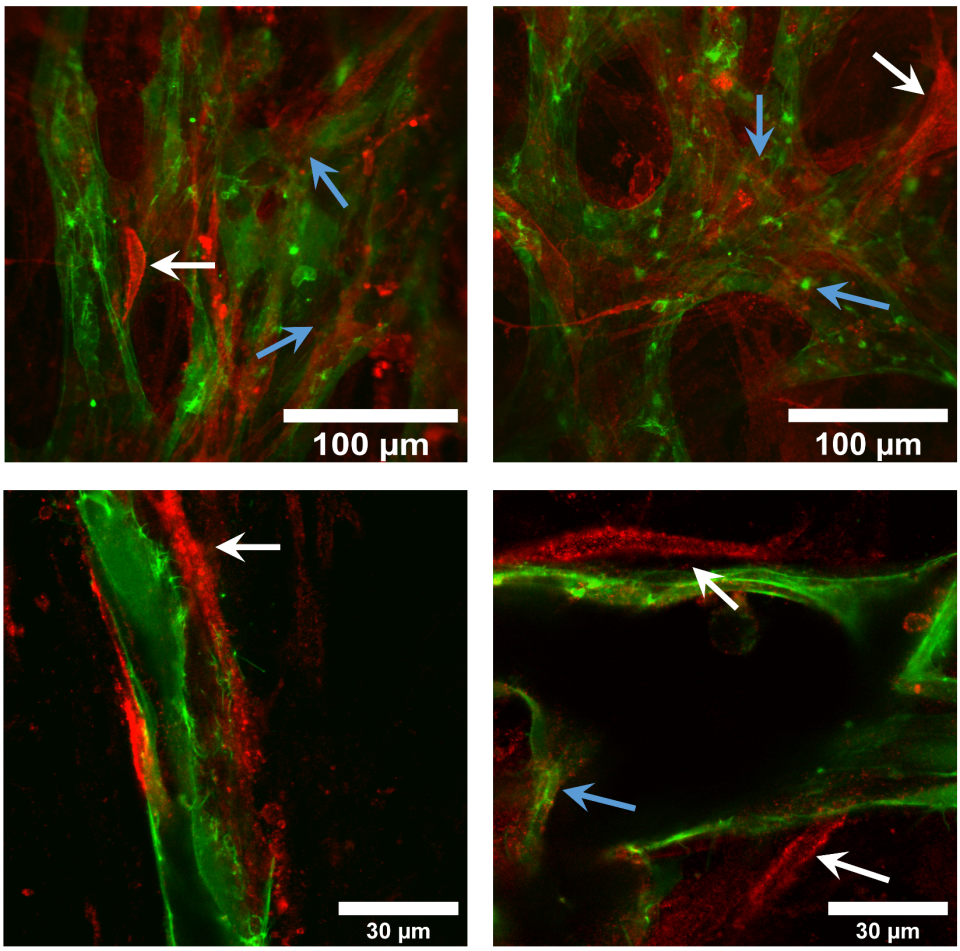

Figure 75 – Fluorescent confocal microscopy images taken of microfluidic vasculature cultures fixed and immunostained against integrin $\alpha_v\beta_3$. Integrin emission (red) can be observed to be co-localised with GFP-HUVECs (blue arrows) along with the crescent-shaped NHLF cells supporting the vasculature (white arrows).

Co-localisation of GFP-HUVEC emission (green) and integrin emission (red) demonstrated that integrin $\alpha_v\beta_3$ is being expressed across the endothelial surface (blue arrows), as expected. Intense fluorescent emission of crescent-shaped cells supporting the vasculature was also observed (white arrows) which were attributed to NHLFs. This is consistent with previous observations throughout literature, which have observed integrin expression in supporting stromal cells due to their binding to similar ECM proteins as endothelial cells.

5.3.2 Inducing Integrin $\alpha_v\beta_3$ upregulation with TCM

5.3.2.1 Upregulation in HUVEC Monolayers

To first determine the effects of TCM on integrin $\alpha_v\beta_3$ expression, GFP-HUVECs were grown in a 24-well plate for 4 days, using EGM: TCM ratios of [1:0], [2:1], [1:1] and [1:2]. As described in section 3.2.7.5 (page 94), TCM media was taken from confluent HCT116 cell cultures grown for 4 days without a media change, then centrifuged at 15,000g for 10 minutes to remove all dead cells and debris. HUVEC media changes were performed after 48 hours, then cells were fixed and immunostained after a further 48 hours, following the methods outlined in section 3.2.6.2 (page 91).

Bright-field imaging revealed that cells had grown faster in media containing a higher ratio of EGM, suggesting that the growth factors contained within the media drove cell proliferation faster than any soluble factors secreted by HCT116 cells. Imaging of immunofluorescence, shown in Figure 76a, appeared to reveal increased levels of $\alpha_v\beta_3$ integrin expression with increasing TCM concentrations. This was observed by an increasing intensity of patchwork-like emission around the edge of each cell. This experiment was repeated, and the immunofluorescent emission was analysed using flow cytometry.

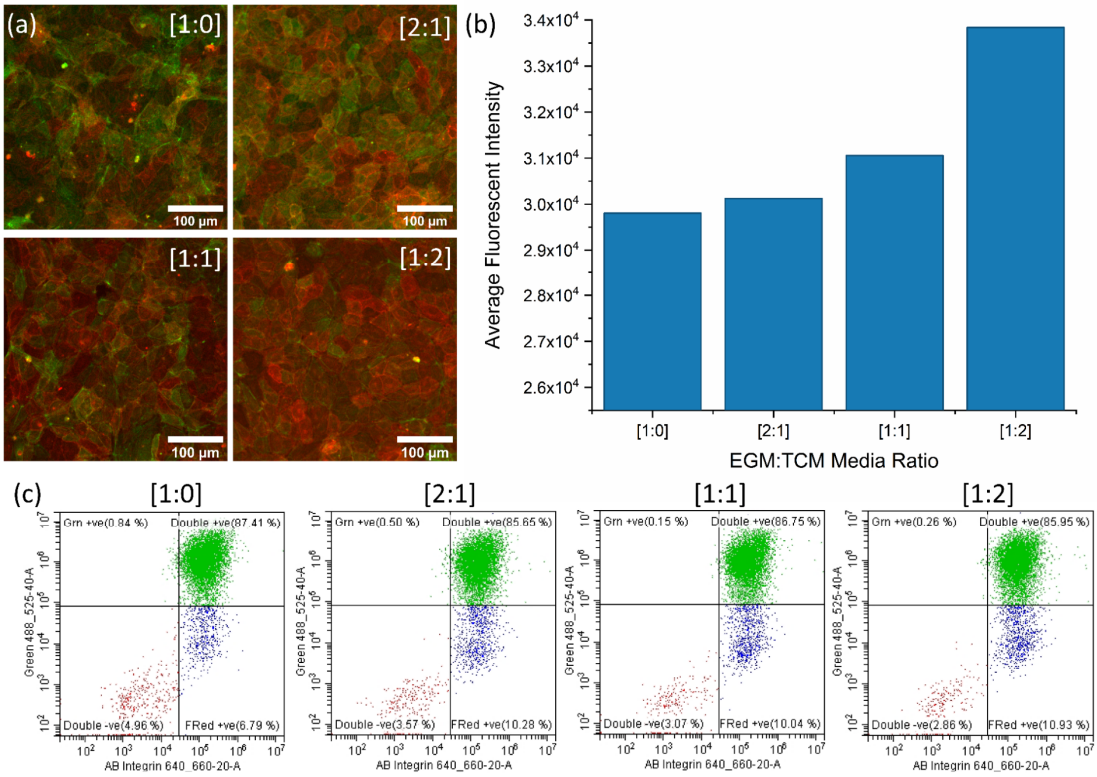

Figure 76 – a) Fluorescent images of GFP-HUVEC monolayers immunostained for $\alpha_v\beta_3$ integrin expression (red). HUVECs were grown in a range of [EGM:TCM] media ratios, as labelled. b) Graph of $\alpha_v\beta_3$ integrin immunofluorescent emission quantified using flow cytometry. c) Flow cytometry distributions showing red and green fluorescence emission for cells grown in each media ratio. The top right quadrant shows double positive (red and green) cells and can be seen to shift right with increasing TCM concentrations, showing increased integrin expression.

Figure 76b and c show the flow cytometry results, which show increased $\alpha_v\beta_3$ integrin expression with increasing TCM concentrations. The highest TCM media ratio resulted in a 14 % increase in $\alpha_v\beta_3$ emission compared to the EGM only condition. Whilst this experiment revealed that TCM could induce increased $\alpha_v\beta_3$ expression, the use of cell monolayers limited the validity of the results. Integrin $\alpha_v\beta_3$ primarily binds endothelial cells to ECM proteins which will be nominally present in the above setup due to the lack of fibroblasts or hydrogel. Experiments, therefore, proceeded to observe the effects of TCM on HUVECs cultured alongside NHLFs in the same configurations previously used in section 5.2.1.1 to assess the angiogenic potential of endothelial cells and fibroblasts.

5.3.2.2 Upregulation in NHLF - HUVEC Co-cultures

NHLF cells were first seeded in a 24-well plate and allowed to form a complete monolayer for 4 days. Over this time, fibroblasts will secrete ECM proteins providing a scaffold for HUVECs to adhere and interact with. After 4 days, HUVECs were seeded onto the fibroblast monolayers and the same range of EGM: TCM media ratios were added to each set of wells. Confocal microscopy images of GFP-HUVECs, shown in Figure 77, were taken 48 and 96 hours after HUVEC seeding, to observe the effect of differing TCM concentrations of HUVEC morphology and growth. Comparison of these images with those taken of HUVECs grown on a layer of HDF cells (shown in Figure 63) reveals significant differences in HUVEC morphologies. HUVECs grown on HDF monolayers formed long branching structures as expected however, HUVECs grown on NHLF (in EGM-2 only) appeared to assemble into closed clusters resembling 2D monolayer morphologies. This monolayer-like morphology could be an indication that sufficient matrix had not been produced by the fibroblasts to support HUVEC branching.

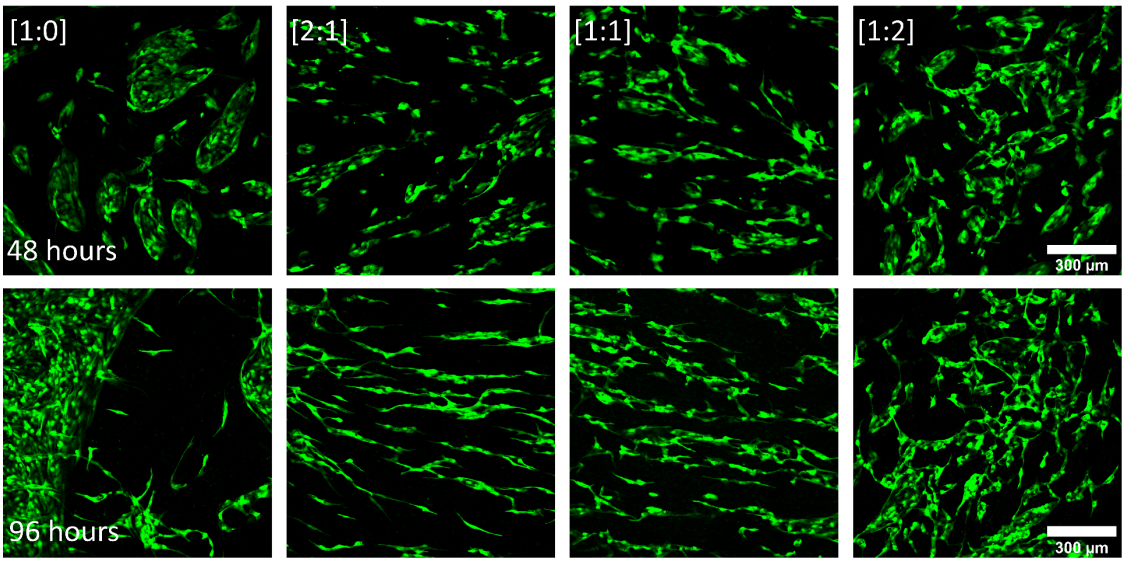

Figure 77 - Confocal microscopy images acquired of GFP-HUVECs growing on NHLF monolayers. Co-cultures were grown in a range of [EGM:TCM] ratios and their morphology imaged 48 and 96 hours after HUVEC seeding.

The use of increasing TCM concentrations appeared to result in cells moving away from this closed structure morphology and towards a branched network. TCM induced more branching and elongation however the concentration of TCM used did not appear to have a significant effect after only 48 hours. Observations after 96 hours revealed further differences in HUVEC morphology between EGM-2 only and TCM containing conditions. HUVECs formed increasingly larger closed structures when grown in EGM-2, with relatively few elongated HUVECs around the structure periphery. HUVECs grown in TCM media continued to form branched networks which also appeared to align in parallel tracks. This alignment would be expected to occur under flow conditions but not in a static environment such as this. It has been reported that fibroblasts associated with aggressive breast cancers deposit collagen matrix with the fibres in tracks perpendicular to the endothelium. This aids cancer cell motility and enhances metastatic ability [100,198]. TCM conditioned fibroblasts may be displaying the same behaviour in this setup, causing HUVECs to adhere and elongate to the collagen in parallel tracks.

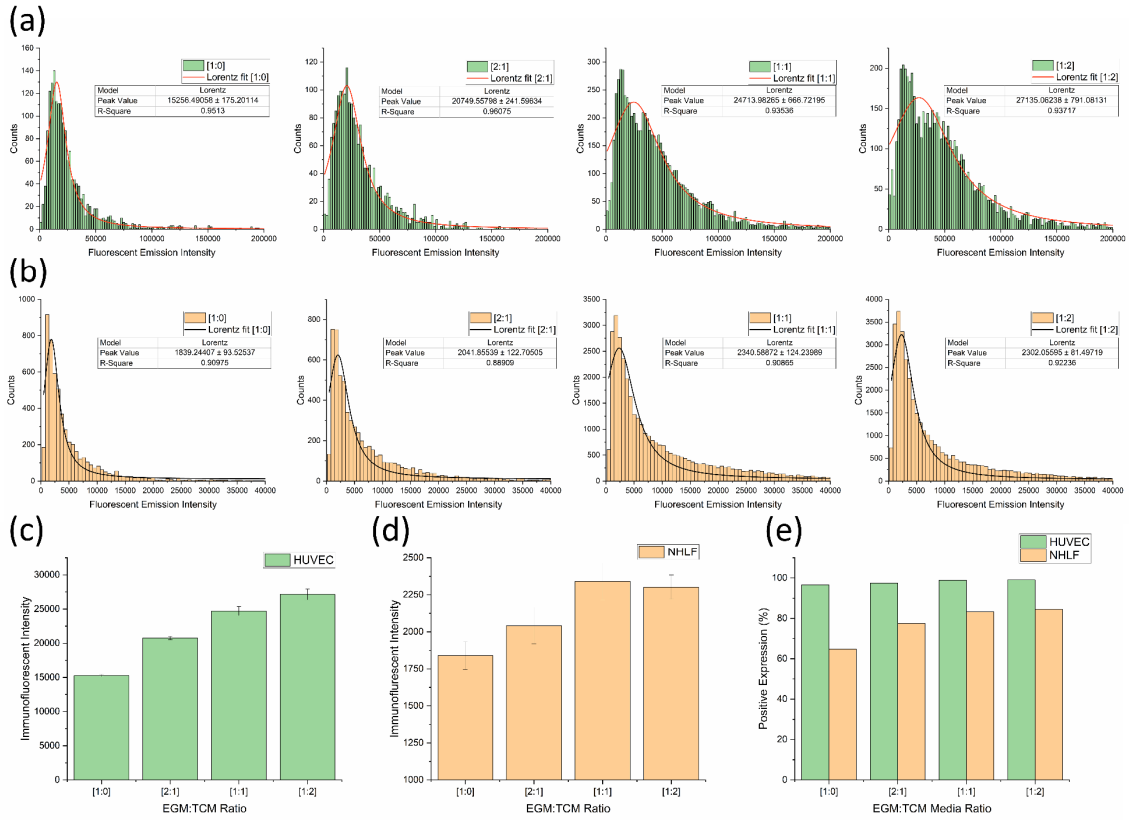

Figure 78 – Flow cytometry data showing (a) A series of graphs showing histogram plots and peak fits of $\alpha_v\beta_3$ integrin immunofluorescent emission intensities from GFP-HUVECs. (b) A series of graphs showing histogram plots and peak fits of $\alpha_v\beta_3$ integrin immunofluorescent emission intensities from NHLFs. The lowest TCM concentrations ([1:0]) are shown on the left and highest TCM concentrations ([1:2]) on the right. (c) A graph of peak immunofluroescent intensities for GFP-HUVECs. An increase of 78 % was observed from the no-TCM [1:0] value (15,300 ± 200) to the highest [1:2] TCM value (27,100 ± 800). (d) A graph of peak immunofluroescent intensities for NHLFs. An increase of 26 % was observed from the no-TCM [1:0] value (1800 ± 100) to the highest [1:2] TCM value (2300 ± 100). (e) A graph showing the percentage of HUVECs and NHLFs positive for $\alpha_v\beta_3$ integrin expression for the same range of [EGM:TCM] ratios. The vast majority (95 % +) of HUVECs were positive regardless of TCM concentration whereas NHLFs show an increase in cells positive for $\alpha_v\beta_3$ integrin expression from 65 % up to 85 %.

4 days after HUVEC seeding, cells were washed, detached from the wells and immunostained for $\alpha_v\beta_3$ integrin following the methods outlined in section 3.2.6.2 (page 91). Flow cytometry was then used to determine the intensity of $\alpha_v\beta_3$ integrin expression in both HUVECs and NHLFs – with the GFP expressing HUVECs allowing each cell type to be distinguished. As described in section 3.2.6.2 (page 91), immunofluorescent $\alpha_v\beta_3$ integrin intensity values for each cell type were plotted as histograms and a peak fitting function was used to find the modal emission intensity. This allowed for the expression of $\alpha_v\beta_3$ to be accurately determined for each EGM:TCM ratio. Figure 78a and b show histogram plots overlayed with the Lorentz peak functions fitted to each distribution for the four EGM:TCM media ratios previously used, for HUVEC and NHLF, respectively. An increase in emission intensity can be observed, most notably in HUVECs, with the distributions broadening as a result of higher intensity values. Figure 78c and d show the peak intensity values for each media ratio, for HUVECs and NHLFs, respectively. Increasing TCM concentrations induced both HUVECs and NHLFs to increase their $\alpha_v\beta_3$ integrin expression. Overall, HUVEC immunofluorescent intensities were observed to be approximately 10 x higher than that of NHLFs (~20,000 U compared to ~2000 U) – demonstrating that integrin $\alpha_v\beta_3$ is primarily expressed by endothelial cells in an angiogenic state. The use of [2:1] media resulted in a 36 % and 11 % increase in expression intensity for HUVECs and NHLFs, respectively. $\alpha_v\beta_3$ integrin expression peaked in cells grown in the highest TCM concentration, which showed a 78 % and 26 % increase in HUVECs and NHLFs compared to the EGM only condition.

The percentage of cells positive for $\alpha_v\beta_3$ integrin expression was also analysed to observe the effect of TCM on the amount of expression as well as the intensity. Observation of the percentage of cells positive for $\alpha_v\beta_3$ integrin expression, shown in Figure 78e, revealed that close to all HUVECs were expressing $\alpha_v\beta_3$ with an average of 97 % positive. This is expected as $\alpha_v\beta_3$ is known to be crucial for angiogenesis and HUVECs grown in this configuration will be in an angiogenic state. Observation of NHLF expression showed that approximately 65 % were positive for $\alpha_v\beta_3$ integrin expression when grown in EGM-2 only. This was observed to steadily increase with increasing TCM concentrations up to a maximum of 85 %. Comparison with results observed in this cellular configuration and results observed in the HUVEC only configuration showed that low TCM ratios had a greater impact on $\alpha_v\beta_3$ integrin expression when HUVECs were grown alongside NHLFs.

Expression in HUVECs was also observed to be initially lower in the EGM only conditions when they were grown alongside NHLFs, however, the direct comparison is difficult as immunostaining efficiency may have differed between experiments. Overall, results across both configurations have revealed that conditioning cells with TCM results in upregulation of $\alpha_v\beta_3$ integrin expression and this upregulation is not exclusive to HUVECs alone.

5.3.2.3 Upregulation in NHLF – HUVEC Co-cultures with Fibrin

GFP-HUVEC cells were also embedded in a fibrin matrix and seeded on top of a monolayer of NHLF to further investigate the presence of fibrin on the magnitude of $\alpha_v\beta_3$ upregulation. This configuration is closest to that used for the on-chip formation of vasculature, with the main difference being the NHLFs seeded as a monolayer and not within the fibrin gel. As described previously, fibroblasts are able to influence endothelial cells in a paracrine manner meaning the difference in HUVEC behaviour in this configuration should be minimal. After 4 days of NHLF growth, the fibrin clots were deposited into the wells and allowed to polymerise before media was added. As in the previous section, EGM:TCM media ratios of [1:0], [2:1], [1:1] and [1:2] were used.

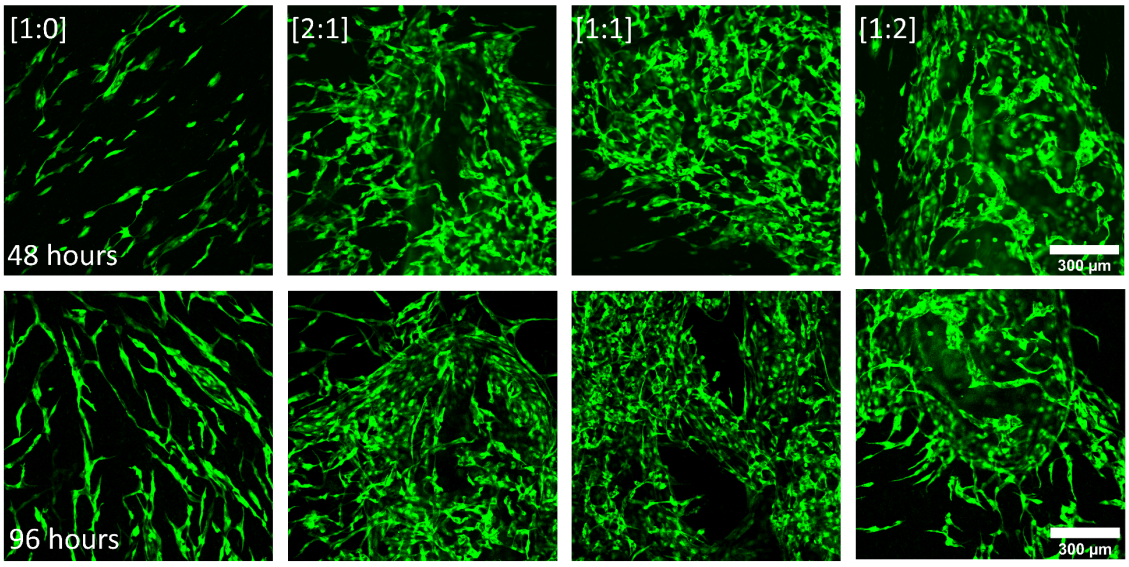

Figure 79 - Confocal microscopy images acquired of GFP-HUVECs embedding fibrin and growing on NHLF monolayers. Co-cultures were grown in a range of [EGM:TCM] ratios and their morphology imaged 48 and 96 hours after HUVEC seeding.

Images taken 48 hours after fibrin deposition, shown in Figure 79, revealed that HUVECs were showing similar behaviour to on-chip cultures, with cells elongating to form a continuous branched network. Imaging after 96 hours showed that cultures had progressed into continuous branched networks as expected. The use of [1:2] TCM media appeared to result in acceleration of vessel formation and the development of more mature vessels in the centre of the fibrin clot. After 96 hours, cells were again prepared for flow cytometry now using Nattokinase, an enzyme that digests fibrin, to detach cells from the wells and digest the fibrin clots containing the HUVECs. After a 60 minute incubation, cells appeared to be free of the fibrin clot and ready for immunostaining.

Flow cytometry was repeated as before with the results shown in Figure 80. Figure 80a and b show histogram plots overlayed with the Lorentz peak functions fitted to each distribution for the four EGM:TCM media ratios previously used, for HUVEC and NHLF, respectively. An increase in emission intensity can be observed, again most notably in HUVECs, with the distributions broadening as a result of higher intensity values. Figure 80c and d show the peak intensity values for each media ratio, for HUVECs and NHLFs, respectively. As with the previous non-fibrin containing assay, increasing TCM concentrations induced both HUVECs and NHLFs to increase their $\alpha_v\beta_3$ integrin expression however, the trend and magnitude of the increase was significantly different. HUVECs grown in EGM only in a fibrin clot were shown to express $\alpha_v\beta_3$ integrin with 44 % more intensity compared to HUVECs grown without fibrin (15,300 ± 200 compared to 22,000 ± 500). The increase in this expression in response to TCM was significantly more substantial, with a 290 % increase observed with [2:1] EGM:TCM media (60,000 ± 500) and a 430 % increase observed with the highest, [1:2] EGM:TCM media ratio (81,000 ± 2000). NHLF expression intensity was also observed to increase drastically when fibrin was incorporated into the system. Without any TCM present, NHLF emission intensity was over 10 × the value observed in the previous cultures (19,000 ± 300 compared to 1800 ± 100) and showed a similar intensity to that of the HUVECs. Unexpectedly, NHLF emission intensity was relatively unchanged in response to [1:2] and [1:1] EGM:TCM media, however, an increase of 75 % (up to 35,000 ± 6000) was then observed with [1:2] EGM:TCM media.

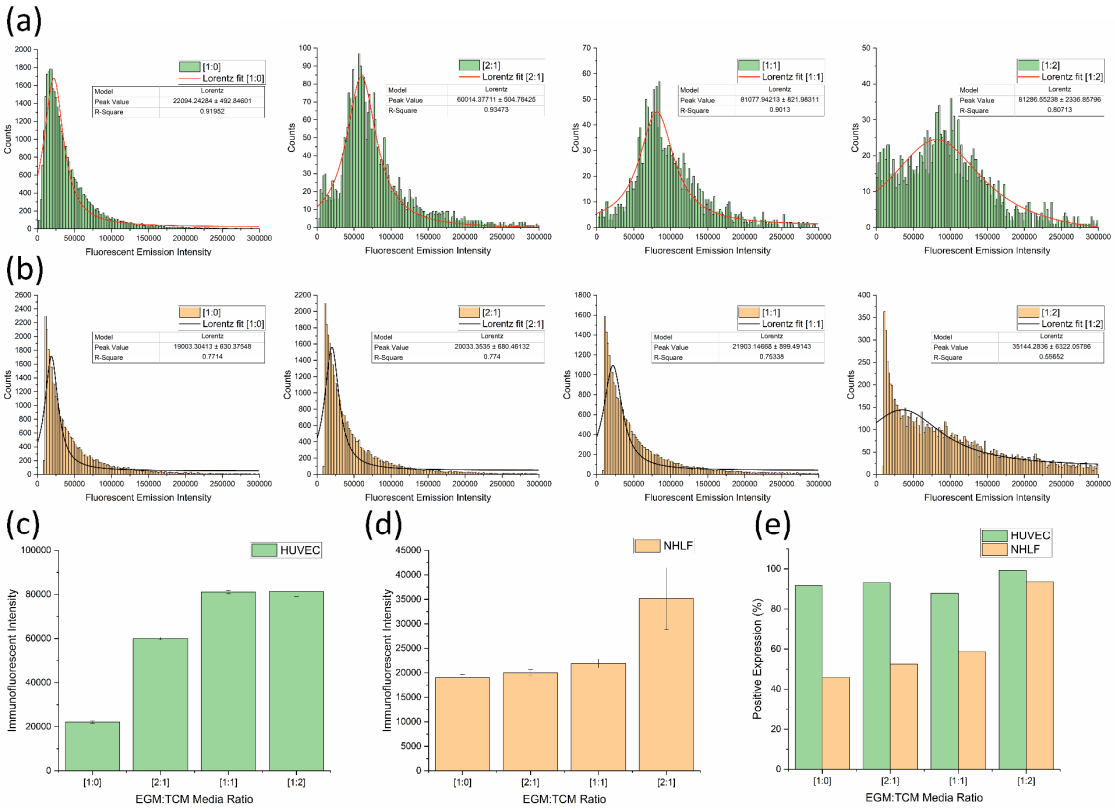

Figure 80 - Flow cytometry data for fibrin-containing cutlures showing (a) A series of graphs showing histogram plots and peak fits of $\alpha_v\beta_3$ integrin immunofluorescent emission intensities from GFP-HUVECs. (b) A series of graphs showing histogram plots and peak fits of $\alpha_v\beta_3$ integrin immunofluorescent emission intensities from NHLFs. The lowest TCM concentrations ([1:0]) are shown on the left and highest TCM concentrations ([1:2]) on the right. (c) A graph of peak immunofluroescent intensities for GFP-HUVECs. An increase of 430 % was observed from the no-TCM [1:0] value (22,000 ± 500) to the highest [1:2] TCM value (81,000 ± 2000). (d) A graph of peak immunofluroescent intensities for NHLFs. An increase of 75 % was observed from the no-TCM [1:0] value (19,000 ± 300) to the highest [1:2] TCM value (35,000 ± 6000). (e) A graph showing the percentage of HUVECs and NHLFs positive for $\alpha_v\beta_3$ integrin expression for the same range of [EGM:TCM] ratios. The vast majority (90 % +) of HUVECs were positive regardless of TCM concentration whereas NHLFs show an increase in cells positive for $\alpha_v\beta_3$ integrin expression from 65 % up to 85 %.

Observation of the percentage of cells positive for $\alpha_v\beta_3$ integrin expression, shown in Figure 78e, revealed that close to all HUVECs were expressing $\alpha_v\beta_3$ with an average of 92 % positive. Observation of NHLF expression showed that approximately 45 % were initially positive for $\alpha_v\beta_3$ expression which was then observed to increase dramatically up to 94 % when a [1:2] media ratio was used. One potential explanation for the low expression is that the HUVEC-containing fibrin clot was difficult to spread evenly across the NHLF monolayer, meaning the fibrin was not in contact with all fibroblasts. Many of the fibroblasts not in contact with HUVECs or fibrin matrix may then not be positive for $\alpha_v\beta_3$ integrin expression. This may also have resulted in the unexpected plateau in expression intensity observed for NHLFs from [2:1] and [1:1] cultures. It should also be noted that the use of NattoKinase to dissolve the fibrin clot was not as successful as appeared. Flow cytometry measurements revealed significantly lower HUVEC cell counts than in the previous section. The overall result of this meant that very few positive (<100) HUVEC events were used for the flow cytometry data.

Overall, flow cytometry results throughout this fibrin-containing angiogenesis assay suggest that the presence of fibrin facilitates the upregulation of integrin $\alpha_v\beta_3$. Fibrin has not been reported to be a direct ligand of integrin $\alpha_v\beta_3$ however, fibrinogen, the precursor used to form fibrin, has been reported to bind strongly to integrin $\alpha_v\beta_3$. Residual unpolymerised fibrinogen in the clot may have allowed for increased integrin $\alpha_v\beta_3$ expression in both HUVECs and NHLFs. This would explain the overall baseline increase in the EGM only conditions but would not explain why HUVEC expression increases so dramatically with TCM concentrations. Integrin $\alpha_v\beta_3$ expression is directly associated with angiogenesis, and fibrin is known to be a crucial early matrix protein required for angiogenesis in wound healing. It is reasonable to attribute the observed increase in integrin expression to the result of fibrin allowing HUVECs to undergo increased rates of angiogenesis when compared to the previous assay which did not include fibrin. This agrees well with imaging observations which found more advanced vessel structures in the fibrin cultures (Figure 79) compared to the monolayer-like structures in the non-fibrin cultures (Figure 77). The fibrin clot configuration also closely matches the on-chip seeding configuration which is known to result in the product 3D perfusable vessels whereas the non-fibrin angiogenesis assay merely produces a 2D branched network of vessels.

5.3.3 Conditioning Vasculature Networks with TCM

The effect of conditioning on-chip vasculature cultures with TCM media was investigated to observe whether the effects of TCM conditioning observed throughout previous studies would extend to affect the characteristics of entire vasculature networks. Networks were grown as usual for the first 48 hours to allow cultures to become established, then the EGM-2 (-VEGF, -FGF) media was replaced with media containing TCM. The basal media for EGM-2 was diluted with TCM then supplemented with growth factors to ensure that the overall growth factor concentration remained constant. An EGM-2:TCM ratio of [2:1] was initially tested and time-lapse images were taken to observe any differing morphologies as the networks developed. Figure 81 shows confocal microscopy images taken of GFP-HUVECs self-assembling into healthy (a) and TCM (b) networks at 48, 120 and 168 hour time points. High magnification images of healthy (c) and TCM (d) networks are also shown in Figure 81, which enables the morphological differences to be further observed.

Both healthy and TCM networks showed similar progression for the first 48 hours when the same media was used however, the effects of conditioning networks with TCM became apparent after 120 hours. TCM networks were found to initially form more fragmented networks with continually branching structures protruding from vessels – highlighted by white arrows. In comparison, healthy networks formed continuous networks more readily and showed little branching after 120 hours. As described throughout the previous section, healthy networks were observed to mature after 144 hours, at which point lumen formation stabilised and perfusion was possible. Whereas vasculature formed using TCM was not observed to stabilise, and vessels continued to form additional branches and wider lumens. This was reflected in images taken after 168 hours, which show healthy networks having a smooth consistent morphology compared to TCM networks which have disjointed, tortuous structures which are highlighted by red arrows in Figure 81b and d.

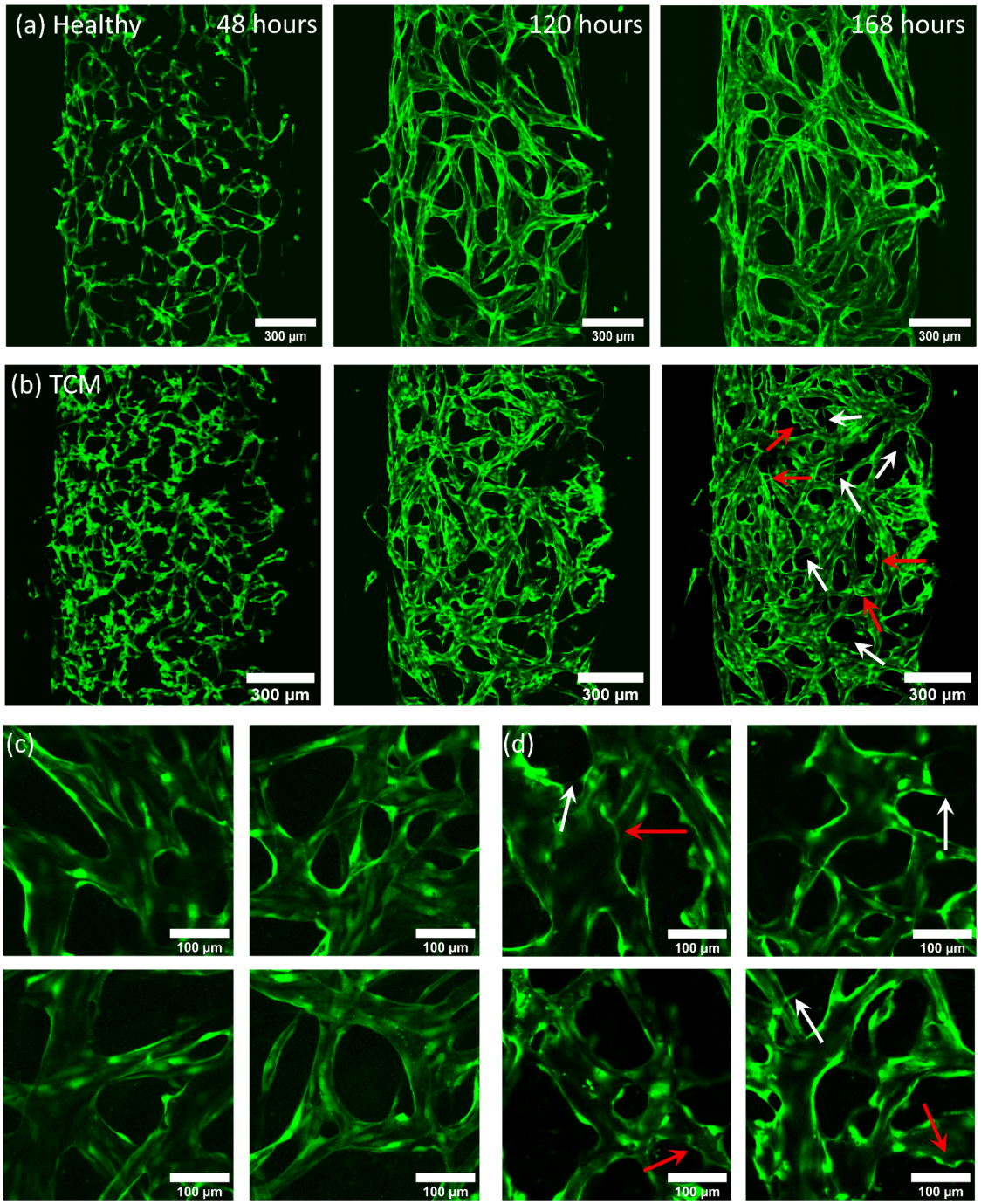

Figure 81 – Fluorescent images acquired (using 10× objective) of GFP-HUVECs self-assembling into fully perfusable vasculature networks 48. 120 and 168 hours after seeding. (a) shows healthy cultures grown using EGM-2 media and (b) shows cultures conditioned with EGM:TCM [2:1] media for the final 5 days of culture. White arrows highlight branching structures and red arrows highlight tortuous, bulbous vessel morphologies. (c) and (d) show higher magnification images of healthy and TCM networks, respectively.

Networks formed with TCM conditioning showed some characteristics similar to those formed with EGM-2 media without VEGF and FGF growth factors removed – shown in Figure 82a. The constant pro-angiogenic VEGF and FGF stimuli ultimately resulted in networks failing to form realistic structures, but the rounded, bulbous vessel morphologies were similar to structures observed in TCM networks. This indicated that the use of TCM induced networks to undergo continued angiogenesis, inhibiting vessel maturation and driving the overgrowth of vessel lumens. This agrees with observations from previous studies which have found high levels of VEGF in media taken from tumour cells [186].

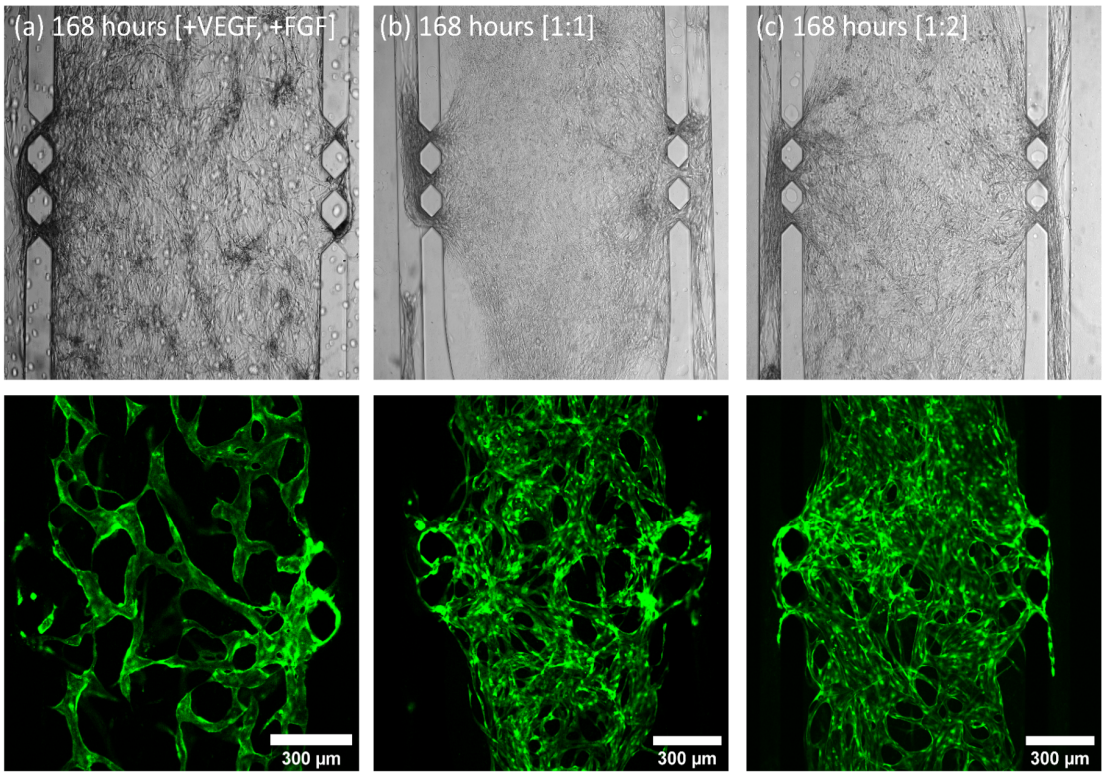

Figure 82 – Brightfield (top) and GFP-HUVEC fluorescent (bottom) images of - (a) A network formed using EGM-2 media complete with VEGF and FGF for the entire 168 hour culture. Maintaining VEGF and FGF resulted in the overgrowth of dilated, bulbous vessels similar to morphologies observed in TCM containing cultures. (b) A network formed using EGM:TCM media in a [1:1] ratio. (c) A network formed using EGM:TCM media in a [1:2] ratio. TCM media was added 48 hours after seeding. After 168 hours of growth, networks grown in both [1:1] and [1:2] TCM media were observed to collapse and contract away from the sides of the culture chamber.

The effects of conditioning networks with higher TCM concentrations used throughout the off-chip co-cultures was also briefly explored. Networks were grown in the two highest TCM concentrations used throughout the previous flow cytometry experiments ([1:1] and [1:2]) and images of their formation after 168 hours can be observed in Figure 82b and c. Higher TCM concentrations resulted in the formation of networks with extreme morphologies. Vessels formed increasingly wide lumens, which were measured to be over 400 µm in some areas and showed no evidence of maturation. Furthermore, after 144 hours cultures began to contract and withdraw from the chamber walls - appearing to collapse. The collapse of cultures resulted in networks being unable to be perfused as fluid was free to flow over the top of the networks. This was suggested to be due to the overgrown vessels being unable to support the surrounding ECM and fibroblasts. Furthermore, this may be a result of the TCM-conditioned NHLFs displaying a contractile phenotype consistently observed with cancer-associated fibroblasts (CAFs) [30,199,200]. Evidence of NHLFs displaying CAF properties was also previously observed in $\alpha_v\beta_3$ upregulation in response to TCM conditioning (section 5.3.2, page 186). In addition to these characteristics, CAFs have been observed to increase their production of pro-angiogenic factors, primarily VEGF and FGF [200,201]. As discussed previously in section 2.1.3 (page 59), reduction of exogeneous VEGF and association of peri-vascular stromal cells with the vessel walls is indicative of vessel maturation and stabilisation. This process only partially occurs in tumour-associated vasculature as overproduction of VEGF by CAFs prevents vessel stabilisation and, in turn, inhibits peri-vascular cell association. The increase in vessel diameter shows indirect evidence of this process occurring, and observation of the lack of fibroblast associated with vessels would provide further proof.

Evidently, the networks formed using the higher TCM concentrations were not realistic or representative of a tumour vasculature network. These extreme morphologies demonstrated the potential of TCM to impact network formation and also highlighted the need for an appropriate choice of TCM concentration. It was therefore decided that an EGM: TCM ratio of [2:1] would be used to condition healthy networks to display tumour vasculature properties.

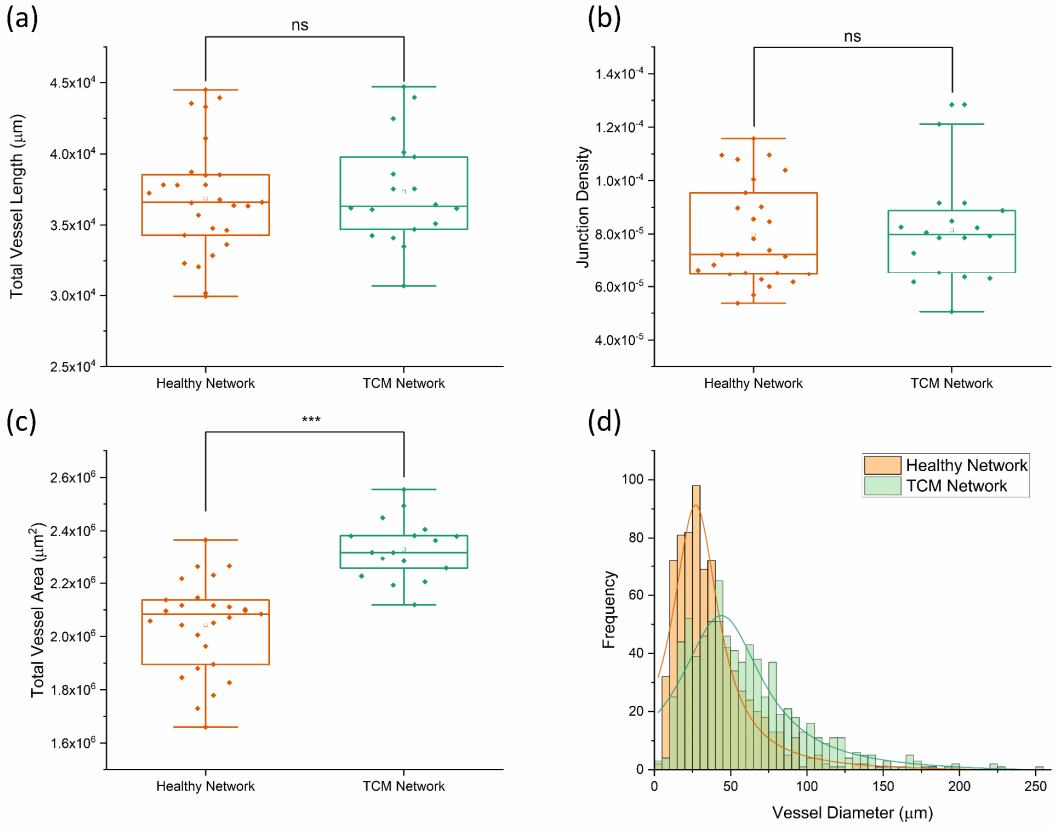

Figure 83 - Boxplots of total vessel length (a), junction density (b), and total vessel area (c) for healthy and TCM networks, determined using AngioTool image analysis. Each data point corresponds to a single network. Comparison of healthy and TCM networks found no statistical difference between total vessel length or junction density. Total vessel area was consistently larger for TCM networks, resulting a 14 % increase on average. (d) Histogram plot of vessel diameters measured using ImageJ. Lorentzian fits used to find modal diameter peak, corresponding to 24.5 ± 1.1 µm for healthy networks and 37.5 ± 2.3 µm for TCM conditioned networks.

The morphological effects of TCM conditioning were quantified by again using AngioTool to analyse networks. Figure 83a – c shows the resultant plots comparing previously shown healthy network values and TCM network values. Analysis revealed no significant difference in values for total vessel length (Figure 83a) and junction density (Figure 83b) whereas total vessel area (Figure 83c) was observed to increase 14 % from healthy values, to (2.3 ± 0.1) x 10^6 µm^2. This reflected imaging observations which observed an increasing trend in network area with TCM concentration. ImageJ was again used to measure vessel diameters, the histogram of which is shown in Figure 83d. The increased lumen formation induced by the apparent pro-angiogenic signalling from TCM

media results in the peak median vessel diameter increasing approximately 50 % - from 24.5 ± 1.1 µm in healthy networks to 37.5 ± 2.3 µm in TCM networks. This was primarily influenced by the observation of significantly more vessels exceeding a diameter of 50 µm.

Observations of increased vessel dilation and overall network area are well aligned with observations throughout previous tumour vasculature models. Eddy and Casarett studied the development of tumour vasculature in a malignant neurilemoma hamster model using a transparent cheek pouch chamber [202]. Vessels close to the tumour implant were found to have dilated, increased in tortuosity and formed bulbous structures. Angiogenic sprouting from host vessels was also observed and resulted in remodelling of the host venules as the tumour increased in size. Tumour vessels were observed to reach diameters as large as 200 µm, consistent with maximum diameters observed throughout this system. The effect of tumours on vasculature morphology was also investigated by Yamaura and Sato, who observed a 3-fold increase in vascular surface area and a 5-fold increase in vascular length, per unit volume of tissue [203,204]. Together, these observations support those made throughout this study, and further support the supposition that TCM can indirectly induce a similar tumour vasculature morphology to vasculature produced through direct contact with tumour cells.

5.4 Conclusion

This chapter outlines the design, development, and characterisation of a fully perfusable microfluidic vasculature model. The microfluidic system was first designed by considering the interstitial flow and pressures required to induce angiogenesis – the formation of new blood vessels. Reservoirs integrated into the system provided passive, hydrostatically-driven flow which was shown to match physiological rates of flow. A range of cell types and passage numbers were tested both on and off-chip to determine the optimal configuration for vasculature production. It was discovered that NHLFs resulted in the most reliable network formation, with HDFs proving unreliable, and HFFF2s showing no angiogenic potential whatsoever. HUVECs were found to have the greatest angiogenic ability when their passage was minimised and kept below p5. Characterisation of flow rates and vasculature permeability found that networks closely

recreated many physiological characteristics of *in vivo* vasculature. Finally, it has been shown that the conditioning of networks with TCM results in the formation of vasculature which displays many characteristics consistent with *in vivo* tumour-associated vasculature. Increased vessel area, diameter, and integrin $\alpha_v\beta_3$ expression were all observed as a result of TCM conditioning. This presents a novel method of producing tumour-associated vasculature using the paracrine cytokines and growth factors secreted by tumour cells. This simplistic method of producing tumour-associated vasculautre overcomes many of the difficulties presented when tumour cells are directly incorporated into vascualture models. Whilst the use of indirect tumour conditioning prevents the direct evaluation of anti-cancer therapeutics on tumour cell viability, this approach still allows for the evaluation of potential novel targeting and drug-delivery strategies.

As described previously, the attachment of targeted antibodies to MBs and LSs has been explored as a method of increasing MB and LS accumulation in tumour tissues. Antibodies targeting VEGF have previously been of interest due to the upregulation of VEGF found in tumour tissues undergoing angiogenesis [205]. As $\alpha_v\beta_3$ is often found to be expressed in and around cell-ECM contacts on the surface of the endothelium, its location is of particular interest to MB-related treatments. Applying US to MBs targeted to these regions could potentially create significantly larger gaps in the endothelium than targeting the surface of all endothelial cells. A recent study using $\alpha_v\beta_3$-targeted MBs found that some sonoporation events induced endothelial cells to retract from neighbouring cells, resulting in the formation of a large gap in the endothelium as proposed [86]. However, this investigation was conducted using a basic endothelial cell monolayer model, which neglected to incorporate sufficient flow conditions or supporting ECM components - thus limiting the validity of these observations. The use of integrin $\alpha_v\beta_3$-targeted MB has also been investigated as a means of using imaging tumour angiogenesis and vasculature using US [206–208]. Anderson et al observed a 5-fold increase in targeted MB US intensity compared to controls and found significantly decreased intensity when mouse tumours were pre-treated with an antibody to block integrin $\alpha_v\beta_3$ [209]. It is evident that $\alpha_v\beta_3$-targeted MBs offer a promising means of targeting tumour vasculature, however further research into the impact of targeting on MB-mediated drug delivery is still required.

Experiments, therefore, progressed into implementing the use of healthy and tumour vasculature networks to evaluate the efficacy of integrin $\alpha_v\beta_3$-targeted MB. An increase in LS accumulation in networks displaying tumour-vasculature properties compared to healthy networks would demonstrate the efficacy of the localised tumour-specific treatment proposed by the use of integrin $\alpha_v\beta_3$ targeted-LS-MB conjugates.

6 RESULTS III: MICROBUBBLE-MEDIATED DELIVERY OF A_VB_3-TARGETED LIPOSOMES TO TUMOUR VASCULATURE NETWORKS

The successful development of both healthy and tumour vasculature networks now allowed experiments to progress to investigating the effects of microbubble (MB)-mediated sonoporation on the endothelium. The two main aims of this series of experiments were the evaluation of targeting model drug carriers (liposomes) to integrin $\alpha_v\beta_3$ - an integrin upregulated in tumour vasculature and evaluation of MB-mediated sonoporation on the extent of liposome (LS) accumulation within vasculature networks. If shown to be successful, targeted LSs conjugated to MBs would offer a two-fold localised delivery mechanism, using targeting and ultrasound (US) to deliver therapeutics primarily to tumour tissue. It has previously been shown that endothelial cells conditioned with TCM increase $\alpha_v\beta_3$ expression, agreeing with observations made from *in vivo* tumour vasculature. Targeted LSs conjugated with $\alpha_v\beta_3$ antibodies were perfused through both healthy and tumour networks to observe the effects of $\alpha_v\beta_3$ integrin upregulation on the accumulation of liposomes. Experiments then proceeded with the observation of LS accumulation after MB exposure.

6.1 Perfusion of $\alpha_v\beta_3$-targeted Liposomes through Vasculature Networks

Prior to any MB related experiments, it was first necessary to observe the passive accumulation of targeted and non-targeted LSs within the vasculature networks. The efficacy of targeting drug carriers to integrin $\alpha_v\beta_3$ has yet to be properly evaluated in a system as complex as this therefore, accurate quantification of the effect of targeting was required. The first series of experiments aimed to observe the accumulation of targeted LSs in healthy and tumour-conditioned vasculature networks, with results being compared to non-targeted LS and those conjugated with isotype control antibodies.

6.1.1 Targeted Liposome Perfusion through Healthy Networks

As outlined in section 3.3.4 (page 98), LSs used throughout this study were formed via extrusion through a 400 nm membrane. Nanosight and DLS analysis revealed LSs were typically produced at a concentration of 2×10^{12} /mL with an average diameter of 340 ± 30 nm. Red fluorescent atto647N-DOPE lipids (0.2 %) were incorporated into the LS to allow for their perfusion to be imaged and their accumulation quantified. LS were diluted to a working concentration of 10^{11} /mL then $\alpha_v\beta_3$ antibodies were conjugated to the surface using the protocol outlined in section 3.3.4.3 (page 99). 2µg/mL and 4µg/mL antibody concentrations were each tested to observe whether an increase in targeting resulted in an increase in accumulation – providing evidence that the inclusion of $\alpha_v\beta_3$ targeting was driving LS accumulation. Isotype control antibodies were also tested at each concentration to observe whether any increased accumulation was a result of non-specific antibody binding, as opposed to binding specifically to integrin $\alpha_v\beta_3$. These two initial antibody concentrations were chosen to be similar to concentrations of antibodies used for $\alpha_v\beta_3$ and VEGF targeting previously reported throughout literature [86,149,196,210]. Accumulation results observed with 2µg/mL and 4µg/mL would determine whether higher antibody concentrations were required and also allow for observation of any trend in the increased accumulation with increasing targeting concentration.

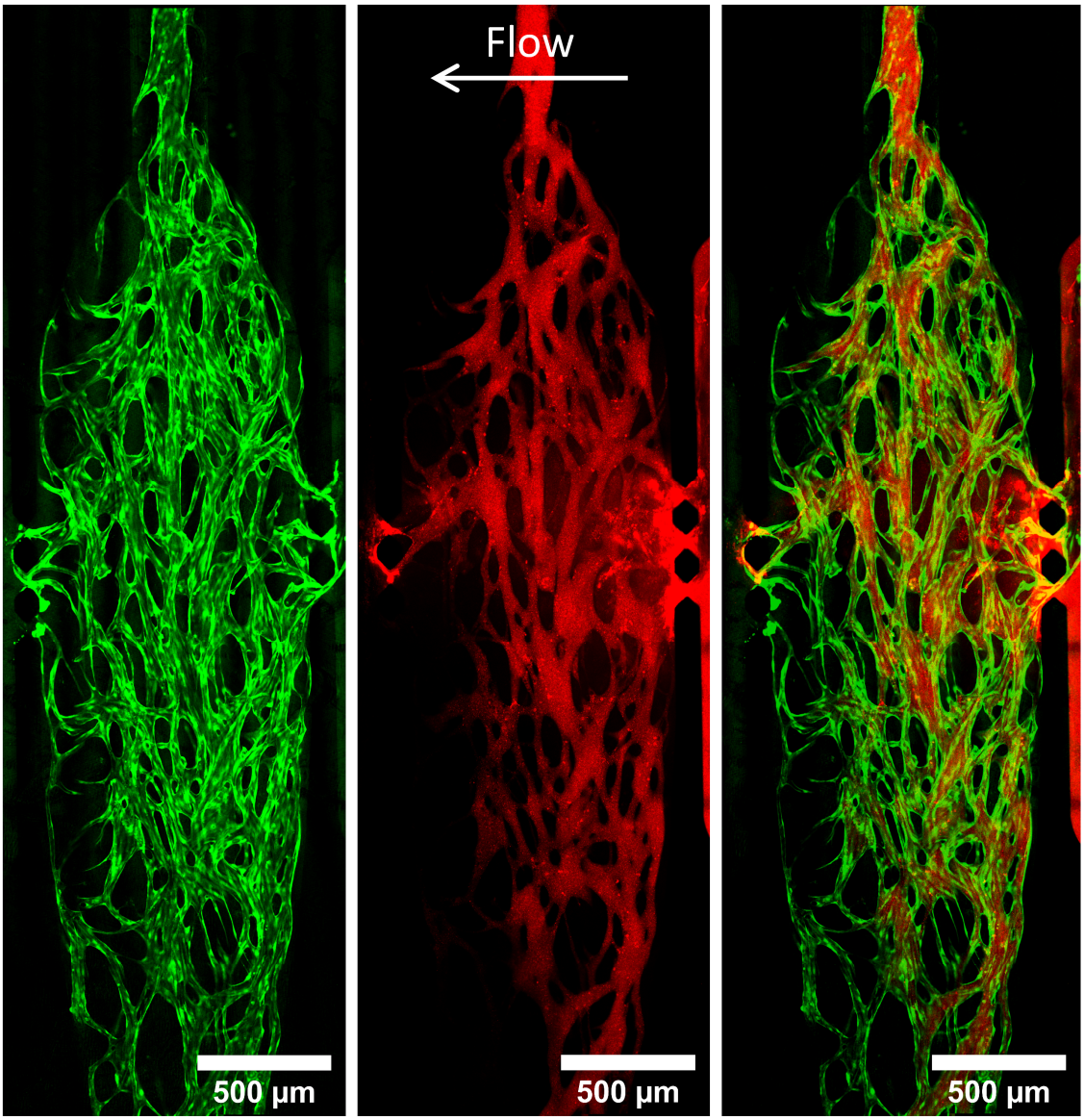

Figure 84 – a) Merged tile scan image of GFP-HUVECs after 6 days of on-chip growth. A continuous network was formed, complete with anastomosed vessels at the micropillar gaps. b) Merged tile scan image of red fluorescent (atto647N) liposomes perfusion through the network. Liposomes can be seen to perfuse through almost all vessels within the network and exit through the adjacent side channel. c) Overlay of images shown in a) and b) - showing confinement of liposomes to the vessels.

Healthy vasculature networks grown using only EGM-2 were first perfused with LSs to observe the extent of accumulation. Figure 84 shows images taken of LSs perfusing through a healthy network, with an overlayed image showing how LSs are confined exclusively within the vessels. Flow throughout each network was generally homogeneous and the majority of the vessels were perfused with LSs. Regions without flow were occasionally observed and suspected to be a result of insufficient anastomosis, creating back-pressure in the vessels due to the lack of an outlet. Regions without flow were identified and excluded from accumulation imaging so results were not skewed. Regions close to the pillar gap entrance were also excluded due to the leakage of LSs into the surrounding matrix.

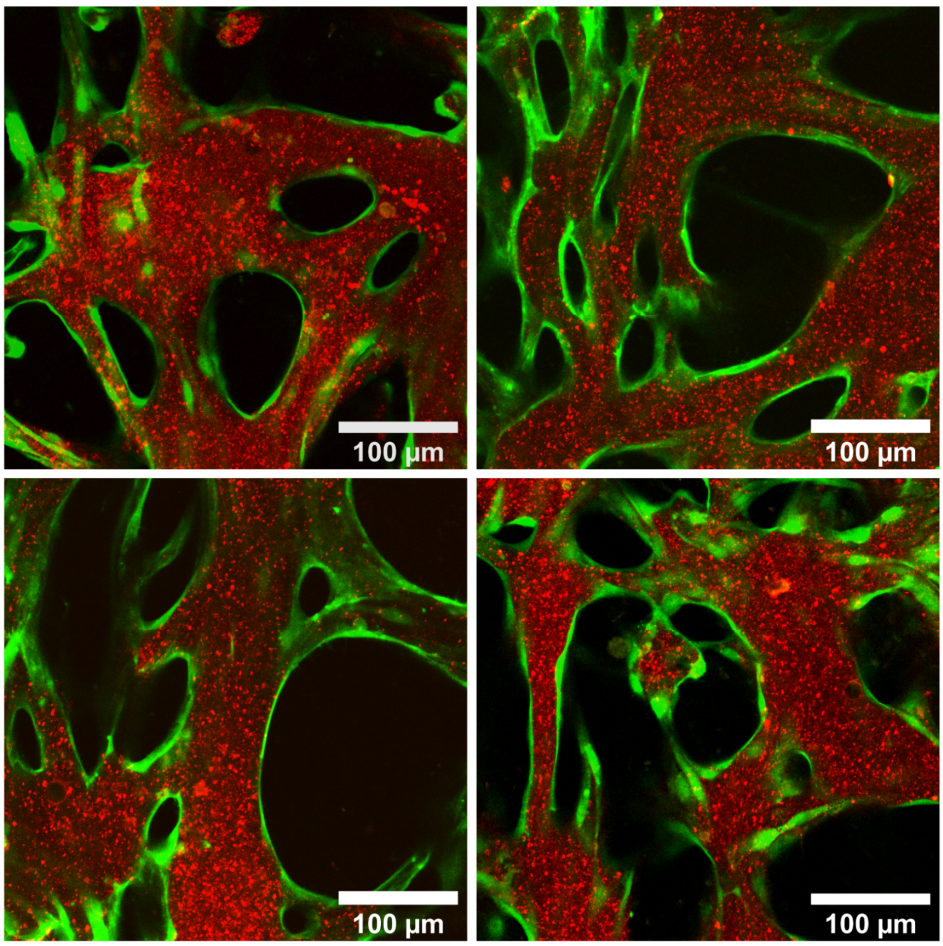

Figure 85 – Confocal fluorescent microscopy images of liposomes (red) perfusing through vasculature networks (green) taken using 40x objective. Lack of leakage of liposomes from vessels further demonstrates network and endothelial barrier functionality.

LSs were allowed to perfuse through the network for one hour, in which time several time-lapse images were taken to observe the extent of the perfusion. Figure 85 shows examples of these perfusion images, taken at a higher resolution than in the previous figure. These images further show endothelial barrier functionality with LSs being well confined within the lumens. Time-lapse imaging at the same locations allowed for LS accumulation to be imaged as perfusion occurred. Figure 86a shows an example of several images taken of the same location in 5-minute intervals. Targeted LSs can be seen to accumulate at several points which are highlighted by white arrows. This was an early indication that the use of targeting antibodies was influencing the accumulation of LSs and resulting in LSs adhering to regions where integrin $\alpha_v\beta_3$ was being sufficiently expressed. Figure 86b shows an image captured towards the end of LS perfusion, allowing for regions of increased accumulation to be observed – again highlighted by white arrows. In general, LSs appeared to accumulate more in smaller vessels which indicates higher $\alpha_v\beta_3$ integrin expression occurring on the surface of smaller vessels. $\alpha_v\beta_3$ is known to be upregulated in angiogenesis and it is reasonable to assume that the smaller vessels throughout the network will be undergoing increased rates of angiogenesis compared to the larger, more mature, vessels. This is further supported by the fact that the rate of flow through smaller vessels was observed to be higher than that in larger vessels, meaning the increased rate of shear stress should make it more difficult for LSs to adhere to the surface of smaller vessels. However, the increased pressure throughout smaller vessels may also be driving the mass transport of LSs into the surrounding tissues, resulting in the increased accumulation of LSs observed.

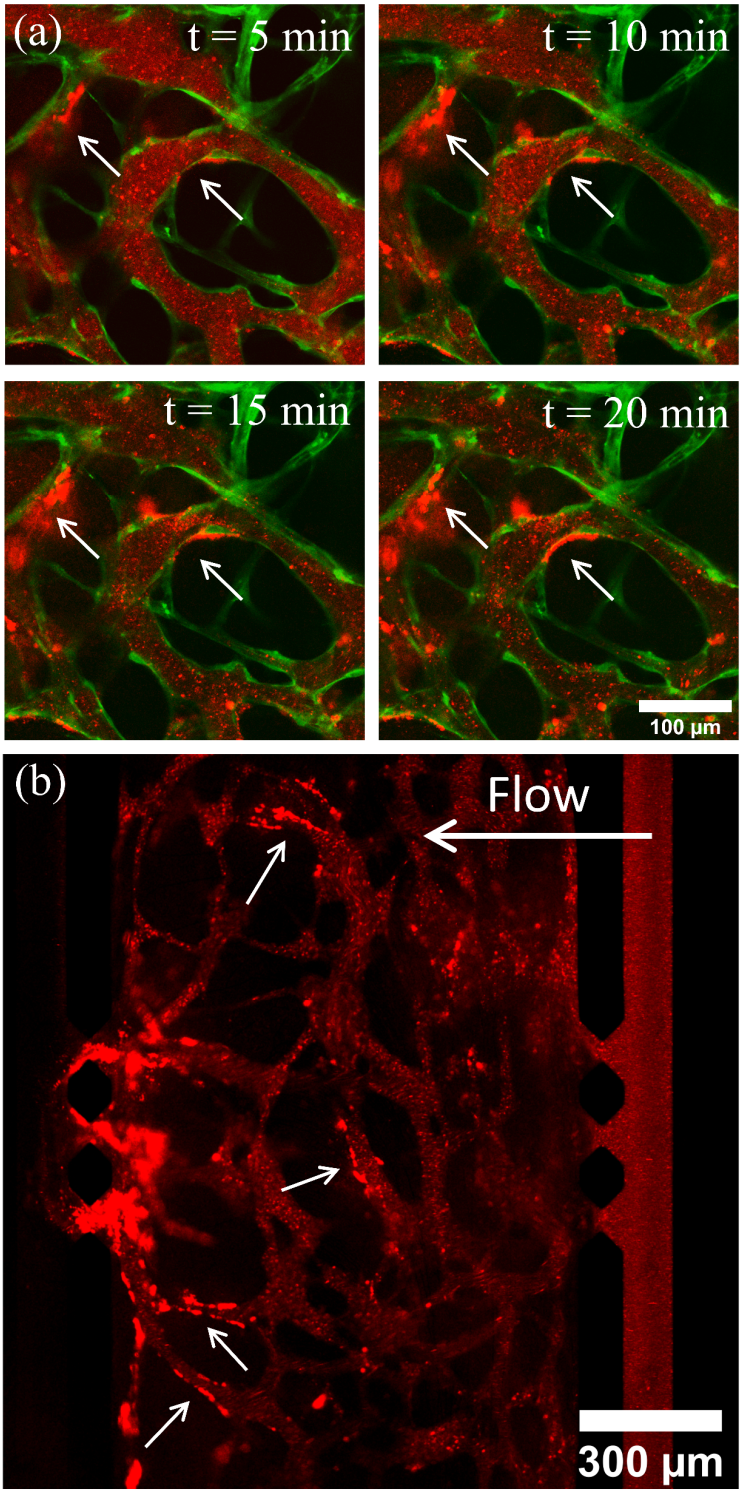

Figure 86 – a) Time lapse images showing LS accumulation across several points on the vessel surface. Images were taken in 5 minute intervals using a 40x objective. b) Image taken of an entire network towards then end of LS perfusions. White arrows show regions of LS accumulation which typically correspond to smaller vessels.

After one hour, fresh media was added to the reservoirs and allowed to perfuse for a further hour. This removed all unbound LSs from the network, leaving only LSs that had bound and accumulated within the network. Imaging was then performed across several regions of each chip, using a 100x objective and z-stacks to capture entire profiles of vessels. Accumulation was quantified using the particle analysis tool in ImageJ, then the average intensity for each z-stack was plotted as a single data point in a boxplot. Between 4 – 6 z-stacks were captured across each network and each exposure condition was repeated with at least 1 chip in 3 separate experiments. Figure 87 shows a series of images taken of LS accumulation after LSs conjugated with 2 µg/mL isotype control antibodies (IC-LS 2 µg/mL), 2 µg/mL $\alpha_v\beta_3$ antibodies (T-LS 2 µg/mL), 4 µg/mL isotype control antibodies (IC-LS 4 µg/mL) and, 4 µg/mL $\alpha_v\beta_3$ antibodies (T-LS 4 µg/mL) were perfused through healthy vasculature networks.

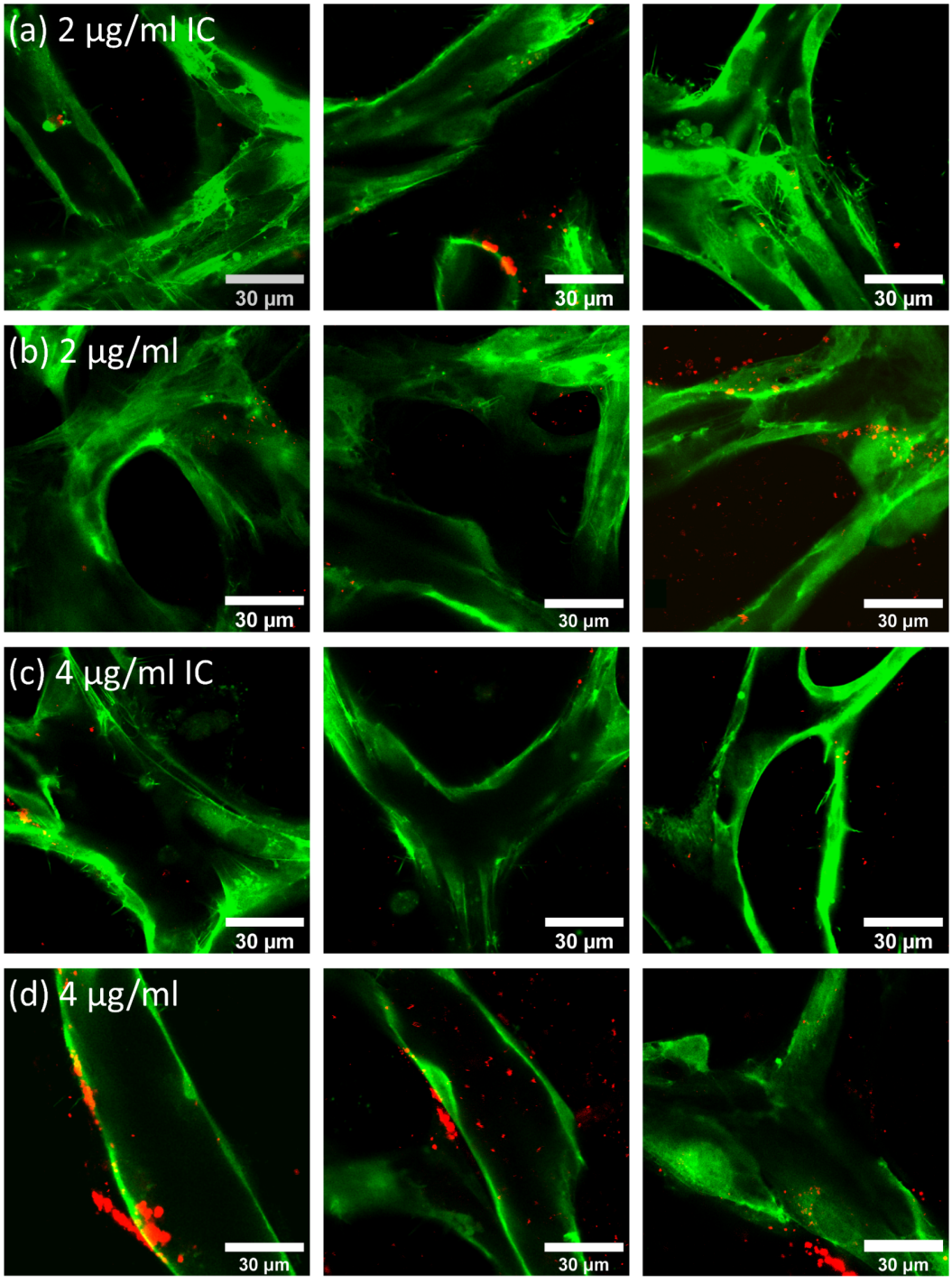

Figure 87 – Post-perfusion fluorescent images of LS (red) accumulation after perfusion of 2 µg/mL isotype control LS (a), 2 µg/mL targeted LS (b), 4 µg/mL isotype control LS (c), and 4 µg/mL targeted LS . Images are taken in 1.5 µm z-stack slices with a 100x oil immersion objective.

Figure 88 shows a graph of quantified LS accumulation for each of the above conditions, along with a non-targeted (NT-LS) control. NT-LS with the same lipid composition but without any antibodies present showed very little accumulation within the vasculature networks and resulted in an average fluorescent intensity of 180 ± 20. T-LS 2 µg/mL resulted in an average accumulation intensity of 600 ± 70, showing a significant increase compared to the non-targeted condition. LSs were observed to accumulate diffusely throughout the vasculature, not appearing to bind to any regions specifically. Perfusions performed with IC-LS 2 µg/mL, found a similar degree of accumulation (600 ± 120), suggesting the increase in accumulation is primarily due to the non-specific binding of antibodies to the vessel walls.

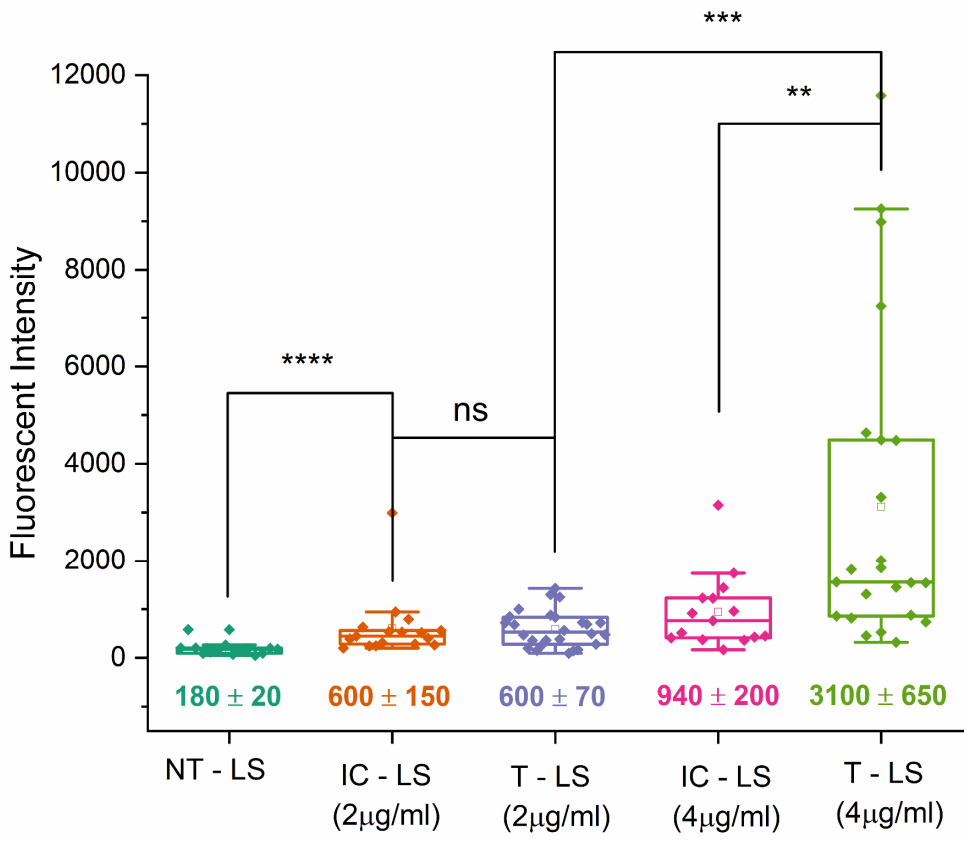

Figure 88 – Graph showing quantified fluorescent intensity of liposome accumulation for non-targeted liposomes (NT-LS) and liposomes conjugated with 2 µg/mL isotype control antibodies (IC-LS 2 µg/mL), 2 µg/mL $\alpha_v\beta_3$ antibodies (T-LS 2 µg/mL), 4 µg/mL isotype control antibodies (IC-LS 4 µg/mL) and, 4 µg/mL $\alpha_v\beta_3$ antibodies (T-LS 4 µg/mL). Images such as those in Figure 87 were used to quantify accumulation with each z-stack corresponding to a single box plot point.

Perfusion of T-LS 4 µg/mL LSs was previously observed to result in accumulation of LSs on the surface of the vasculature as perfusion occurred (shown in Figure 86). This increase was reflected in the quantified accumulation values, with the average intensity found to be 3100 ± 600 – a 5-fold increase on the 2 µg/mL LS accumulation average. Several regions imaged and analysed were found to contain large numbers of LSs bound to specific regions of the vasculature – as shown in Figure 87. These regions resulted in fluorescent intensity values of typically 2000 or above. Regions analysed below this value were found to show accumulations more consistent with non-specific antibody binding. This was reflected in the 4 µg/mL isotype control (IC-LS 4 µg/mL) results which also showed an increase in accumulation compared to 2 µg/mL perfusions but did not result in regions of significant LS binding. This, therefore, suggests that several of the lower value intensities observed for T-LS 4 µg/mL perfusions were due to non-specific binding, whereas accumulations above 2000 were due to specific $\alpha_v\beta_3$ integrin binding. Performing a Mann-Whitney U-test revealed no statistical significance between 2 µg/mL isotype or targeted LS accumulations, whereas 4 µg/mL targeting showed ** significance when tested against the 4 µg/mL isotype control. The lack of specific binding observed with 2 µg/mL targeting suggested that there was insufficient binding occurring between LS and integrin $\alpha_v\beta_3$ proteins to overcome the shear forces being induced by the continuous flow occurring in this system. A targeting concentration of 4 µg/mL was required to observe significant increases in accumulation compared to that of isotype controls - suggesting a threshold concentration for effective integrin $\alpha_v\beta_3$ targeting in this configuration. It is difficult to compare these observations to previous studies as little investigation has been carried out on similar systems with $\alpha_v\beta_3$ antibodies. Successful targeting of particles to endothelial cells has been reported with the use of 6 µg/mL $\alpha_v\beta_3$ antibodies in static monolayer conditions, which suggests that $\alpha_v\beta_3$ expression may be occurring at an increased rate in this configuration, as targeting has been observed at a lower concentration and under flow conditions [86]. This is to be expected, as this system closely recreates the angiogenic process – in which integrin $\alpha_v\beta_3$ is heavily involved [192,211].

6.1.2 Targeted Liposome Perfusion through Tumour Vasculature Networks

Results throughout section 5.3 (page 183) have demonstrated that TCM can be used to condition vasculature networks to display tumour-associated characteristics. $\alpha_v\beta_3$ integrin upregulation, increased vessel diameter, and a tortuous morphology were all observed when cell cultures were exposed to TCM – indicating that the soluble factors secreted by tumour cells were sufficient to influence cell behaviour. The previous perfusion experiments through healthy networks revealed that targeting LSs to integrin $\alpha_v\beta_3$ resulted in increased accumulation when an antibody concentration of 4 µg/mL was used. Experiments, therefore, progressed with the perfusion of $\alpha_v\beta_3$-targeted LSs through networks conditioned with TCM, to observe whether the induced $\alpha_v\beta_3$ upregulation observed in flow cytometry experiments translated to increased LS accumulations in vasculature networks. As only the 4 µg/mL targeting concentration was shown to result in statistically significant LS accumulation compared to the isotype control, this was the only concentration considered in these experiments.

Perfusion experiments were performed using the same protocols as previously described, and post perfusion imaging was again used to determine the extent of LS accumulation. Figure 89 shows post perfusion images of LS accumulation in TCM networks, alongside a graph of quantified accumulation values. The graph contains the previously shown accumulation values with 2 µg/mL and 4 µg/mL LSs in healthy networks along with the 4 µg/mL LS TCM network accumulation values. Post perfusion imaging revealed regions of large clusters of LSs bound to specific regions of the endothelium, as was observed in healthy networks. The frequency and magnitude of the accumulations were found to increase compared to previous conditions, which resulted in maximum fluorescent intensity values of approximately 18,000 – an increase of 50 % on the previous healthy network value of 11,500. In addition to this, significantly more regions of LS accumulation were observed to be above the 2000 fluorescent intensity value previously proposed to be indicative of specific $\alpha_v\beta_3$ integrin binding. This increase in the overall distribution of TCM accumulation values can be best observed when comparing the median intensity values for each distribution. Healthy network median intensity values were calculated to be 1500 ± 800 whereas TCM network values were found to be 3000 ± 1200 – showing a consistent increase across the entre accumulation intensity range. This

indicates that integrin $\alpha_v\beta_3$ is being expressed more consistently and homogeneously across TCM conditioned networks, suggesting that many vessels within these networks are being induced to remain in an angiogenic state rather than stabilise into mature, healthy vessels.

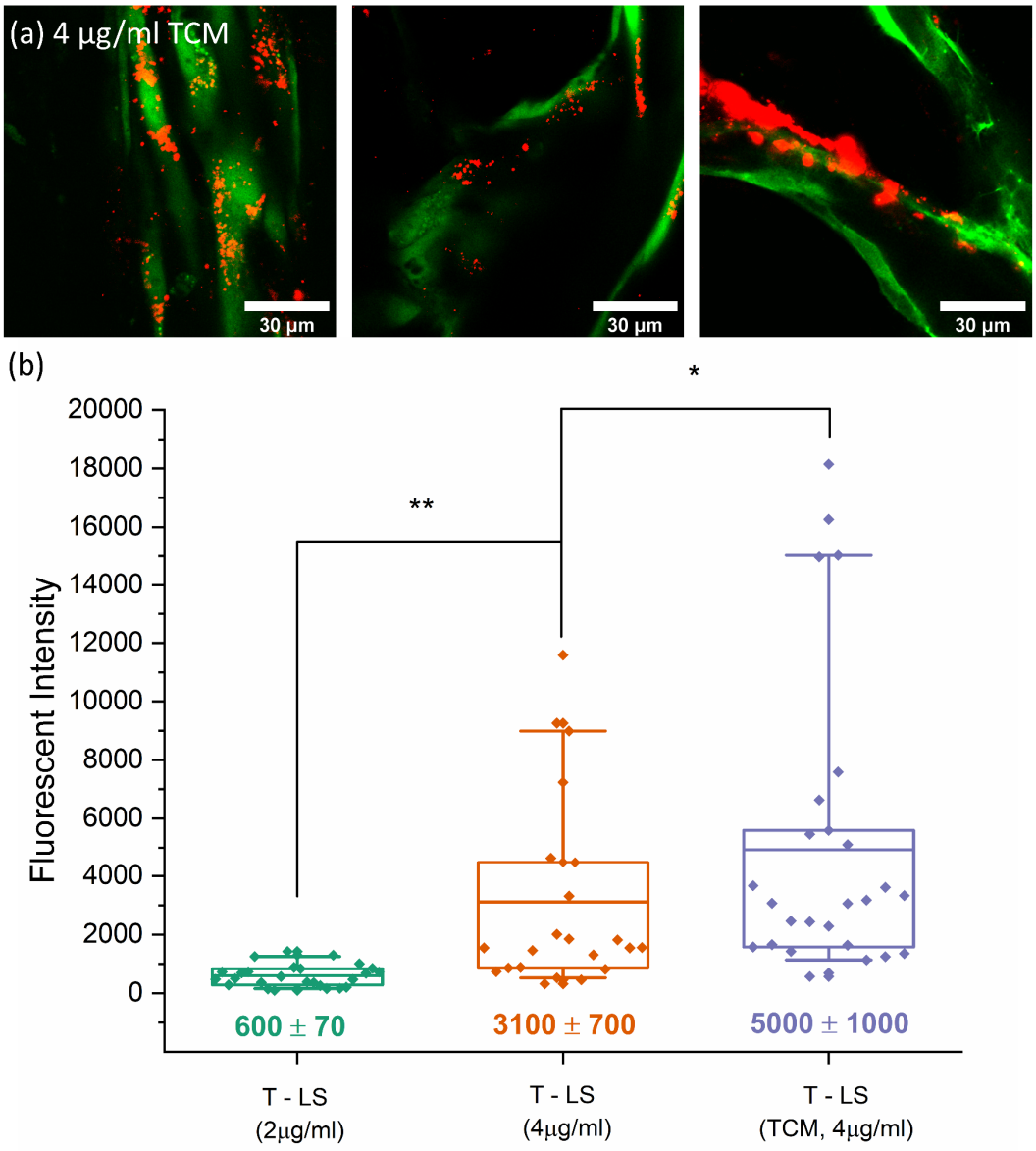

Figure 89 - (a) Post-perfusion images of 4ug/mL targeted LS (red) accumulation within TCM-conditioned vasculature networks (green). Images were taken with a 100x oil immersion objective. (b) Graph of quantified fluorescent intensity values for targeted LS accumulation within healthy and TCM vasculature networks.

After perfusions through 7 separate networks, across 4 experiments, the average LS accumulation intensity value was calculated to be 5000 ± 1000. This was a 61 % increase on the previous 3100 ± 700 average intensity value for 4 µg/mL healthy network perfusions. A Mann-Whitney t-test was performed between datasets and found a * significance between healthy and TCM accumulations with 4 µg/mL. Despite the significant increase in average fluorescent intensity, the statistical significance was limited due to the several high-intensity accumulation regions observed throughout healthy networks. Together, the increase in median and maximum LS accumulation values with TCM conditioned networks agrees well with previous flow cytometry observations, which found an increase in integrin $\alpha_v\beta_3$ expression intensity as well as an increase in the number of cells positive for integrin expression. Whilst a series of follow-up experiments using drug-loaded LS would be required to further quantify the therapeutic effect of using integrin $\alpha_v\beta_3$ targeting, these results provide strong evidence that integrin $\alpha_v\beta_3$ targeting could facilitate the increased accumulation of LS in tumour-associated vasculature and, in turn, increase drug delivery to tumours.

6.2 Perfusion of $\alpha_v\beta_3$-Liposome-Microbubble Conjugates through Vasculature Networks

Work so far has demonstrated that this microfluidic vasculature system is capable of mimicking both healthy and tumour-vasculature networks and can therefore be used to evaluate the efficacy of targeting model drug carriers to tumour vasculature. Experiments progressed into evaluating the use of MBs as a potential method of improving the delivery of targeted LS to tumour vasculature. As described previously, MBs offer a means of facilitating local drug carrier accumulation within cells and tissues, through the creation of pores in the cell membrane or associted ECM. Investigations into the effect of targeting MB to integrin $\alpha_v\beta_3$ have also been discussed, with US imaging reported to show a 5-fold increase in imaging intensity [209,212]. Whilst significant investigation has been carried out in observing the impact of blocking integrin $\alpha_v\beta_3$ signalling in cells and inducing endothelial cell apoptosis [191,193], limited investigation into the effects of targeted MB on the ability to deliver therapeutics to cells through sonoporation has been conducted.

As described in section 0 (page 100), 4 µg/mL targeted LS were conjugated to the surface of MB again using biotin-neutravidin binding and incorporating biotinylated DSPE-PEG-

2000 lipids into MB. This formed what is referred to as targeted-LS-MB conjugates (T-LS-MB). The ratio of MB:LS: Neutravidin used to form these conjugates has been previously shown to produce MB-LS conjugates with fluorescent LS being observed to be associated with the surface of MB [213]. As discussed previously in section 3.3.7 (page 104), Neutravidin was added in a 10 × excess compared to the calculated concentrations required, to ensure complete binding of antibodies, LSs and MBs. Along with the complete exposure condition of T-LS-MB perfused through TCM networks the burst with US, two control conditions were tested. The first control looked to observe the impact of bursting MB with US by allowing T-LS-MB to perfuse through TCM networks without the use of an US trigger. Differing LS accumulation intensities would then demonstrate the impact of MB-mediated sonoporation on LS deposition within the vasculature. The second control condition sought to observe the impact of using targeted conjugates in TCM networks by exposing healthy networks to the complete, T-LS-MB and US condition. As MBs are significantly larger than LS, increased adhesion will be required for MBs to remain successfully bound to the vessel surface. This may affect the previously observed targeting efficacy found when using 4 μg/mL integrin $\alpha_v\beta_3$ antibodies.

Perfusion experiments were repeated in the same configuration previously used with US now being incorporated. After perfusion was initiated, T-LS-MB were given 5 – 10 minutes to populate the vasculature network then a 2 second, 2.25 MHz US pulse (1 kHz PRF, 1 % duty cycle) was applied to the vasculature chamber through a gel standoff pad positioned above the chamber. These US parameters have been previously used in MB-related experiments and have been shown to burst approximately 99.6 % of MBs contained within a PDMS device with a 1 mm wall thickness [213]. Characterisation of US attenuation through 1 mm of PDMS has been shown to reduce peak negative pressure to 0.81 ± 0.04 MPa, a 16 % reduction from the 0.94 ± 0.01 MPa pressure measured in a degassed ultrapure water chamber. This resulted in a mechanical index (M.I) value of 0.54 ± 0.03. Figure 90 shows images captured of fluorescent T-LS-MB conjugates perfusing throughout a vasculature network, using the same imaging parameters used to capture LS only images shown in Figure 85. Comparison with images shown in Figure 90 with images shown in Figure 85 reveals the size difference between unconjugated LS perfusing through a network and those conjugated to the surface of MB.

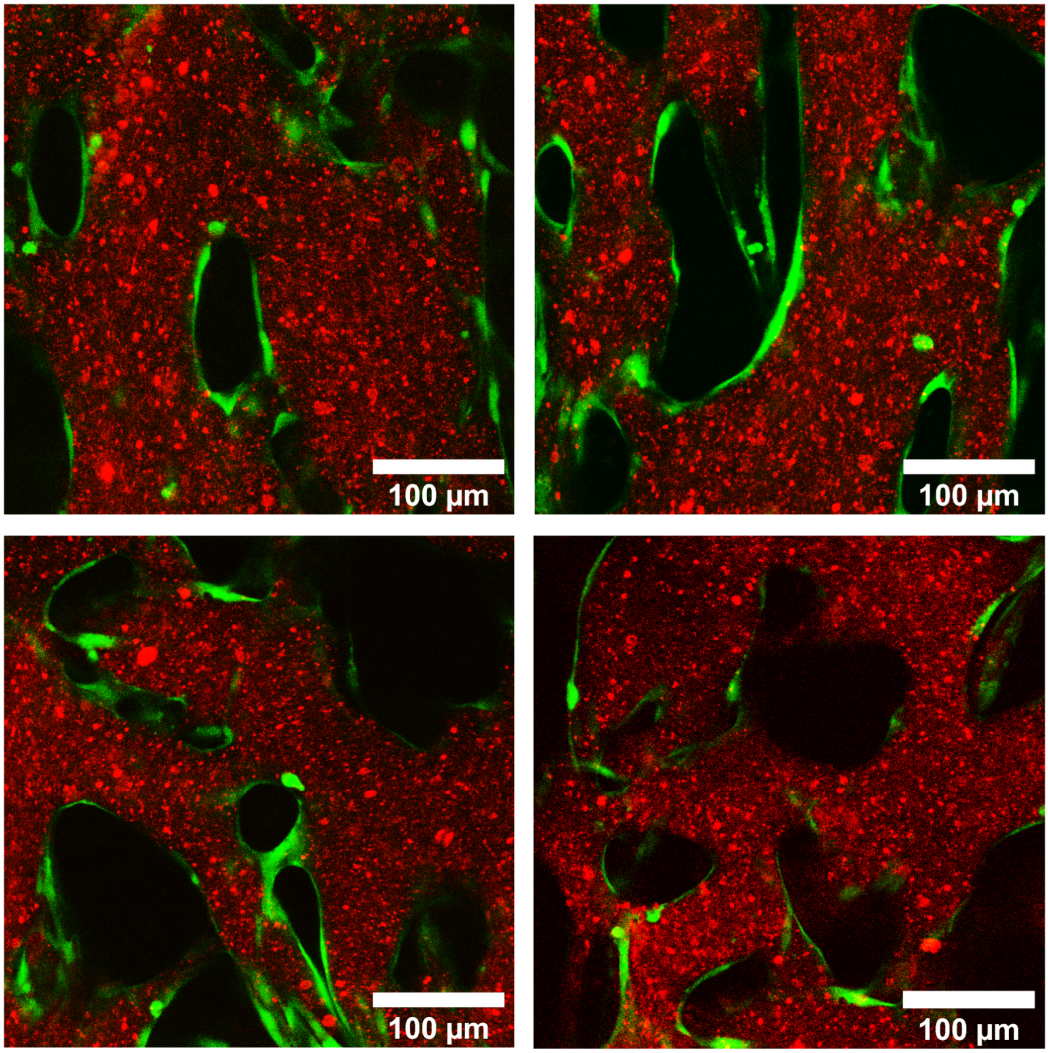

Figure 90 – Confocal fluorescent images of red flourescent LS conjugated to MB perfusing through vasculature (green). The adhesion of LS to the MB surface can be observed by the increased fluorescent particle size compared to LS only perfusions shown in figure Figure 85.

Due to the limitations of the US and imaging setup, it was difficult to capture images immediately post-US exposure. The continuous flow conditions resulted in MBs repopulating the network before images could be acquired. As with LS only perfusions, fresh media was added to the reservoirs 1 hour after perfusion was initiated, and allowed to perfuse for a further hour to remove any unbound LS. Post-perfusion imaging was then performed to evaluate the extent of LS accumulation.

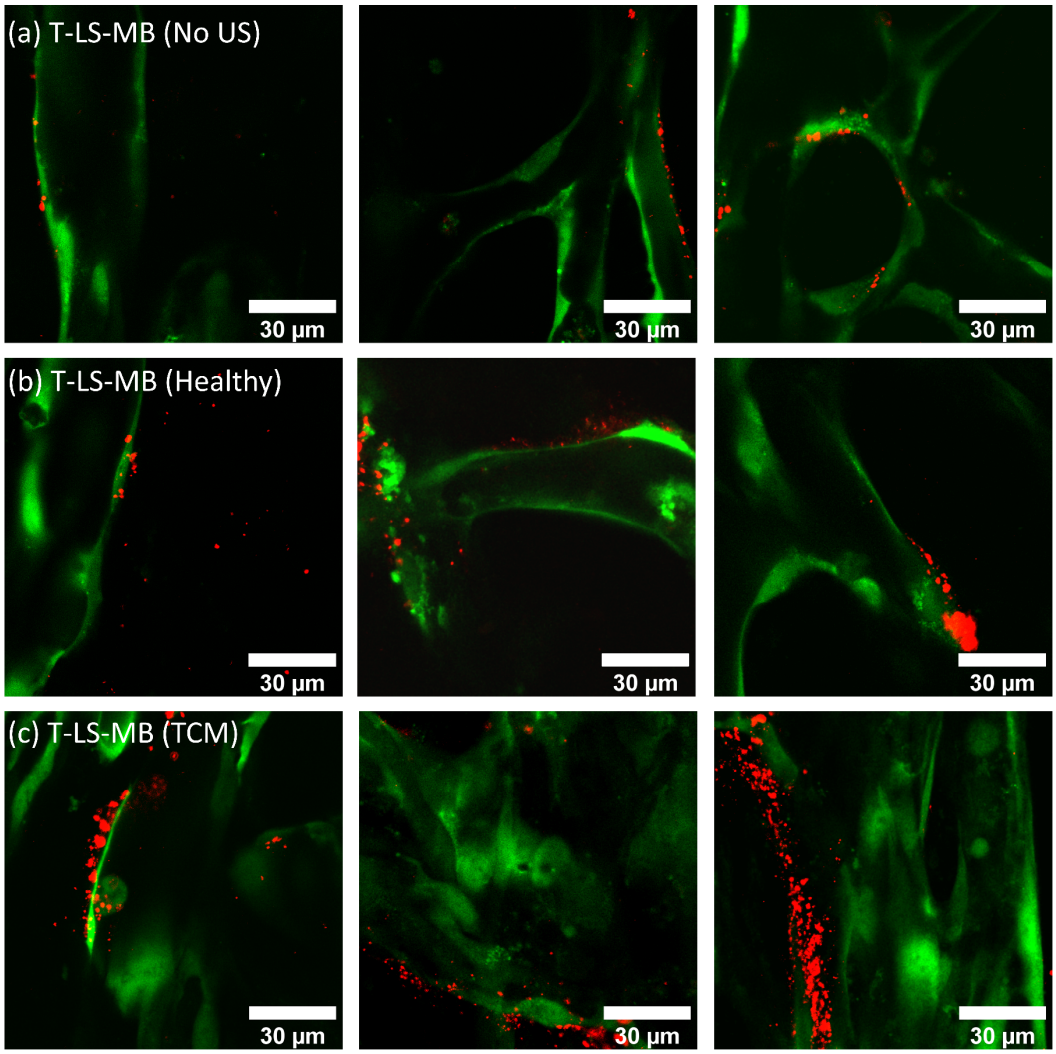

Figure 91 - Post-perfusion fluorescent images of LS (red) accumulation after perfusion of 4 µg/mL T-LS-MB through TCM networks without an US trigger (a), 4 µg/mL T-LS-MB through healthy networks with an US trigger (b), and 4 µg/mL T-LS-MB through TCM networks with an US trigger (c). Images are taken in 1.5 µm z-stack slices with a 100x oil immersion objective.

Figure 91 shows the post-perfusion images captured after perfusion of 4 µg/mL T-LS-MB through TCM networks without an US trigger (a), 4 µg/mL T-LS-MB through healthy networks with an US trigger (b) and the complete exposure condition of 4 µg/mL T-LS-MB through TCM networks with an US trigger (c). Observation of LS accumulation after perfusion of T-LS-MB in TCM networks without an US trigger found relatively few LS across the vessel surfaces. Regions of LS accumulation were commonly observed however the magnitude of LS accumulation in each region was much lower than

previously observed. The high frequency of LS regions suggests that integrin $\alpha_v\beta_3$ is being expressed regularly throughout the network, agreeing with previous TCM conditioning observations. However, the low-intensity values suggest that minimal numbers of LS were free to accumulation within the networks. This shows that a lack of US trigger prevents a significant number of LS from being released from the MB surface. It is difficult to determine whether the use of 4 µg/mL targeting was sufficient to allow for MB adherence to the vessel surface as it is possible that some regions of LS accumulation are a result of MB accumulation and subsequent dissolution. However, the low intensities would suggest that targeting adhesion is insufficient in allowing significant numbers of MBs to persist within the network. Alternatively, free LS in the MB solution may be resulting in the observed accumulation intensities, which may also explain the low intensities but high frequencies observed.

Perfusion and subsequent bursting of T-LS-MB conjugates in healthy vasculature networks were found to result in significantly increased numbers of LS compared to the previous control condition. LS were found to be distributed across many regions of the vasculature surface, resulting in an average fluorescent intensity value of 2200 ± 400. Despite these perfusions being performed in healthy networks, this intensity value was higher than the 1400 ± 200 value found after perfusions through TCM networks without an US trigger – as shown in Figure 92. This demonstrates the impact of bursting MBs on the extent of LS accumulation. Finally, exposing networks to T-LS-MB in TCM networks with an US trigger was observed to significantly increase LS accumulation. Post perfusion imaging observed large swathes of LS across several points on the vessel surface, consistent with observations made throughout 4 µg/mL targeted LS perfusions. Quantification of accumulations found an average intensity of 6800 ± 1200, a 3-fold increase in intensity compared to the same perfusion performed in healthy vasculature. This result provided compelling evidence that the inclusion of 4 µg/mL integrin $\alpha_v\beta_3$ antibodies successfully facilitated the targeting of MB-LS conjugates and allowed for significantly improved LS delivery when MBs were burst with US. Intensity values for this complete exposure condition were found to consistently exceed control values, resulting in a *** statistical significance value when subject to a Mann-Whitney t-test.

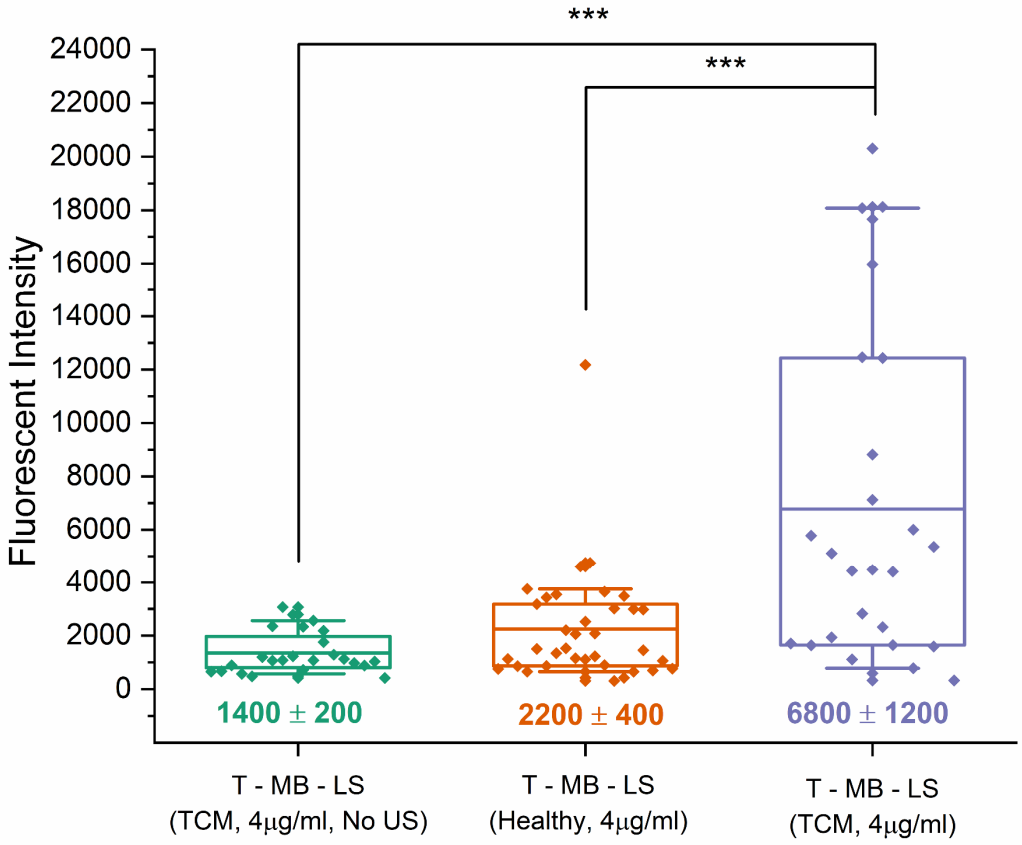

Figure 92 – A boxplot graph showing quantified liposome fluroescence intensities in TCM-networks exposed with T-MB-LS (4 µg/ml) with and without US, and healthy networks perfused with T-MB-LS (4 µg/ml) and US. Each point represents the average intensity across a single z-stack capured.

Images taken after US exposure were unable to observe any immediate effects of MB sonoporation on endothelial integrity. Unlike observations made throughout previous studies, the opening of gaps at cell-cell contacts did not appear to occur. This is suggested to be a consequence of using a physiologically accurate vasculature model which is complete with supporting ECM and stromal components. Observations of junciton opening are often made in systems comporising of endothelial cells seeded onto polycarbonate or PDMS surfaces, which minimally supports the adhesions of cells compared to a functional basement membrane layer [86]. In contrast ot this, many *in vivo* studies have observed the opening of the blood brain barrier (BBB) with the use of MBs and focused US, suggesting that the integrity of the endothelium is affected signifcantly by sonoporation [214,215]. A study by Tung et al. observed that the BBB was only opened

by non-linear MB oscillation hen the MB diameter was similar to the capillary diameter but in all instances of inertial cavitation [213]. As the vessel diameters in the vasculature networks in this study were more comparable to precapillary vessels (> 25 µm) than capillaries (< 10 µm), this may explain the lack of MB impact on cell-cell junction integrity. Continued vasculature integrity after US and MB exposures also suggested that any events resulting in irreversible sonoporation were not sufficient enough to compromise vessel function. However, imaging and analysis were performed on a relatively short timescale therefore the long term effects of MB sonoporation were not observed. Several follow up experiments could be performed to further investigate the MB-related phenomena observed throughout previous studies. It is suggested that very similar experiments previously conducted on simplistic 2D systems could be repeated using this system to observe the impact of improving the physiological relevance of the system. Propidium iodide, dead cell staining, and calcium fluctuations could all be implemented to probe the effects of MB on cell-cell contacts, vessel permeability and overall endothelial integrity [216].

6.3 Conclusion

This series of experiments implemented the use of fully perfusable healthy and tumour-associated vasculature models to evaluate the use of integrin $\alpha_v\beta_3$-targeted LS as model drug carriers with the potential to target tumour-associated vasculature. Initial testing throughout healthy networks revealed that an $\alpha_v\beta_3$ antibody concentration of 4 µg/ml was required to observe statistically significant LS accumulation when compared to isotype control antibodies. The perfusion of 4 µg/ml $\alpha_v\beta_3$ T-LS through TCM-conditioned networks was found to result in a 60 % increase in LS accumulation intensity when compared to identical perfusions throughout healthy networks. This agreed well with previous flow cytometry measurements in section 5.3.2 (page 186), which observed an increase in integrin $\alpha_v\beta_3$ expression intensity and frequency in response to TCM conditioning. Together this revealed the potential of indirectly inducing a tumour-associated phenotype using TCM conditioning.

Experiments progressed with the conjugation of MB to T-LS to form the complete T-LS-MB particles which were suggested to be a means of improving LS accumulation in

tumour-associated vasculature. Analysis of LS accumulation after perfusion of T-LS-MB with an US trigger to burst the MBs, found a 3-fold increase in LS intensity in TCM networks when compared to healthy networks. Again, highlighting the impact of using conditioning networks with TCM. T-LS-MB perfusions through TCM networks without an US trigger found very few LS had accumulated within the vasculature – demonstrating the ability of MB-mediated sonoporation to facilitate the accumulation of LS within the vasculature.

Overall, these results indicated that the delivery of drug-loaded LS to tumour tissues could be enhanced through the combinatory use of integrin $\alpha_v\beta_3$ targeting and MB-mediated sonoporation. Whilst initial results appear promising, several additional experiments are still required to further elucidate the efficacy of integrin targeting and MB-mediated drug delivery. Experiments throughout this study have also demonstrated the ability of this system to evaluate potential anti-cancer therapeutics. Whilst the use of indirect tumour conditioning prevents the direct evaluation of tumour cell viability, increase accumulation and uptake of therapeutics can still be used as an indicator of improved drug delivery. The use of TCM conditioning also enables the straightforward production of tumour-associated vasculature compared to previous tumour vasculature systems, demonstrating the advantages of this relatively simplistic system. It is anticipated that this system will serve as a physiologically accurate platform for the evaluation of various potential anti-cancer treatments which aim to target the tumour vasculature.

7 CONCLUSIONS AND FUTURE WORK

7.1 Conclusions

The overall aim of this project was to develop microfluidic disease models of colorectal cancer with the goal of using these models to evaluate MB-mediated drug delivery. Two distinct models were developed throughout this project each of which was designed, fabricated, characterised, tested and used to investigate MB-related effects. This section summarises the results of each chapter and the impact this work has had on the microfluidic organ-on-chip and MB fields.

Chapter 4 contains the work involved in the development of a microfluidic spheroid trap system. The use of 3D tumour spheroids as more physiologically accurate tumour models is now common practice in many drug development investigations however a lack of fluid flow still limits the relevance of these models. This system was therefore designed to allow for the capture of pre-grown spheroids and testing of drug-delivery strategies under constant flow. Unlike other pre-existing microfluidic spheroid systems, this system was designed by scaling up the framework used to optimise the trapping of microspheres and cells (~10 μm in diameter) to the trapping of spheroids (~350 μm in diameter). The primary design considerations included the optimisation of trap diameters and hydraulic resistances to ensure sufficient numbers of spheroids could be captured. Flow through the system, provided through the use of reservoirs, was designed such that spheroids were exposed to physiological rates of flow and shear stress. A primary advantage of this design was the ability to easily retrieve spheroids post-exposure, for viability evaluation using off-chip assays. Subsequent evaluation of MB-enhanced delivery of Doxorubicin (DOX) revealed that MBs increased the efficacy of both free and liposomal DOX. Limited initial release of DOX from liposomes (LS) was observed after MBs were burst,

which agreed with similar observations throughout the literature. However, across the 48-hour experimental period, substantially increased release was observed compared to similar studies. It was suggested that the presence of ammonia in the spheroids due to hypoxia and glycolytic energy production may have facilitated the release of DOX from LS in a similar process to the one used to actively load DOX into the LS. This suggested that there may be a relationship between spheroid size and DOX release, due to increased hypoxia at the centre of larger spheroids. Ammonia may diffuse from the centre of the spheroid to the outer layers containing LSs, whereas hypoxic gradients are formed throughout the spheroid structure due to the oxygen depletion from cell consumption in the outer layers. Whilst several questions remain unanswered in the field of MB-mediated drug delivery, this investigation provided further evidence that MBs can be used to enhance the delivery of anti-cancer therapeutics in increasingly physiologically accurate systems. Overall, this system provided a platform by which novel anti-cancer treatment strategies could be tested under physiologically relevant flow conditions.

Chapter 5 details the work performed in developing a microfluidic tumour vasculature system capable of evaluating the use of MB to enhance the accumulation of targeted LS. This system further developed the work from groups led by A. Lee and C. Hughes which pioneered the development of fully perfusable microfluidic vasculature systems. A significant part of this chapter consists of the pressure and flow design considerations used to ensure the appropriate biomechanical and biochemical queues were provided to the vasculature cultures. Work then progressed to determining the optimal cell types and passages required to ensure consistent perfusable vasculature could be formed. Finally, experiments progressed to producing networks that displayed tumour vasculature characteristics, namely the upregulation of the target of interest, integrin $\alpha_v\beta_3$. The conditioning of healthy tumour networks with tumour cell media (TCM) was a novel strategy implemented throughout this project. Previous work using TCM was contained to the conditioning of 2D monolayers of immune and endothelial cells. The use of TCM was found to upregulate the integrin $\alpha_v\beta_3$ as well as induce vasculature to display dilated, tortuous structures consistent with those observed from *in vivo* tumour vasculature.

The final results chapter 6 contains the perfusion experiments performed using integrin $\alpha_v\beta_3$-targeted LS (T-LS) and MB in healthy and tumour vasculature systems. This series of experiments aimed to evaluate the use of targeting and MB to enhance the accumulation of LS within tumour vasculature networks. Initial T-LS experiments observed increased LS accumulation in tumour vasculature networks compared to healthy networks, indicating that the previously observed upregulation of integrin $\alpha_v\beta_3$ in response to TCM conditioning translates to an increase in T-LS accumulation within vasculature networks. Next, the impact of conjugating T-LS to MBs was tested. Perfusion through healthy vasculature and exposure to US resulted in the accumulation of relatively few T-LS. Whereas, the same perfusions through TCM-conditioned tumour vasculature resulted in a 3-fold increase in T-LS accumulation. Perfusion without an US trigger to burst MBs resulted in very low amounts of T-LS accumulation, indicating that the bursting of MBs facilitates the uptake of T-LS onto the endothelial surface. Whilst imaging and US limitations prevented any observation of the direct mechanism of this uptake mechanism, this series of experiments provided evidence that the use of integrin targeting and MB-mediated liposome delivery can greatly improve the localised delivery of drug-loaded liposomes to tumour-associated vasculature.

Overall, the series of work displayed across chapters 5 and 6 presents a novel method of producing fully perfusable vasculature cultures which display properties consistent with tumour-associated vasculature. This model allows for perfusion of model therapeutics exclusively through the vessels, with rates of flow and shear stress similar to those found within *in vivo* vasculature. Experiments involving the evaluation of T-LS and MB demonstrated the ability of this system to evaluate potential anti-cancer therapeutics. The use of indirect tumour conditioning prevented the direct evaluation of tumour cell viability in response to treatments, however increased accumulation and uptake of model therapeutics could still be used as an indicator of improved drug delivery. Further applications and development of this system will be discussed in the next section.

7.2 Future Work

7.2.1 Production of a Vascularised Microfluidic Tumour Model

Work throughout the final results chapter outlined the production of a vasculature system that closely mimicked tumour-associated vasculature. Whilst this simplistic approach to producing tumour-like cultures allows for the evaluation of therapeutics aiming to target the tumour vasculature, the lack of tumour cells prevents any cytotoxic evaluation of drug treatments. One future avenue of work briefly explored throughout this project was the incorporation of tumour cultures alongside the healthy vasculature chamber to create a system that would allow for the direct formation of tumour vasculature. Figure 93a shows the microfluidic system designed for this series of experiments, which uses an additional chamber separated by a narrower micropillar array.

Figure 93b shows images from an initial experiment testing the system functionality. RFP-HCT116 CRC cells (red) were seeded alongside healthy GFP-HUVEC vasculature networks (green) and imaged across a 2-week period. The tumours can be observed to invade the vasculature chamber and begin forming tumour associated vasculature. This aims to recreate the process in which a solid, slow-growing tumour undergoes the angiogenic switch and begins to form its own vasculature. As described throughout section 2.1.3 (page 59), hypoxia is one of the main drivers of tumour angiogenesis. Ensuring the tumours cultured in this system develop a sufficiently hypoxic core is therefore crucial to recreating the formation of tumour-associated vasculature. Future work with this system would require optimisation of tumour seeding times to ensure the vasculature is sufficiently developed before the tumour cells begin invading the lower chamber. Consideration of seeding density, matrix composition and co-culture composition will all be required to ensure system functionality.

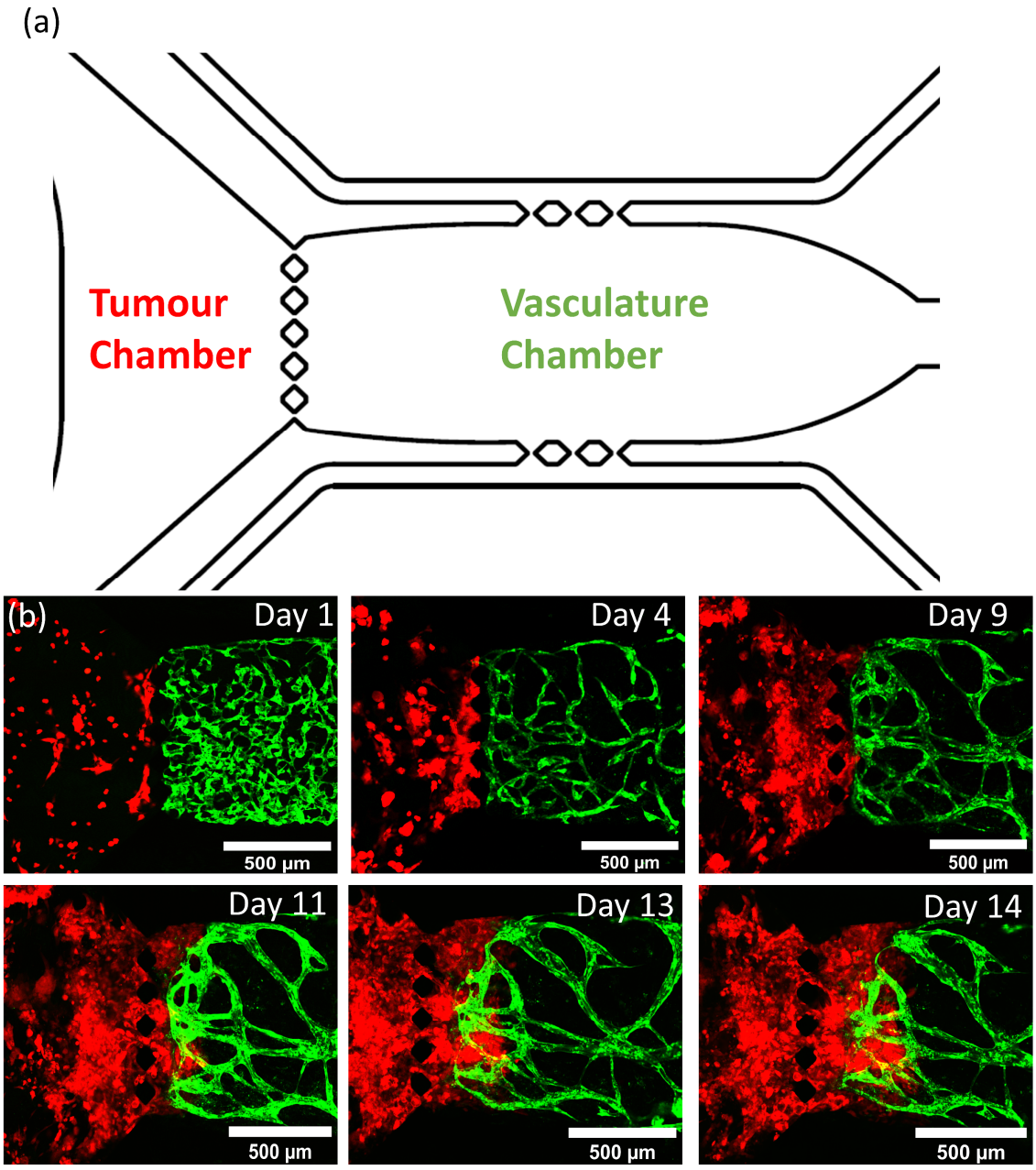

Figure 93 – (a) AutoCAD design of the two-chamber system used to produce a vascularised tumour model. (b) Fluorescent confocal microscopy images taken across a 2-week period of the two-chamber system with red fluroescent HCT116 cells seeded alongside GFP-HUVECs – both sets of cells are co-cutlured with NHLFs. Tumour cells can be observed to invade the vasculature chamber.

7.2.2 Vasculature Models using Endothelial Progenitor Cells

It has been shown throughout this project that low-passage HUVECs are capable of self-assembling into perfusable vasculature networks. Whilst HUVECs possess sufficient angiogenic potential to form vasculature, alternative endothelial cell types with greater angiogenic potential present promising alternatives. Endothelial progenitor cells (EPC) are immature cells that are responsible for the formation of new blood vessels *in vivo*. EPCs mature into adult Endothelial Colony Forming Cells (ECFCs) which circulate in the bloodstream and navigate to areas of injury - where they then differentiate into endothelial cells. As opposed to HUVECs which are isolated from the already formed umbilical cord, EPCs are instead isolated from the blood found within the umbilical cord. Until recently, sufficient populations of immature EPCs were difficult to isolate and culture in large numbers. Recent advances have allowed for EPCs to be isolated and sold commercially. This, therefore, presents a means of improving the validity and success rate of vasculature cultures through the use of cells with a high angiogenic capability. These cells were purchased with the intention of observing the differences in vasculature development and morphology however, time did not allow for these experiments to be performed.

7.2.3 Further Applications of Microfluidic Tumour Models

Both vascularised and solid tumour models have a range of applications that were not covered throughout this report. One application that was briefly visited as part of a collaboration on a project with Joe Fox and Prof Steve Evans, was the use of solid colorectal (CRC) tumours to investigate the secretion and detection of carcinoembryonic antigen (CEA). CEA is a tumour marker that is often used as an invasive method of detecting CRC. New methods of detecting CEA are being developed and have been proposed as a means of monitoring tumour response to specific treatments. This is of particular interest in adaptive tumour treatments which aim to restrict tumour growth with constant low-level treatments. This treatment regime works on the theory that treating cancers with maximum tolerated dose (MTD) chemotherapeutics results in all but the drug-resistant cells being killed. This then allows for the development of an entirely drug-resistant tumour. The use of low-dose, regular drug treatments to kill only a small